

A NOVEL UNCOUPLED METHOD FOR STATIC AEROELASTIC ANALYSIS  
TOWARDS MORPHING STRUCTURES DESIGN

A Dissertation

by

WILLIAM DAVID SCHOLTEN

Submitted to the Office of Graduate and Professional Studies of  
Texas A&M University  
in partial fulfillment of the requirements for the degree of

DOCTOR OF PHILOSOPHY

Chair of Committee, Darren Hartl  
Committee Members, Thomas Strganac  
Richard Malak  
Paul Cizmas  
Head of Department, Rodney Bowersox

May 2020

Major Subject: Aerospace Engineering

Copyright 2020 William David Scholten

## ABSTRACT

Fluid-structure interaction (FSI) analysis is a common tool used to analyze aeroelastic problems. The traditional FSI scheme couples independent structure and fluid solvers in space and time. For many aerospace applications the final equilibrium configuration of the structure is of interest, which can only be obtained by incrementally iterating the fluid and structure solvers until convergence is obtained in time, resulting in a computationally expensive process. This work develops a new method for conducting FSI analysis that greatly expedites design studies. This new scheme, referred to as the uncoupled static aeroelastic analysis (SAA) method, removes the necessarily serial interaction of the structure and fluid solvers. Instead of running a single serially coupled analysis, the uncoupled SAA method evaluates many decoupled structural and fluid analyses for given displacement and pressure fields, these evaluations being highly parallelizable. Surrogate modeling of the results from these two evaluation classes allows an interpolative calculation of their intersection; this is proposed to represent the solution of the coupled FSI analysis. This method of conducting aeroelastic analysis allows for extensions of obtaining aeroelastic solutions for multiple flow velocities without requiring further simulations, and predicting the dynamic loaded free response characteristics and divergence of the structure. This work finds that the proposed uncoupled SAA method results in accurate solutions for a range of aeroelastic problems. Additionally, this work develops an optimization scheme incorporating the uncoupled SAA method and finds that the capability to retain data sets significantly reduces computational expense associated with performing many aeroelastic analyses, enabling new possibilities for aero-structural design.

To my family, who raised and supported me.

## ACKNOWLEDGEMENTS

Firstly, I would like to acknowledge God for all the gifts he has granted me throughout my life including my parents. I thank my parents for raising me and supporting me throughout my entire academic career. They were always there for me and provided voices of comfort and reason especially when academic life became stressful. Both of them imparted to me a desire for learning, especially in mathematics and science, and a drive to be committed to any task I am a part of such as this dissertation.

I wish to acknowledge my advisor, Dr. Darren Hartl. Since my first research experience during the summer of my sophomore year, he has been a great source of knowledge and a good role model. He has taught me how to be a researcher and showed me that it is possible to have a healthy work/life balance as an engineer. He additionally helped me make connections with engineers outside of academia and encouraged me to participate in internships during both my undergraduate and graduate studies that exposed me to different aspects of a research engineer. His influence in my life was a major factor in my decision to pursue graduate studies.

I am also thankful for my graduate committee members, who guided and influenced my research during both my Master of Science and Doctor of Philosophy degrees. Dr. Thomas Strganac served as my co-adviser while I obtained my Master of Science degree, provided me with a background in aeroelasticity, and guided me during my undergraduate senior design project. Dr. Paul Cizmas provided me a formal education in the performance of computational fluid dynamics analysis, and helped me as a student with a background in structural analysis gain an appreciation for the complexities of fluid-structure interaction analysis. While I never took one

of Dr. Richard Malak's classes, his input during my preliminary exam defense have helped me improved the quality of this dissertation. Finally, Dr. Travis Turner, a special appointment to the committee, has served as an adviser to me since my time as an undergraduate research assistant and was the first to show me how research is performed outside of an academic setting.

I would also like to thank the members of the MAESTRO Lab who have gone through similar experiences and struggles while pursuing their own degrees. Discussions with them provided insightful feedback on how to explain my work in an understandable manner. I hope I was able to reciprocate in kind. Specifically, I would like to thank Pedro Leal, whose work on the Class-Shape Transformation method was invaluable to this work. I would also like to acknowledge Trent White, who will be progressing the work presented in this dissertation further at Texas A&M as he prusues his own Doctor of Philosophy degree, and who performed the fluid analyses that utilized Star-CCM+. I acknowledge Brent Bielefeldt for his work on analyzing structures in a batched and parallelized manner and for providing a template of the DEAP NSGA-2 optimization algorithm. I also acknowledge undergraduate assistants, Kevin Lieb, Sam Murley, and Keval Shah for their work on the wind tunnel prototype.

Computational structural analysis was performed with a SIMULIA Abaqus research license. Computational fluid analysis was performed with a Cradle SC/Tetra license.

Thank you.

## CONTRIBUTORS AND FUNDING SOURCES

### *Contributors*

This work was supported by a dissertation committee consisting of Dr. Darren Hartl (chair of committee), Dr. Thomas Strganac, and Dr. Paul Cizmas of the Department of Aerospace Engineering, Dr. Richard Malak of the Department of Mechanical Engineering and Dr. Travis Turner, a special appointment, of the Structural Acoustics Branch from NASA Langley.

Geometry of the Common Research Model and slat-cove filler used in Chapters 2 and 5 was provided by Dr. Travis Turner from NASA Langley. Composite layups analyzed in Section 2.3 of Chapter 2 provided by Gaetano Arena from the University of Bristol. Codes for the Class-Shape Transformation method used in Chapters 3 and 4 provided by Pedro Leal of the Aerospace Engineering Department. Fluid analysis with Star-CCM+ and the calculation of associated the uncoupled solution at the end of Section 3.4.4 in Chapter 3 performed by Trent White of the Aerospace Engineering Department. Wind tunnel prototype shown in Chapter 4 designed by Kevin Lieb, Sam Murley, and Keval Shah of the Aerospace Engineering Department.

All other work conducted for the dissertation was completed by the student independently.

### *Funding Sources*

This work is done in collaboration with support of the NASA Structural Acoustics Branch at the NASA Langley Research Center under prime award number NNL09AA00AA and is also funded through the National Science Foundation Graduate Research Fellowship Program.

# TABLE OF CONTENTS

	Page
ABSTRACT . . . . .	ii
DEDICATION . . . . .	iii
ACKNOWLEDGEMENTS . . . . .	iv
CONTRIBUTORS AND FUNDING SOURCES . . . . .	vi
TABLE OF CONTENTS . . . . .	vii
LIST OF FIGURES . . . . .	x
LIST OF TABLES . . . . .	xvi
NOMENCLATURE . . . . .	xix
1. INTRODUCTION . . . . .	1
1.1 Introduction . . . . .	1
1.2 Fluid-Structure Interaction of Morphing Structures . . . . .	4
1.3 Optimization with Fluid-Structure Interaction Analysis . . . . .	7
1.4 Approximating High-Fidelity Multidisciplinary Problems . . . . .	9
1.5 Motivating Problem: Shape Memory Alloy-Based Slat-Cove Filler . . . . .	13
1.6 Summary of Objectives . . . . .	16
2. FULL COUPLED FSI ANALYSIS OF THE SLAT-COVE FILLER . . . . .	20
2.1 Computational Framework . . . . .	20
2.1.1 SMA Constitutive Model Description . . . . .	21
2.1.2 Turbulence Model Description . . . . .	29
2.2 Model Scale SCF* . . . . .	33
2.2.1 Finite Element Structural Model . . . . .	34
2.2.2 Finite Volume Computational Fluid Dynamics Model . . . . .	36
2.2.3 FSI Framework and Remeshing Scheme . . . . .	40
2.2.4 FSI Analysis: Fully Deployed SCF . . . . .	41
2.2.5 FSI Analysis: Transient Retraction/Deployment . . . . .	43
2.3 Full Scale SCF* . . . . .	48

2.3.1	Finite Element Structural Model . . . . .	49
2.3.2	Finite Volume Computational Fluid Dynamics Model . . . . .	52
2.3.3	FSI Analysis of Full Scale SCF . . . . .	55
2.4	Summary . . . . .	62
3.	UNCOUPLED METHOD FOR STATIC AEROELASTIC ANALYSIS . . . . .	63
3.1	General Overview of Uncoupled Method . . . . .	63
3.2	Mathematical Implementation of Uncoupled Method for Single Velocity . . . . .	69
3.3	Existence and Uniqueness of the Uncoupled Method Solution . . . . .	80
3.4	Demonstration Examples . . . . .	82
3.4.1	Example Demonstration 1: Single Degree-of-Freedom Baffle . . . . .	82
3.4.2	Example Demonstration 2: Two Degree-of-Freedom Baffle . . . . .	93
3.4.3	Example Demonstration 3: Two Degree-of-Freedom Discrete Pressure Baffle* . . . . .	98
3.4.4	Example Demonstration 4: Continuously Flexible Baffle . . . . .	104
4.	EXTENSION OF UNCOUPLED METHOD AND OPTIMIZATION APPLICATION . . . . .	116
4.1	Implementation and Demonstration of Uncoupled Method for Multiple Freestream Velocities . . . . .	116
4.1.1	Solving Aeroelastic Problems for Multiple Freestream Velocities . . . . .	116
4.1.2	Demonstration 1: Two Degree-Of-Freedom Discrete Pressure Baffle . . . . .	119
4.1.3	Demonstration 2: Continuously Flexible Baffle . . . . .	126
4.1.4	Demonstration 3: Aeroelastic Pitch-Plunge Wing . . . . .	128
4.2	Free-Response Behavior and Divergence . . . . .	138
4.3	Design Optimization with the Uncoupled Method* . . . . .	140
4.3.1	Optimization Framework Incorporating Uncoupled Method . . . . .	140
4.3.2	Optimization Application: Shape Memory Alloy Flow Diverter . . . . .	144
5.	APPLICATION OF UNCOUPLED METHOD TO MODEL SCALE SLAT- COVE FILLER . . . . .	170
5.1	General Descriptions of Fluid and Structure Models . . . . .	170
5.2	Development of Shape and Pressure Coefficient Fits . . . . .	172
5.2.1	Shape Fit . . . . .	172
5.2.2	Pressure Coefficient Fit . . . . .	177
5.2.3	Determining Significant Fitting Parameters . . . . .	178
5.3	Uncoupled Solutions for the SCF . . . . .	180
5.3.1	Uncoupled Solutions for Single Freestream Velocity . . . . .	180
5.3.2	Uncoupled Solutions for Multiple Freestream Velocities and Divergence . . . . .	185

6. CONCLUSIONS AND FUTURE WORK . . . . .	195
6.1 Summary and Conclusions . . . . .	195
6.2 Future Work . . . . .	199
REFERENCES . . . . .	201
APPENDIX A. MODEL SCALE SCF: FLUID MESH STUDIES, HINGE PLACEMENT OPTIMIZATION, AND FLAP KINEMATICS . . . . .	220
A.1 Mesh and Prism Layer Studies . . . . .	220
A.1.1 Mesh Study . . . . .	220
A.1.2 Prism Layer Study . . . . .	221
A.2 Hinge Optimization . . . . .	224
A.3 Flap Kinematics . . . . .	227
APPENDIX B. CLASS/SHAPE TRANSFORMATION METHOD FOR THE DESCRIPTION OF SOLID-FLUID BOUNDARIES . . . . .	230
APPENDIX C. DEFORMABLE BAFFLE EXAMPLE: SCATTERMATRIX PLOTS . . . . .	232
APPENDIX D. AEROELASTIC WING EXAMPLE: MESH REFINEMENT STUDY AND FITTING PARAMETER BOUNDS . . . . .	234
D.1 Mesh Refinement Study . . . . .	234
D.2 Fitting Parameter Bounds . . . . .	237
APPENDIX E. SMA FLOW DIVERTER: MESH STUDY AND SHAPE PA- RAMETER STUDY . . . . .	238
E.1 Mesh Refinement Study . . . . .	238
E.2 Shape Parameter Study . . . . .	240
E.3 LHS Variation Study . . . . .	241
APPENDIX F. UNCOUPLED SOLUTIONS OF MODEL SCALE SCF . . . . .	245

## LIST OF FIGURES

FIGURE	Page
1.1 Schematic of the conventional serial FSI coupling scheme of aeroelastic analysis. . . . .	4
1.2 Streamlines in the vicinity of the leading-edge slat. Circulation region indicates noise production. . . . .	14
1.3 Streamlines in the vicinity of the leading-edge slat with a SCF. . . . .	15
1.4 SMA SCF retraction/deployment. . . . .	15
1.5 Morphing aero-structures requirement triangle. . . . .	17
2.1 Stress-strain data of the superelastic SMA material at multiple temperatures. . . . .	24
2.2 Phase diagram of SMA material associated with the calibrated constitutive model. . . . .	25
2.3 Comparison of hysteresis loop from calibrated UMAT and experimental data. . . . .	27
2.4 Solidworks model of 3D CRM wing configuration used to obtain 2D section. Note that the 2D section shown is not the same scale as the 3D wing. . . . .	34
2.5 Structural FEA model of 2.5D SMA SCF assembly. . . . .	35
2.6 Fluid model and overset mesh implementation of the SCF-treated, deployed configuration. . . . .	37
2.7 Flowchart of FSI analysis with remeshing scheme. . . . .	41
2.8 Displacement of SMA SCF during FSI analysis for the fixed fully deployed case. Contour plots are from the final time increment. . . . .	42
2.9 Velocity contours of CRM at various retraction and deployment stages of the high-lift devices. . . . .	44

2.10	Lift coefficient of wing versus % deployment for retraction and deployment cycles. . . . .	46
2.11	Lift coefficient of wing versus % deployment for different retraction rates. . . . .	47
2.12	Structural FEA model of 2.5D SCF assembly with isolated SCF with sections targeted for elastic tailoring. . . . .	50
2.13	Superelastic stress-strain response of the SMA material in Table 2.2 and elastic stress-strain response of E-Glass 913 for various fiber orientations. Adapted from [116]. . . . .	50
2.14	Fluid model of the full scale CRM wing. . . . .	53
2.15	Deflection of different SCF designs: (a) Monolithic SMA; (b) Tailored SMA; (c) Tailored Composite 1; and (d) Tailored Composite 2. Two steady deflection solutions for each of the SCF designs are also shown. . . . .	57
2.16	Velocity contour during deployment for (a) Tailored Composite 1 design and (b) Monolithic SMA design under Mach 0.24 flow. . . . .	59
2.17	Comparison between undeformed SCF and final configuration for tailored designs after FSI analysis for (a) shape and (b) pressure distribution. . . . .	60
2.18	Velocity contour plot during deployment for Tailored Composite 2. . . . .	61
3.1	Simple schematic of the uncoupled SAA method. . . . .	64
3.2	Illustration of obtaining USiS solution using USI solution as inputs. . . . .	75
3.3	Flowchart of uncoupled method implemented for SAA to find solution at single freestream velocity. . . . .	77
3.4	Structure and fluid models of one degree-of-freedom rigid baffle. . . . .	84
3.5	Intersection of fluid surrogate model and three structure surrogate models corresponding to three different torsional stiffnesses for a one degree-of-freedom rigid baffle. . . . .	87
3.6	Comparison of coupled solution and uncoupled surrogate intersection; increasing the order of the pressure fit leads to a very low error USI solution. . . . .	89

3.7	Structure and fluid models of two degree-of-freedom rigid baffle. . . . .	94
3.8	Comparison of pressure distribution on two degree-of-freedom baffle for coupled and uncoupled solutions. . . . .	98
3.9	Structure and fluid models for two plate/bar assembly. . . . .	99
3.10	Visualization of the intersection of the structure and fluid surrogate models and USI solution. . . . .	102
3.11	Structure and fluid models for the deformable baffle example problem.	105
3.12	Comparison of approximations and actual shape/pressure. . . . .	107
3.13	Scatterplot matrix of $x_{tip}$ contours for all combinations of pressure fitting parameters along with the USI solution. . . . .	110
3.14	Scatterplot matrix of $q_{\infty}C_1$ contours for all combinations of shape fitting parameters along with the USI solution. . . . .	111
3.15	Coupled and uncoupled static aeroelastic results for deformable baffles having different elastic moduli (Single set of 27 fluid runs performed across all results). . . . .	113
3.16	Sample pressure distribution of deformable baffle using StarCCM+. . . . .	115
4.1	Flowchart of uncoupled method for finding SAA solutions at multiple freestream velocities (c.f. Fig. 3.3). . . . .	118
4.2	Fitting parameters versus freestream velocity for the two plate/bar assembly. . . . .	120
4.3	In-development wind tunnel model of the two degree-of-freedom dis- crete pressure baffle. . . . .	121
4.4	Uncoupled solutions versus velocity of wind tunnel model two degree- of-freedom discrete pressure baffle. . . . .	123
4.5	Uncoupled solutions versus velocity of wind tunnel model two degree- of-freedom discrete pressure baffle with larger structure DOE bounds.	124
4.6	Visualization of structure and fluid surrogate model intersection at 13 m/s for wind tunnel model of two degree-of-freedom discrete pres- sure baffle. . . . .	125

4.7	Pressure field over the for deformable baffle under multiple flow velocities (Single set of fluid/structure runs for all uncoupled results). . . .	126
4.8	Shape fitting parameters (in pressure) for deformable baffle under multiple flow velocities (Single set of fluid/structure runs for all uncoupled results). Average percent error between USiS and FSI solutions also shown. . . . .	127
4.9	Schematic of aeroelastic wing example. . . . .	129
4.10	Structure and fluid domain models for aeroelastic wing example. . . .	131
4.11	Comparison of CFD pressure coefficient distributions and RBF fits for aeroelastic wing example. . . . .	134
4.12	Comparison of uncoupled results with analytical and FSI results across multiple velocities and angles of attack. . . . .	136
4.13	Flowchart of optimization incorporating uncoupled method implemented for SAA. . . . .	141
4.14	Illustration of SMA flow diverter problem. . . . .	145
4.15	Structure and fluid models for SMA flow diverter. . . . .	146
4.16	Net pressure coefficient distributions on SMA flow diverter from four-level full factorial DOE. . . . .	149
4.17	Error between fit and CFD calculated pressure distribution for different number of fitting parameters and RBF type. . . . .	151
4.18	Shape fitting parameters, maximum stress, and maximum martensitic volume fraction of USI and USiS solutions for multiple inlet velocities from the sample (median) design of the SMA flow diverter. . . . .	154
4.19	Pressure fitting parameters and outlet velocities from USI and USiS solutions for multiple inlet velocities from the sample (median) design of the SMA flow diverter. . . . .	155
4.20	Illustration of SMA flow diverter optimization objectives. . . . .	157
4.21	Summary of the SMA flow diverter optimization problem. . . . .	158
4.22	$v_{1,max}$ - $\Delta v_{\infty}$ objective space with martensitic volume fraction. . . . .	160

4.23	$v_{1,max}$ - $\Delta v_\infty$ objective space for optimization with added design variables.	162
4.24	Comparison of all three optimizations.	163
4.25	Overset mesh implementation of fluid model for FSI analysis of the SMA flow diverter.	164
4.26	Shape fitting parameters and outlet velocity from USI and coupled solutions for multiple inlet velocities.	165
4.27	Tip displacement and outlet velocity from coupled FSI and USI solutions with $n_s=3$ and $n_s=4$ for multiple inlet velocities.	166
4.28	Tip displacement and maximum martensitic volume fraction of the diverter in fluid flow with inlet velocity increasing from 1 m/s to 5 m/s.	168
4.29	Eigenvalues for first four mode shapes with $n_s=3$ and $n_s=4$ for multiple inlet velocities.	169
5.1	Structure and fluid domains of SMA SCF with uncoupled method applied.	171
5.2	Undeformed SCF shape and pressure distribution from CFD analysis using undeformed shape.	173
5.3	Illustration of shape fitting parameters are used to generate SCF shape.	174
5.4	Mean square error of shape for different number of CST coefficients.	176
5.5	Mean square error of pressure for different number of CST coefficients.	176
5.6	Root mean square error of pressure coefficient distribution fit for different RBF types and number of fitting parameters.	178
5.7	Shapes considered during fluid LHS of SCF. Dashed black line indicates the slat and undeformed SCF.	181
5.8	Distribution of thickness for multi-thickness SCF.	182
5.9	Error (measured as $\Delta\zeta$ ) relative to the coupled solution for each design. For reference, the curvilinear length of the SCF is 53.3 mm	185
5.10	Shape fitting parameters from USI and USiS solutions for multiple freestream velocities from 0.0508 mm monolithic SCF.	188

5.11	USI pressure fitting parameters for multiple freestream velocities from 0.0508 mm monolithic SCF. . . . .	189
5.12	Deformed SCF shapes for multiple freestream velocities and comparison to FSI solution at 25 m/s freestream velocity. . . . .	189
5.13	Natural frequency vs. freestream velocity for two monolithic SCF designs. . . . .	190
5.14	Mode shapes of the deformed SCF for different freestream velocities extracted from eigenvalue analysis along with buckling mode shape. . . . .	192
5.15	Displacement of SCF during FSI analysis with linearly increasing freestream velocity (c.f. Fig. 5.13) along with uncoupled solution. Displacement corresponds to the node marked in red. . . . .	194
A.1	Illustration of optimization problem for hinge placement. . . . .	226
A.2	Surrogate models and calibration points for contact loading. . . . .	226
A.3	$F_{x,max}$ - $F_{y,max}$ objective space from the final generation. . . . .	227
A.4	Illustration of flap motion. . . . .	228
C.1	Scatterplot matrix of $D_1$ and $D_2$ contours for all combinations of pressure fitting parameters along with USI solution. . . . .	232
C.2	Scatterplot matrix of $C_2$ - $C_5$ contours for all combinations of shape fitting parameters along with USI solution. . . . .	233
E.1	Pressure coefficient distributions from length study. . . . .	242
E.2	Pressure coefficient distributions from thickness study. . . . .	242
E.3	Outlet velocity vs. inlet velocity for different structure LHSs. . . . .	244

## LIST OF TABLES

TABLE	Page
2.1 SMA material properties from [107]. . . . .	26
2.2 SMA material properties from [107]. . . . .	29
2.3 E-glass 913 properties from [116]. . . . .	52
2.4 Ply properties, stacking sequences and thickness distributions along the SCF arc-length. From . . . . .	53
3.1 Fitting parameters for considered demonstration examples of generally increasing complexity with both continuous and discrete pressure fields.	83
3.2 Surrogate model input bounds of pressure coefficient fitting parame- ters for one degree-of-freedom baffle. . . . .	90
3.3 Comparison of computational times to obtain static aeroelastic solu- tions for one degree-of-freedom baffle. In parenthesis is the estimated time required to obtain each uncoupled solution if all runs are per- formed in parallel. . . . .	91
3.4 Comparison of solution increments to obtain static aeroelastic solu- tions for one degree-of-freedom baffle. . . . .	91
3.5 Surrogate model input bounds of pressure coefficient and shape fitting parameters for two degree-of-freedom baffle. . . . .	96
3.6 Pressure and shape fitting parameters for two degree-of-freedom baffle.	97
3.7 Pressure and shape fitting parameters for the two degree-of-freedom discrete pressure baffle. . . . .	103
3.8 Surrogate model input bounds of pressure coefficient and shape fitting parameters for deformable baffle. . . . .	108
3.9 Pressure and shape fitting parameters for deformable baffle example.	109

3.10	USI solution for deformable baffle using Star-CCM+. Differences between solutions believed to be due to differences in mesh refinement and type of flow analysis performed. Note that the displacement values represent the solution of engineering interest. . . . .	114
4.1	Surrogate model input bounds of shape fitting parameters for the flow diverter example. . . . .	149
4.2	Surrogate model input bounds of pressure coefficient fitting parameters for SMA flow diverter. . . . .	153
5.1	Surrogate model input bounds of fitting parameters for SCF. . . . .	181
5.2	NRMSE (%) relative to the coupled solution in $\psi$ - $\zeta$ frame for each SCF design. . . . .	186
5.3	Surrogate model input bounds of pressure coefficient for 0.0508 mm monolithic SCF to find solutions at multiple freestream velocities. . .	187
6.1	Computational times associated with finding aeroelastic solutions in a design study using the serial FSI coupling scheme and the uncoupled method. In parenthesis are the times associated with finding uncoupled solutions if all evaluations (fluid and/or structure) are performed in parallel. . . . .	197
6.2	Solution increments associated with finding aeroelastic solutions in a design study using the serial FSI coupling scheme and the uncoupled method. . . . .	198
A.1	Mesh study of outer region. . . . .	221
A.2	Mesh study of middle region. . . . .	222
A.3	Mesh study of inner region. . . . .	222
A.4	Total thickness of prism layer study. . . . .	223
A.5	First layer thickness of prism layer study. . . . .	224
A.6	Number of layers and thickness variation of prism layer study. . . . .	225
D.1	Mesh study of Region 1 for aeroelastic wing example. Region 2 element size set to 1.95 mm. . . . .	235

D.2	Mesh study of Region 2 for aeroelastic wing example. Region 1 element size set to 15.625 mm. . . . .	235
D.3	Prism layer study for aeroelastic wing example. . . . .	236
D.4	Surrogate model input bounds of pressure coefficient fitting parameters for pitch-plunge airfoil. . . . .	237
E.1	Mesh study of Region 2 for flow diverter. Region 1 mesh size set to 0.3125 mm. . . . .	239
E.2	Mesh study total prism layer thickness. . . . .	239
E.3	Mesh study of Region 1 for flow diverter example. . . . .	240
E.4	Mesh study prism layer. . . . .	241
E.5	Fitting parameter bounds for LHS variation study. . . . .	244
F.1	p-value table from structure DOE of the SMA SCF. <i>p</i> -values in green indicate statistical significance. <sup>1</sup> . . . . .	245
F.2	p-value table from fluid DOE of the SMA SCF. <i>p</i> -values in green indicate statistical significance <sup>2</sup> . . . . .	246
F.3	Pressure and shape fitting parameters for 0.0508 mm monolithic SCF. . . . .	247
F.4	Pressure and shape fitting parameters for 0.04572 mm monolithic SCF. . . . .	248
F.5	Pressure and shape fitting parameters for multi-thickness SCF. . . . .	249

## NOMENCLATURE

This nomenclature excludes notations used in Chapter 2 as that chapter utilizes symbols/variable names established in other works.

$a$	Parameter defining location of airfoil rotation center
$A_{FSI}$	Surface area of $\Omega_{FSI}$
$B, C$	Shape and class functions
$b$	Half-chord of airfoil
CFD	Computational fluid dynamics
CST	Class-shape transformation
$c_i$	Constants for polynomial fit
$C_p, \hat{C}_p$	Pressure coefficient field and fit
$C_{l\alpha}$	Lift-curve slope
$\mathbf{C}=\{C_1, \dots, C_{n_p}\}$	Pressure coefficient fitting parameters
$C_L, C_D$	Lift, drag coefficient
$C_f$	Friction coefficient
DOE	Design of experiment
DOF	Degree of freedom
$\mathbf{d}_i$	Design variables
$\mathbf{d}_{int,i}$	Design variables internal to structure
$\mathbf{d}_{s,i}$	Design variables that describe undeformed shape
$\mathbf{d}_{s,i}$	All other design variables
$D_i$	Shape coefficient
$e$	Parameter defining location of airfoil center of mass
FSI	Fluid-structure interaction

$\mathbf{F}$	Applied force vector
$F_x, F_y$	Horizontal and vertical forces
$\mathbf{f}(\mathbf{d}_i)$	Objective function
$\mathcal{F}^s = \{\mathcal{F}_1^s, \dots, \mathcal{F}_{n_s}^s\}$	Function relating $\mathbf{P}$ to $\mathbf{S}$
$\mathcal{F}^f = \{\mathcal{F}_1^f, \dots, \mathcal{F}_{n_p}^f\}$	Function relating $\mathbf{S}$ to $\mathbf{P}$
$\mathcal{F}^{fo} = \{\mathcal{F}_1^{fo}, \dots, \mathcal{F}_{n_p}^{fo}\}$	Function relating $\mathbf{S}$ to $\mathbf{Y}^f$
$\mathcal{F}^{so} = \{\mathcal{F}_1^{so}, \dots, \mathcal{F}_{n_p}^{so}\}$	Function relating $\mathbf{P}$ to $\mathbf{Y}^s$
$\mathcal{G}^s(\mathbf{S}, q_\infty \mathbf{C}), \mathcal{G}^f(\mathbf{S}, q_\infty \mathbf{C})$	Functions used in Jacobian calculation
$\mathbf{g}_i$	Inequality constraint
$\mathbf{h}_i$	Equality constraint
$h$	Stretch of linear spring
ICS	Initial coupled solution
IDF	Individual discipline feasible
$I_p$	Inertia of airfoil about rotation center
$I^s, I^f$	Number of solution increments from structure and fluid solvers
$J$	Jacobian
$[K(\mathbf{u}_s)]$	Nonlinear stiffness matrix
$[K_A]$	Aerodynamic stiffness matrix
$[K_{eff}]$	Effective stiffness matrix
$K_h, K_\theta$	Stiffness of linear and torsional springs
$l$	Span of airfoil
$l_h$	SCF-hinge arm length
$l_{SMA}$	Length of SMA flow diverter
$l_{ab}$	Length between flap pins
$L$	Lift

LHS	Latin hypercube sampling
MDF	Multidisciplinary feasible
$[M]$	Mass matrix
$m$	Mass
$m_p, m_s$	Number of variations of pressure, shape fitting parameters
NRMSE	Normalized root mean square error
$n_p, n_s$	Number of pressure and shape fitting parameters
$n_{CST}$	Number of CST coefficients
$n_{y,f}, n_{y,s}$	Number of model responses from fluid, structure analyses
$N, N_f$	Current and final increment
$N_1, N_2$	Fitting parameters for class function
$p, \hat{p}$	Pressure field and fit
$\mathbf{P}=\{P_1, \dots, P_{n_p}\}$	Pressure fitting parameters
$q_\infty$	Dynamic pressure
RBF	Radial basis function
$R_e$	Reynolds number
$r_a, r_b$	Radii of flap tracks
RMSE	Root mean square error
$s$	Distance along surface
SAA	Steady aeroelastic analysis
SCF	Slat-cove filler
SMA	Shape memory alloy
$s_{FSI}$	Implicit function that defines $\Omega_{FSI}$
$\hat{s}_{FSI}$	Implicit function that defines $\hat{\Omega}_{FSI}$
$\mathbf{S}=\{S_1, \dots, S_{n_s}\}$	Shape fitting parameters
$\mathbf{S}_c=\{S_{c,1}, \dots, S_{c,n_{s,c}}\}$	Constant shape fitting parameters during optimization

$\mathbf{S}_s = \{S_{s,1}, \dots, S_{s,n_{s,s}}\}$	Non-constant shape fitting parameters during optimization
$t, t_f$	Current and final time
$t_{SMA}$	Thickness of SMA flow diverter
$tol_s, tol_c$	Tolerance of fitting parameters
$\mathbf{u}$	Displacement field
$\ddot{\mathbf{u}}$	Acceleration
$\mathbf{u}_s$	Steady displacement field
USI	Uncoupled surrogate intersection
USiS	Uncoupled surrogate-informed solution
$v_\infty$	Freestream (inlet) flow velocity
$v_D$	Divergence velocity
$w^s, w^f, w^{so}, w^{fo}$	Weights in surrogate models
$\mathbf{x}, x, y$	Cartesian coordinates
$x_{tip}, y_{tip}$	Coordinates of baffle or diverter tip
$y^+$	Nondimensional parameter related to first layer thickness
$\mathbf{Y}^f = \{Y_1^f, \dots, Y_{n_{y,f}}^f\}$	Model responses from fluid analyses
$\mathbf{Y}^s = \{Y_1^s, \dots, Y_{n_{y,s}}^s\}$	Model responses from structure analyses
$\mathbf{C}_{USI}, \mathbf{S}_{USI}, \mathbf{Y}_{USI}^s, \mathbf{Y}_{USI}^f$	Fitting parameters and model responses of USI solution
$\mathbf{C}_{USiS}, \mathbf{S}_{USiS}, \mathbf{Y}_{USiS}^s, \mathbf{Y}_{USiS}^f$	Fitting parameters and model responses of USiS solution
$\alpha, \alpha_0$	Angle of attack and set angle of attack
$\beta$	Rotation during coordinate transformation
$\Delta x, \Delta y$	Translation during coordinate transformation

$\Delta L, \Delta y$	Scale factor during coordinate transformation
$\delta_h$	Location of hinge axis
$\Phi$	Mode shape
$\Psi$	Basis function
$\psi, \zeta$	Nondimensional coordinates
$\rho$	Density of fluid
$\epsilon_p, \epsilon_s$	Pressure and shape fitting error
$\theta$	Rotation
$\gamma^s, \gamma^f, \gamma^{so}, \gamma^{fo}$	Weights in surrogate models from polynomial tail
$\Omega$	Wetted surface
$\Omega_{FSI}$	Portion of wetted surface that deforms
$\Omega_{rigid}$	Static region of wetted surface
$\hat{\Omega}_{FSI}$	Fit of surface region $\Omega_{FSI}$
$\omega$	Natural frequency
$\sigma$	Stress, Pa
$\xi$	Martensitic volume fraction
$\mu$	Viscosity

# 1. INTRODUCTION

## 1.1 Introduction

Aeroelasticity, the study of the interaction between a structure and an impinging flow field, is a multidisciplinary field that utilizes concepts from aerodynamics, structural mechanics and dynamics [1]. Aeroelasticity is critical in the design of many engineered systems as failure to account for aeroelastic effects can lead to catastrophic failure of the system [1]. The coupled aeroelasticity problem can be posed as the following: as a body deforms due to aerodynamic loading, the shape presented to the flow field changes, resulting in a change of the aerodynamic loading. There are two primary types of aeroelasticity: 1) static aeroelasticity, which addresses the coupled fluid-structure problem, assuming that inertial effects are small and that the coupling between the structure and fluid reaches an equilibrium (“steady”) state, and 2) dynamic aeroelasticity, which evaluates how the structure and flow change in time.

Multidisciplinary computational processes such as fluid-structure interaction (FSI) analysis, a type of aeroelastic analysis which couples fluid and structural solvers, are typically required when solving aeroelastic problems involving continua such as arterial blood flow [2], wind turbine blades [3], turbomachinery [4], parachutes [5], and a complete fighter jet configuration [6]. The fluid and structure solvers used in FSI analysis are typically developed separately and use disparate numerical approaches to integrate the underlying partial differential equations and solve for their respective physical quantities [7]. Additionally, the models and numerical methods used can be of different fidelity (i.e., similarity to the real world phenomenon). Structural methods used in FSI analysis include Bernoulli beam theory [8], the von Kàrmàn

plate theory [9], and the finite element method [10, 11]. Similarly, there have been a number of flow solving methods incorporated into FSI frameworks including panel methods [12], lifting line theory [13], and mesh-based (commonly finite volume) computational fluid dynamics (CFD) analysis [14, 11].

Development of a stable coupling scheme between each set of fluid/structure models is not trivial and may require significant time to develop [15]. Coupling schemes can be categorized as partitioned or monolithic. A monolithic scheme implements a single solver that integrates the structure and fluid equations simultaneously. While generally more accurate, a monolithic scheme is also more computationally expensive and harder to implement as compared to a partitioned coupling scheme [16], and as a result is not of interest in this work. In the partitioned (or serial) FSI coupling scheme, fluid and structure solvers calculate physical quantities separately and exchange field information across a model interface (i.e., surface of the structure) at specified times. In the review paper by Hou, et al. [16], the authors detail many developments to improve the partitioned coupling scheme including transfer of data at the fluid-structure interface, accuracy and efficiency. Note that partitioned schemes are further categorized as weakly or strongly coupled. In a weak partitioned coupling scheme, the solvers exchange field information once per time increment while for the strong partitioned coupling scheme, field information is exchanged for multiple iterations until convergence [17].

Figure 1.1 illustrates this serial FSI scheme for aeroelastic analysis. At any time  $t$ , the displacement field  $\mathbf{u}(\mathbf{x}, t)$  is calculated by the structure solver for a given aerodynamic pressure  $p(\mathbf{x}, t)$ , where  $\mathbf{x}$  is the 3-dimensional position vector. Likewise, the fluid solver calculates the pressure field  $p(\mathbf{x}, t)$  over the current wetted surface of the body  $\Omega$ . The body  $\Omega$  may be the union of two regions: 1)  $\Omega_{FSI}$ , which changes as the solid body deforms, and 2)  $\Omega_{rigid}$ , or a static (or rigid) region. For flows with

a Reynolds number greater than 10,000, shear forces on a surface due to viscous effects are orders of magnitude smaller than pressure forces [18], and thus are not typically transferred during an FSI analysis. At any given time increment  $t_n$ , multiple iterations of field information exchange between the solvers may be required for convergence to a physically compatible solution, when the error between the displacement field imposed in the fluid domain  $\mathbf{u}(\mathbf{x}, t_n)$  and the displacement field obtained from structure analysis  $\mathbf{u}(\mathbf{x}, t_n; p(\mathbf{x}, t_n))$  for a given pressure load is within some tolerance. For many aerospace applications, for which large dynamic oscillations are not acceptable or expected, the final equilibrium configuration  $\Omega(u(\mathbf{x}, t_f))$  is of interest. Due to multiple internal solver iterations and field information exchanges, obtaining a coupled set of fluid and structure solutions using this scheme for aeroelastic analysis is computationally expensive.

An alternative approach for FSI analysis with the serial coupling scheme, for which a final equilibrium configuration is of interest, is to couple a steady fluid solver with a static structure solver (referred to as steady FSI analysis). In this variant of the partitioned coupling scheme where time is removed, for each increment of the FSI analysis a steady fluid analysis is performed followed by static structure analysis [19, 20]. Both solvers exchange the resulting final displacement and pressure fields every increment until some convergence criteria is met. Utilizing these solvers may require less exchanges of field information as compared to time dependent solvers. However, each exchange is more computationally expensive since new steady fluid and static structure analyses are performed every iteration. Applications utilizing this variant of the partitioned coupling scheme include camber morphing airfoils [21], lightweight flexible structures [22], and aircraft wings [20, 23, 24, 19].

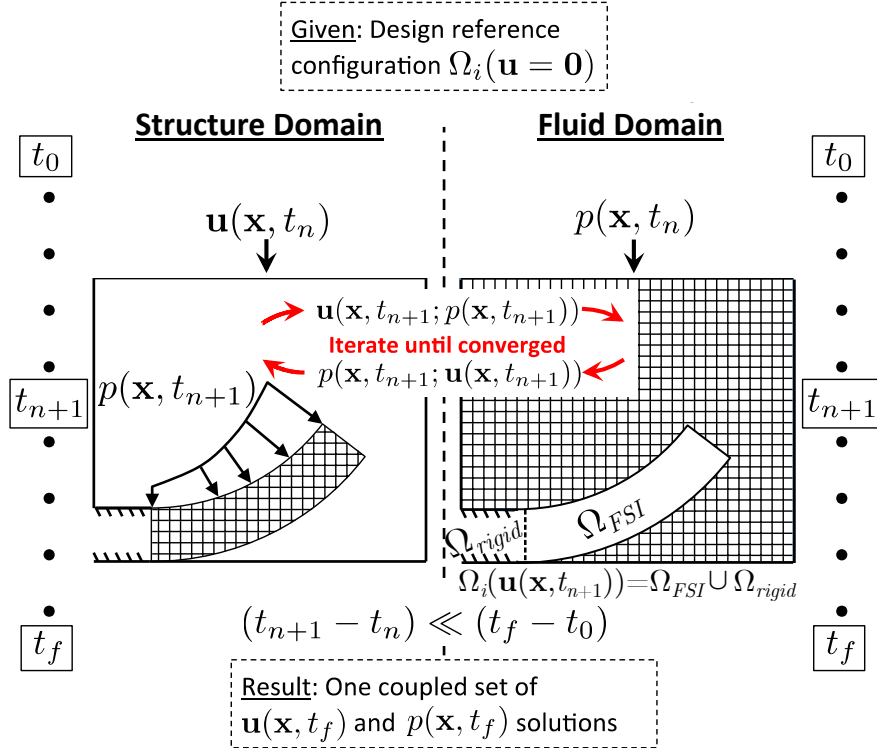


Figure 1.1: Schematic of the conventional serial FSI coupling scheme of aeroelastic analysis. Fluid and structure solvers iterate in time by exchanging pressure and displacement fields until convergence. For a given design  $\Omega_i(\mathbf{u}(\mathbf{x}, t_0) = \mathbf{0})$ , one coupled set of physically compatible fields,  $\mathbf{u}(\mathbf{x}, t_f)$  and  $p(\mathbf{x}, t_f)$  is obtained.

## 1.2 Fluid-Structure Interaction of Morphing Structures

Motivating this work is the fact that serial FSI analysis must be repeated if either the fluid or structure domain are altered, making design studies and optimizations of associated engineered structures or systems computationally prohibitive. The design of morphing aerostructures is particularly difficult as it requires consideration of large structural deformations in the presence and under the influence of flow. These structures exhibit a change in geometry (outer mold line) for the purpose of

meeting specific requirements or improving flight performance under multiple flow conditions [25]. Note that the motion of the morphing structure can occur over a long period of time thus requiring increased computational time for both flow stabilization and morphing. Morphing aerostructure applications that exhibit a final steady-state equilibrium condition for a given flow condition are of particular interest in this work. The computational cost, complexity of implementation, and fidelity of an FSI framework for morphing structures is highly dependent on the chosen fluid and structure solvers.

Mesh-based CFD analysis, a high-fidelity computational method for analyzing fluid flow, discretizes the fluid domain and surface of the solid boundary into elements/volumes and is commonly incorporated into FSI frameworks. While powerful and capable of capturing complex flow effects such as stall and turbulence, the use of CFD models in FSI analysis can present some additional difficulties with regards to analyzing morphing structures with large deformations. Due to the potential large motions of the structure, which are passed to the fluid solver as translation and rotation of the solid boundary, the fluid domain can significantly change during FSI analysis, resulting in loss of accuracy or in fluid elements with near-zero volume that can destabilize the analysis. Note that accommodation of this motion in a fluid solver may require specialized mesh morphing techniques [15, 26] and/or remeshing algorithms [11, 27], the implementation of which further increases runtime in the analysis. Stanford, et al. performed aeroelastic tailoring on the wing of a micro air vehicle using FSI analysis to simulate the low Reynolds number flow [28]. During every iteration of the analysis, the fluid domain was remeshed based on deformation of the wing and a new steady fluid analysis was performed, leading to a computationally expensive process. Using FSI analysis with commercial finite volume/element codes, Heo, et al. investigated the use of cellular cores within airfoils subjected

to aerostatic loading to demonstrate their effectiveness in a passive camber morphing application [21]. In a similar manner, Miller, et al. performed FSI analysis of an active camber morphing airfoil and compared results with wind tunnel experiments [29]. Another option for accommodating large motion of the fluid domain is the use of overset meshes [30], which overlay deformable (and moveable) meshes onto a fixed background mesh. These deformable meshes are typically a localized region of the overall fluid domain that comprises the structure. Fluid data is transferred between the boundary of the deformable meshes and the surrounding background mesh through interpolation. Morphing applications utilizing overset meshes in FSI analysis include high-lift device modifications [11], flapping and deformable insect wings [14], wind turbine rotors [31], and shape memory actuated supersonic wind tunnel models [32]. Arena, et al. [33] developed an FSI model that immersed a structure mesh into a fluid domain for the purpose of tailoring the design of a composite layup for both monostable and bistable adaptive air inlets. By exploiting both non-linear behaviour and instabilities, the authors developed designs that would passively morph between two configurations based on the flow speed.

FSI schemes incorporating solvers with no discretized fluid domain avoid the need for mesh morphing techniques, remeshing schemes, and overset meshes that are typically needed in FSI analysis with mesh-based CFD solvers to accommodate large deformation/morphing of the structure. While generally a lower-fidelity approach compared to mesh-based CFD analysis, these approaches are computationally inexpensive making them favorable for low-medium fidelity FSI schemes. Popular meshless fluid solvers used in FSI analysis include the vortex lattice method [34, 35] and panel method [36, 37] (also known as aerodynamic potential flow method). Both solvers are based on potential flow and assume that the flow is inviscid, incompressible, irrotational, and steady, though some codes have viscous corrections and

unsteady implementations. However, the vortex lattice method neglects the effects of thickness. Instead of discretizing the surface of the body and surrounding flow field into elements, panel method codes only discretize the body surface. FSI schemes incorporating a panel method code can handle large morphing so long as the solid boundary can be accurately defined and the configuration of the body does not violate critical panel method assumptions (e.g., flow separation).

Panel methods have been applied to many morphing applications including camber morphing airfoils [12, 8, 38], turbine blades [39], flapping wings [13], variable-span wings [40], and adaptive trailing edges [41]. Leal, et al. [12] conducted FSI analysis of an airfoil with skin-mounted shape memory alloy actuators that morphed the airfoil between cruise and landing configurations, resulting in both a change in shape of the airfoil and flight conditions. Daynes and Weaver developed a 2D FSI model of a morphing airfoil with an adaptive trailing edge flap using a coupling of a finite element structural model and a panel method code, and compared results to an experimental model [41].

### 1.3 Optimization with Fluid-Structure Interaction Analysis

Consideration of aeroelastic effects within an analysis-driven design optimization framework can be cast as a multidisciplinary design optimization (MDO) approach in that it considers design requirements from all fields simultaneously, allowing for interactions between them [42].<sup>1</sup> A number of frameworks are utilized to perform multidisciplinary optimizations [42, 44, 45].

The most common MDO framework, known as multidisciplinary feasible (MDF) method, performs a full multidisciplinary analysis for every design considered. While

---

<sup>1</sup>While not of interest to this work, optimization of aeroelastic problems can also be conducted using a sequential (or multi-step) approach where separate optimizations for each field (structure and aerodynamics) are performed [43].

accurate, MDF frameworks can be expensive due to the computational cost of running a single multidisciplinary analysis. The MDF framework has been applied to a number of FSI applications, incorporating both gradient and genetic optimization algorithms, including a quasi-three-dimensional adaptive wing [43], a micro-air-vehicle with flexible wings [46], a shape memory alloy actuated, reconfigurable airfoil [38], and a supersonic business jet [47].

Another optimization framework of interest to this work is the individual discipline feasible (IDF) method [42, 45]. In an IDF framework, a complete multidisciplinary analysis is avoided by decoupling the disciplines into separate analyses. For each considered design, the separate disciplines are evaluated once. The optimizer treats both the design variables and the imposed coupling variables in the same manner, using them as inputs into each discipline analysis. With regards to aerostructural optimization, in a structure analysis the imposed coupling variables form an aerodynamic loading, while in the fluid analysis, the imposed coupling variables define the shape. The individual discipline analyses return the output variables and the actual coupling variables to the optimizer. The optimizer utilizes a constraint that the imposed and actual coupling variables must match, driving the disciplines towards multidisciplinary feasibility by the end of the optimization process. The IDF framework has been applied to the optimization of aircraft wings [48], nozzles [49] and rail vehicles [50]. Perez, et al. compared multiple multidisciplinary design optimization frameworks, including IDF, using a conceptual, supersonic business jet example [51]. The authors demonstrated for their specific application that while an MDF framework was the most accurate architecture, an IDF framework was more efficient and still retained high accuracy. A potential drawback of the IDF method is that if a large number of imposed coupling variables are required, the optimization problem may become quite large.

## 1.4 Approximating High-Fidelity Multidisciplinary Problems

The significant cost to perform multiple FSI analyses and other expensive computational analyses in design and optimization studies has led to development of less expensive approximate models such as response surface (surrogate) models [52, 53, 54, 55]. Surrogate models are mathematical equations calibrated to match previously computed high-fidelity (and expensive) simulations, thereby relating sets of input variables to observed or computed responses in a direct and analytical way [56, 57, 58]. Multiple review papers detail the development and performance of surrogate models as well as implementation in optimization frameworks [59, 60, 61] for a variety of fields including aerodynamics [62], propulsion [63], acoustics [64] and structures [65]. Multiple runs of the high-fidelity model with different combinations of input variables are required to accurately calibrate (or “train”) the surrogate model. Note that the number of high-fidelity runs required to train a surrogate model exponentially increases with the number of variables (the “curse of dimensionality” [66]). Accurately calibrated, surrogate models enable fast evaluation of new input variable data sets, allowing for computationally efficient design studies and optimizations. Examples of surrogate models include Kriging surfaces [67] and radial basis functions (RBF) [68].

Commonly used in multidisciplinary problems and aerospace applications, Kriging is a spatial interpolation method that estimates the value of an unknown point using a combination of a global model (typically constant) and local departures from the global model. The local departures in the Kriging model are determined using a stochastic process. The construction of a Kriging model, specifically the localized departures, requires optimization of model parameters that maximize a likelihood function [52, 58]. Simpson, et al. developed Kriging models to approximate the FSI

analysis of a nozzle [52]. Approximate models of thrust, weight, and gross liftoff weight were created using sample FSI analyses of different designs. Multiple design optimizations with objectives such as maximizing thrust and minimizing weight were then conducted using the Kriging models as substitutes for the actual FSI analyses. Wu, et al. [69] developed an FSI framework to model and optimize a hydraulic arresting gear. The FSI framework used an immersogeometric approach that placed the structure within a background mesh. Instead of running the optimization with the expensive FSI analysis, a Kriging surrogate model relating the objective function to design variables was developed using trial FSI simulations as specified by Latin hypercube sampling. Other applications of Kriging models in FSI problems include wing design [70, 71], gas turbine fins [72], and biological devices [55].

Of particular interest in this work, radial basis functions (RBF) [68] are surrogate models that are continuous, smooth functions generated from the summation of basis functions  $\Psi(r)$ , each based on the Euclidean distance  $r$  from one of the members of a set of known data points (referred to herein as calibration or training points) such that  $\Psi(r=0)=0$ . RBF surrogate models are considered in this work due to their ability to 1) model arbitrary functions, 2) be implemented via simple algorithms, and 3) handle multidimensional data. Volpi, et al. [53, 73] conducted multidisciplinary design optimization over an RBF surrogate model of a composite hydrofoil for maximum hydrodynamic efficiency. Volpi initially performed FSI analyses of different designs using a high fidelity model and applied a proper orthogonal decomposition to the results, reducing the dimensionality of the problem significantly. The RBF surrogate model was then constructed from the reduced results. Additionally, during the optimization procedure, new FSI simulations were conducted to update the surrogate model as it approached an optimum solution. Glaz, et al. [54] developed a model incorporating multiple types of surrogate models for the analysis of a

rotating helicopter rotor blade in flow. Individual surrogate models, including polynomial response surfaces, radial basis function surfaces, and Kriging surfaces, were developed from a Latin hypercube sampling of a FSI analysis and then combined into a weighted-average surrogate model. With the combined surrogate model, the authors conducted a design optimization on the rotor blade for reduced vibration, demonstrating that their approach was effective at finding multiple feasible designs.

Though not considered in this work, another application of radial basis functions in FSI analysis is the interpolation (and application) of displacements and forces at the solid-fluid interface [7, 15]. A potential drawback of using RBFs is the creation of nonphysical, numerical local minima during surrogate model generation. The extended radial basis function (E-RBF), developed by Mullur and Messac [74, 75], combines RBFs with nonradial basis functions (N-RBFs), creating a flexible response surface that eliminates local minima and is overall more accurate than the traditional RBF. Due to the improved accuracy E-RBFs will be of interest in future extensions of this work.

Another means of approximating high-fidelity models is a reduced-order model (ROM), which is a physics-based, low-dimensional, computationally inexpensive system based on key features of the expensive, full order model. Similar to surrogate models, the construction of a ROM requires running many simulations. Results from simulations are then projected into a smaller set of generalized coordinates with a reduced basis such as eigenmodes [76]. Since ROMs are physics-based, these types of approximate models may provide better predictions as compared to mathematical, data-driven surrogate models [76]. Review papers by Lucia and Dowell [77] discuss many ROM techniques and application to a variety of multidisiplinary problems [78]. With regards to FSI, Lieu, et al. modeled the aeroelastic response of a complete F-16 fighter configuration using a CFD-based aeroelastic ROM [6]. Additionally the

authors developed a means of adapting a ROM for different Mach numbers without complete reconstruction of the ROM which was further extended by Amsallem and Farhat [79]. Surrogate models, specifically RBFs, are chosen over ROMs in this work since the development of RBF surrogate models only requires solving a linear system of equations to calibrate the mathematical approximation while creation of a ROM such as a proper orthogonal decomposition requires solving an eigenvalue problem to find relevant modes and mode shapes, a potentially more computationally expensive process. Additionally, when relating inputs from one domain to the outputs of another, a ROM still requires solving a reduced form of the governing equations while surrogate models are mathematical equations that directly relate the two domains. Note that the usage of ROMs is of interest in future extensions of this work as they can be combined with surrogate models [53, 80]. In such works, modes were directly related to design variables or inputs from other domains.

While not used in the current work, machine learning, a growing field in engineering, is also of interest. Machine learning techniques create maps between data sets of inputs and outputs for which a conventional mathematical approximation may not be adequate [81]. While machine learning has been applied to a number of aeroelasticity problems [82, 83, 84, 85], it is not considered in this work due to the increased number of training points as compared to surrogate modeling.

Representing geometries in a parameterized manner is also of particular interest to this work, as it will be important in the approximation of deformed shapes used in the proposed static aeroelastic scheme. Multiple parametrization methods have been introduced throughout literature such as the PARSEC method [86], Bezier curves [87], and Non-Uniform Rational Basis Spline [88]. However, the methods typically make compromises between accuracy for general and specific shapes [89]. Introduced by Kulfan, the class/shape transformation (CST) method are a universal shape repre-

sentation [90]. The CST method has been used to represent both subsonic [91] and supersonic wings [92] in addition to many other structural forms [93, 94]. Leal, et al. further developed the CST method to include structurally consistent constraints to include camber morphing of airfoils [89]. A general description of the method is presented herein, while a more detailed description of the CST method can be found in the Appendix B.

### 1.5 Motivating Problem: Shape Memory Alloy-Based Slat-Cove Filler

An aerospace application that provides strong motivation for this work is the slat-cove filler (SCF), a morphing structure used in the noise reduction of general transport aircraft during approach and landing. During cruise, high-lift devices such as the leading-edge slat and trailing-edge flap are stowed flush against the main wing, presenting a clean body to flow for reduced drag. However, during the approach and landing phases of flight the slats/flaps are deployed to improve aircraft performance while also exposing geometric discontinuities to the airflow (see Fig. 1.2). These geometric discontinuities lead to the development of unsteady flow, and in turn, aeroacoustic noise [95]. As shown in Fig. 1.2, flow bifurcates at the stagnation point of the leading-edge slat. The upper portion of the flow remains attached to the surface of the slat while the lower portion of the flow separates at the slat cusp resulting in the creation of a circulation region, a major source of flow unsteadiness and airframe noise. Noise reduction of aircraft, especially during approach and landing, is a growing interest in the aerospace community due to the increased number of airports near residential areas. The noise produced by the leading-edge slat is a significant contribution to the overall noise produced by the aircraft.

Many treatments have been proposed to mitigate slat noise. One that is particularly promising and of interest to this work is known as the slat-cove filler (SCF).

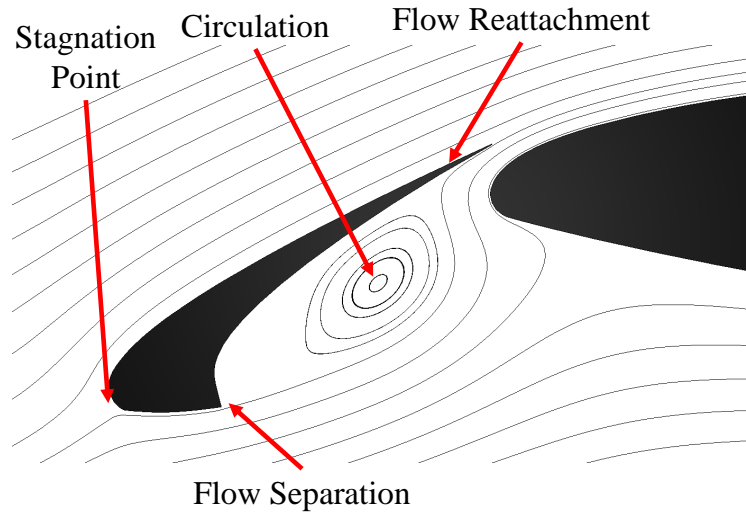


Figure 1.2: Streamlines in the vicinity of the leading-edge slat. Circulation region indicates noise production.

Originally proposed by Gleine, et al. [95], the SCF concept fills the cove aft of a deployed leading-edge slat (see Fig. 1.3), redirecting airflow along an acoustically advantageous path. Previous work has shown both experimentally and computationally that the SCF is effective at noise reduction [96, 97, 98]. Several approaches for development of a SCF have been considered. The most promising consists of superelastic shape memory alloy (SMA) sheets that have been shape-set to appropriately guide the gap flow. During cruise when the slat is retracted, the SCF must stow in a small space (see Fig. 1.4) between the main wing leading edge and slat-cove wall. The strain produced by this configuration change (2-5% [99]) exceeds typical aerospace materials.

The SCF is an interesting application for this work due to its incorporation of superelastic SMA sheets in the design as flexures. SMAs are a type of active material that can undergo a solid phase transformation between austenite and martensite

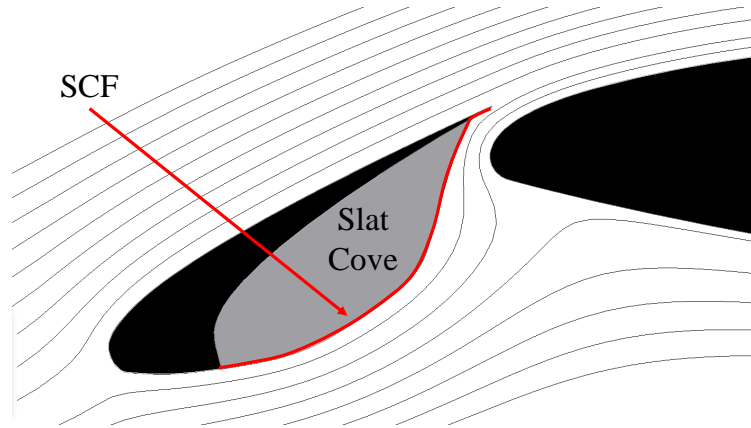


Figure 1.3: Streamlines in the vicinity of the leading-edge slat with a SCF.

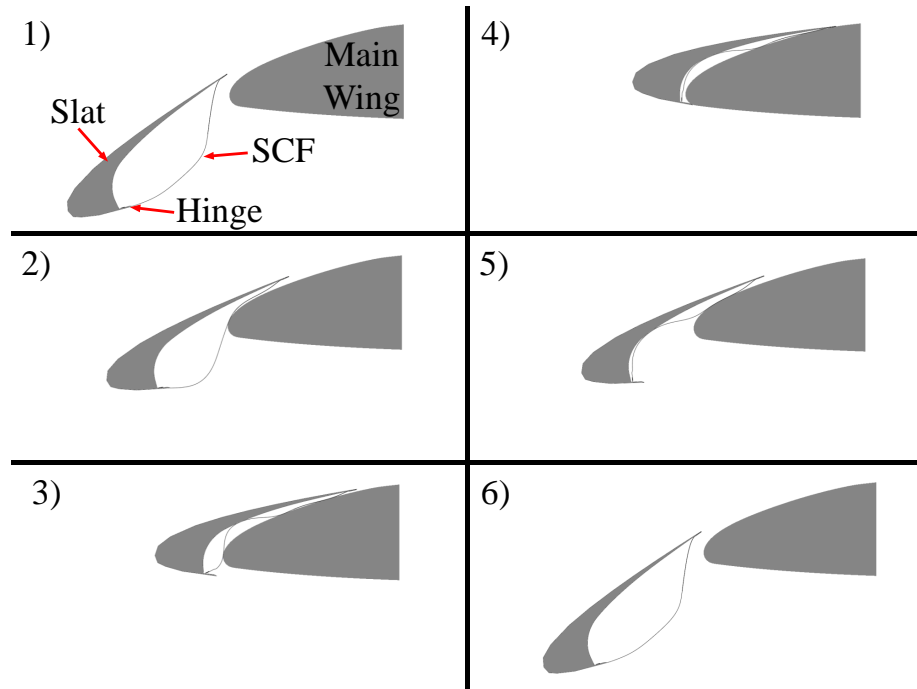


Figure 1.4: SMA SCF retraction/deployment.

either through mechanical or thermal loading to achieve large recoverable deformations [100]. SMAs are used in morphing applications due to their large recoverable deformation, high energy density and compactness (reduction of overall system complexity and weight) [101]. Specifically for the SCF, superleastic SMAs are considered due to three conflicting requirements common amongst morphing aerostructures [102] (see Fig. 1.5): 1) low weight, 2) stiffness while aerodynamically loaded, and 3) compliance for morphing. Figure 1.4 shows the retraction/deployment process of the SMA SCF. The SCF system considered in this work includes the main wing, slat, SCF, and a hinge attached to the slat that assists with SCF retraction/deployment. During slat retraction (starting from the deployed configuration **(1)**), the SCF contacts the main wing **(2)** resulting in localized stress concentrations in the SMA flexures. Sufficiently high stresses result in localized transformation from austenite to martensite, allowing the SCF to morph into a configuration suitable for storage **(3 and 4)**. As the slat is deployed **(5)**, the SCF loses contact with the main wing which unloads the SMA flexures and in turn results in the redeployment of the SCF into its original configuration **(6)**.

## 1.6 Summary of Objectives

The previous works discussed thus far have focused on FSI analysis for various applications and/or surrogate models constructed from a sampling of FSI analyses. It is clear in literature that an optimization incorporating an FSI analysis is computationally expensive to the point of being potentially infeasible. The use of surrogate models reduces the cost for conducting optimization; however, their construction requires multiple samples of the FSI analysis, which can be expensive especially when high-fidelity models are used or the number of design variables is large.

This work introduces a new method for conducting aeroelastic analysis referred to

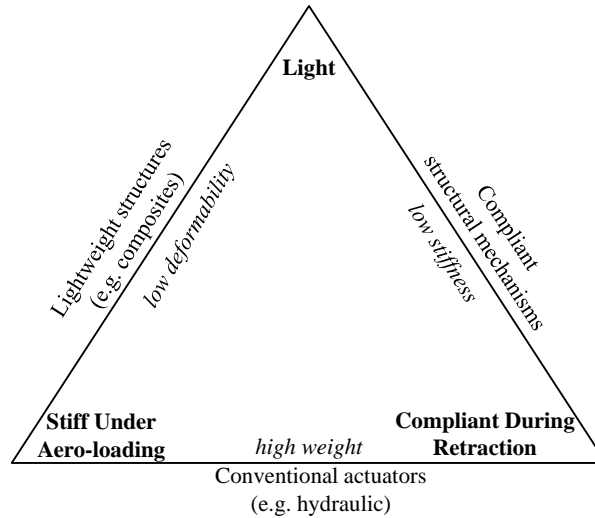


Figure 1.5: Morphing aero-structures requirement triangle [99]\*.

herein as the uncoupled static aeroelastic analysis (SAA) method, which should offer substantial reduction in cost during design studies and optimization specifically with design problems that seek structure/fluid response at a final time of interest. Instead of iterating coupled sets of displacement and pressure loading at every time increment until some final (or “steady-state”) time in an FSI analysis, this new method performs many individual (and uncoupled) analyses with different, constant fits of the pressure and displacement fields imposed on the structure and fluid models, respectively, which are described using a limited number of fitting parameters. Response surface modeling [57, 56] is then used to find the solution where the fit of the displacement matches the displacement calculated in the surrogate structural model (and similarly for the pressure). This new method reduces computational cost for static aeroelastic analysis due to 1) simultaneous, parallelizable and independent flow and structure

---

\*Figure 1.5 is reprinted with permission from “Development and Analysis-Driven Optimization of Superelastic Slat-Cove Fillers for Airframe Noise Reduction” by Scholten, W. and Hartl, D. and Turner, T. and Kidd, R., 2015, *AIAA Journal*, 54, Copyright 2015 by The American Institute of Aeronautics and Astronautics, Inc..

analyses for constructing response surface models, 2) retention of one set of results should there be modification of the other (i.e., changing stiffness, thickness, etc., of the structure only requires rerunning structural analyses and not fluid), and 3) elimination of the need for developing a coupling scheme between different structure and fluid solvers.

The main objectives of the research in this dissertation are the following:

- **Conduct aeroelastic analysis of the slat-cove filler using serial FSI scheme:** Develop structure and fluid models, conduct FSI analysis of the SCF for fixed, fully deployed conditions and retraction/deployment cycles, and provide motivation for the uncoupled scheme.
- **Develop the uncoupled SAA scheme for estimating static aeroelastic solutions:** Introduce uncoupled scheme, discuss uniqueness requirements, demonstrate uncoupled SAA scheme on simple problems, compare results to a serial FSI scheme, and develop means of visualizing the intersection of the surrogate model intersections.
- **Implementation of uncoupled SAA to optimization:** Develop optimization framework for uncoupled method and apply to a test problem.
- **Incorporate extensions of uncoupled scheme for predicting solutions at multiple freestream velocities and dynamic behaviour:** Explore prediction of the uncoupled SAA solutions at multiple freestream velocities, consider calculation of dynamic, free-response of structure, and explore structural aeroelastic divergence estimation.
- **Implement uncoupled SAA scheme on the slat-cove filler:** Develop approximations for pressure and displacement fields, find uncoupled solution

for multiple SCF designs, and compare to FSI solutions. This is considered to be the ultimate demonstration example of the method and its utility for morphing structures

## 2. FULL COUPLED FSI ANALYSIS OF THE SLAT-COVE FILLER

The first part of this work addresses fluid-structure interaction analysis of the motivational problem, the superelastic SMA SCF, using the legacy serial coupling scheme to demonstrate current capabilities. In this chapter, the underlying equations of the computational processes used throughout this dissertation are introduced and efforts at both model scale and full scale are addressed.

### 2.1 Computational Framework

Aeroelastic analysis with the legacy serial FSI coupling scheme is performed throughout this work using a computational framework comprised of Abaqus, a commercial finite element suite, and SC/Tetra, a thermo-fluid CFD solver, for the structure and fluid models, respectively. Both solvers are coupled using the Abaqus Co-Simulation Engine. Abaqus is considered in this work for its contact capabilities, automation with Python, wide range of boundary conditions and loadings, and use of custom constitutive model implementations for capturing the thermomechanical response of SMAs. SC/Tetra utilizes density and pressure based finite volume methods and unstructured meshing to solve both turbulent and laminar flows. Additionally, SC/Tetra utilizes 1) overset meshes that enable the modeling of complex relative translations and rotations of parts such as slat/flap articulation, and 2) deformable meshes that account for deformation such as the outer mold line of the slat/SCF during articulation. A native link in SC/Tetra to the Abaqus Co-Simulation engine allows for coupled transient FSI analysis to be easily performed.

### 2.1.1 SMA Constitutive Model Description

SMA materials exhibit complex thermomechanical behaviors that require the use of specialized constitutive models. For this work, the phenomenological constitutive model based on continuum thermodynamics by Lagoudas, et al. [103] is utilized. The constitutive model developed by Auricchio [104] is also used, but only for FSI analysis of the full scale SCF, which is performed in a collaborative work with the University of Bristol. The Auricchio model is pre-compiled in Abaqus, enabling collaborative work to be performed with the same structural models. The Lagoudas model is implemented in Abaqus as a Fortran custom User MATerial (UMAT) subroutine. Both models are calibrated using experimental data. A general description of the Lagoudas model for the behavior of the SMA flexures is provided next and followed by a brief overview of the Auricchio model. More detailed descriptions can be found elsewhere [105, 104].

#### 2.1.1.1 Lagoudas SMA Constitutive Model

The Lagoudas constitutive model considers two tensorial external state variables, stress  $\boldsymbol{\sigma}$  and strain  $\boldsymbol{\varepsilon}$ , in addition to the scalar, absolute temperature  $T$ . The two internal state variables, the scalar martensitic volume fraction  $\xi$  and the recoverable inelastic transformation strain tensor  $\boldsymbol{\varepsilon}^t$ , account for the microstructural state of the SMA. The temperature and total strain are assumed to be given values in displacement-driven FEA, leaving three unknowns (total of 13 scalar components) to be calculated. Additive strain decomposition is assumed per

$$\boldsymbol{\varepsilon} = \boldsymbol{S}(\xi)\boldsymbol{\sigma} + \boldsymbol{\alpha}(T - T_0) + \boldsymbol{\varepsilon}^t, \quad (2.1)$$

where  $T_0$  is a reference temperature,  $\boldsymbol{S}(\xi)$  is the phase-dependent, fourth-order com-

pliance tensor, and  $\boldsymbol{\alpha}$  is the second-order coefficient of thermal expansion tensor.  $\mathbf{S}(\xi)$  is calculated by the rule of mixtures via

$$\mathbf{S}(\xi) = \mathbf{S}^A + \xi(\mathbf{S}^M - \mathbf{S}^A). \quad (2.2)$$

The time rate of change of the inelastic transformation strain can be determined by

$$\dot{\boldsymbol{\epsilon}}^t = \dot{\xi} \boldsymbol{\Lambda}^t; \quad \boldsymbol{\Lambda}^t = \begin{cases} H \frac{3}{2} \frac{\boldsymbol{\sigma}'}{\bar{\sigma}} & \dot{\xi} > 0 \\ \frac{\boldsymbol{\epsilon}^{t-r}}{\xi^r} & \dot{\xi} < 0 \end{cases}, \quad (2.3)$$

where  $\boldsymbol{\Lambda}^t$  is the transformation direction tensor,  $\boldsymbol{\sigma}'$  is the deviatoric stress tensor, and  $H$  is the maximum uniaxial transformation strain. During forward transformation from austenite to martensite (i.e., during loading or retraction of the slat/SCF;  $\dot{\xi} > 0$ ), transformation strain is generated as in Mises plasticity. The Mises equivalent stress  $\bar{\sigma}$  is given as

$$\bar{\sigma} = \left( \frac{3}{2} \boldsymbol{\sigma}' : \boldsymbol{\sigma}' \right)^{1/2}, \quad (2.4)$$

In reverse transformation (unloading or deployment of the slat/SCF;  $\dot{\xi} < 0$ ), the transformation strain direction and magnitude are specified in such a way that the transformation strain present at the end of forward transformation is fully recovered, allowing the SMA to fully transform back into austenite. The memory variables  $\boldsymbol{\epsilon}^{t-r}$  and  $\xi^r$  are the transformation strain tensor and the martensitic volume fraction at transformation reversal, respectively.

The criteria for phase transformation during loading and unloading is quantified by the transformation function  $\Phi^t$ . The constraints on the evolution are specified as

$$\Phi^t \leq 0, \quad \dot{\xi} \Phi^t = 0, \quad 0 \leq \xi \leq 1. \quad (2.5)$$

The martensitic volume fraction can only range from 0 (pure austenite) to 1 (pure martensite). Due to the different stress levels inducing forward and reverse transformation, the branched form of  $\Phi^t$  is considered, given by

$$\Phi^t = \begin{cases} \Phi_{fwd}^t & 0 \leq \xi < 1; \quad \dot{\xi} \geq 0 \\ \Phi_{rev}^t & 0 < \xi \leq 1; \quad \dot{\xi} \leq 0 \end{cases}. \quad (2.6)$$

The forward transformation function is given as

$$\begin{aligned} \Phi_{fwd}^t &= (1 - D)H\bar{\sigma} + \frac{1}{2}\boldsymbol{\sigma} : \tilde{\mathbf{S}}\boldsymbol{\sigma} + \rho\tilde{s}_0T - \rho\tilde{u}_0 \\ &\quad - \left[ \frac{1}{2}a_1(1 + \xi^{n_1} - (1 - \xi)^{n_2}) + a_3 \right] - Y_0^t, \end{aligned} \quad (2.7)$$

while the reverse transformation function is given by the following

$$\begin{aligned} \Phi_{rev}^t &= -(1 + D)\frac{\boldsymbol{\sigma} : \boldsymbol{\varepsilon}^t - r}{\xi^r} - \frac{1}{2}\boldsymbol{\sigma} : \tilde{\mathbf{S}}\boldsymbol{\sigma} - \rho\tilde{s}_0T + \rho\tilde{u}_0 \\ &\quad + \left[ \frac{1}{2}a_2(1 + \xi^{n_3} - (1 - \xi)^{n_4}) - a_3 \right] - Y_0^t \end{aligned} \quad (2.8)$$

The parameters  $\mathbf{S}_A$ ,  $\mathbf{S}_M$ ,  $\boldsymbol{\alpha}$ ,  $\rho\tilde{s}_0$ ,  $\rho\tilde{u}_0$ ,  $Y^t$ ,  $D$ ,  $a_1$ ,  $a_2$ ,  $a_3$ ,  $n_1$ ,  $n_2$ ,  $n_3$ , and  $n_4$  are calibrated using the method described in Section 2.1.1.2.

### 2.1.1.2 Constitutive Model Parameters and Calibration

The constitutive model is calibrated using previously obtained experimental data from tension tests (per ASTM standard E345 [106]) on superelastic SMA supplied by Johnson Matthey Inc. that is used in a scaled wind tunnel model implementation of the SCF [107]. The stress-strain behaviour for this material at various temperatures is shown in Fig. 2.1 [107].

The thermoelastic behavior is described by  $\mathbf{S}_A$ ,  $\mathbf{S}_M$ , and  $\boldsymbol{\alpha}$  (Eq. (2.1) and Eq. (2.2)), which are easily calibrated using standard isotropic forms [100, 108]. The maximum magnitude of the evolving transformation strain is described by the scalar  $H$ ; in this

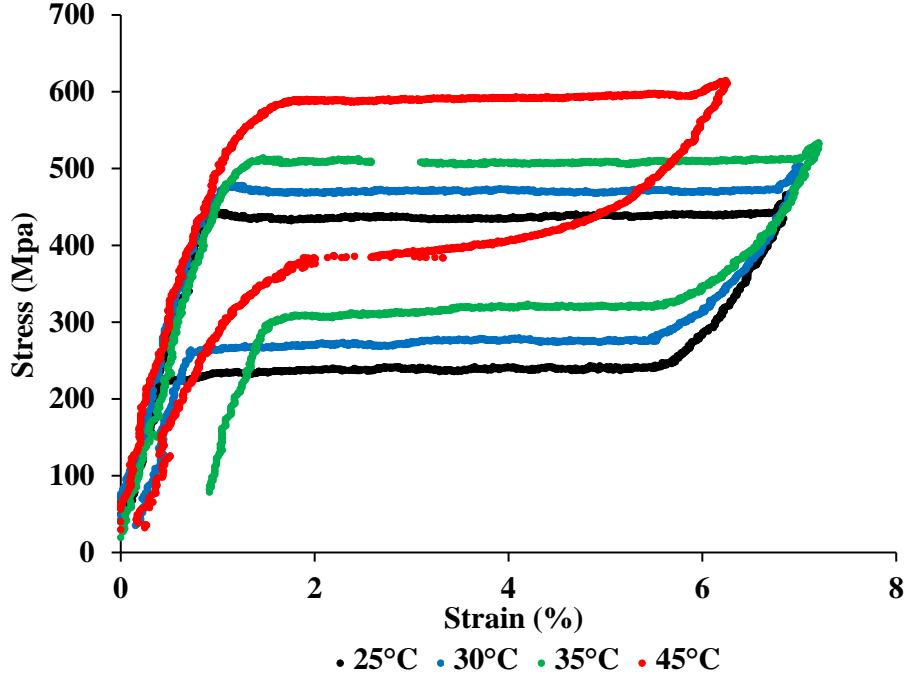


Figure 2.1: Stress-strain data of the superelastic SMA material at multiple temperatures.

study is assumed to be a constant. It is common to employ a stress-temperature *phase diagram* to graphically describe the transformation criterion and then to calibrate the thermodynamic model parameters ( $D$ ,  $Y_0^t$ ,  $\rho\tilde{u}_0$ ,  $\rho\tilde{s}_0$ ,  $a_1$ ,  $a_2$ , and  $a_3$ ). The phase diagram assumed for the SMA material used in this portion of the work (cf. Fig. 2.1) is shown in Fig. 2.2. The slanted pairs of lines denote the transformation limits and have slopes  $C_M$  and  $C_A$  for forward and reverse transformation, respectively. The constitutive model is formulated to consider the zero stress transformation temperatures ( $M_s$ ,  $M_f$ ,  $A_s$ ,  $A_f$ ).

Knowing the value of  $H$  (see Fig. 2.1) and the properties from the phase diagram (Fig. 2.2), the criteria for the transformation criterion  $\Phi_{fwd}^t$  and  $\Phi_{rev}^t$  are calibrated as shown [105]:

$$a_1 = \rho\tilde{s}_0(M_f - M_s), \quad (2.9)$$

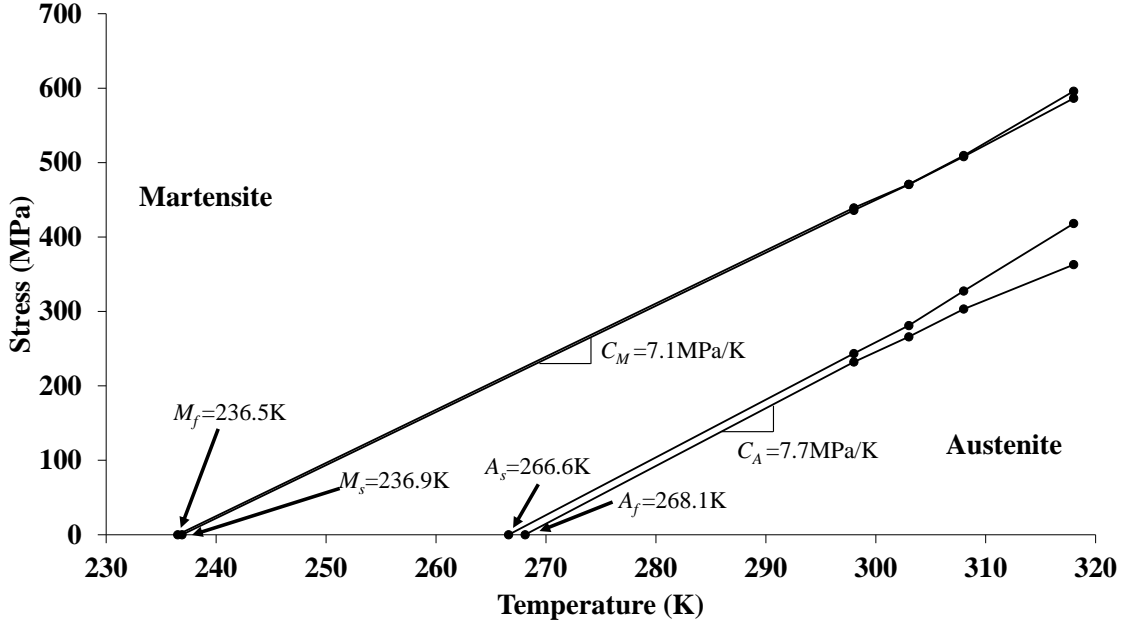


Figure 2.2: Phase diagram of SMA material associated with the calibrated constitutive model.

$$a_2 = \rho \tilde{s}_0 (A_s - A_f), \quad (2.10)$$

$$a_3 = -\frac{a_1}{4} \left( 1 + \frac{1}{n_1 + 1} - \frac{1}{n_2 + 1} \right) + \frac{a_2}{4} \left( 1 + \frac{1}{n_3 + 1} - \frac{1}{n_4 + 1} \right), \quad (2.11)$$

$$\rho \tilde{u}_0 = \frac{\rho \tilde{s}_0}{2} (M_s + A_f), \quad (2.12)$$

$$Y_0^t = \frac{\rho \tilde{s}_0}{2} (M_s - A_f) - a_3, \quad (2.13)$$

$$\rho \tilde{s}_0 = \frac{-2H (C_M C_A)}{(C_M + C_A)}, \quad (2.14)$$

$$D = \frac{(C_M - C_A)}{(C_M + C_A)}. \quad (2.15)$$

The transformation hardening coefficients  $n_1$ ,  $n_2$ ,  $n_3$ , and  $n_4$  are selected such that the best fit for the four corners of the transformation hysteresis can be obtained.

The material properties for the SMA material considered in this portion of the

work are shown in Table 2.1. Properties are based on the tension tests ( $E_A$ ,  $E_M$ ,  $M_s$ ,  $M_f$ ,  $A_s$ ,  $A_f$ ,  $H$ ,  $C^A$ , and  $C^M$ ) or are assumed to be a typical value for this type of material ( $\nu_A$ ,  $\nu_M$ , and  $\rho$ ). These properties were validated by superimposing the hysteresis loop generated by the calibrated model onto experimental results as shown in Fig. 2.3. Clearly the hysteresis loop generated by the model matches the experimental response closely.

Table 2.1: SMA material properties from [107].

Property	Value
(Elastic Properties)	
$E_A, E_M$	44.2 GPa, 26.4 GPa
$\nu_A = \nu_M$	0.33
(Phase Diagram Properties)	
$M_s, M_f$	236.9 K, 236.5 K
$A_s, A_f$	266.6 K, 268.1 K
$C^A, C^M$	7.1 MPa/K, 7.7 MPa/K
(Transformation Strain Properties)	
$H = H_v$	5.15%
(Smooth Hardening Properties)	
$n_1, n_2, n_3, n_4$	0.5
(Other Properties)	
$\rho$	6480 kg/m <sup>3</sup>
$\alpha_M = \alpha_A$	0

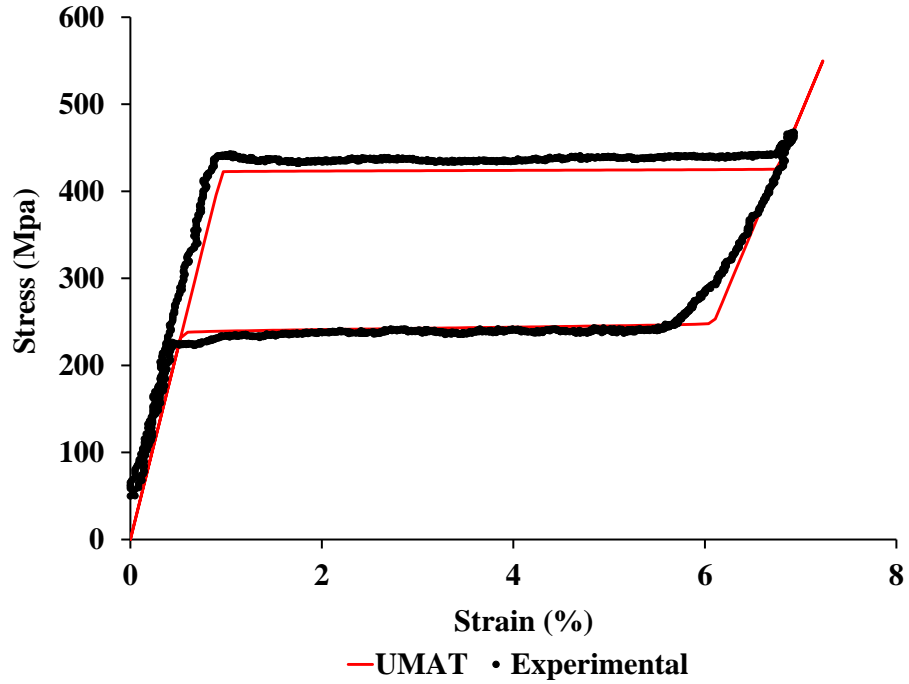


Figure 2.3: Comparison of hysteresis loop from calibrated UMAT and experimental data [107].

### 2.1.1.3 Auricchio Constitutive Model

The Auricchio constitutive model considers stress  $\boldsymbol{\sigma}$  and scalar, absolute temperature  $T$  (constant) as external state variables. The state of the SMA material is accounted for with two internal variables: 1) martensitic fraction  $\xi_s$  and the scaled transformation strain  $\mathbf{u}$ . Transformation strain is defined as

$$\boldsymbol{\epsilon}^{tr} = \boldsymbol{\epsilon}^{tr} + \epsilon_L \mathbf{u} \quad (2.16)$$

where  $\epsilon_L$  is the maximum transformation strain. Total strain  $\boldsymbol{\epsilon}$  is assumed as

$$\boldsymbol{\epsilon} = \boldsymbol{\epsilon}^e + \boldsymbol{\epsilon}^{tr} \quad (2.17)$$

where  $\boldsymbol{\epsilon}^e$  is elastic component of strain. The elastic strain is assumed to related the stress as:

$$\boldsymbol{\epsilon}^e = \mathbf{S}(\xi)\boldsymbol{\sigma} = (\mathbf{S}^A + \xi(\mathbf{S}^M - \mathbf{S}^A))\boldsymbol{\sigma} \quad (2.18)$$

The forward transformation loading function is given as

$$F^{AM}(\boldsymbol{\sigma}, T) = \|\boldsymbol{\sigma}'\| - C^M T \quad (2.19)$$

where  $\boldsymbol{\sigma}'$  is the deviatoric stress. For forward transformation to occur, the following conditions must be satisfied.

$$F^{AM} > \sigma^{Ms}, \quad F^{AM} < \sigma^{Mf}, \quad \dot{F}^{AM} > 0 \quad (2.20)$$

where  $\sigma^{Ms}$  and  $\sigma^{Mf}$  are the start and finish stress levels of forward transformation for the given temperature  $T$ .

Similarly, the reverse transformation loading function is given by the following

$$F^{MA}(\boldsymbol{\sigma}, T) = \|\boldsymbol{\sigma}'\| - C^A T \quad (2.21)$$

For reverse transformation to occur, the following conditions must be satisfied.

$$F^{MA} < \sigma^{As}, \quad F^{MA} > \sigma^{Af}, \quad \dot{F}^{MA} < 0 \quad (2.22)$$

where  $\sigma^{As}$  and  $\sigma^{Af}$  are the start and finish stress levels of reverse transformation for the given temperature  $T$ . Note that, the properties  $C^M$  and  $C^A$  are the same between the Auricchio and Lagoudas constitutive models. Additionally, if considering only isothermal load cases, then the behavior of the Lagoudas and Auricchio models should match. The material properties for the Auricchio model are shown in Table 2.2. The

properties are either taken directly from the properties for the Lagoudas constitutive model in Table 2.1 ( $E_A$ ,  $E_M$ ,  $\nu_A$ ,  $\nu_M$ ,  $\rho$ ,  $C^A$ ,  $C^M$ ,  $H$ ) or based on the superelastic response of the Lagoudas constitutive model at 25 C° shown in Fig. 2.3 ( $\sigma^{Ms}$ ,  $\sigma^{Mf}$ ,  $\sigma^{As}$ , and  $\sigma^{Af}$ ) such that the constitutive models approximately match.

Table 2.2: SMA material properties from [107].

Property	Value
(Elastic Properties)	
$E_A$ , $E_M$	44.9 GPa, 26.4 GPa
$\nu_A = \nu_M$	0.33
(Phase Diagram Properties)	
$\sigma^{Ms}$ , $\sigma^{Mf}$	422 MPa, 425 MPa
$\sigma^{As}$ , $\sigma^{Af}$	247 MPa, 231 MPa
$C^A = C^M$	7.12 MPa/K
(Transformation Strain Properties)	
$H$	5.15%
(Other Properties)	
$\rho$	6480 kg/m <sup>3</sup>

### 2.1.2 Turbulence Model Description

In this section, a general description of turbulence modeling, specifically the Shear-Stress Transport (SST)  $k$ - $\omega$ , is provided. More detailed descriptions of the SST  $k$ - $\omega$  can be found elsewhere [109, 110].

For laminar, incompressible flow (single species), fluid solvers such as SC/Tetra solve the conservation of mass, conservation of momentum and conservation of energy equations. For applications of interest in this work, the change in temperature is not

of interest so temperature is held constant. This simplifies the conservation equations and removes the need to solve the conservation of energy.

The conservation of mass is given as,

$$\frac{\partial u_i}{\partial x_i} = 0 \quad (2.23)$$

where  $x_i$  is the  $i$ th coordinate ( $i= 1-3$  for a 3-dimensional system) and  $u_i$  is the velocity in the  $x_i$  direction. The conservation of momentum equation is,

$$\frac{\partial \rho u_i}{\partial t} + \frac{\partial u_j \rho u_i}{\partial x_j} = -\frac{\partial P}{\partial x_i} + \frac{\partial}{\partial x_j} \mu \left( \frac{\partial u_i}{\partial x_j} + \frac{\partial u_j}{\partial x_i} \right) \quad (2.24)$$

where  $\rho$  is the density (constant for incompressible fluid),  $t$  is time,  $p$  is the fluid pressure and  $\mu$  is the viscosity.

Unlike the smooth, steady movement of laminar flow, turbulent flow is the unsteady movement of fluid. Turbulent flow can develop from laminar flow when the Reynolds number exceeds a critical value. A key characteristic of turbulent flow is the development of eddies (vortical motion of flow) that increases the mixing of fluid. Eddies of various length scales are formed and need to be resolved to solve the turbulent flow. Capturing all of the eddies in turbulent flow is impossible due to computer limitations. Instead, the change in mean velocity (or heat transfer) due to turbulence is obtained. For this reason instantaneous pressure and velocity are expressed as a summation of the mean values (denoted as  $\bar{P}$  and  $\bar{u}_i$ ) and the fluctuation (denoted as  $P'$  and  $u'_i$ ).

$$u_i = \bar{u}_i + u'_i \quad (2.25)$$

$$P = \bar{P} + P' \quad (2.26)$$

Substituting these values into conservation of mass and conservation of momentum results in the following, equations

$$\frac{\partial \bar{u}_i}{\partial x_i} = 0 \quad (2.27)$$

$$\frac{\partial \rho \bar{u}_i}{\partial t} + \frac{\partial \bar{u}_j \rho \bar{u}_i}{\partial x_j} = -\frac{\partial \bar{P}}{\partial x_i} + \mu \frac{\partial}{\partial x_j} \left( \frac{\partial \bar{u}_i}{\partial x_j} + \frac{\partial \bar{u}_j}{\partial x_i} \right) - \frac{\partial}{\partial x_j} (\rho \overline{u_i' u_j'}) \quad (2.28)$$

Equation (2.28) is known as the Reynolds equation. The term  $-\rho \overline{u_i' u_j'}$  is known as the Reynolds shear stress and represents the shear stress produced by turbulent flow. This term cannot be solved practically without making some assumptions.

Joseph Boussinesq proposed treating the Reynolds stress as the following

$$-\rho \overline{u_i' u_j'} = \mu_t \left( \frac{\partial \bar{u}_i}{\partial x_j} + \frac{\partial \bar{u}_j}{\partial x_i} \right) - \frac{2}{3} \rho k \delta_{ij} \quad (2.29)$$

where  $\mu_t$  is a proportionality constant known as the eddy viscosity and  $k$  is the turbulent energy expressed as,

$$k = \frac{1}{2} \overline{u_i' u_i'} \quad (2.30)$$

The only remaining information to specify in Eq. (2.29) is the eddy viscosity  $\mu_t$ . However, since the eddy viscosity changes with location and state it needs to be constantly redefined. This is accounted for by introducing fundamental quantities of turbulence and solving the transport equations related to the quantities.

The  $k$ - $\omega$  turbulence model proposed by Wilcox [111], uses the turbulent energy  $k$  and the dissipation rate per unit of turbulence energy  $\omega$ . The dissipation rate per unit turbulent energy  $\omega$  is proportional to  $\varepsilon/k$  where  $\varepsilon$  is the dissipation rate. In this model, eddy viscosity is expressed as,

$$\mu_t |_{k-\omega} = \rho \frac{k}{\omega} \quad (2.31)$$

The transport equations for  $k$  and  $\omega$  are expressed as:

$$\frac{\partial \rho k}{\partial t} + \frac{\partial \bar{u}_i \rho k}{\partial x_i} = \frac{\partial}{\partial x_i} \left[ \left( \mu + \frac{\mu_t}{\sigma_k} \right) \frac{\partial k}{\partial x_i} \right] G_s - \rho \varepsilon \quad (2.32)$$

$$\frac{\partial \rho \omega}{\partial t} + \frac{\partial \bar{u}_j \rho \omega}{\partial x_j} = \frac{\partial}{\partial x_j} \left[ \left( \mu + \frac{\mu_t}{\sigma_\omega} \right) \frac{\partial \omega}{\partial x_j} \right] + \frac{\gamma \rho}{\mu_t} + G_s - \beta \rho \omega^2 \quad (2.33)$$

$$G_s = \mu_t \left( \frac{\partial \bar{u}_i}{\partial x_j} + \frac{\partial \bar{u}_j}{\partial x_i} \right) \frac{\partial \bar{u}_i}{\partial x_j} \quad (2.34)$$

where  $\varepsilon = C_\mu k \omega$ . Note that  $C_\mu$ ,  $\sigma_k$ ,  $\sigma_\omega$ ,  $\beta$  and  $\gamma$  are all empirical model constants. The model constant  $\gamma$  is calculated from the other constants by the following equation

$$\gamma = \frac{\beta}{C_\mu} - \frac{\kappa^2}{\sigma_\omega \sqrt{C_\mu}} \quad (2.35)$$

where  $\kappa$  is another model constant [111, 109]. Note that the  $k$ - $\omega$  model can be analytically equivalent to the  $k$ - $\varepsilon$  model (another popular turbulence model [109]) with the addition of the cross-diffusion term to the right side of the  $\omega$  transport equation as follows,

$$CD_{k\omega} = 2 \frac{\rho}{\sigma_\omega \omega} \frac{\partial k}{\partial x_j} \frac{\partial \omega}{\partial x_j} \quad (2.36)$$

In near-wall flow, the  $k$ - $\omega$  model has advantages over other turbulence models. It better estimates the boundary layer separation in flow with adverse pressure-gradients, and damping functions are not required for calculating the near-wall velocity. The  $k$ - $\omega$  model, however, is very dependent on boundary conditions such as the free stream turbulence properties. Also, in the outer free-stream layer of a boundary layer, the  $k$ - $\omega$  model loses accuracy. For these reasons, we consider a vari-

ation of the standard  $k-\omega$  model known as the SST  $k-\omega$ . This model, developed by Menter [110] uses a zonal treatment to avoid the numerical errors associated with the  $k-\omega$  model in the outer boundary layer region. In the near-wall regions, the standard  $k-\omega$  equations are used, while towards the outer regions, the equations are adjusted to match the behavior of  $k-\varepsilon$  turbulence models that are more accurate in the outer region. The shift in model behavior is performed using a product of the cross-diffusion term shown in Eq. (2.36) and a blending function that is dependent on the wall distance and turbulence quantities. In addition, the blending function is used to interpolate the model constants from given values for both the inner and outer regions. The eddy viscosity for SST  $k-\omega$  model is represented by the following equation,

$$\mu_t |_{SST} = \rho \frac{a_1 k}{\Omega} \quad (2.37)$$

where  $a_1$  is a constant ( $=0.31$ ) and  $\Omega$  is the magnitude of mean vorticity. Equations (2.31), (2.37), and (2.35) are interpolated using a blending function with arguments of wall distance and turbulence quantities.

## 2.2 Model Scale SCF\*

FSI analysis of the model scale SMA SCF using the serial coupling scheme is first discussed. The SCF profile considered herein is for the high-lift variant of the Boeing-NASA Common Research Model (CRM), an open-source geometry of a transport-class aircraft developed for the purpose of validating CFD results and evaluating new technologies [112, 113]. The base geometry of the computational

---

\*With the exception of Fig. 2.4 all work in this section is reprinted with permission from “Aerodynamic and Structural Evaluation of an SMA Slat-Cove Filler Using Computational and Experimental Tools at Model Scale” by Scholten, W. and Patterson, R. and Eustice, M. and Cook, S. and Strganac, T. and Turner, T. and Hartl, D., 2018 *ASME 2018 Conference on Smart Materials, Adaptive Structures and Intelligent Systems*, 8129 [11], Copyright 2018 by The American Society of Mechanical Engineers.

models is from a 6.25% scale 2D section of the CRM at the midspan of the outboard slat aligned with the freestream-direction (see Fig. 2.4), which has a stowed chord of 0.3216 m.

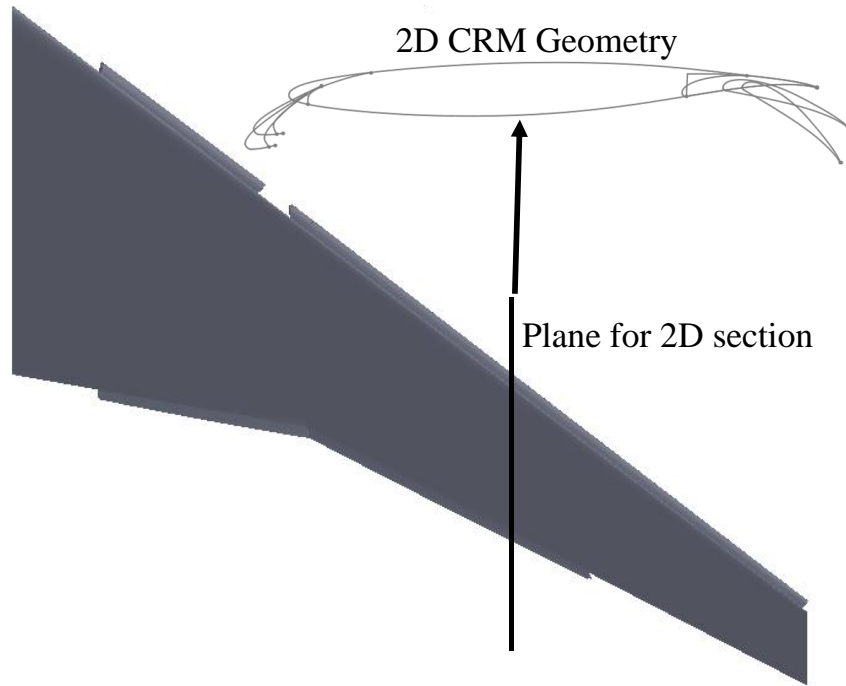


Figure 2.4: Solidworks model of 3D CRM wing configuration used to obtain 2D section. Note that the 2D section shown is not the same scale as the 3D wing.

### 2.2.1 Finite Element Structural Model

The finite element structural model, shown in Fig. 2.5(a), is created using Abaqus [114]. All components in the model are one element wide in the spanwise direction with a length of 1.0 mm. The entire outer mold line (OML) of the slat and SCF is modeled as a single deformable shell (see Fig. 2.5(b)) for the purpose of improving the FSI implementation by linking the structure and fluid models with the surface of a single closed volume (the slat/SCF). The negative offset of the slat cusp, indicated

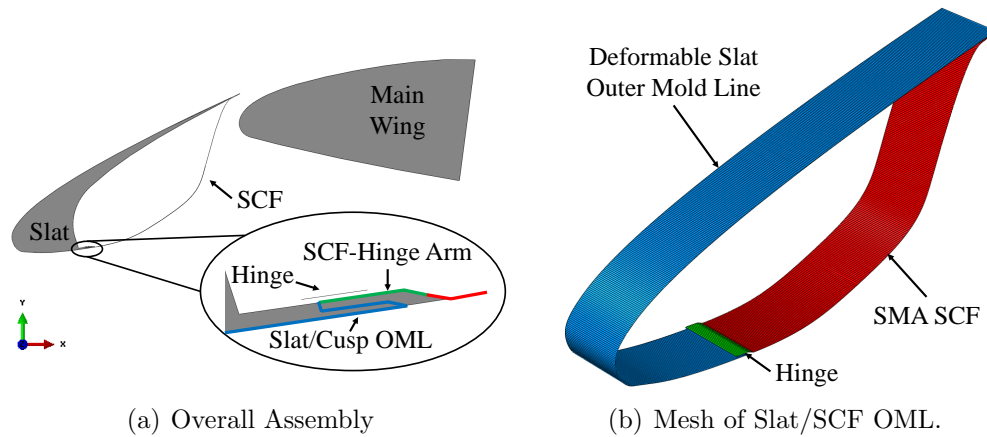


Figure 2.5: Structural FEA model of 2.5D SMA SCF assembly.

by the blue outline in the inset of Fig. 2.5(a), was introduced in the computational model to assist in the accommodation of FSI analysis, specifically the articulation of the hinge during deployment and retraction. Rigid bodies in the model include the hinge, main wing leading-edge, and a rigid slat. The slat OML portion of the deformable slat/SCF is connected via tie constraints to the rigid slat, thus making it rigid during the analysis. Applying a rotational displacement about the rigid slat reference point simulates slat retraction and deployment, which is a circular arc in the physical model. A rotation of  $0.44 \text{ rad}$  ( $25.2^\circ$ ) fully retracts the slat from the deployed configuration for this freestream parallel section of the CRM wing. Note that for the full scale 3D geometry, the hingeline nominal rotation angle for slat retraction/deployment is  $30^\circ$  [112]. The potential for transient dynamic behavior of the SCF during slat articulation, e.g., SCF stowage, or due to aerodynamic fluctuating pressures requires the use of an implicit dynamic solver (a `*Dynamic Implicit` step in Abaqus).

The thickness of the SCF portion of the OML shell is set to  $0.0762 \text{ mm}$  ( $0.003 \text{ in}$ ), which matches the 6.25% scaled experimental prototype of a SCF employed on a

wind-tunnel model. The SMA SCF portion has a mesh of 262 general shell elements (type S4R). For this work, the Lagoudas constitutive model captures the thermomechanical behaviour of the SMA SCF. An infinitely-long SCF in the spanwise direction is simulated through the application of symmetry conditions on the edges of the OML shell aligned with the X-Y plane. The length (2.16 mm) of the SCF-hinge arm (projection of the hinge onto the SCF) and placement of the hinge (1.13 mm from cove wall) are based on results from an optimization study (similar to previous work [99]) with an objective of minimizing the actuation force components (horizontal and vertical) required to retract the slat/SCF (see Appendix A). To model contact between the SCF and the various parts, surface-to-surface contact is implemented. A linear penetration penalty law should state the stiffness used here is utilized to prevent surface-surface penetration in the normal direction while contact in the tangential direction is modeled with a friction coefficient of 0.42, which was measured experimentally [107].

### *2.2.2 Finite Volume Computational Fluid Dynamics Model*

The fluid model used in this work is also 2D (infinite in the spanwise direction), built in SC/Tetra, and consists of the wing and the test section (2.74 m in length) of the Texas A&M University 3 ft-by-4 ft (0.91 m-by-1.22 m) wind tunnel (see Fig. 2.6). Aspects of the modeled test section include the inlet, outlet, bottom (floor) wall, and top (ceiling) wall.

During slat retraction, the SMA SCF stows between the main wing and the slat, leading to a significant reduction of fluid volume in the slat cove, while during slat deployment, there is a large increase in fluid volume as the SMA SCF returns to its original configuration. Both volume changes can lead to elements with poor aspect ratio and zero volume through compressing and/or stretching, resulting in numerical

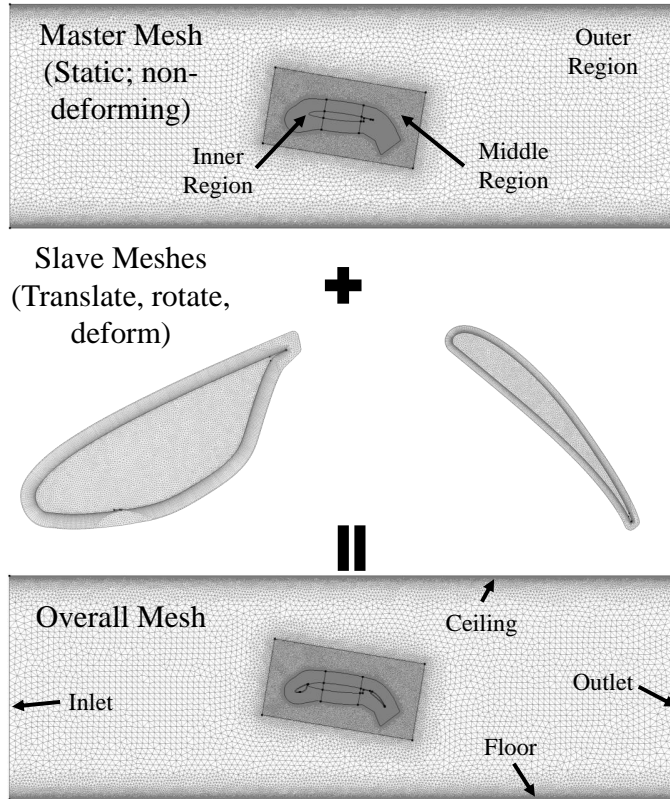


Figure 2.6: Fluid model and overset mesh implementation of the SCF-treated, deployed configuration.

instabilities during the analysis. The volume changes are accommodated through the use of overset meshes, which allow deformable, movable slave meshes to coincide in the same location as a fixed master mesh. Interpolation transmits flow data between the outer boundary of the slave meshes and master mesh. For this work, the test section and main wing are incorporated into the master mesh as neither component moves during FSI analysis, while the high lift devices are incorporated in the slave meshes. Previous work separated the SMA SCF and slat into two slave meshes [107], but interaction between the two slave meshes led to difficulties in running FSI analysis. In this work, the slat and SCF are included in a single slave mesh that reduces the complexity associated with building the FSI model.

For ease of mesh specification, the master mesh of the fluid model consists of three closed volume regions: 1) outer, 2) middle, and 3) inner, the latter of which includes the solid closed volumes of the wing. The boundary of the inner volume region is based on an offset from the wing outer mold line equal to 10% of the retracted chord. The middle volume region is defined as a 1-chord-by-2-chord box centered about the midchord of the retracted configuration. The remaining domain of the model is the outer volume region. Each volume region is assigned an element size. The element size in the outer and middle volume regions are 25.6 mm and 3.2 mm respectively. Sizes of 0.4 mm and 0.8 mm are assigned in the inner volume region in the vicinity of the high-lift devices and main wing, respectively. These element size selections maintain accuracy of the analysis while reducing computational cost. Note that the element size along the surfaces of the test section floor and ceiling in the outer volume region are refined to the same level as the inner volume region in order to capture the viscous effects and boundary layer properly. Layers of hexahedron elements are inserted along the surfaces of the wing and test section floor/ceiling to improve the fidelity of the boundary layer. Element sizes of the model and parameters for the hexahedron layers are based on mesh studies that examine how lift and drag are affected by changes in the mesh (see Appendix A). Mesh and prism parameters for the flap and slat slave meshes are based on those of the inner region.

Boundary conditions applied to the fluid model include 1) freestream flow (both velocity and turbulence properties) at the inlet, 2) zero static pressure (i.e., no pressure gradient) at the outlet, and 3) smooth, no-slip/penetration walls on the surface of the floor, ceiling, and wing. For all flow analysis, the fluid is incompressible air with viscosity of  $1.83 \times 10^{-5}$  Pa-s and density of  $1.206 \text{ kg/m}^3$ . Turbulent aspects of the flow, such as separation on the high-lift devices and recirculation of flow in the slat-cove, are modeled with the SST  $k - \omega$  turbulence model [110]. At the inlet,

turbulent kinetic energy  $k$  and turbulent dissipation rate  $\varepsilon$  are specified. Note that, approximately laminar flow at the inlet is modeled when  $k$  and  $\varepsilon$  are  $0.0001 \text{ m}^2/\text{s}^2$  and  $0.0001 \text{ m}^2/\text{s}^3$ , respectively. Accurate values of both properties are required to properly model the flow through the test section. Turbulent kinetic energy can be experimentally determined using a hot wire anemometer, which measures velocity to a high precision at a single point in the flow. The fluctuation in velocity, represented as the root-mean square of the velocity ( $U_{RMS}$ ), is directly related to the turbulent kinetic energy through the following equation

$$k = \frac{3}{2}(U_{RMS})^2. \quad (2.38)$$

The turbulent dissipation rate is estimated using the relation,

$$\varepsilon = \frac{0.09^{\frac{3}{4}} \cdot k^{\frac{3}{2}}}{0.07D}, \quad (2.39)$$

where  $D$  is the equivalent diameter of the rectangular inlet. Preliminary velocity measurements were taken over a single plane in an empty test section of the wind tunnel using a hot wire anemometer mounted to a newly, renovated three degree-of-freedom traversing system. In the vicinity of where the wing is to be mounted, the turbulent kinetic energy at flow speed of  $15 \text{ m/s}$  was measured to be  $0.68 \text{ m}^2/\text{s}^2$  (4.5% turbulent) with a corresponding dissipation rate of  $1.15 \text{ m}^2/\text{s}^3$  while the turbulent energy and dissipation rate were  $0.57 \text{ m}^2/\text{s}^2$  and  $0.68 \text{ m}^2/\text{s}^2$  at a flow speed of  $20 \text{ m/s}$  (3.1% turbulent).

Movement of the slat/SCF is dictated by model (see following section) while movement of the flap is controlled by SC/Tetra. The flap is not controlled in the structural model since only the forward part of the wing is modeled in the structure.

User-defined functions in SC/Tetra apply prescribed translations and rotations to the flap based on kinematic relations of the physical model. Equations of motion for the flap are derived in Appendix A. Both the flap and slat are articulated at consistent rates to ensure the high-lift devices move across their respective range of motion over the same time period.

### *2.2.3 FSI Framework and Remeshing Scheme*

The Abaqus Co-Simulation Engine (CSE) is utilized in the coupling of the structure and fluid models for FSI analysis. The partitioned coupling is weak and easy to implement due to a built-in link in SC/Tetra to the CSE. The weak coupling allows the two programs to solve physical quantities separately and transmit necessary data at specified time increments, enabling the use of user functions in Abaqus to capture SMA behavior. Displacement of specified surfaces are transmitted from Abaqus to SC/Tetra while SC/Tetra provides the pressure loading. For this work, the outer mold line of the slat/SCF is the only surface linked between the two models. FSI analysis is performed for two cases: 1) high-lift devices fixed and fully deployed, and 2) high-lift device retraction/deployment.

During FSI analysis of slat/SCF articulation, the portion of the slave mesh representing the slat-cove is significantly reduced, resulting in the creation of zero volume elements. This led to the development of a slave mesh remeshing scheme. A flowchart of the scheme is shown in Fig. 2.7. At specified stages of the slat articulation, when the mesh is deemed poor, the FSI analysis is stopped and the slave mesh is rebuilt. Flow results from the final cycle of the previous FSI analysis are mapped as initial conditions to the new analysis. The remeshing process of the fluid model also requires rebuilding of the structural model to relink the structural and fluid models.

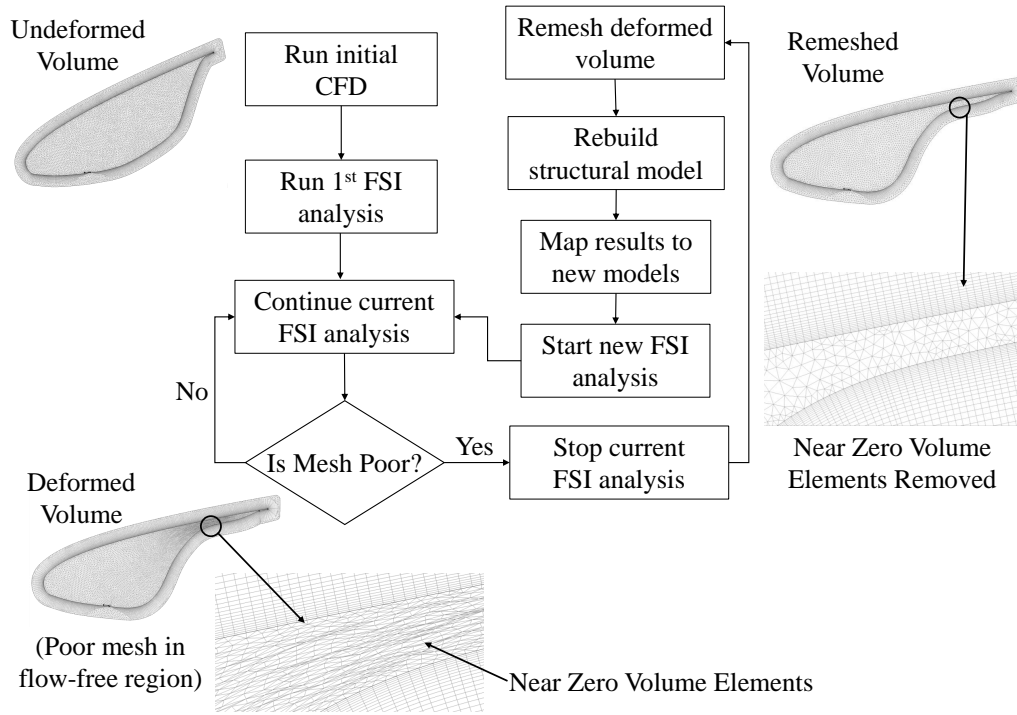


Figure 2.7: Flowchart of FSI analysis with remeshing scheme.

#### 2.2.4 FSI Analysis: Fully Deployed SCF

FSI analysis is conducted on the SMA SCF with the slat in a fixed, fully deployed configuration at  $6^\circ$  and  $8^\circ$  angle of attack and with inlet speeds of 15 m/s and 20 m/s (and corresponding turbulence properties). Prior to each FSI analysis, CFD is conducted to develop the flow to a near-steady condition, allowing for reduction of overall computational runtime. The analysis is conducted over 0.75 s with a time step of 0.000025 s. The computational cost for each analysis is 52 hr on a standard workstation with 10CPU. Figure 2.8 shows the displacement time response of the node with the maximum deflection at the end of the analysis and contour plots of the displacement field for all four flow conditions. As seen in the figure, the maximum displacement occurs for all four cases generally in the same location in the aft third of

the SCF. The SCF deflection shows a transient response at the start of the analysis but decays to a very small amplitude about a steady value as the fluid and structure reach a steady response. The displacement is virtually constant near the end of analysis for all flow conditions except the  $6^\circ$ , 15 m/s, case which exhibits noticeable oscillatory behavior remaining. At 15 m/s, the average maximum displacement for both angles is similar in value (approximately 0.04 mm). However, at the higher flow speed, the steady displacements for the two angles are further apart suggesting that the angle of attack may have an increasing effect on the SCF displacement as the flow speed is increased. Additionally, the 33% increase in flow speed (from 15 to 20 m/s) results in approximately 75% increase in the maximum deflection. This is reasonable since the pressure acting on the SMA SCF is quadratically proportional to velocity.

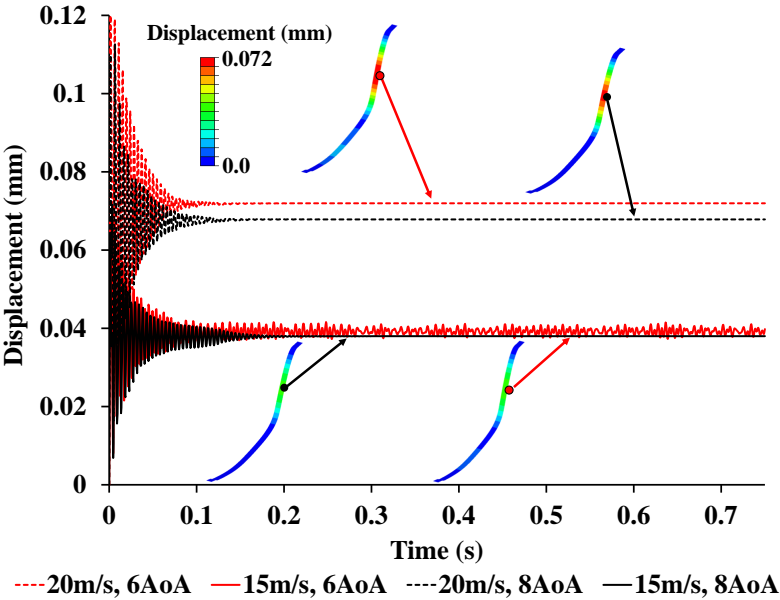


Figure 2.8: Displacement of SMA SCF during FSI analysis for the fixed fully deployed case. Contour plots are from the final time increment.

### 2.2.5 FSI Analysis: Transient Retraction/Deployment

The other case considered for the FSI analysis is retraction and deployment of the SMA SCF with flow. This analysis is believed to be one of the first FSI analyses of an SMA-based morphing structure attached to a rigid body (the slat) that is moving relative to a fixed rigid body (the main wing) and exhibits significant volume change and contact between bodies. As with the fixed, fully deployed case, an initial CFD analysis is used to develop the flow for both the fully deployed and retracted configurations. Turbulence measurements in the test section had not been conducted at the time of the analysis. Instead, inlet conditions are assumed to be approximately laminar. Inlet velocity is set to 15 m/s and the wing is oriented at  $8^\circ$  angle of attack. During this analysis, the remeshing scheme of Fig. 2.7 is implemented to fully retract and deploy the SCF. For slat retraction, the SCF/slat slave mesh is remeshed at slat positions corresponding to 50% retraction and 90% retraction. For slat deployment, the SCF in the structural model is initially retracted into its stowed configuration separately from the fluid model to setup the slat/SCF slave mesh. During the deployment, remeshing occurs once at 85% deployment as the hinge articulates into its deployed state. Note that a few fluid elements in the vicinity of the hinge are deleted to accommodate the redeployment of the hinge due to a localized, significant reduction of fluid volume as the hinge redeploys. Both retraction and deployment simulations are conducted over 0.5 s (articulation rate of 0.88 rad/s) with a time step of 0.00005 s. The computational cost of the retraction and deployment FSI analyses are both approximately 33 hr on a standard workstation with 10CPU. Note that the articulation of the high-lift devices in the analysis (full retraction or deployment in 0.5 s,) is much faster than the actual system in an aircraft (typically  $\approx 20$  s).

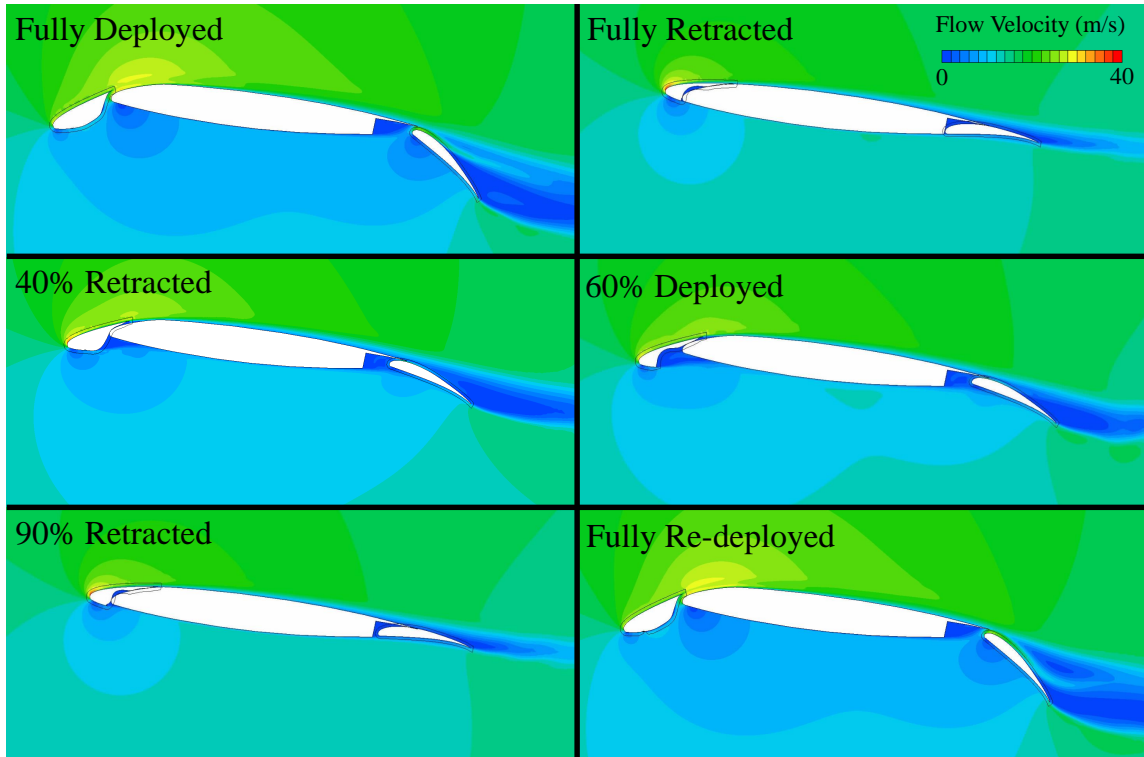


Figure 2.9: Velocity contours of CRM at various retraction and deployment stages of the high-lift devices.

Figure 2.9 shows the velocity contours around the CRM wing at various stages of slat/flap articulation. The SMA SCF is able to fully stow into its retracted position and redeploy while under aerodynamic loading. The flow separation on the flap, particularly in the fully deployed, high-lift configuration, is mainly due to the low Reynolds number of the flow, i.e., low flow speed and small scale. As the high-lift devices are stowed, the overall magnitude of velocity across the surface of the wing (with the exception of the slat leading-edge) decreases due to the reduction in the camber of the wing and elimination of the suction peaks for the flap and main wing. Another interesting behavior, first observed in previous work [107], occurs when the SMA SCF is in contact with the main wing. Flow over the leading edge of the main

wing is prevented, leading to flow separation off the slat/SCF and reattachment further downstream on the main wing. The behavior simulates a drooped leading edge, but the effect reduces as the high-lift devices near full stowage. The velocity contours return to the original distribution as the high-lift devices are redeployed. During deployment, the SMA SCF remains in contact with the main wing and in a stowed configuration simulating an alternative SMA-based aeroacoustic noise reduction system known as the slat-gap filler (SGF) [115]. The SCF configuration during most of the retraction cycle is significantly different than the SCF configuration during deployment at the same percent deployment, which could potentially affect the flow around the wing. This can be observed in Fig. 2.9 at 40% retracted and 60% deployed where the wing is at the same percent deployment. Overall the distribution of the velocity contour is fairly similar between the partially retracted and partially deployed configurations. The main differences are in the vicinity of the slat. The flow speed is slightly higher at the leading edge and higher speed extends further into the flow field away from the main wing for the 40% retracted configuration. Additionally, the 60% deployed configuration has a larger low velocity region between the slat and main wing due to the SCF being stowed. These differences in velocity contours for the two configurations may result in different global responses such as lift and drag of the wing.

The lift coefficient versus percent deployment for the FSI analysis is shown in Fig. 2.10 for both retraction and deployment phases of slat articulation. As expected, the lift decreases during retraction of the slat as the wing transitions from the high-lift to the cruise configuration and then increases as the high-lift devices are deployed. However, there are some differences in the predicted lift between the retraction and deployment phases of articulation. The discrepancies in lift at 0% and 100% deployment are unexpected and may be due to differences in the deformed and

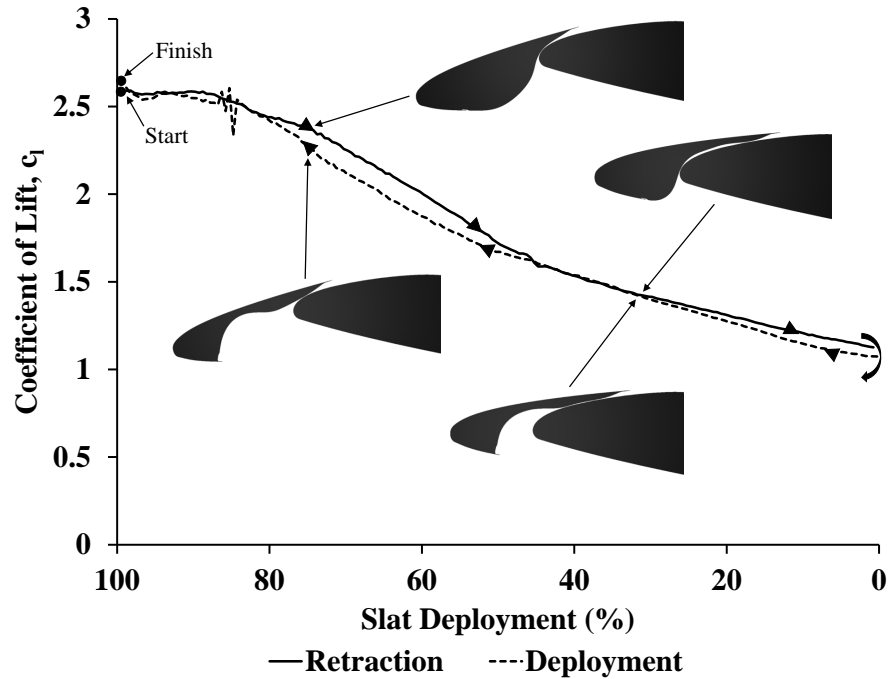


Figure 2.10: Lift coefficient of wing versus % deployment for retraction and deployment cycles.

undeformed meshes in those configurations. The differences in lift between 50% and 80% deployment are at least partially attributable to physical differences in configuration. For example, the flow remains attached over a larger portion of the slat/SCF OML in the retraction phase and produces greater lift than the corresponding slat position in the deployment phase (see Fig. 2.9). The erratic fluctuation in lift during deployment at 85% is due to SCF/hinge redeployment, which is accompanied by oscillation of the SCF and a brief period of a variable, small gap between the SCF and main wing. Flow through that small, variable gap produces fluctuations in the boundary layer on the top of the wing that commensurately affect the lift production.

The effect of the retraction rate is also studied by reducing the rate of retraction for the slat and flap. Figure 2.11 shows lift versus percent deployment for four retraction rates. The same FSI model is used for each case with a time step of

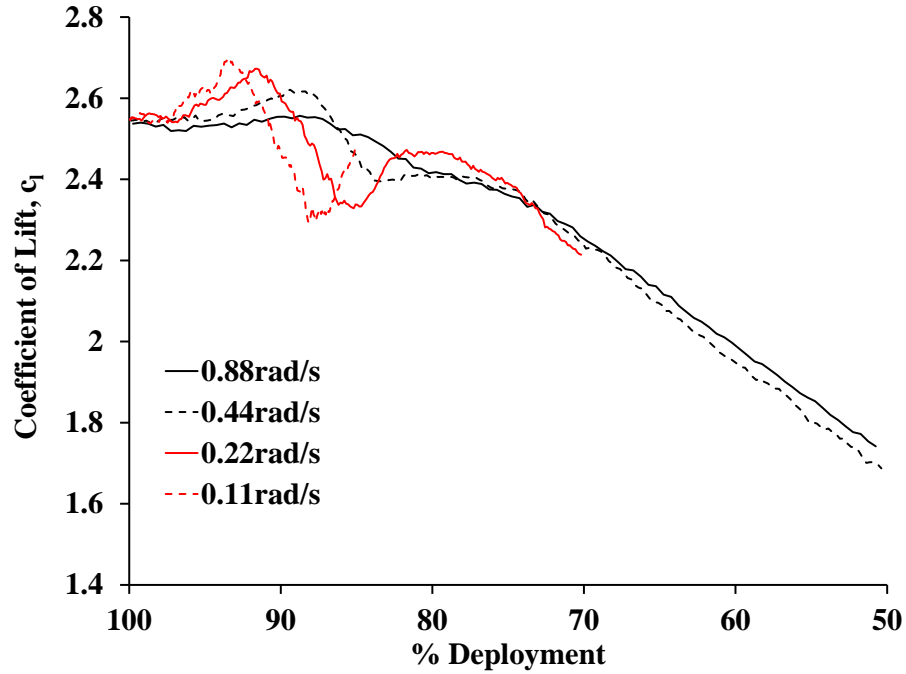


Figure 2.11: Lift coefficient of wing versus % deployment for different retraction rates.

0.00005 s. Note that the 0.88 rad/s retraction rate case requires 0.5 s to achieve full retraction and corresponds to results shown in Fig. 2.10. Only partial retraction<sup>1</sup> is considered due to the computational runtime required to conduct full retraction for slower cases. Simply reducing the retraction rate by a factor of two (0.44 rad/s) changes the lift-deployment curve compared to the original 0.88 rad/s case. Between fully deployed and 88% deployment, the lift increases for the 0.44 rad/s case while the 0.88 rad/s case exhibits a fairly constant lift. Additionally for the 0.44 rad/s case, lift decreases between 88% and 84% deployment, then is constant until approximately 78% deployment where it follows a similar path as the 0.88 rad/s case. Past 70% deployment, the lift for the 0.44 rad/s retraction rate case is between the lift

<sup>1</sup>The 0.44 rad/s, 0.22 rad/s, and 0.11 rad/s are retracted to 50%, 30%, and 15% deployment, respectively.

for the 0.88 rad/s retraction/deployment cycles of Fig. 2.10. Decreasing the retraction rate further to 0.22 rad/s and 0.11 rad/s results in the increase in lift (which grows with decreased retraction rate) followed by the rapid decrease in lift (between 88% and 84% deployment for the 0.44 rad/s case) occurring sooner in the retraction cycle. Additionally, both the 0.22 rad/s and 0.11 rad/s cases exhibit an increase in lift following the significant drop. These results suggests that a phenomenon is not captured at fast retraction rates and may resolve some of the discrepancies discussed for Fig. 2.10. Examination of the velocity contour plot between 5% and 15% deployment, where the SCF comes into contact with the main wing (occurs at 14%), shows that a jet of high speed flow is created as the distance between the SCF and the main wing decreases. This jet appears to initially increase the lift, but soon results in separation of flow over the surface of the main wing and thus decreases the lift. Note that a jet of high speed flow also occurs during retraction/deployment of the untreated slats due to a similar small gap between the main wing and slat.

### 2.3 Full Scale SCF\*

Due to the success of performing FSI analysis at model scale (6.25% scale), a full scale version of the SCF is evaluated using FSI analysis.<sup>2</sup> Additionally, an ‘adaptation-by-instability’ approach developed by the University of Bristol [33] is applied to tailor the nonlinear structural response of both SMA and fiberglass composite designs. As stated in the previous section, the superelastic response of SMA enables the SCF to be stiff under aerodynamic loading and compliant during retraction/deployment. However, a similar superelastic behavior can also be achieved geometrically, rather than constitutively, with composite materials by exploiting elastic

---

\*Work in this section is from “Tailoring the Superelastic response of a deployable Slat-Cove Filler for Airframe Noise Reduction” by Arena, G and Scholten, W. and Groh, R. and Turner, T. and Pirrera, A. and Hartl, D.; paper currently in development.

<sup>2</sup>The full scale version of the geometry from the previous section is used herein.

instabilities, *i.e.* snap-through buckling [33, 116]. In this case, laminated composites are particularly attractive due to their excellent specific properties and because the elastic properties of a laminate can be readily tailored by varying the stacking sequence. Note that the tailoring process is beyond the scope of this work. Only FSI analysis of the tailored designs is discussed herein. The reader is encouraged to read [116] and [117] for more detailed descriptions of the tailoring process.

### 2.3.1 Finite Element Structural Model

The structural finite element model is a full scale version<sup>3</sup> of the one used in Section 2.2.1 (see Fig. 2.5). For size reference, the retracted chord of the full scale model is 5.1 m. As shown in Fig. 2.12, the SCF is split into multiple sections including the SCF-hinge arm (assigned steel properties) and six sections of equal length that are modified during the tailoring process. For SMA SCF designs, the tailorable sections are assigned different thicknesses, while for composite SCF designs, these sections are assigned different layups. The material chosen for the layups work is E-glass 913, a unidirectional glass fiber epoxy resin composite. A linear penetration law models contact in the direction normal to the SCF thickness, while in the tangential direction contact is assumed to be frictionless.

The mechanical constitutive responses of the SMA material and E-glass 913 composite lamina are shown in Fig. 2.13, highlighting both the superelastic behavior of the SMA and the effect of the fiber orientation for the composite. The SMA material initially exhibits a linear stress-strain relationship. Upon reaching a critical stress value, the microstructure transforms from austenite to martensite, allowing for large recoverable deformations. In contrast, the composite material exhibits a linear elas-

---

<sup>3</sup>Structural model is identical (same material, same element types, etc.) to the 6.25% model scale one from Fig. 2.5 with the exception of geometry. All geometry of this full scale version is 16 times larger than the model scale version.

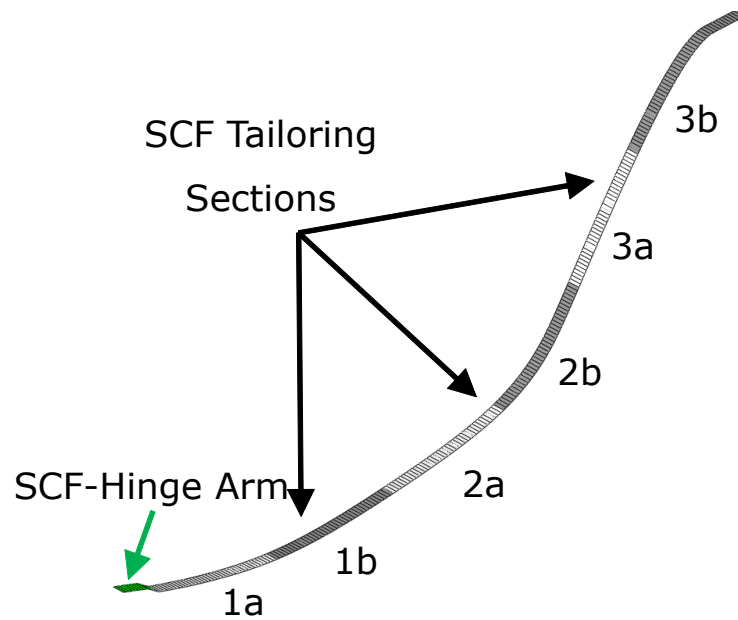


Figure 2.12: Structural FEA model of 2.5D SCF assembly with isolated SCF with sections targeted for elastic tailoring.

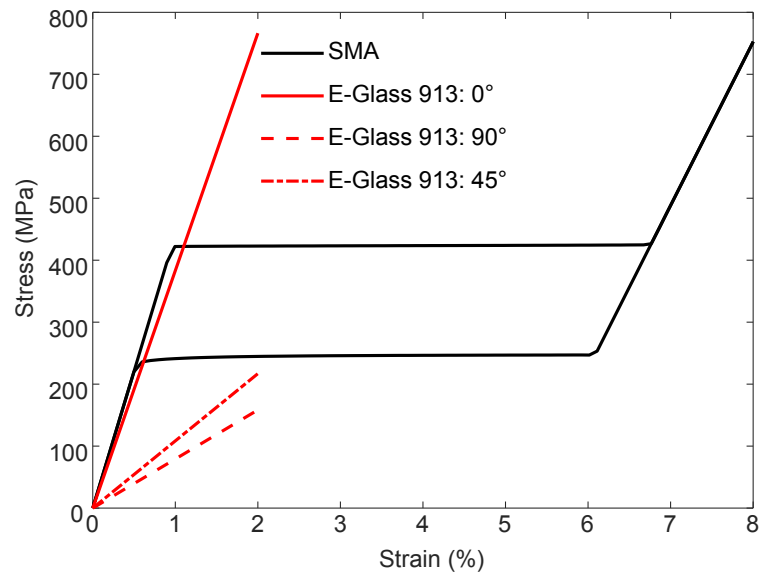


Figure 2.13: Superelastic stress-strain response of the SMA material in Table 2.2 and elastic stress-strain response of E-Glass 913 for various fiber orientations. Adapted from [116].

tic response with the modulus depending on the fiber direction. Comparing only the elastic response of the two materials, superelastic SMAs appear to be better suited for the large deformations and snapping behavior associated with the stowage and deployment of the SCF. However, by incorporating elastic instabilities into the composite SCF, an alternative *structural* superelastic behavior can be obtained. A significant advantage of exploiting such elastic instabilities is the ability to change system response by both varying geometric and material parameters [33, 118]. For this work, the SCF profile cannot be changed since its shape is prescribed for optimal noise reduction. The snap-through response of the SCF is thus modified via stiffness tailoring. An additional possibility would be tailoring the response by pre-stressing or pre-deforming the SCF. Practically, this would make the deployed state different in geometry from the manufactured shape and non stress free. For simplicity, however, this design option is also not considered in this work.

In order to capture the response of superelastic SMA materials under isothermal conditions, this portion of the work uses the Auricchio constitutive model [104]. This constitutive model is particularly useful in collaborative works since it is pre-compiled in Abaqus as a UMAT subroutine. Composite SCFs are modeled using the composite lamina feature in Abaqus to create a stack of plies with fibers oriented in different directions. Properties of the chosen composite material, E-glass 913, are shown in Table 2.3.

The tailoring process considers SCF response to six static aerodynamic loadings ( $4^\circ$ ,  $6^\circ$  and  $8^\circ$  angle of attack in Mach 0.2 and Mach 0.24 flow) and slat retraction/deployment [117]. The pressure distributions for the aerodynamic loading are extracted from CFD analyses of the CRM wing with both the slat and flap in a fully deployed configuration (see proceeding section). Note that the Mach 0.2 flow is considered the nominal landing condition and Mach 0.24 flow is considered to be the

Table 2.3: E-glass 913 properties from [116].

Property	Value
$E_1, E_2$	38.7 GPa <sup>‡</sup> , 8 GPa <sup>‡</sup>
$\nu_{12}$	0.28 <sup>‡</sup>
$\rho$	1900 kg/m <sup>3</sup> <sup>†</sup>

<sup>†</sup>Based on Hexcel data. <sup>‡</sup>Based on Ref. [119, 120].

most adverse case. For the slat/SCF retraction/deployment load case, aerodynamic loading is not considered since the calculation of pressure distribution on the SCF for different levels of deployment requires an FSI analysis. Rotational displacement is applied to the rigid body reference point assigned to the slat, allowing for control of the slat articulation through a 25.2° arc (i.e., full articulation for this freestream parallel section of the CRM wing).<sup>4</sup>

As mentioned previously, the details of the tailoring process are beyond the scope of this work. Interested readers are encouraged to read Arena’s work [117]. Instead, only the results of the tailoring process, both tailored SMA and tailored SCF designs, are of interest. Table 2.4 shows the stacking sequences of two tailored composite SCF designs (denoted as Tailored Composite 1 and Tailored Composite 2) and thickness distribution of a tailored SMA SCF design alongside a baseline uniform thickness (monolithic) SMA SCF design.

### 2.3.2 Finite Volume Computational Fluid Dynamics Model

The fluid model shown in Fig. 2.14 consists of a rectangular fluid domain centered around the CRM wing which is 20 chords long in the flow direction and 14 chords

<sup>4</sup>As previously stated, for the full scale 3D geometry, a 30° hingeline nominal rotation is required for slat retraction/deployment [112].

Table 2.4: Ply properties, stacking sequences and thickness distributions along the SCF arc-length. From

Sample	1a	1b	2a	2b	3a	3b
CORE [C]	[(0) <sub>2</sub> / ± 15/ ± 30/ ± 15/0] <sub>s</sub>					
Tailored Composite 1	[C]		[0/[C]/0]		[(0) <sub>2</sub> /[C]/(0) <sub>2</sub> ]	
Tailored Composite 2	[C]				[(0) <sub>2</sub> /[C]/(0) <sub>2</sub> ]	
Monolithic SMA	thickness = 2.25 mm					
Tailored SMA	thickness = 2.18 mm			thickness = 2.32 mm		

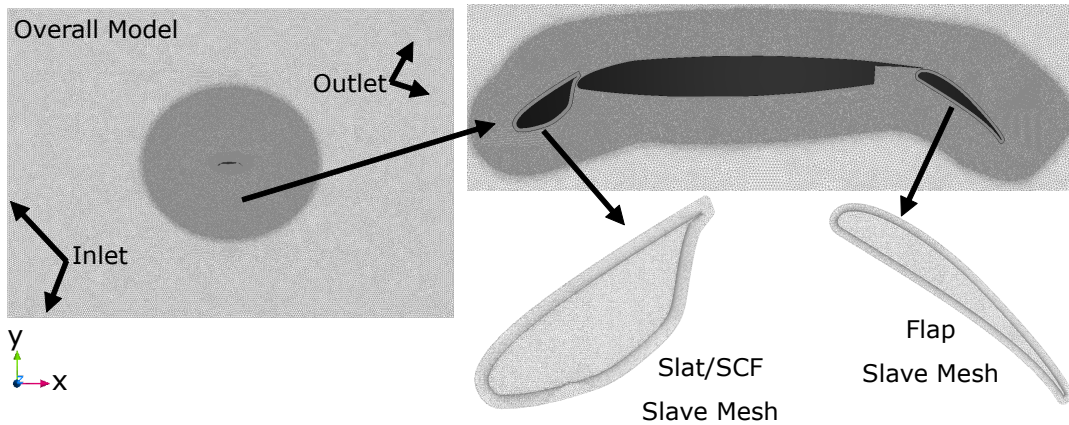


Figure 2.14: Fluid model of the full scale CRM wing.

high in the vertical direction. To reduce computational cost and maintain consistency with the structural model, the fluid model is meshed with a single element in the spanwise direction. As with the model scale version, overset meshes are implemented to accommodate large volume change associated with SCF deformation and the rigid body motion of the flap and slat.

The fluid domain containing the main wing and overall flow field is defined using multiple volume regions that are assigned different element sizes with those near the wing having a more refined mesh as compared to freestream volumes further away from the wing. The volume regions associated with the slat and flap are meshed

with the same element size as the innermost region of the master mesh. The mesh is further refined at the surface of the wing where layers of hexahedron elements are also inserted, increasing the resolution of the flow field to capture the boundary layer. CFD work at wind tunnel model scale of the CRM wing (Section 2.2) serves as a basis for the mesh generation parameters in the current work [107]. After combining the three meshes, the resulting fluid model has approximately 850,000 elements (805,000 prism and 45,000 hexahedron elements).

The fluid domain is assigned incompressible air properties with viscosity and density of  $1.83 \times 10^{-5}$  Pa-s and  $1.206 \text{ kg/m}^3$ , respectively. Turbulent characteristics of the flow are captured using the Shear-Stress Transport  $k-\omega$  turbulence model [110]. Boundary conditions for the fluid model consider the existence of an inlet, an outlet, and walls. Inlet conditions are applied on the left and lower surfaces of the outermost volume region, where the  $x$ - and  $y$ -components of the inlet velocity (magnitude of either Mach 0.2 (68 m/s) or Mach 0.24 (82 m/s)) are specified. Angle of attack for the wing is defined by the specification of the inlet velocity components. This allows the same fluid model to be used for all considered flow conditions. Additionally, the flow through the inlet is assumed to be approximately laminar, and thus the turbulent kinetic energy  $k$  and turbulent dissipation rate  $\varepsilon$  are set to default values of  $0.0001 \text{ m}^2/\text{s}^2$  and  $0.0001 \text{ m}^2/\text{s}^3$ . The outlets for the fluid model (0 Pa static pressure) are specified as the upper and right boundaries of the outermost fluid region. Smooth no-slip and no-penetration wall conditions are assigned to every surface of the wing, deformable or rigid.

Transient CFD analysis is performed to develop the flow around the wing in a fully deployed configuration at  $4^\circ$ ,  $6^\circ$ , and  $8^\circ$  angle of attack with freestream conditions of Mach 0.2 and Mach 0.24. Each analysis is conducted for 3.0 s with a time step of 0.00005 s. Following each analysis, the pressure distribution on the SCF is extracted

and used in the tailoring process. Additionally, the developed flow field is used as initial conditions in FSI analysis of the fully deployed wing.

### *2.3.3 FSI Analysis of Full Scale SCF*

The SMA and composite SCF-tailoring process only considered 1) constant pressure loads on the fully deployed SCF, and 2) retraction/deployment with no pressure loading. However, understanding the true behavior of the flexible SCF in dynamic fluid flow, requires full FSI analysis. Thus, FSI analysis is performed to check if the tailored SCF designs obtained in the previous section are viable. FSI analysis is performed with the same computational framework used in the model scale SCF work (Section 2.2.3) that weakly couples Abaqus and SC/Tetra. Additionally, similar to the model scale work, two cases are considered for FSI analysis: 1) fixed and fully deployed slat/flap, and 2) deployment of the slat and flap.

#### *2.3.3.1 FSI Analysis: Fixed, Fully Deployed*

The first FSI load case assumes that the slat is fixed (i.e., no retraction/deployment) and that both slat and SCF are fully deployed. Due to the cost of a single FSI analysis (85 hr on a standard workstation with 10CPU), evaluating each SCF design for each flow condition is not feasible. Instead, only four SCF designs are considered for FSI analysis: (i) Monolithic SMA; (ii) Tailored SMA; (iii) Tailored Composite 1; and (iv) Tailored Composite 2. Recall that the tailoring process evaluated the SCF response to constant pressure loadings from six flow conditions using static FEA. Instead of performing FSI analysis for each flow condition, each SCF design is evaluated using the flow condition that resulted in the highest deflection from static FEA analysis. This flow condition is Mach 0.24 at 8° angle of attack for composite SCFs and Mach 0.24 at 4° angle of attack for SMA SCFs. The difference in flow conditions may be due to the larger variation in stiffness along the curve of the composite SCFs

as compared to SMA SCFs. Each analysis is conducted for 2.5 s with a time step of 0.00005 s.

Figure 2.15 shows the displacement time history of the node in the structural model with the maximum displacement during the analysis, for each of the SCF designs considered. The displacement for all SCF designs exhibits an oscillatory behavior with a large amplitude at the start of the analysis due to the initiation of the interaction between the structure and the fluid. For all designs except Tailored Composite 2, this oscillatory behavior decays towards a smaller constant amplitude. It is expected that in a longer analysis, the oscillation of the SCF would further reduce, suggesting that the SCF may reach a steady equilibrium configuration with the surrounding fluid for these cases. Both the Tailored Composite 1 and the Tailored SMA designs exhibit a lower oscillation in displacement at the end of the analysis as compared to the Monolithic SMA and Tailored Composite 2.

Denoted by FEA (Def. Config.) in Fig. 2.15 is the displacement of the same node on the SCF under aerodynamic loading using the mean pressure distributions from the CFD-only analysis (used to produce the “steady” CFD solutions) and the FSI analysis. It can be seen that the resulting nodal displacement from the static analysis with the FSI pressure distribution is approximately equal to the mean of the displacement from the FSI analysis. However, with the exception of Tailored Composite 2, the displacement of the structure using the CFD-only mean pressure distribution is significantly lower than the mean displacement from the FSI analysis. The lower displacement of Tailored Composite 2 from static analysis using the FSI mean pressure distribution is attributed to asymmetric oscillatory response due to intermittent contact between the SCF and slat cusp (lower trailing edge).

Based on the results of the FSI and static analyses with the average FSI pressure distribution—both of which result in a higher displacement for all designs, except

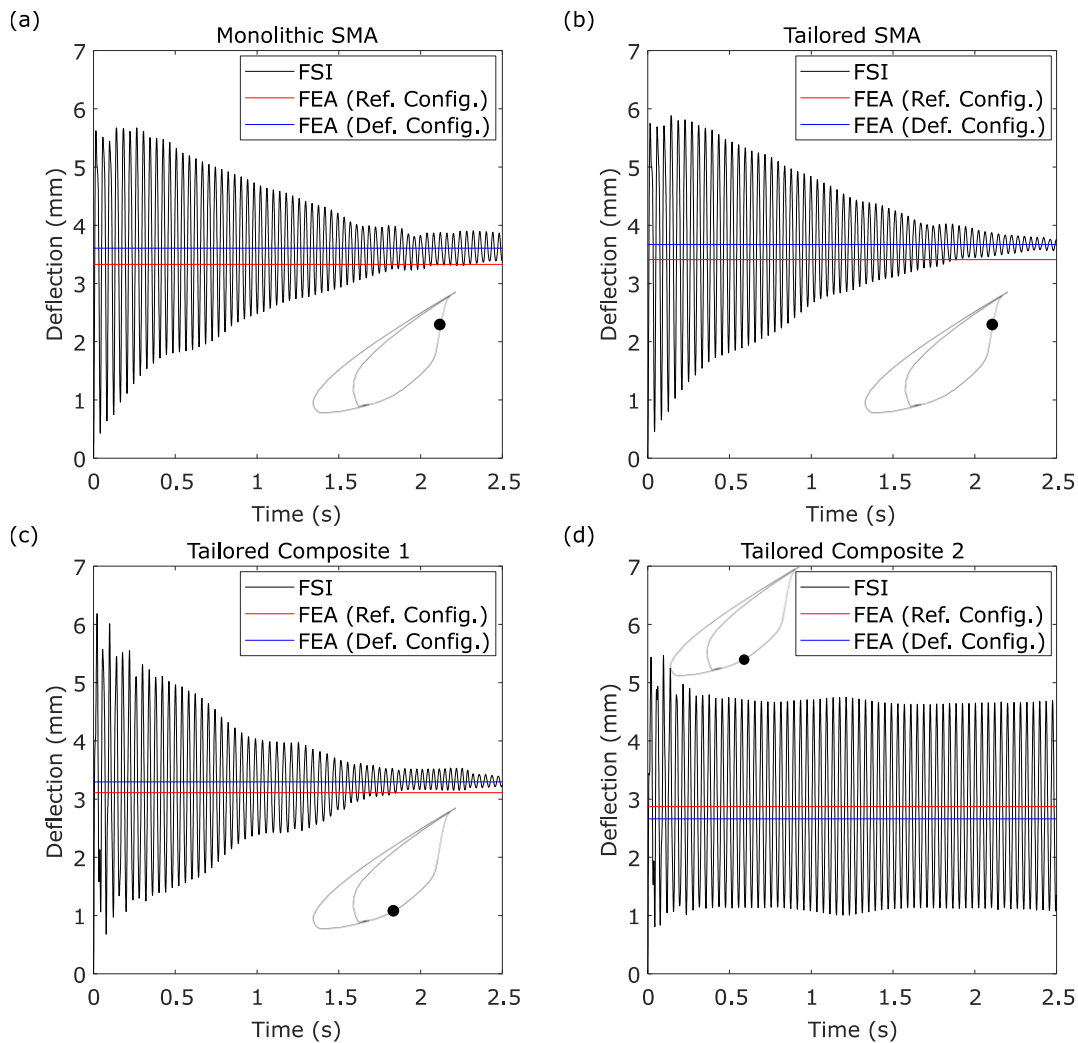


Figure 2.15: Deflection of different SCF designs: (a) Monolithic SMA; (b) Tailored SMA; (c) Tailored Composite 1; and (d) Tailored Composite 2. Two steady deflection solutions for each of the SCF designs are also shown.

Tailored Composite 2—only the Tailored Composite 1 design still satisfies the displacement constraint of 3.4 mm from the tailoring process. These results suggest that the coupling between the pressure field and the displacement of the SCF tends towards destabilization of the SCF, further reinforcing observations from previous work [121]. As the SCF is deformed due to aerodynamic loading, the local pressure

field changes such that the SCF displaces further. Note that while this behavior is undesirable, the Mach 0.24 flow speed is the most adverse condition. Under nominal Mach 0.2 flight conditions, the SCF has a lower displacement and is thus more resistant to this destabilizing coupling.

### 2.3.3.2 FSI Analysis: Deployment

The second load case assumed for FSI analysis considers deployment of the slat and SCF, critical since any viable tailored SCF designs must be able to redeploy in dynamic flow conditions. For each SCF design, an initial structural analysis is performed to fully retract the SCF. The resulting assembly geometry is extracted and used to generate a slave mesh for the overset fluid model. An initial CFD analysis is again performed to develop the flow around the wing, and the flow conditions are identical to the previous FSI load case (*i.e.*, Mach 0.24 and the same angles of attack). During the FSI analysis, both the slat and flap are synchronously deployed over 2 s with a time step of 0.00005 s and then held in a fully deployed position for 0.5 s. Note that the deployment of the slat and flap in this analysis is significantly faster than an actual system ( $\approx 20$  s). Additionally, the remeshing scheme introduced in Section 2.2.3 is applied to rebuild the fluid mesh during deployment.

Figure 2.16 shows the velocity contour during deployment for the Tailored Composite 1 and Monolithic SMA SCFs.<sup>5</sup> For both the tailored and monolithic designs, the magnitude of velocity across the surface of the slat and main wing leading edges generally increases as the high-lift devices deploy. This is due to the increasing camber of the wing and the creation of suction peaks on the main wing leading edge. For all designs, in the range of 80%–90% deployment, a jet of high velocity is present in the small gap between the main wing and the SCF, similar to the jet of high speed

---

<sup>5</sup>The Tailored Composite 2 and Tailored SMA designs structurally behave in a similar manner to the Tailored Composite 1 SCF design and are thus not shown for brevity.

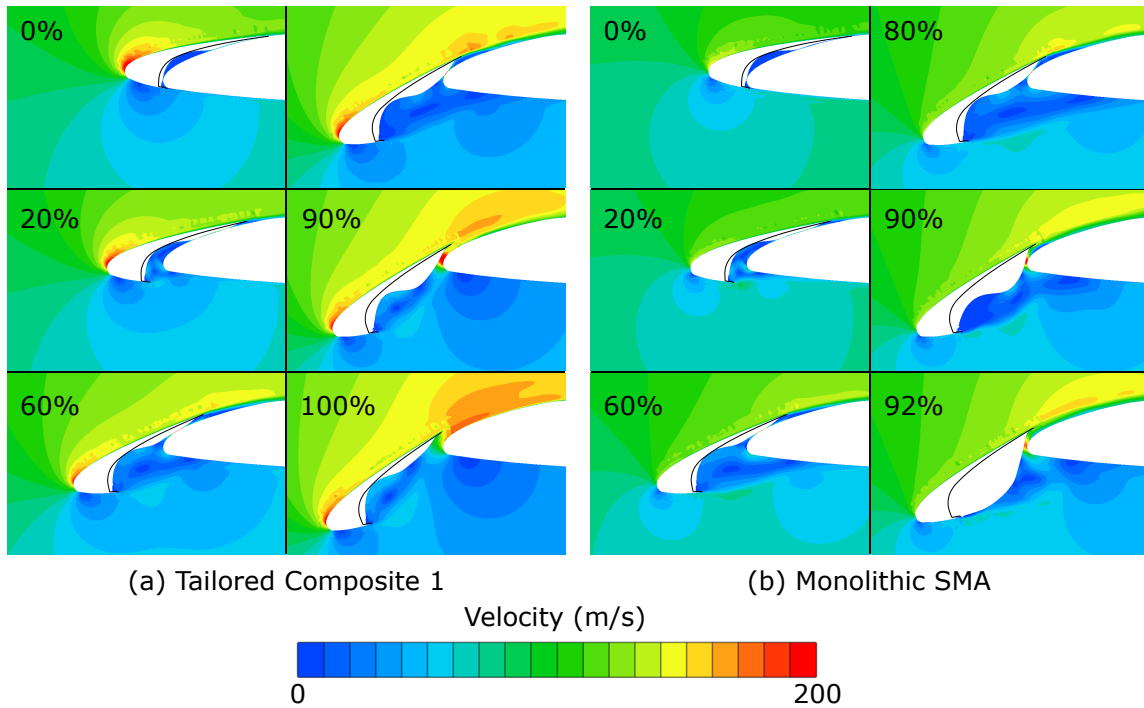


Figure 2.16: Velocity contour during deployment for (a) Tailored Composite 1 design and (b) Monolithic SMA design under Mach 0.24 flow.

flow during slat articulation of the model scale SCF. As previously stated, this jet is also observed during retraction/deployment of the untreated slats. Additionally, during much of the deployment, flow over the main wing leading edge is prevented, resulting in flow separation off the slat cusp that reconnects downstream on the lower surface of the main wing, as in a drooped leading-edge. As seen in Fig. 2.16, of the considered SCF designs only the Monolithic SMA SCF successfully redeploys.

Examination of the pressure distribution acting on the SCF at full slat deployment reveals a distribution that is considerably different from the one obtained from CFD analysis of the undeformed, fully deployed SCF. As shown in Fig. 2.17, the tailored designs exhibit a significantly higher positive pressure on the aft portion of the SCF. The pressure distribution acting on the tailored designs, which could

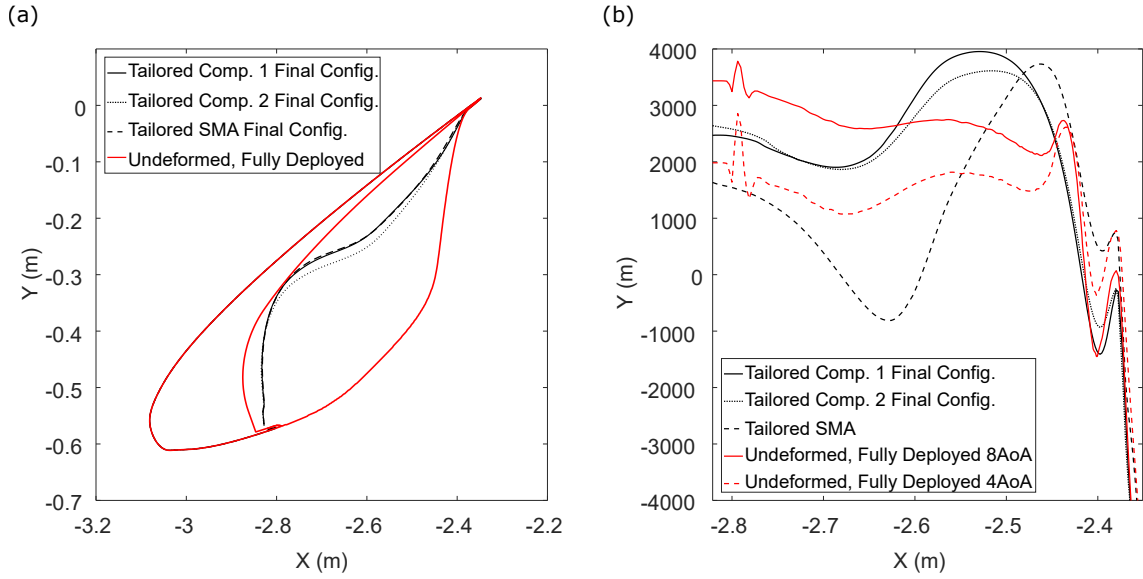


Figure 2.17: Comparison between undeformed SCF and final configuration for tailored designs after FSI analysis for (a) shape and (b) pressure distribution.

only be obtained through an FSI analysis, is not accounted for during the tailoring process. As a result, these designs, which satisfy displacement constraints when fully deployed, do not store sufficient strain energy during the retraction process to redeploy under the dynamic pressure loadings encountered. Additionally, the inability to redeploy is at least partly attributed to differences in the impulsiveness of the hinge articulation of the SCF, *i.e.* release of kinetic energy. The tailoring process of Tailored Composite 1 design reduces the release of kinetic energy, preventing heavy collisions with the slat during retraction/stowage, and also results in a smooth redeployment. However, a large release of kinetic energy may aid in redeployment of the SCF. It is suspected that refinement of the tailoring process, such as incorporating of FSI analyses, considering of a representative pressure field during redeployment, or allowing for more release of kinetic energy would result in a tailored SCF design that is able to both meet the displacement constraints and fully redeploy under dynamic

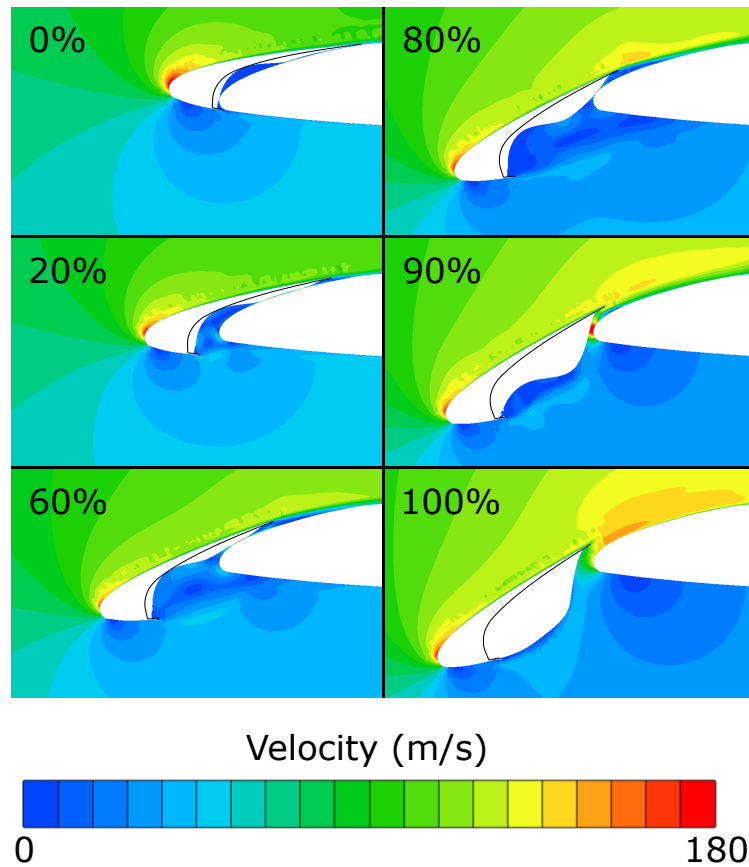


Figure 2.18: Velocity contour plot during deployment for Tailored Composite 2.

flow. Additionally, incorporation of an optimization algorithm may further improve tailored SCF designs.

Of the considered tailored designs, the Tailored Composite 2 design is believed to be the most likely to redeploy in flow, and is thus further tested in Mach 0.2 flow, the nominal landing speed. As shown in Fig. 2.18, under the nominal flow condition, this design is able to redeploy, demonstrating that the tailoring process, namely modifying the stacking sequence to increase the release of kinetic energy, can result in viable SCF designs.

## 2.4 Summary

As seen at both model and full scale, FSI analysis of the SCF is both complex and computationally expensive. Additionally, FSI analysis is required to develop viable SCF designs due to the strong aeroelastic coupling between the SCF and surrounding flow field. Under constant static aerodynamic loading or during retraction/deployment with no aerodynamic loading, the SCF may satisfy design requirements, such as autonomous redeployment or limited deflection, which may not be satisfied in an FSI analysis where the flow field evolves with the shape of the SCF. However, the computational costs required to both obtain a final (or time averaged) equilibrium configuration of the fully deployed SCF for a single flow condition makes optimizations that incorporate FSI analysis prohibitive. Note that under sufficiently slow high-lift device articulation, the SCF may also reach an equilibrium configuration. The scheme proposed in this work seeks to reduce the cost of obtaining aeroelastic solutions of which the final equilibrium configuration is of interest, enabling design optimization of complex aerostructures such as the SCF.

### 3. UNCOUPLED METHOD FOR STATIC AEROELASTIC ANALYSIS

Focus shifts towards describing the implementation of the uncoupled method for finding a SAA solution at single freestream flow velocity and associated demonstration problems that intentionally utilize a number of pressure and shape fitting parameters sufficiently low to visualize results.

#### 3.1 General Overview of Uncoupled Method

While the proposed uncoupled method can be applied to many coupled, multidisciplinary analyses, its mathematical formulation is presented herein in the context of aeroelastic analysis. In the uncoupled method, structure and fluid solvers are separated such that individual static structure and steady fluid analyses are performed with the same freestream conditions; a single set of converged physically compatible solution fields  $\mathbf{u}(\mathbf{x}, t_f)$  and  $p(\mathbf{x}, t_f)$  at  $t_f$  remains the goal. For each structure or fluid analysis, instead of incrementing time, the solvers obtain uncoupled final displacement or pressure field with multiple solution increments  $N$ .<sup>1</sup> Figure 3.1 illustrates this new method with regards to aeroelastic analysis (see Fig. 1.1). With the interaction between the solvers removed, field information is no longer exchanged, and pressure and displacement fields do not develop with any physical compatibility. Therefore, the pressure and displacement fields are replaced with fits of some functional (and thus, adjustable) form that accurately approximate the CFD/FEA computed fields, allowing for the development of a physically compatible solution. Development of the pressure and displacement fields for the physically compatible solution shall be discussed in detail.

---

<sup>1</sup>Note that the static structural solver may be replaced with a dynamic solver if morphing or large deformation is occurring however only the final displacement field  $\mathbf{u}(\mathbf{x}, t_f)$  is of interest.

Time-invariant fits of both the pressure distribution, denoted  $\hat{p}$ , and the flexible wetted surface region over which fluid-structure interaction occurs, denoted  $\hat{\Omega}_{FSI}$ , are created. Specifically, the flexible wetted surface region is described by an implicit function  $\hat{s}_{FSI}$  such that any  $\mathbf{x}$  satisfying  $s_{FSI}(\mathbf{x})=0$  lies on the surface, or  $\{\mathbf{x}: \hat{s}_{FSI}(\mathbf{x})=0\} \equiv \hat{\Omega}_{FSI}$ .

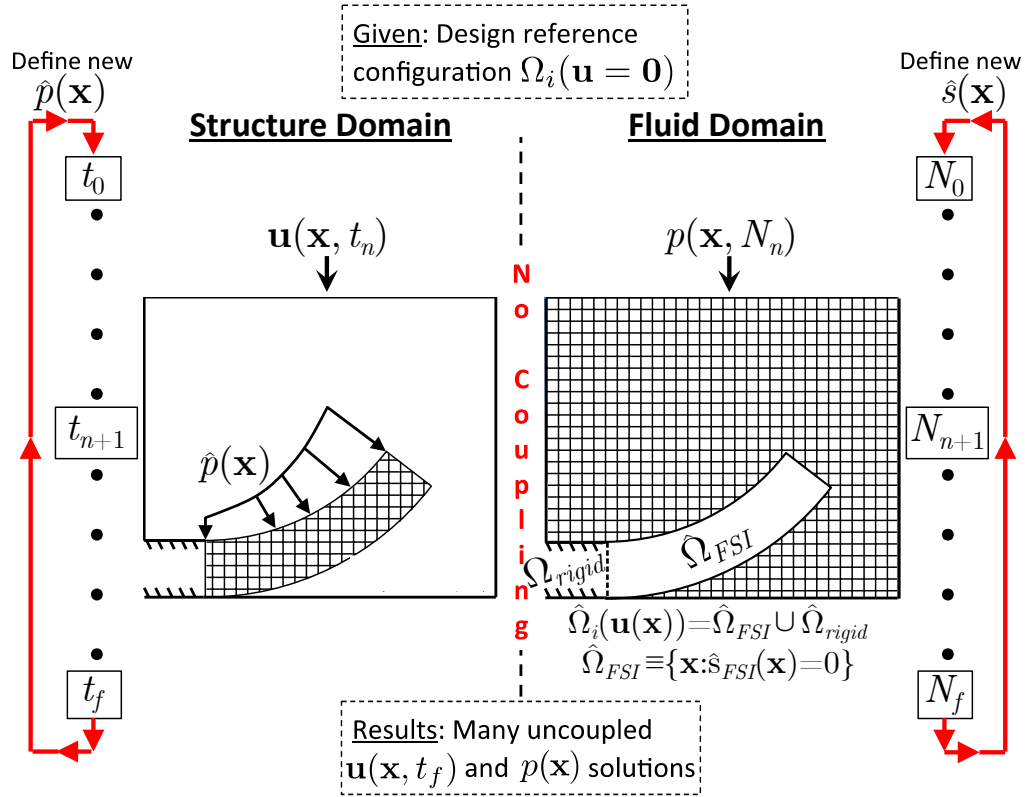


Figure 3.1: Simple schematic of the uncoupled SAA method. Many constant pressure distributions and structural shapes are created and imposed in the structure and fluid solvers, respectively. A sufficiently large set of uncoupled pressure and displacement solutions are obtained from which a physically compatible solution is found.

The pressure distribution fit  $\hat{p}(\mathbf{x})$  and surface fit  $\hat{s}_{FSI}(\mathbf{x})$  are described using a mathematical function calibrated via a number of pressure  $P$  and shape  $S$  fitting parameters, respectively, such that

$$\hat{p} = \hat{p}(\mathbf{x}; \mathbf{P}) \quad \forall \mathbf{x} \subseteq \Omega_{FSI}, \quad \text{where } \mathbf{P} = \{P_1, \dots, P_{n_p}\} \quad (3.1)$$

and

$$\hat{s}_{FSI} = \hat{s}_{FSI}(\mathbf{x}; \mathbf{S}), \quad \text{where } \mathbf{S} = \{S_1, \dots, S_{n_s}\}, \quad (3.2)$$

where  $n_s$  and  $n_p$  are the number of shape and pressure fitting parameters, respectively. Given a sufficient number of fitting parameters, these fits shall accurately represent the computed pressure field and structural shape. Variation of these fits, specifically through modification of the fitting parameters, represents potential shapes or pressures that may be exhibited by the structure and fluid domains, respectively, during a coupled analysis as it converges towards a physically compatible solution. As shall be discussed below, variations of these parameters create a **C-S** space from which physically compatible solutions are obtained.

Additionally, it is assumed that within a reasonable range of Reynold's number (for this work within an order of magnitude with values greater than 10,000), the spatial distribution of *pressure coefficient*  $C_p(\mathbf{x}) = \frac{2p(\mathbf{x})}{\rho v_\infty^2}$  is constant as flow velocity  $v_\infty$  is changed. This assumption enables estimation of SAA solutions at domain inlet (freestream) velocities beyond those used in the original fluid simulations, as will be demonstrated later in this work. As a consequence of the assumption, extrapolated pressure distributions (and the resulting SAA solutions) for different freestream velocities have some error since the locations and magnitude of flow features such as the suction peak and separation are assumed to be constant with changing freestream

velocities. This error is expected to grow as freestream conditions further away from those used in original fluid simulations are considered. However, the magnitude of the error introduced by this assumption is problem dependent. For many airfoils [122, 123, 124, 125] and other bodies in flow [126, 127, 128, 129], the pressure coefficient distribution along portions of a body (or along the entire body) is approximately constant across a small range of Reynold’s numbers.<sup>2</sup> For this work, if the pressure coefficient distribution acting on the body in flow exhibits 1) negligible change with Reynold’s number or 2) changes in the distribution that are either highly localized or not on a flexible portion of the body (i.e, change occurs somewhere on  $\Omega_{rigid}$ ), then the assumption is used to provide a means of estimating the overall loading applied to the deformable structure for a variety of freestream conditions without running further fluid evaluations. Before implementing the assumption of constant pressure coefficient distribution for a given problem, initial fluid analyses for a number freestream velocities of interest should be performed to ensure that the distribution applied to the flexible portion of a structure and any performance metrics from the fluid domain are relatively constant. Alternatively once solutions for multiple freestream velocities are obtained with the uncoupled method, the results can be verified by fluid analyses.

With this assumption regarding the general applicability of  $C_p(\mathbf{x})$ , the pressure coefficient distribution is replaced by a mathematical functional fit, denoted  $\hat{C}_p$ , that is described by a number of pressure coefficient fitting parameters  $\mathbf{C}$ :

$$\hat{C}_p = \hat{C}_p(\mathbf{x}; \mathbf{C}) \quad \forall \mathbf{x} \subseteq \Omega_{FSI}, \quad \text{where } \mathbf{C} = \{C_1, \dots, C_{n_p}\} \quad (3.3)$$

Using this pressure coefficient distribution fit, the pressure distribution fit is gener-

---

<sup>2</sup>For airfoils specifically, this behavior can also be observed with the effect Reynold’s number as on lift coefficient for many angles of attack before stall [130].

ated as follows

$$\hat{p}(\mathbf{x}) = q_\infty \hat{C}_p(\mathbf{x}) = \frac{1}{2} \rho \hat{C}_p(\mathbf{x}; \mathbf{C}) v_\infty^2 \quad (3.4)$$

where  $q_\infty$  is the freestream domain inlet dynamic pressure and  $\rho$  is the freestream density.

Initial steady fluid and static structure analyses of a few reference designs are used to determine the functional form (i.e., specific equation such as a polynomial, RBF, etc.) of the fits and number of fitting parameters required to define them. The initial fluid analysis is for flow over the undeformed shape while the initial structure analysis is performed using the pressure distribution extracted from the initial fluid analysis. These initial analyses are essentially the first iteration of a steady serially coupled FSI scheme (one steady fluid analysis followed by one static structure analysis) and are herein known as the initial coupled solution (ICS). An initial steady analysis of flow over the undeformed body  $\Omega_0$  is performed from which the pressure coefficient distribution  $C_p^0(\mathbf{x})$  is obtained. A fit of the pressure coefficient distribution  $\hat{C}_p$  is then formed such that,

$$\hat{C}_p^0(\mathbf{x}; \mathbf{C}_0) \approx C_p^0(\mathbf{x}) \quad (3.5)$$

where  $\mathbf{C}_0$  is the set of pressure coefficient fitting parameters calibrated such that  $\hat{C}_p^0$  approximates the pressure coefficient distribution acting on  $\Omega_{FSI}$ . Similarly, the structural shape fit is based on the deformed shape  $\Omega_{FSI}^0$  obtained from an initial static structural analysis of the body subjected to pressure distribution  $q_\infty C_p^0(\mathbf{x})$  such that

$$\hat{s}_{FSI}^0(\mathbf{x}; \mathbf{S}_0) \approx s_{FSI}^0(\mathbf{x}), \quad (3.6)$$

where  $\mathbf{S}_0$  is the set of shape fitting parameters calibrated such that  $\hat{s}_{FSI}^0$  approximates the implicit function  $s_{FSI}^0(\mathbf{x})$  that describes  $\Omega_{FSI}^0$ .

The functional form and parametric calibrations of the fits should be defined such that the error between the fit and computed data is sufficiently small to ensure a physically meaningful approximate solution. The fitting error for the pressure coefficient distribution  $\epsilon_p^0$  is defined using the following surface integral

$$\epsilon_p^0 = \frac{1}{A_{FSI}} \int_{\Omega_{FSI}} |C_p^0(\mathbf{x}) - \hat{C}_p^0(\mathbf{x})| dA, \quad (3.7)$$

where  $A_{FSI}$  is the surface area of  $\Omega_{FSI}$  such that  $A_{FSI} = \int_{\Omega_{FSI}} 1 dA$ . The fitting error for the shape  $\epsilon_s^0$  is defined as:

$$\epsilon_s^0 = \mathcal{H}(\Omega_{FSI}^0, \hat{\Omega}_{FSI}^0), \quad (3.8)$$

where  $\mathcal{H}$  is here more generally defined as a function for computing the shape error (e.g., the mean Hausdorff distance). Note that as the number of fitting parameters increases for properly chosen fitting functions, the fits come to represent the physical fields with negligible error. With accurate fits of the pressure and shape defined, physically meaningful and compatible approximate solutions can be obtained.

For the uncoupled method, the physically compatible approximate solution is reached when the difference between the shape fit  $\hat{\Omega}_{FSI}$  imposed in the fluid domain and the shape fit of a deformed body  $\hat{\Omega}_{FSI}(q_\infty \hat{C}_p(\mathbf{x}))$ , obtained from structural analysis for a given approximate pressure load  $q_\infty \hat{C}_p(\mathbf{x})$ , is within some tolerance. Since the fits are fully defined by fitting parameters, this physically compatible solution is expressed as

$$|\mathbf{C} - \mathbf{C}(\mathbf{S})| \leq tol \quad (3.9)$$

and

$$|\mathbf{S} - \mathbf{S}(q_\infty \mathbf{C})| \leq tol, \quad (3.10)$$

where  $\mathbf{C}$  and  $\mathbf{S}$  are fitting parameters imposed in structure and fluid analyses, respectively, and where  $\mathbf{C}(\mathbf{S})$  and  $\mathbf{S}(q_\infty \mathbf{C})$  are fitting parameters obtained from results of those analyses. We represent the terms  $\mathbf{C}(\mathbf{S})$  and  $\mathbf{S}(q_\infty \mathbf{C})$  using the following equations:

$$\mathbf{C}(\mathbf{S}) = \mathcal{F}^f(\mathbf{S}), \quad \mathcal{F}^f(\mathbf{S}) = \{\mathcal{F}_1^f(\mathbf{S}), \dots, \mathcal{F}_{n_p}^f(\mathbf{S})\}, \quad (3.11)$$

and

$$\mathbf{S}(q_\infty \mathbf{C}) = \mathcal{F}^s(q_\infty \mathbf{C}), \quad \mathcal{F}^s(q_\infty \mathbf{C}) = \{\mathcal{F}_1^s(q_\infty \mathbf{C}), \dots, \mathcal{F}_{n_s}^s(q_\infty \mathbf{C})\}, \quad (3.12)$$

where  $\mathcal{F}_i^f$  is a function relating  $n_s$  imposed shape fitting parameters to a pressure coefficient fitting parameter  $C_i$  and where  $\mathcal{F}_i^s$  is a function relating  $n_p$  imposed pressure coefficient fitting parameters and a dynamic pressure to a shape fitting parameter  $S_i$ . These functions relating fitting parameters from different domains are developed herein as surrogate models.

### 3.2 Mathematical Implementation of Uncoupled Method for Single Velocity

To develop the surrogate models  $\mathbf{C}(\mathbf{S}) = \mathcal{F}^f(\mathbf{S})$  and  $\mathbf{S}(q_\infty \mathbf{C}) = \mathcal{F}^s(q_\infty \mathbf{C})$  for the uncoupled method, many individual analyses are conducted with various assumed fits for pressure and shape (see Eq. (3.1) and Eq. (3.2)). In the structural solver,  $m_p$  different pressure fits  $\hat{p}^j(\mathbf{x}) = q_\infty \hat{C}_p^j(\mathbf{x}; \mathbf{C}^j) \quad \forall j = 1, \dots, m_p$  are defined by varying the pressure coefficient fitting parameters and applied to the reference configuration of the structure. Structural analysis calculates the deformed surface region  $\Omega_{FSI}^j$  for each set of fitting parameters  $\mathbf{C}^j$  and a given dynamic pressure  $q_\infty$  from which a representative surface fit  $\hat{\Omega}_{FSI}^j \equiv \{\mathbf{x}; \hat{s}_{FSI}^j(\mathbf{x}; \mathbf{S}^j) = 0\}$  of the deformed surface region and the shape fitting parameters  $\mathbf{S}^j(q_\infty \hat{C}_p^j(\mathbf{x}; \mathbf{C}^j)) \quad \forall j = 1, \dots, m_p$  are obtained. Additionally, following each structural analysis,  $n_{y,s}$  model specific responses  $\mathbf{Y}^{s,j} = \{Y_1^{s,j}, \dots, Y_{n_{y,s}}^{s,j}\} \quad \forall j = 1, \dots, m_p$  (e.g., stress, strain, etc.) are extracted. Simi-

larly, for the fluid solver,  $m_s$  different surface functions  $\hat{s}_{FSI}^k(\mathbf{x}; \mathbf{S}^k) \forall k = 1, \dots, m_s$  are defined by varying the shape fitting parameters  $\mathbf{S}$  and used to define the boundaries of the overall fluid domain. Fluid analysis calculates the pressure distribution  $p^k(\mathbf{x})$  for each imposed surface fit assuming the same freestream flow conditions, from which a representative pressure coefficient fit  $\hat{C}_p^k(\mathbf{x}; \mathbf{C}^k)$  and corresponding pressure coefficient fitting parameters  $\mathbf{C}^k(\hat{s}_{FSI}^k(\mathbf{x}, \mathbf{S}^k))$  are extracted. Additionally,  $n_{y,f}$  chosen model specific responses  $\mathbf{Y}^{f,j} = \{Y_1^{f,j}, \dots, Y_{n_{y,f}}^{f,j}\} \forall j = 1, \dots, m_s$  (e.g., mass flow and max velocity) are obtained. The variation of the fitting parameters that generate the  $m_p$  different pressure fits and  $m_s$  different shape fits are defined using a design of experiment, Latin Hypercube Sampling, or similar technique to adequately explore the  $\mathbf{C}$ - $\mathbf{S}$  space [58]. Note that it is a great advantage of this method that these structure and fluid evaluations can be conducted at any time, on any workstation, and that execution is massively parallelizable. Upper and lower bounds for the variation in fitting parameters are generally set as percent changes of the ICS fitting parameters to ensure that relevant and localized regions of the  $\mathbf{C}$ - $\mathbf{S}$  space are explored. If the structure/fluid evaluations are performed at different times, then the outputs from one set of evaluations can be used to identify input bounds for the other set of evaluations. Alternatively, if all evaluations are performed in a parallelized manner, then the  $\mathbf{C}$ - $\mathbf{S}$  spaces generated by the two sets of evaluations can be compared, identifying new combinations of fitting parameters to be analyzed. This will ensure that the training process is exploring similar regions of the  $\mathbf{C}$ - $\mathbf{S}$  space. Though not currently implemented, following each structure or fluid evaluation, the error of the extracted shape or pressure fit relative to the FEA or CFD computed result, respectively, can be calculated (Eq. (3.8) or Eq. (3.7)) to check if the fit is still accurate. If the error significantly increases, then the structure and fluid evaluations are stopped, preventing further evaluations that extract a the poor fit of the com-

puted results. New functional forms for the fits are then developed from the results, and the structure/fluid evaluations are restarted.

Once the  $m_p$  structure and  $m_s$  fluid evaluations are completed, surrogate models of the shape and pressure coefficient fitting parameters and model-specific responses are constructed. Considering RBF fits with polynomial tails, this gives

$$S_i = \mathcal{F}_i^s(q_\infty \mathbf{C}) = \sum_{j=1}^{m_p} w_{i,j}^s \Psi(q_\infty \|\mathbf{C} - \mathbf{C}^j\|_2) + \gamma_i^s \cdot \{q_\infty \mathbf{C}, 1\} \quad \forall i = 1, \dots, n_s, \quad (3.13)$$

$$C_i = \mathcal{F}_i^f(\mathbf{S}) = \sum_{k=1}^{m_s} w_{i,k}^f \Psi(\|\mathbf{S} - \mathbf{S}^k\|_2) + \gamma_i^f \cdot \{\mathbf{S}, 1\} \quad \forall i = 1, \dots, n_p, \quad (3.14)$$

$$Y_i^s = \mathcal{F}_i^{so}(q_\infty \mathbf{C}) = \sum_{j=1}^{m_p} w_{i,j}^{so} \Psi(q_\infty \|\mathbf{C} - \mathbf{C}^j\|_2) + \gamma_i^{so} \cdot \{q_\infty \mathbf{C}, 1\} \quad \forall i = 1, \dots, n_{y,s}, \quad (3.15)$$

and

$$Y_i^f = \mathcal{F}_i^{fo}(\mathbf{S}) = \sum_{k=1}^{m_s} w_{i,k}^{fo} \Psi(\|\mathbf{S} - \mathbf{S}^k\|_2) + \gamma_i^{fo} \cdot \{\mathbf{S}, 1\} \quad \forall i = 1, \dots, n_{y,f}, \quad (3.16)$$

where  $w_{i,k}^f$ ,  $w_{i,j}^s$ ,  $w_{i,k}^{fo}$ ,  $w_{i,j}^{so}$ ,  $\gamma_i^s$ ,  $\gamma_i^f$ ,  $\gamma_i^{so}$ , and  $\gamma_i^{fo}$  are weights calculated analytically during calibration of the surrogate models by solving systems of linear equations [68], and where  $\mathcal{F}^{so}$  and  $\mathcal{F}^{fo}$  are functions relating the model specific outputs to fitting parameters. Note, to consider RBFs without polynomial tails, simply remove the terms with  $\gamma_i^s$ ,  $\gamma_i^f$ ,  $\gamma_i^{so}$ , and  $\gamma_i^{fo}$ . To calibrate the structure RBF surrogate models,  $n_s$  systems of linear equations based on the structure evaluations are solved:

$$\begin{bmatrix} S_i^1 \\ \vdots \\ S_i^{m_p} \\ 0 \\ \vdots \end{bmatrix} = [A_s] \begin{bmatrix} w_{i,1}^s \\ \vdots \\ w_{i,m_p}^s \\ \gamma_{i,1}^s \\ \vdots \\ \gamma_{i,n_p+1}^s \end{bmatrix}, i = 1, \dots, n_s. \quad (3.17)$$

and

$$\begin{bmatrix} Y_i^{s,1} \\ \vdots \\ Y_i^{s,m_p} \\ 0 \\ \vdots \end{bmatrix} = [A_s] \begin{bmatrix} w_{i,1}^{so} \\ \vdots \\ w_{i,m_p}^{so} \\ \gamma_{i,1}^{so} \\ \vdots \\ \gamma_{i,n_p+1}^{so} \end{bmatrix}, i = 1, \dots, n_{y,s}. \quad (3.18)$$

where

$$[A_s] = \begin{bmatrix} \Psi(q_\infty \| \mathbf{C}^1 - \mathbf{C}^1 \|_2) & \cdots & \Psi(q_\infty \| \mathbf{C}^1 - \mathbf{C}^{m_p} \|_2) & q_\infty C_1^1 & \cdots & q_\infty C_{n_p}^1 & 1 \\ \vdots & \vdots & \vdots & \vdots & \vdots & \vdots & \vdots \\ \Psi(q_\infty \| \mathbf{C}^{m_p} - \mathbf{C}^1 \|_2) & \cdots & \Psi(q_\infty \| \mathbf{C}^{m_p} - \mathbf{C}^{m_p} \|_2) & q_\infty C_1^{m_p} & \cdots & q_\infty C_{n_p}^{m_p} & 1 \\ q_\infty C_1^1 & \cdots & q_\infty C_1^{m_p} & 0 & \cdots & \cdots & 0 \\ \vdots & \vdots & \vdots & \vdots & \vdots & \vdots & \vdots \\ q_\infty C_{n_p}^1 & \cdots & q_\infty C_{n_p}^{m_p} & 0 & \cdots & \cdots & 0 \\ 1 & \cdots & 1 & 0 & \cdots & \cdots & 0 \end{bmatrix} \quad (3.19)$$

Similarly, to calibrate the fluid surrogate models,  $n_p$  systems of linear equations based on fluid evaluations are solved:

$$\begin{bmatrix} C_i^1 \\ \vdots \\ C_i^{m_s} \\ 0 \\ \vdots \end{bmatrix} = [A_f] \begin{bmatrix} w_{i,1}^f \\ \vdots \\ w_{i,m_s}^f \\ \gamma_{i,1}^f \\ \vdots \\ \gamma_{i,n_s+1}^f \end{bmatrix}, i = 1, \dots, n_p. \quad (3.20)$$

and

$$\begin{bmatrix} Y_i^{f,1} \\ \vdots \\ Y_i^{f,m_s} \\ 0 \\ \vdots \end{bmatrix} = [A_f] \begin{bmatrix} w_{i,1}^{fo} \\ \vdots \\ w_{i,m_s}^{fo} \\ \gamma_{i,1}^{fo} \\ \vdots \\ \gamma_{i,n_s+1}^{fo} \end{bmatrix}, i = 1, \dots, n_{y,f}. \quad (3.21)$$

where

$$[A_f] = \begin{bmatrix} \Psi(\|\mathbf{S}^1 - \mathbf{S}^1\|_2) & \dots & \Psi(\|\mathbf{S}^1 - \mathbf{S}^{m_s}\|_2) & S_1^1 & \dots & S_{n_s}^1 & 1 \\ \vdots & \vdots & \vdots & \vdots & \vdots & \vdots & \vdots \\ \Psi(\|\mathbf{S}^{m_s} - \mathbf{S}^1\|_2) & \dots & \Psi(\|\mathbf{S}^{m_s} - \mathbf{S}^{m_s}\|_2) & S_1^{m_s} & \dots & S_{n_s}^{m_s} & 1 \\ S_1^1 & \dots & S_1^{m_s} & 0 & \dots & \dots & 0 \\ \vdots & \vdots & \vdots & \vdots & \vdots & \vdots & \vdots \\ S_{n_s}^1 & \dots & S_{n_s}^{m_s} & 0 & \dots & \dots & 0 \\ 1 & \dots & 1 & 0 & \dots & \dots & 0 \end{bmatrix} \quad (3.22)$$

The  $n_p + n_s$  surrogate models of the fitting parameters create a nonlinear system of equations of the form

$$\{\mathbf{S}, \mathbf{C}\}^T = \{\mathcal{F}^s(C), \mathcal{F}^f(S)\}^T, \quad (3.23)$$

which can be solved using a number of numerical techniques, such as fixed-point iteration or the Newton method. The solution to this system of equations describes the intersection of the surrogate models and is called the uncoupled surrogate intersection (USI). In the case of fixed-point iteration, which is sufficient for all examples shown herein, the following two sets of equations are applied to Eq. (3.23):

$$\mathbf{S}_g = \mathcal{F}^s(q_\infty \mathbf{C}_g), \quad (3.24)$$

$$\mathbf{C}_{g+1} = \mathcal{F}^f(\mathbf{S}_g), \quad (3.25)$$

where  $g$  is the iteration number. These two equations are iterated until convergence, which is defined as:

$$|\mathbf{C}_{g+1} - \mathbf{C}_g| \leq tol_c, |\mathbf{S}_k - \mathbf{S}_{g-1}| \leq tol_s$$

The converged set of pressure and shape fitting parameters is the approximate solution to Eq. (3.23). Thus, we define  $\mathbf{C}_{USI} \equiv \mathbf{C}_{g+1}$  and  $\mathbf{S}_{USI} \equiv \mathbf{S}_g$ . In this work these are taken to represent the solution of a given steady-state FSI analysis and from them the pressure coefficient distribution fit  $\hat{C}_{p,USI}(\mathbf{x})$  and surface fit  $\hat{s}_{FSI,USI}(\mathbf{x})$  are obtained. Note that since this method uses steady fluid and static structural solvers, it can not predict any limit cycle oscillations (frequency and amplitude) that may be exhibited by the body in flow during a transient FSI analysis. In cases where the body does exhibit limit cycle oscillations, the USI solution is expected to be the time-averaged solution. The shape and pressure coefficient fitting error comparing

the uncoupled SAA solution to an FSI solution are calculated using Eq. (3.7) and Eq. (3.8). Any model specific outputs for the USI solution  $\mathbf{Y}_{USI}^s$  and  $\mathbf{Y}_{USI}^f$  are calculated as

$$\mathbf{Y}_{USI}^s = \mathcal{F}^{so}(q_\infty \mathbf{C}_{USI}), \quad (3.26)$$

and

$$\mathbf{Y}_{USI}^f = \mathcal{F}^{fo}(\mathbf{S}_{USI}), \quad (3.27)$$

The accuracy of the uncoupled solution may be further increased by performing a single concluding fluid and structure evaluation using the fitting parameters from the uncoupled surrogate intersection as inputs (illustrated in Fig. 3.2). The result of these final evaluations is called the uncoupled surrogate-informed solution (USiS).

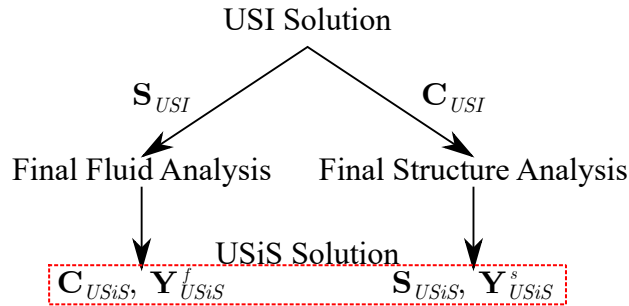


Figure 3.2: Illustration of obtaining USiS solution using USI solution as inputs.

Method 3.1 and the flowchart in Fig. 3.3 summarize the entire uncoupled process. This new approach offers two significant advantages for performing aeroelastic analysis: 1) assuming sufficient computational resources, this method provides the means of running simultaneous, independent, and highly parallelizable fluid and structure

analyses, significantly reducing the time required to obtain a SAA solution<sup>3</sup>, and 2) since the fluid and structure models are independent, results from one model can be reused when design variables of the other is changed. The capability to reuse data sets is key for the use of the uncoupled method in aerostructural design and optimization studies, which consider hundreds of structures subjected to the same flow condition.

### Method 3.1: Computational process of uncoupled method for SAA

<b>Uncoupled Method for SAA</b>
1) Perform initial fluid and structure analyses; obtain $C_p^0(\mathbf{x})$ and $\Omega_{FSI}^0$
2) Define $\hat{C}_p$ , $\hat{s}_{FSI}$ , $n_p$ , and $n_s$ For accurate solutions, $\epsilon_p^0$ (Eq. (3.7)) and $\epsilon_s^0$ (Eq. (3.8)) $\leq tol$
3) Generate $\mathbf{C}^j$ , $j=1,\dots,m_p$ and $\mathbf{S}^k$ , $k=1,\dots,m_s$ Note that Steps 4a, 4b and 5a, 5b can be conducted independently
4a) Do for $j=1,\dots,m_p$ : i) Perform structural analysis with load $\hat{p}^j(\mathbf{x})=q_\infty \hat{C}_p^j(\mathbf{x}; \mathbf{C}^j)$ (Eq. (3.4)) ii) Extract $\mathbf{S}^j(q_\infty \hat{C}_p^j(\mathbf{x}; \mathbf{C}^j))$ and $\mathbf{Y}^{s,j}(q_\infty \hat{C}_p^j(\mathbf{x}; \mathbf{C}^j))$ from results
4b) Do for $k=1,\dots,m_s$ : i) Perform fluid analysis of body described by $\hat{s}_{FSI}^k(\mathbf{x}; \mathbf{S}^k)=0$ (Eq. (3.2)) ii) Extract $\mathbf{C}^k(\hat{s}_{FSI}^k(\mathbf{x}; \mathbf{S}^k))$ and $\mathbf{Y}^{f,k}(\hat{s}_{FSI}^k(\mathbf{x}; \mathbf{S}^k))$ from results
5a) Calibrate structure surrogates $\mathbf{S}=\mathcal{F}^s(q_\infty \mathbf{C})$ (Eq. (3.13)) and $\mathbf{Y}^s=\mathcal{F}^{so}(q_\infty \mathbf{C})$ (Eq. (3.15))
5b) Calibrate fluid surrogates $\mathbf{C}=\mathcal{F}^f(\mathbf{S})$ (Eq. (3.14)) and $\mathbf{Y}^f=\mathcal{F}^{fo}(\mathbf{S})$ (Eq. (3.16))
6) Make initial guess $\mathbf{C}_1$
7) Do while $\mathbf{C}_{g+1} - \mathbf{C}_g \leq tol_c$ and $\mathbf{S}_g - \mathbf{S}_{g-1} \leq tol_s$ : i) Solve $\mathbf{S}_g = \mathcal{F}^s(q_\infty \mathbf{C}_g)$ ii) Solve $\mathbf{C}_{g+1} = \mathcal{F}^f(\mathbf{S}_g)$
8) Set $\mathbf{S}_{USI}=\mathbf{S}_g$ and $\mathbf{C}_{USI}=\mathbf{C}_{g+1}$
9) Solve $\mathbf{Y}_{USI}^f=\mathcal{F}^{fo}(\mathbf{S}_{USI})$ (Eq. (3.26)) and $\mathbf{Y}_{USI}^s=\mathcal{F}^{so}(q_\infty \mathbf{C}_{USI})$ (Eq. (3.27))
10) Optional: Obtain $\mathbf{S}_{USiS}(q_\infty \mathbf{C}_{USI})$ , $\mathbf{C}_{USiS}(\mathbf{S}_{USI})$ , $\mathbf{Y}_{USiS}^f(\mathbf{S}_{USI})$ , and $\mathbf{Y}_{USiS}^s(q_\infty \mathbf{C}_{USI})$ from final structure and fluid evaluations (Fig. 3.2)

<sup>3</sup>Time required to solve the system of equations created by RBFs is trivial.

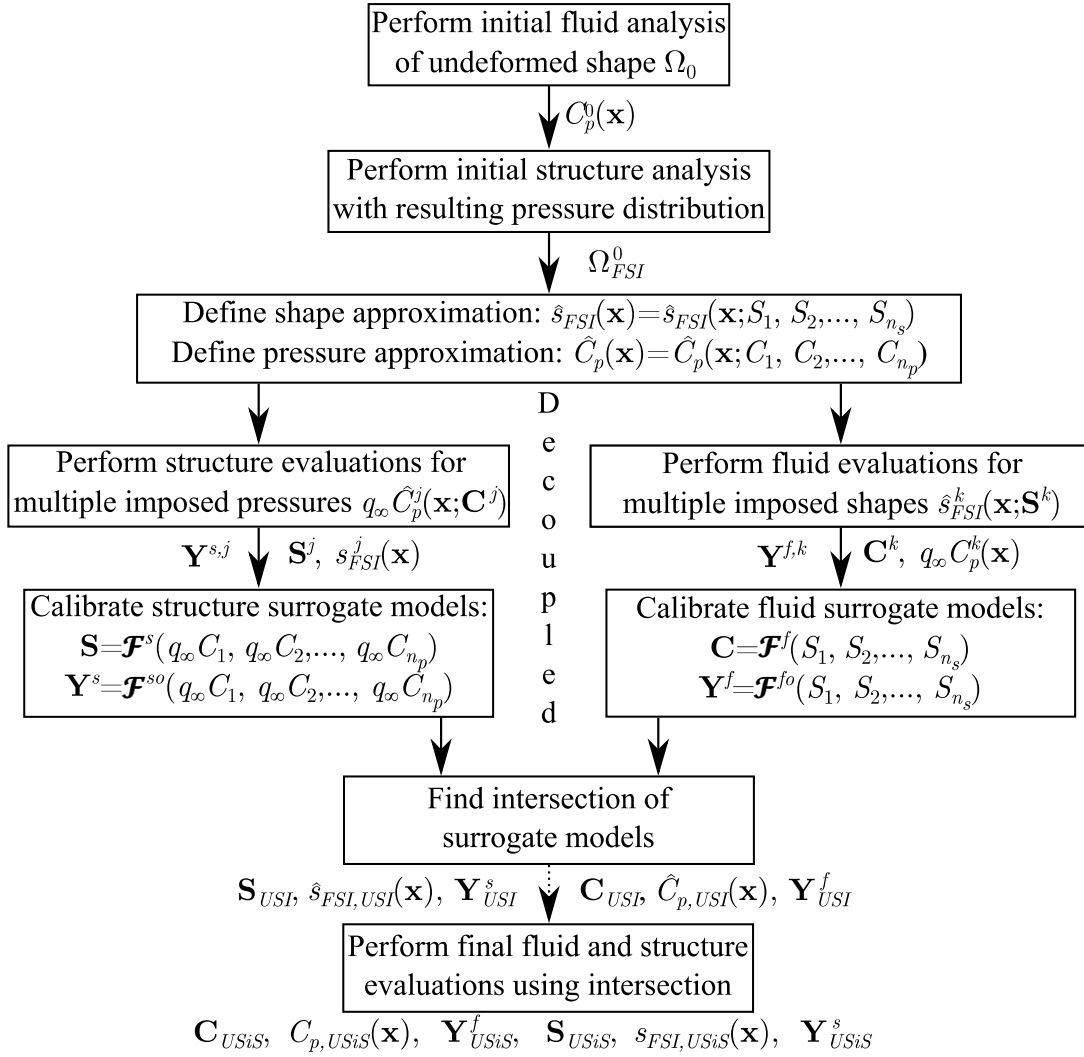


Figure 3.3: Flowchart of uncoupled method implemented for SAA to find solution at single freestream velocity.

The uncoupled method is evaluated in this work relative to the serial FSI coupling scheme by two criteria: 1) computational time for each design and the overall design problem, and 2) accuracy. For computational time, by performing all structure and fluid evaluations in parallel, the uncoupled method should be more efficient (computationally faster) than the serial FSI coupling scheme at obtaining a SAA

solution for a single design. The time required to obtain an uncoupled solution is approximately equal to the most computationally expensive static structural or steady fluid analysis. Either of these analyses is faster than a transient FSI analysis or all sequentially performed steady fluid and static structure analyses in a steady FSI analysis. Additionally, in an aerostructural design problem/optimization, the ability to reuse data sets, such as the expensive fluid evaluations, further reduces time required to obtain a SAA solution with the uncoupled method while the time required with the serial FSI scheme remains unchanged. Accuracy of the uncoupled method is highly dependent on how well both the fits of shape and pressure approximate the actual data. This can be measured with a number of metrics such as Eq. (3.7) and Eq. (3.8). If an FSI solution is available, then the accuracy of the uncoupled method can be evaluated by the previously mentioned equations or by comparison of the fitting parameters from the two solutions. Another means of evaluating the accuracy of the uncoupled method is by comparing the USI and USiS solutions. If the fitting parameters change significantly between the two solutions, then it suggests that 1) the fits are poor and thus require more fitting parameters or a different functional form, or 2) the surrogate models of the fitting parameters are not fully representing some physical phenomenon, thus requiring either more training points or redefined upper/lower bounds of the training points during surrogate model construction. To further boost confidence in the uncoupled solution and drive the error of the surrogate models (and thus the USI solution) towards zero, once initial training evaluations are complete, new points can be added to the surrogate models until satisfaction of some infill criteria [58] is met.

Coelho, et al. proposed a similar method called the bi-level model reduction (BLMR) [80, 131], which combines proper orthogonal decomposition-based (POD) reduced order modeling with surrogate models. This method is similar to the un-

coupled method since surrogate models are developed for fits of the displacement or pressure fields that are described by a few variables. However in BLMR, construction of the POD requires running multiple coupled analyses while the uncoupled method assumes fields are approximated using a functional fit and evaluates the structure and fluid domains separately. The main advantage of the uncoupled method over BLMR method is that running a coupled analysis between the structure and fluid solver is not required for the uncoupled method, reducing computational expense. Additionally, since structure surrogate models are constructed for each design considered, the solution from the uncoupled scheme may be more accurate than that of the BLMR method.

McNamara, et al. proposed another framework of interest that develops Kriging surrogate models of the pressure distribution acting on a deformed body in hypersonic flow using steady-state fluid evaluations [132, 133, 134]. With an enriched piston theory, McNamara performs transient FSI analysis by coupling the Kriging surrogate model to either a structural model or a POD-based reduced order model of the structure, developed from structural responses to random loadings. McNamara's framework and the uncoupled method are similar since a prescribed shape is imposed in the fluid domain and evaluated with steady-state fluid analysis. However, the uncoupled method utilizes generalized forms for both the imposed shape and pressure distribution, while McNamara's framework is dependent on mode shapes of the structure. Additionally, McNamara's framework still performs a coupled analysis while the uncoupled method solves the system of equations created by surrogate models of fitting parameters.

### 3.3 Existence and Uniqueness of the Uncoupled Method Solution

The uncoupled method relies on the existence of a solution to the system of non-linear equations created by the surrogate models. Each surrogate model is assumed to be a continuous function within the bounds of its training points. Additionally, each surrogate model is a hypersurface of dimension  $n+1$ , where  $n$  is the number of fitting parameters [135]. The intersection of these  $n_p+n_s$  hypersurfaces is the solution to the system of equations in Eq. (3.23) [136, 137] and the USI solution. Uniqueness of the USI solution is important such that numerical methods used in the uncoupled method only converge to one solution. Both existence and uniqueness of the intersection of hypersurfaces has been addressed by algebraic geometry [138], and more specifically in the area of intersection theory [139]. In this work, existence (and in a sense, uniqueness) of the intersection of the hypersurfaces is addressed using numerical analysis techniques [137].

The inverse function theorem states that if a function  $\mathbf{g}(\mathbf{x})$  has a nonsingular Jacobian at a point  $\mathbf{x}_0$ , then it is both invertible and has a unique solution for the system  $\mathbf{g}(\mathbf{x})=\mathbf{y}$  in the neighborhood of  $\mathbf{x}_0$ . For the uncoupled method, the system of equations is of the form  $\mathbf{f}(\mathbf{x})=\mathbf{x}$ . To be evaluated with the inverse function theorem, the system in Eq. (3.23) is converted into the form  $\mathbf{g}(\mathbf{x})=-\mathbf{x}+\mathbf{f}(\mathbf{x})=\mathbf{0}$  as follows:

$$\mathcal{G}^s(\mathbf{S}, q_\infty \mathbf{C}) = -\mathbf{S} + \mathcal{F}^s(q_\infty \mathbf{C}) = \mathbf{0}, \quad (3.28)$$

and

$$\mathcal{G}^f(\mathbf{S}, q_\infty \mathbf{C}) = -\mathbf{C} + \mathcal{F}^f(\mathbf{S}) = \mathbf{0}. \quad (3.29)$$

The Jacobian matrix for the system  $\{\mathcal{G}^s, \mathcal{G}^f\}=\{\mathbf{0}, \mathbf{0}\}$  is formed by taking partial derivatives of each function in  $\{\mathcal{G}^s, \mathcal{G}^f\}$  with respect to the shape and pressure fitting

parameters. The general form of this Jacobian in terms of  $\mathcal{G}^s$  and  $\mathcal{G}^f$  is

$$J = \begin{bmatrix} \frac{\partial \mathcal{G}_1^s(\mathbf{S}, q_\infty \mathbf{C})}{\partial C_1} & \dots & \frac{\partial \mathcal{G}_1^s(\mathbf{S}, q_\infty \mathbf{C})}{\partial C_{n_p}} & \frac{\partial \mathcal{G}_1^s(\mathbf{S}, q_\infty \mathbf{C})}{\partial S_1} & \dots & \frac{\partial \mathcal{G}_1^s(\mathbf{S}, q_\infty \mathbf{C})}{\partial S_{n_s}} \\ \vdots & \ddots & \vdots & \vdots & \ddots & \vdots \\ \frac{\partial \mathcal{G}_{n_s}^s(\mathbf{S}, q_\infty \mathbf{C})}{\partial C_1} & \dots & \frac{\partial \mathcal{G}_{n_s}^s(\mathbf{S}, q_\infty \mathbf{C})}{\partial C_{n_p}} & \frac{\partial \mathcal{G}_{n_s}^s(\mathbf{S}, q_\infty \mathbf{C})}{\partial S_1} & \dots & \frac{\partial \mathcal{G}_{n_s}^s(\mathbf{S}, q_\infty \mathbf{C})}{\partial S_{n_s}} \\ \frac{\partial \mathcal{G}_1^f(\mathbf{S}, q_\infty \mathbf{C})}{\partial C_1} & \dots & \frac{\partial \mathcal{G}_1^f(\mathbf{S}, q_\infty \mathbf{C})}{\partial C_{n_p}} & \frac{\partial \mathcal{G}_1^f(\mathbf{S}, q_\infty \mathbf{C})}{\partial S_1} & \dots & \frac{\partial \mathcal{G}_1^f(\mathbf{S}, q_\infty \mathbf{C})}{\partial S_{n_s}} \\ \vdots & \ddots & \vdots & \vdots & \ddots & \vdots \\ \frac{\partial \mathcal{G}_{n_p}^f(\mathbf{S}, q_\infty \mathbf{C})}{\partial C_1} & \dots & \frac{\partial \mathcal{G}_{n_p}^f(\mathbf{S}, q_\infty \mathbf{C})}{\partial C_{n_p}} & \frac{\partial \mathcal{G}_{n_p}^f(\mathbf{S}, q_\infty \mathbf{C})}{\partial S_1} & \dots & \frac{\partial \mathcal{G}_{n_p}^f(\mathbf{S}, q_\infty \mathbf{C})}{\partial S_{n_s}} \end{bmatrix}. \quad (3.30)$$

Note that the each function  $\mathcal{G}_i^f(\mathbf{S}, q_\infty \mathbf{C})$  corresponding to the fluid model is only dependent on the  $n_s$  shape fitting parameters and one pressure coefficient fitting parameter  $C_i$ , while for each function  $\mathcal{G}_i^s(\mathbf{S}, q_\infty \mathbf{C})$  corresponding to the structure model is only dependent on the  $n_p$  pressure coefficient fitting parameters and one shape fitting parameter  $S_i$ . This greatly simplifies the Jacobian to

$$J = \begin{bmatrix} \frac{\partial \mathcal{F}_1^s(q_\infty \mathbf{C})}{\partial C_1} & \dots & \frac{\partial \mathcal{F}_1^s(q_\infty \mathbf{C})}{\partial C_{n_p}} & -1 & 0 & \dots \\ \vdots & \ddots & \vdots & 0 & \ddots & \ddots \\ \frac{\partial \mathcal{F}_{n_s}^s(q_\infty \mathbf{C})}{\partial C_1} & \dots & \frac{\partial \mathcal{F}_{n_s}^s(q_\infty \mathbf{C})}{\partial C_{n_p}} & \vdots & \ddots & -1 \\ -1 & 0 & \dots & \frac{\partial \mathcal{F}_1^f(\mathbf{S})}{\partial S_1} & \dots & \frac{\partial \mathcal{F}_1^f(\mathbf{S})}{\partial S_{n_s}} \\ 0 & \ddots & \ddots & \vdots & \ddots & \vdots \\ \vdots & \ddots & -1 & \frac{\partial \mathcal{F}_{n_p}^f(\mathbf{S})}{\partial S_1} & \dots & \frac{\partial \mathcal{F}_{n_p}^f(\mathbf{S})}{\partial S_{n_s}} \end{bmatrix}. \quad (3.31)$$

The nonzero and non -1 components of the Jacobian are simply the partial derivatives of the surrogate models with respect to the shape and pressure coefficient fitting parameters, which are known analytically. For linear RBF structure and fluid surrogate models with polynomial tails, the partial derivatives are

$$\frac{\partial \mathcal{F}_i^s(q_\infty \mathbf{C})}{\partial q_\infty C_i} = \sum_{j=1}^{m_p} w_{i,j}^s \frac{C_i - C_i^j}{\|\mathbf{C} - \mathbf{C}^j\|_2} + \gamma_i \quad \forall i = 1, \dots, n_p \quad (3.32)$$

and

$$\frac{\partial \mathcal{F}_i^f(\mathbf{S})}{\partial S_i} = \sum_{k=1}^{m_s} w_{i,k}^f \frac{S_i - S_i^k}{\|\mathbf{S} - \mathbf{S}^k\|_2} + \gamma_i \quad \forall i = 1, \dots, n_s. \quad (3.33)$$

Similarly, for cubic RBF structure and fluid surrogate models with polynomial tails, the partial derivatives are

$$\frac{\partial \mathcal{F}_i^s(q_\infty \mathbf{C})}{\partial q_\infty C_i} = \sum_{j=1}^{m_p} 3w_{i,j}^s (C_i - C_i^j) (\|\mathbf{C} - \mathbf{C}^j\|_2) + \gamma_i \quad \forall i = 1, \dots, n_p \quad (3.34)$$

and

$$\frac{\partial \mathcal{F}_i^f(\mathbf{S})}{\partial S_i} = \sum_{k=1}^{m_s} 3w_{i,k}^f (S_i - S_i^k) (\|\mathbf{S} - \mathbf{S}^k\|_2) + \gamma_i \quad \forall i = 1, \dots, n_s. \quad (3.35)$$

If the Jacobian has a non-zero determinant at a point in the  $q_\infty \mathbf{C}$ - $\mathbf{S}$  space within the bounds of the surrogate models, then a unique solution to the system of equations exists. This solution is proposed to be the USI solution.

### 3.4 Demonstration Examples

With both the general formulation and mathematical implementation of the uncoupled method presented, focus shifts towards demonstrating the method on a few examples of generally increasing complexity with both continuous and discrete pressure fields (see Table 3.1). These examples intentionally use a low number of fitting parameters for ease of visualizing results.

#### 3.4.1 Example Demonstration 1: Single Degree-of-Freedom Baffle

The first problem considered is a two-dimensional (infinity long, effects in  $z$  neglected) rigid baffle in a wind tunnel-like environment supported by a torsional spring

Table 3.1: Fitting parameters for considered demonstration examples of generally increasing complexity with both continuous and discrete pressure fields.

<b>Demonstration Examples</b>	$n_s$	$n_p$
Single Degree-of-Freedom Baffle	1	2-5
Two Degree-of-Freedom Baffle	2	5
Two Degree-of-Freedom Discrete Pressure Baffle	2	2
Continuously Flexible Baffle	3	5

at its base (see Fig. 3.4). The structure is modeled in Abaqus, a finite element analysis suite [114], while the fluid is modeled in SC/Tetra, a thermo-fluid unstructured mesh CFD solver [109]. While the structural problem is clearly a candidate for analytical analysis, Abaqus is employed because it allows performance for later, more complex analysis, and because it allows for direct comparisons to an FSI solution [114, 109]. For this problem, pressure coefficient fitting parameters ( $C_1, C_2, \dots, C_{n_p}$ ) describe the net pressure across the baffle at evenly distributed locations on the baffle while the sole shape fitting parameter is the rotation of the baffle ( $\theta$ ). The pressure coefficient fitting parameters form a polynomial fit  $\hat{C}_p(s)$ , having the following form:

$$\hat{C}_p(s) = \sum_{i=1}^{n_p} c_i s^{i-1}, \quad (3.36)$$

where  $s$  is the distance along the baffle and  $c_i$  are constants determined by solving a linear system of equations using the pressure coefficient fitting parameters as reference values:

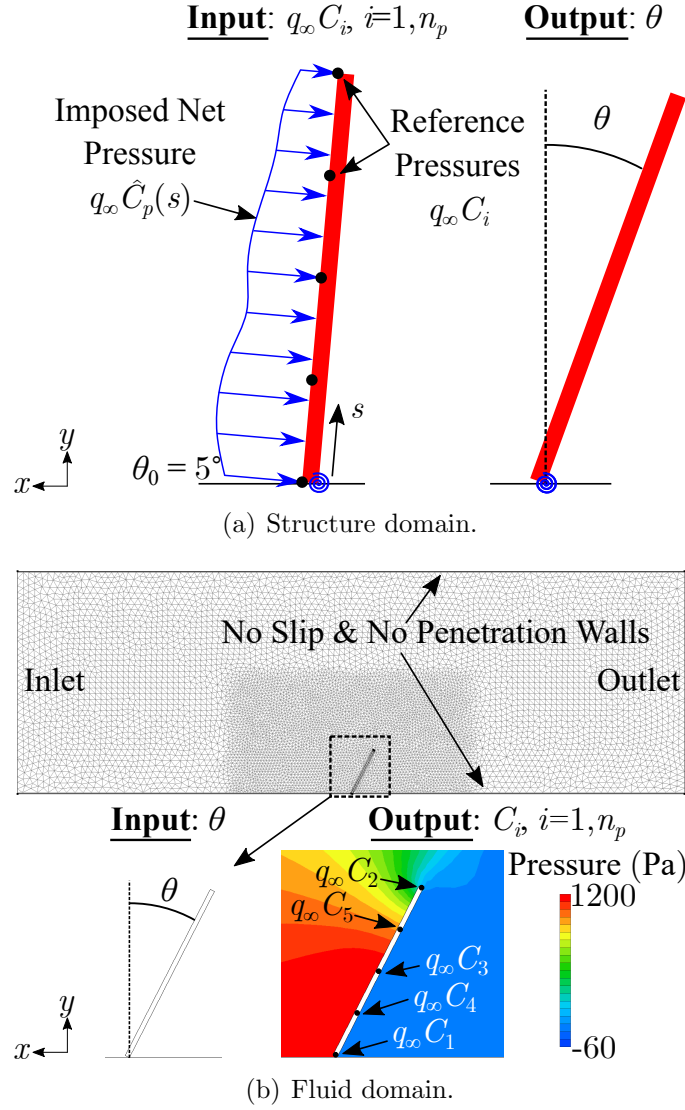


Figure 3.4: Structure and fluid models of one degree-of-freedom rigid baffle.

$$\begin{bmatrix} C_1 \\ C_2 \\ \vdots \\ C_{n_p} \end{bmatrix} = \begin{bmatrix} 1 & s_1 & s_1^2 & \cdots & s_1^{n_p-1} \\ 1 & s_2 & s_2^2 & \cdots & s_2^{n_p-1} \\ \vdots & \vdots & \vdots & \cdots & \vdots \\ 1 & s_{n_p} & s_{n_p}^2 & \cdots & s_{n_p}^{n_p-1} \end{bmatrix} \begin{bmatrix} c_1 \\ c_2 \\ \vdots \\ c_{n_p} \end{bmatrix}. \quad (3.37)$$

The structural model of the baffle consists of a rigid body with a 0.2 m by 0.005 m

rectangular cross-section, a width of 0.01 m and a spring element with a torsional stiffness of 0.5 N-m/rad. Additionally, the spring is given a reference configuration (i.e., zero stretch state) of  $\theta_0=5^\circ$ . Static analysis evaluates the baffle response to each considered pressure loading, and the resulting spring rotation is extracted.

The fluid model is a 0.9 m by 2.7 m by 0.01 m domain with a solid baffle on the floor. Incompressible air with density of 1.206 kg/m<sup>3</sup> and viscosity of 1.83x10<sup>-5</sup> Pa-s is used. Turbulent effects are captured with the Shear-Stress Turbulent  $k - \omega$  model [110]. The following boundary conditions are applied to the model: 1) inlet condition of 30 m/s horizontal velocity on the left face of the fluid domain, 2) outlet condition of zero static pressure on the right face of the fluid domain, and 3) wall conditions on both the surface of the baffle and the top/bottom faces of the fluid domain. Additionally, inlet turbulence is set to default values ( $k=0.0001 \text{ m}^2/\text{s}^2$  and  $\varepsilon = 0.0001 \text{ m}^2/\text{s}^3$ ) for approximately laminar flow at the inlet. For each deformed configuration of the baffle considered, new geometry for the fluid model is generated by rotating the baffle about the axis of the torsional spring followed by mesh generation. The model is coarsely meshed with 15,600 elements (14,800 prism and 800 hexahedron) with sizes ranging from 25.6 mm in the far field to 6.4 mm near the baffle, and one element wide in the  $z$ -direction for two-dimensional flow. Steady flow analysis is conducted for each deformed baffle and the resulting pressure coefficient distribution is recorded and associated fitting parameters  $C_i$  (Eq. (3.36)) are extracted.

To limit the uncoupled SAA problem to three degrees of freedom ( $C_1, C_2, \theta$ ), the pressure coefficient distribution is fit using a linear polynomial based on the pressure at the top ( $s=0.2$  m) and bottom ( $s=0.0$  m) of the baffle. This linear polynomial is a poor fit, but allows for straightforward visualization for the purposes of illustrating the proposed approach. Following the process described in Section 3.2, CFD analysis

is conducted for nine baffle configurations ranging from  $5^\circ$  to  $80^\circ$  while, in the structure domain, a twelve level full factorial ( $12^2=144$  runs) design of experiment (DOE) is conducted varying  $C_1$  and  $C_2$  from 0.0018 to 3.1 and 0.0018 to 2.2, respectively. Large of the fitting parameters are intentionally chosen for the purpose of visualization. For the structure DOE, instead of performing 144 separate analyses (either in parallel or series), a single analysis with 144 copies of the baffle each subjected to a unique pressure loading (after [140]) is performed. For the hardware used (standard workstation, 1CPU and 2CPU for the structure and fluid solvers, respectively), the computational cost of the single structure evaluation and each fluid evaluation (generating the model, running FEA/CFD, extracting results) is approximately 30 s (one structure solution increment) and 6 min (1,170 fluid solution increments), respectively; thus, the *serial* computational time required to generate all data is 54.4 min (144 structure<sup>4</sup> and 17,550 fluid solution increments,  $I^s$  and  $I^f$ , respectively). If all structure and fluid evaluations are performed in parallel, the time decreases to approximately 6 min.

Following the structure and fluid evaluations, surrogate models for the assumed pressure coefficient and displacement fields are created. Using the evaluations as training points, linear surrogate models for the rotation of the baffle and each pressure coefficient fitting parameter are constructed as:

$$\theta = \mathcal{F}^s(q_\infty \mathbf{C}) = \sum_{j=1}^{144} w_j^s \|q_\infty \mathbf{C} - q_\infty \mathbf{C}^j\|_2 + \gamma^s \cdot \{q_\infty C_1, q_\infty C_2, 1\}, \quad (3.38)$$

and

$$C_i = \mathcal{F}_i^f(\theta) = \sum_{k=1}^9 w_{i,k}^f (\theta - \theta^k) + \gamma_i^f \cdot \{\theta, 1\} \quad \forall i = 1, \dots, n_p. \quad (3.39)$$

---

<sup>4</sup>Number of copies of the structure in the single batch analysis (144) multiplied by the number of solutions increments for that analysis (1).

Following construction of the surrogate models, fixed-point iteration is executed per Eq. (3.24) and Eq. (3.25). The intersection is the solution to the system of equations Eq. (3.38) and Eq. (3.39), the USI solution of the problem. As seen in the  $q_\infty C_1$ - $q_\infty C_2$ - $\theta$  space of Fig. 3.5, the line generated by the fluid surrogate model (Eq. (3.39)) intersects the surface generated by the structural surrogate model. This solution is proposed to be an estimate of the true aeroelastic solution and, as both the structural and fluid sampling points and number of fitting parameters are increased, is expected to match it exactly.

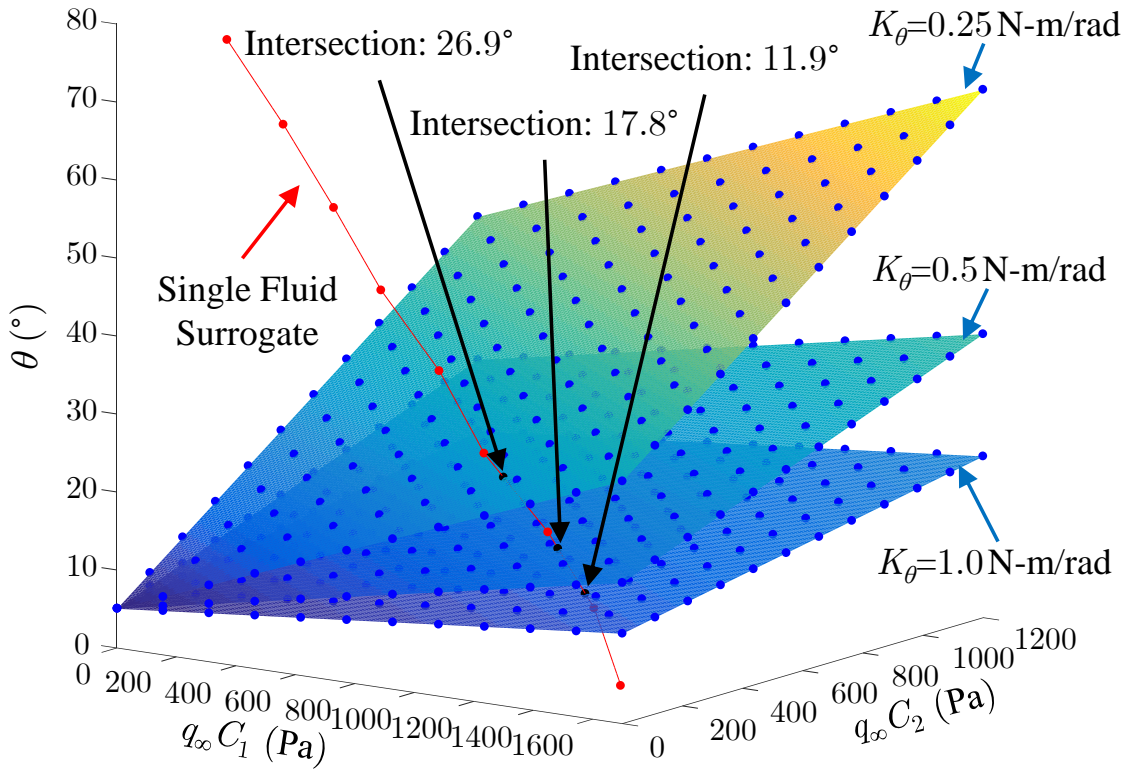


Figure 3.5: Intersection of fluid surrogate model and three structure surrogate models corresponding to three different torsional stiffnesses for a one degree-of-freedom rigid baffle.

To illustrate the substantial advantages of the uncoupled method in structural design, the stiffness of the torsional spring is now explored. Using traditional FSI analysis, each new spring stiffness would be considered in a new serial coupled analysis. With the new uncoupled scheme, new SAA solutions are quickly found as only the structure domain is changed while all previously computed fluid results are retained. For each spring stiffness considered, a new structural surrogate model is constructed at low computational cost (30 s) by conducting new structural evaluations with the modified stiffness, from which a new USI solution is obtained. As shown in Fig. 3.5, the fluid surrogate model intersects three structure surrogate models corresponding to three different torsional spring stiffnesses resulting in three SAA solutions *for a single set of fluid evaluations*.

To test the accuracy of the USI solution for the baffle with  $K_\theta$  of 0.5 N-m/rad, a legacy coupled serial analysis is conducted where the static structure and steady flow solvers are replaced with dynamic and transient flow solvers, respectively.<sup>56</sup> The base time step for both structure and fluid solvers is 0.0005 s and 0.005 s, respectively. Computational resources are same as the structure and fluid evaluations performed for surrogate model training. The coupled analysis is performed until the structure and fluid reach an approximate steady-state solution, which requires approximately 36 min of computational time (14,000 structure and 12,000 fluid solution increments). As seen in Fig. 3.6(a) the approximate steady-state solution of the serially coupled FSI analysis is  $25.9^\circ$ , which is 31% larger than the uncoupled surrogate intersection that assumed a poor linear fit of pressure coefficient distribution (see Fig. 3.6(b)), demonstrating the need for an accurate fit such as a higher order polynomial.

---

<sup>5</sup>During the analysis, inlet flow is linearly increased over 5 s from 1 m/s to 30 m/s allowing the structure to stabilize under the increasing velocity.

<sup>6</sup>The native link between Abaqus and SC/Tetra with the Abaqus Co-Simulation Engine is limited to transient FSI analysis [109].

To improve the accuracy of the fit, a third fitting parameter  $C_3$ , net pressure coefficient at  $s=0.1$  m, is added, resulting in a quadratic polynomial fit. Retaining the fluid results, a more accurate uncoupled solution (5.13% error in  $\theta$ , see Fig. 3.6(a)) is obtained after construction a new structure surrogate using a 6-level full factorial ( $6^3=216$  pressure loadings). Bounds for the pressure coefficient fitting parameters are shown in Table 3.2. Bounds for the pressure coefficient fitting parameters are based on the minimum and maximum values of the fitting parameters observed during fluid evaluations or are based on ranges considered. The accuracy is further increased (0.07% error in  $\theta$ , see Fig. 3.6(a)) with the addition of parameters  $C_4$  and  $C_5$ , net pressure coefficient at  $s=0.05$  m and  $s=0.15$  m, respectively, and development of a new structure surrogate trained with a 3-level full factorial ( $3^5=243$  pressure loadings). Additionally, as shown in Fig. 3.6(b), the fit for the pressure coefficient distribution improves with added fitting parameters.

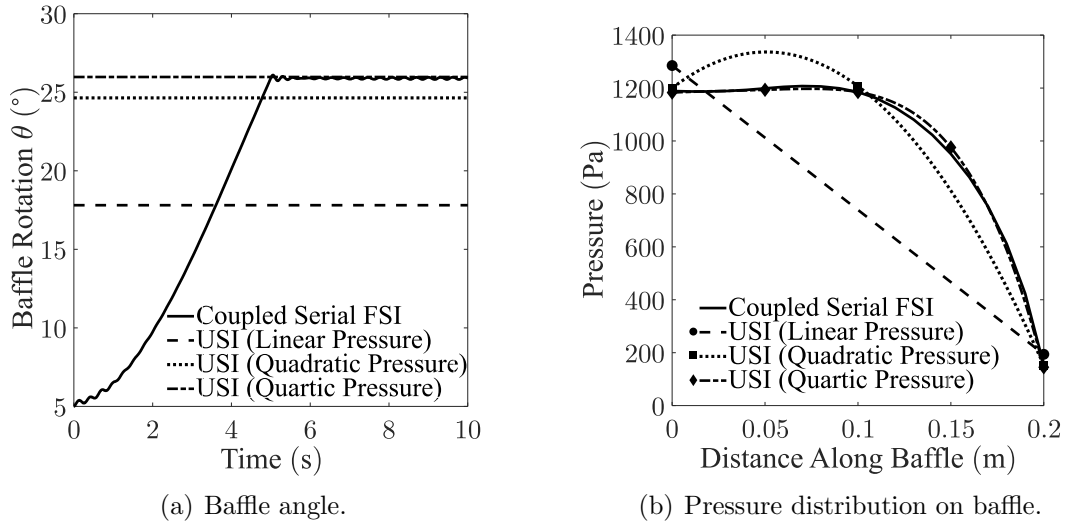


Figure 3.6: Comparison of coupled solution and uncoupled surrogate intersection; increasing the order of the pressure fit leads to a very low error USI solution.

Table 3.2: Surrogate model input bounds of pressure coefficient fitting parameters for one degree-of-freedom baffle.

<b>Fitting Parameter</b>	<b>Linear</b>	<b>Quadratic</b>	<b>Quartic</b>
$C_1$	0.0018-3.1	0.64-2.6	1.8-2.6
$C_2$	0.0018-2.2	0.0018-0.55	0.2-0.3
$C_3$	-	0.18-2.8	1.8-2.6
$C_4$	-	-	1.8-2.6
$C_5$	-	-	1.5-2.2

The computational times and number of solution increments associated with the FSI and uncoupled SAA solutions are summarized in Table 3.3 and Table 3.4, respectively. For all uncoupled analyses, the *serial* time associated with generating all training points for the surrogate models and in turn, the USI solution is  $\approx 50\%$  slower than a single FSI analysis. Note that the uncoupled method requires less structure and fluid solution increments than the FSI analysis, indicating that the model generation and post-processing of the multiple structure and fluid evaluations represents a significant portion of the time required by the uncoupled method to find an aeroelastic solution. If performed in parallel, the uncoupled method is significantly faster. The efficiency of the uncoupled method is further demonstrated in the time required to obtain a new solution (i.e., changing the spring stiffness). A new aeroelastic solution with the serial coupling scheme still requires 36 min while the computational cost for the uncoupled method with a quartic polynomial fit is approximately 39 times faster (0.92 s).

The intersection of the surrogate models using the linear pressure distribution fit is visually shown to exist and have uniqueness in Fig. 3.5. Existence and uniqueness

Table 3.3: Comparison of computational times to obtain static aeroelastic solutions for one degree-of-freedom baffle. In parenthesis is the estimated time required to obtain each uncoupled solution if all runs are performed in parallel.

<b>Analysis</b>	<b>Time For First Solution (min)</b>	<b>Time For New Structural Solution (min)</b>
FSI	36	36
USI (Linear)	54.5 (6.0)	0.5
USI (Quadratic)	54.75 (6.0)	0.75
USI (Quartic)	54.92 (6.0)	0.92

Table 3.4: Comparison of solution increments to obtain static aeroelastic solutions for one degree-of-freedom baffle.

<b>Analysis</b>	<b><math>I^f</math> (<math>I^s</math>) For First Solution</b>	<b><math>I^f</math> (<math>I^s</math>) For New Structural Solution</b>
FSI	12,000 (14,000)	12,000 (14,000)
USI	17,550 (243*)	0 (243*)

\*Structure evaluations performed in parallelized batch manner after [140]. Solution increments listed here are the number of copies of the structure in the single batch analysis (243) multiplied by the number of increments for that analysis (1).

is now demonstrated with regards to the conditions of the inverse function theorem discussed in Section 3.3. The Jacobian (see Eq. (3.31)) for the system of equations formed by the surrogate models is

$$J = \begin{bmatrix} \frac{\partial \mathcal{F}_1^s(q_\infty C_1, q_\infty C_2)}{\partial C_1} & \frac{\partial \mathcal{F}_1^s(q_\infty C_1, q_\infty C_2)}{\partial C_2} & -1 \\ -1 & 0 & \frac{\partial \mathcal{F}_1^f(\theta)}{\partial \theta} \\ 0 & -1 & \frac{\partial \mathcal{F}_2^f(\theta)}{\partial \theta} \end{bmatrix}. \quad (3.40)$$

Evaluating this Jacobian at the center of the **C-S** space for the input bounds of the surrogate models results in the following matrix

$$J = \begin{bmatrix} 0.585 & 0.415 & -1 \\ -1 & 0 & -0.482 \\ 0 & -1 & -1.03 \end{bmatrix}. \quad (3.41)$$

which has a determinant of -1.71, indicating that a solution to the system of equations exists. For the system of equations generated by the surrogate models for either the quadratic and quartic pressure distribution fits, it can be similarly demonstrated that the Jacobian has a nonzero determinant and thus a solution. The Jacobians for the systems using the quadratic and quartic pressure distribution fits are

$$J = \begin{bmatrix} \frac{\partial \mathcal{F}_1^s(q_\infty \mathbf{C})}{\partial C_1} & \frac{\partial \mathcal{F}_1^s(q_\infty \mathbf{C})}{\partial C_2} & \frac{\partial \mathcal{F}_1^s(q_\infty \mathbf{C})}{\partial C_3} & -1 \\ -1 & 0 & 0 & \frac{\partial \mathcal{F}_1^f(\theta)}{\partial \theta} \\ 0 & -1 & 0 & \frac{\partial \mathcal{F}_2^f(\theta)}{\partial \theta} \\ 0 & 0 & -1 & \frac{\partial \mathcal{F}_3^f(\theta)}{\partial \theta} \end{bmatrix}. \quad (3.42)$$

and

$$J = \begin{bmatrix} \frac{\partial \mathcal{F}_1^s(q_\infty \mathbf{C})}{\partial C_1} & \frac{\partial \mathcal{F}_1^s(q_\infty \mathbf{C})}{\partial C_2} & \frac{\partial \mathcal{F}_1^s(q_\infty \mathbf{C})}{\partial C_3} & \frac{\partial \mathcal{F}_1^s(q_\infty \mathbf{C})}{\partial C_4} & \frac{\partial \mathcal{F}_1^s(q_\infty \mathbf{C})}{\partial C_5} & -1 \\ -1 & 0 & 0 & 0 & 0 & \frac{\partial \mathcal{F}_1^f(\theta)}{\partial \theta} \\ 0 & -1 & 0 & 0 & 0 & \frac{\partial \mathcal{F}_2^f(\theta)}{\partial \theta} \\ 0 & 0 & -1 & 0 & 0 & \frac{\partial \mathcal{F}_3^f(\theta)}{\partial \theta} \\ 0 & 0 & 0 & -1 & 0 & \frac{\partial \mathcal{F}_4^f(\theta)}{\partial \theta} \\ 0 & 0 & 0 & 0 & -1 & \frac{\partial \mathcal{F}_5^f(\theta)}{\partial \theta} \end{bmatrix}, \quad (3.43)$$

respectively. The determinants for these Jacobians evaluated at the center of the **C-S** space are -2.19 and -2.18, respectively.

### 3.4.2 Example Demonstration 2: Two Degree-of-Freedom Baffle

The first demonstration problem is extended to consider a second rigid baffle with a second torsional spring, creating a two degree-of-freedom baffle in flow with two shape fitting parameters  $\theta_1$  and  $\theta_2$ . Both Abaqus and SC/Tetra are used again for this demonstration. Additionally, this demonstration example utilizes the quadratic polynomial fit for the pressure coefficient distribution (Eq. (3.36)) from the previous one degree-of-freedom baffle problem.

The baffle assembly structural model (see Fig. 3.7(a)) consists of two rigid bodies with a 0.1 m by 0.005 m rectangular cross-section, a width of 0.01 m, and two spring elements with a torsional stiffness of 0.5 N-m/rad. Both springs have a reference configuration of  $\theta_0=5^\circ$ . Note that  $\theta_2$  is measured relative to the rotation of the first torsional spring. Following each static analysis, the rotation of the two springs is recorded.

The fluid model used in this example (see Fig. 3.7(b)) is a 0.9 m by 2.7 m by 0.01 m domain, identical (same mesh size and boundary conditions) to the one used in the previous example with the exception of the baffle geometry. For this example, new geometries are generated by rotating the baffle assembly about the axes of

both torsional springs before mesh generation. Steady flow analysis around each considered is conducted baffle configuration and the resulting pressure coefficient distribution and fitting parameters are extracted.

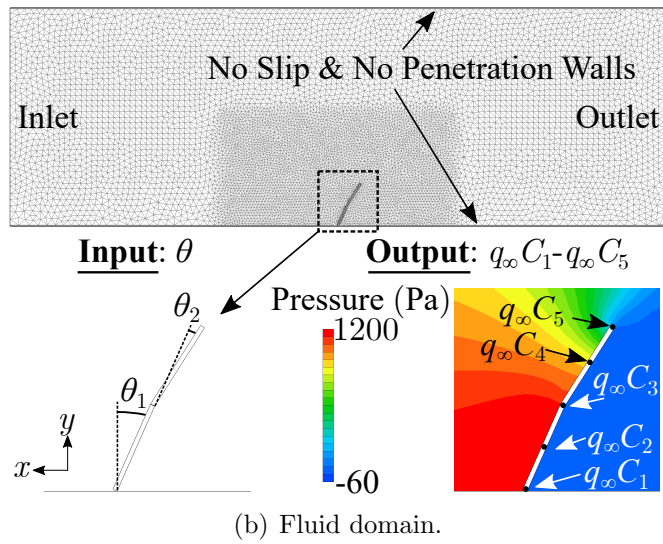
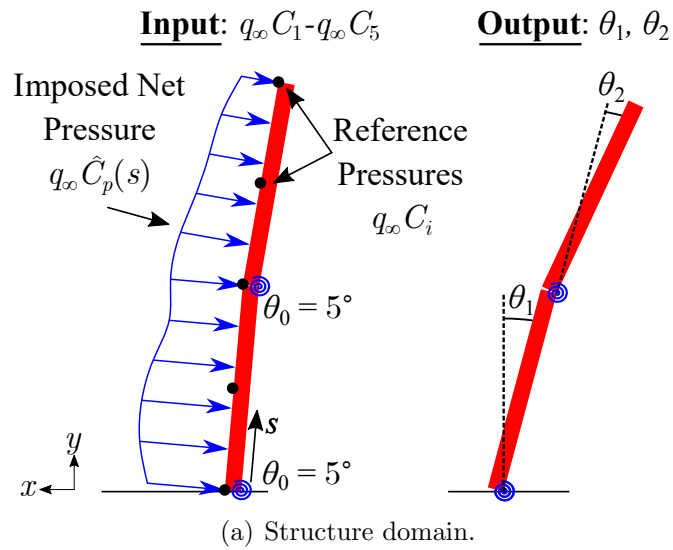


Figure 3.7: Structure and fluid models of two degree-of-freedom rigid baffle.

An initial fluid analysis is performed with both shape parameters equal to  $\theta_0$ , resulting in the ICS pressure coefficient fitting parameters  $(C_1^0, C_2^0, C_3^0, C_4^0, C_5^0) = (2.52, 2.51, 2.57, 2.36, 0.41)$ . Using these parameters, an initial structure analysis is performed resulting in ICS shape fitting parameters  $(\theta_1^0, \theta_2^0) = (31.1^\circ, 10.5^\circ)$ . Based on these ICS fitting parameters, full factorial design of experiments on the structure (3-level,  $3^5=243$  evaluations) and fluid (5-level,  $5^2=16$  evaluations) models with bounds of  $\pm 40\%$  and  $\pm 60\%$  from the ICS solution for pressure coefficient and shape fitting parameters, respectively, are performed (see Table 3.5 for the bounds). The bounds are deemed sufficient to generate a wide variety of shapes and pressure distributions. Instead of performing 243 individual structural analyses, a single structural analysis incorporating the 243 pressure loadings (after [140]) is performed. For the hardware used (standard workstation, 1CPU and 2CPU for the structure and fluid solvers, respectively), computational cost for this analysis is approximately 2 min (one structure solution increment) while each fluid analysis costs approximately 5 min (610 fluid solution increments). Therefore the serial computational cost associated with generating all necessary data to train the surrogate models is 82 min ( $I^s=243^7$ ,  $I^f=9,760$ ). Note that in parallel, the time is 5 min.

Following the fluid and structure evaluations, linear RBF surrogate models of the following form are constructed:

$$\theta_i = \mathcal{F}^s(q_\infty \mathbf{C}) = \sum_{j=1}^{243} w_{i,j}^s \|q_\infty \mathbf{C} - q_\infty \mathbf{C}^j\|_2 + \gamma_i^s \cdot \{q_\infty C_1, q_\infty C_2, 1\} \quad \forall i = 1, 2, \quad (3.44)$$

and

$$C_i = \mathcal{F}_i^f(\theta) = \sum_{k=1}^{16} w_{i,k}^f \|\mathbf{S} - \mathbf{S}^k\|_2 + \gamma_i^f \cdot \{\mathbf{S}, 1\} \quad \forall i = 1, 5. \quad (3.45)$$

---

<sup>7</sup>Number of copies of the structure in the single batch analysis (243) multiplied by the number of solutions increments for that analysis (1).

Table 3.5: Surrogate model input bounds of pressure coefficient and shape fitting parameters for two degree-of-freedom baffle.

<b>Fitting Parameter</b>	<b>Bounds</b>
$C_1$	1.5-3.5
$C_2$	1.5-3.5
$C_3$	1.6-3.7
$C_4$	1.4-3.3
$C_5$	0.17-0.59
$\theta_1$ ( $^\circ$ )	12.4-49.6
$\theta_2$ ( $^\circ$ )	4.2-16.8

The surrogate models form a system of seven nonlinear equations that are solved using fixed-point iteration to obtain the USI solution. The USI solution is then used as an input to perform final fluid and structure evaluations obtaining the USiS solution. As shown in Table 3.6, the USI and USiS solutions are nearly identical indicating that the surrogate models are accurately representing the displacement and pressure fields. With regards to inverse function theorem (Section 3.3), the determinant of the Jacobian ( $7 \times 7$  matrix, not shown for brevity) evaluated at the center of the **S-C** is -2.01, indicating that the solution is unique. As with the previous example, the USI and USiS solutions are verified with an FSI analysis using the serial coupling scheme (same computational resources as uncoupled method). The time step for both solvers during the coupled analysis is 0.005 s, and the analysis is conducted till both domains reach an approximate steady-state solution. Computational cost for the analysis is 37 min ( $I^s=2,130$ ,  $I^f=14,360$ ). Note that for a single design with this problem, the serial coupled scheme is faster than the serial computational cost of the uncoupled method for generating all required surrogate training data. However,

if runs are parallelized, the uncoupled method is faster. Additionally, if a new design is considered, new aeroelastic solutions can be obtained with the uncoupled method in 2 min since the fluid surrogate can be reused while the serial FSI coupling scheme will still require 37 min. As with the previous demonstration, a significant portion of the time in the uncoupled method is due to model generation and post-processing since the uncoupled method requires less structure and fluid solution increments. As shown in Table 3.6 and Fig. 3.8, the fitting parameters and resulting pressure distribution are of similar value with the exception of the pressure near the tip of the baffle. It is suspected that refinement of the mesh near tip will improve the USI and USiS solutions.

Table 3.6: Pressure and shape fitting parameters for two degree-of-freedom baffle.

<b>Fitting Parameter</b>	<b>FSI (Reference)</b>	<b>USI</b>	<b>USI Error (%)</b>	<b>USiS</b>	<b>USiS Error (%)</b>
(Shape Fitting Parameters)					
$\theta_1$ ( $^\circ$ )	23.64	23.88	1.02	23.88	1.02
$\theta_2$ ( $^\circ$ )	8.53	8.62	1.06	8.61	0.93
(Pressure Coefficient Fitting Parameters)					
$q_\infty C_1$ (Pa)	1134	1132	-0.176	1136	0.176
$q_\infty C_2$ (Pa)	1146	1144	-0.175	1149	0.262
$q_\infty C_3$ (Pa)	1073	1081	0.746	1087	1.305
$q_\infty C_4$ (Pa)	833	864	3.721	863	3.601
$q_\infty C_5$ (Pa)	130	119	-8.462	113	-13.077

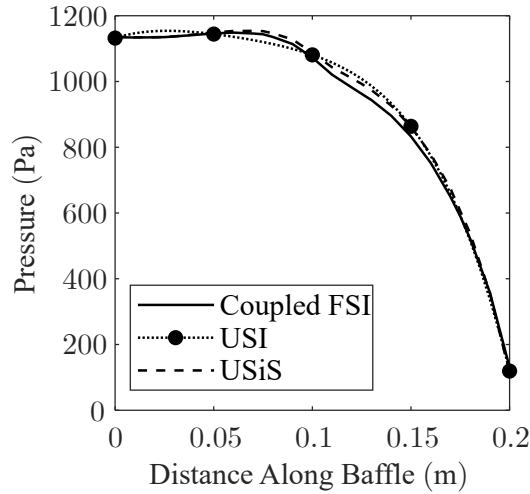


Figure 3.8: Comparison of pressure distribution on two degree-of-freedom baffle for coupled and uncoupled solutions.

### 3.4.3 Example Demonstration 3: Two Degree-of-Freedom Discrete Pressure Baffle\*

The third demonstration problem is a two degree-of-freedom discrete pressure baffle comprised of two circular plates and bars that are supported by two torsional springs in a wind tunnel (see Fig. 3.9(a)). This problem also intentionally uses a limited number of fitting parameters for visualization of the **C-S** space. Unlike the previous two examples, this demonstration problem assumes that the pressure distribution acting on each circular plate can be represented by a single discrete value applied as a uniform pressure of value  $q_\infty C_1$  and  $q_\infty C_2$ . Pressure fitting parameters in this problem could be considered as an equivalent drag coefficient. The shape fitting parameters for this problem are the rotations of the torsional springs ( $\theta_1$  and

---

\*Work in this section is reprinted with permission from “An Uncoupled Method for Fluid-Structure Interaction Analysis with Application to Aerostructural Design” by Scholten, W. and Hartl, D., 2020, *AIAA Scitech 2020 Forum*, 1635 [141], Copyright 2020 by The American Institute of Aeronautics and Astronautics, Inc..

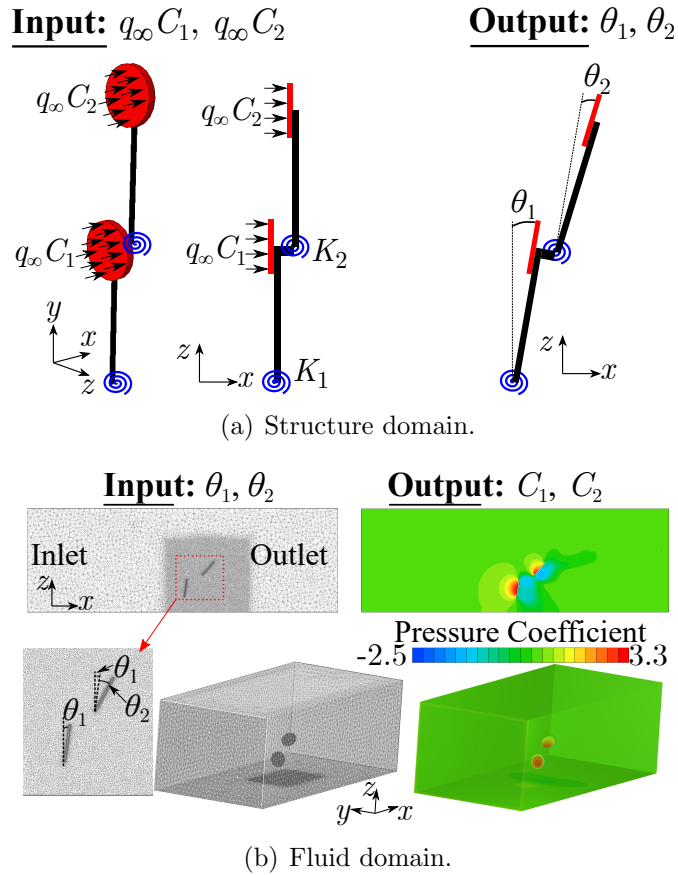


Figure 3.9: Structure and fluid models for two plate/bar assembly.

$\theta_2$ ). As with the previous examples, Abaqus and SC/Tetra are used as the structure and fluid solvers, respectively.

The structure (see Fig. 3.9(a)) consists of two circular plate/bars, modeled as rigid bodies, and two spring elements: 1) one at the base of the assembly and 2) one between the two bodies. Both are torsional springs with a torsional stiffness of 0.5 N-m/rad. The circular plates have a radius of 2 cm and thickness of 0.5 cm. Both bars have a length and width of 10 cm and 0.5 cm, respectively, and are infinitely thin. The rotation axis of the torsional spring connecting the two bars is offset 1.5 cm from the first circular plate. Static analysis evaluates the structural response to constant,

evenly distributed pressure loadings applied to the circular plates from which the rotations  $\theta_1$  and  $\theta_2$  of the spring elements are extracted.

The fluid model (see Fig. 3.9(b)) consists of the two circular plates in a 2.7 m by 0.9 m by 1.2 m wind tunnel section. For this problem, it is assumed that the bars have negligible effects on the flow over the circular plates, and therefore are not modeled. The fluid is modeled using incompressible air (density of  $1.206 \text{ kg/m}^3$  and viscosity of  $1.83 \times 10^{-5} \text{ Pa}\cdot\text{s}$ ). Turbulent effects are captured with the Shear-Stress Turbulent  $k - \omega$  model [110]. Four boundary conditions are applied to the fluid model: 1) no slip/penetration walls on the circular plates and on the floor, ceiling, and side walls of the tunnel section, 2) inlet condition of 30 m/s horizontal velocity with approximately laminar conditions ( $k=0.0001 \text{ m}^2/\text{s}^2$ ,  $\varepsilon = 0.0001 \text{ m}^2/\text{s}^3$ ) on the  $-x$  face of the fluid domain, and 3) outlet condition of zero static pressure  $+x$  face of the fluid domain. The model is meshed with 1,400,000 elements (1,200,000 tetrahedron and 200,000 prism). For each configuration of the circular plates, as defined by  $\theta_1$  and  $\theta_2$ , a new fluid model is generated and steady flow analysis is performed from which the integrated pressure coefficients  $C_1$  and  $C_2$  on the plates are extracted.

Following the method described in Section 3.2, an initial fluid analysis is performed with  $\theta_1=0^\circ$  and  $\theta_2=0^\circ$  to obtain ICS fitting parameters  $(C_1^0, C_2^0)=(1.23, 1.24)$  followed by an initial structure analysis to obtain  $(\theta_1^0, \theta_2^0)=(29.0, 9.71)$ . Full factorial design of experiments are then performed for the structure (ten level,  $10^2=100$  runs) and fluid (six level,  $6^2=36$  runs) models by varying the shape and pressure coefficient fitting parameters, respectively. Bounds for the DOE are  $C_1=0.1-1.25$ ,  $C_2=0.1-1.25$ ,  $\theta_1=15^\circ-35^\circ$ , and  $\theta_2=0^\circ-15^\circ$ . Upper bounds of the pressure coefficient fitting parameters are set approximately equal to the ICS parameters as the pressure loading is expected to decrease with increasing  $\theta_1$  and  $\theta_2$ . Lower bounds of the pressure coefficient fitting parameters and the bounds for the shape fitting param-

eters are set for purpose of visualization of the  $\mathbf{C}\text{-}\mathbf{S}$  space. For the hardware used (standard workstation, 1CPU and 2CPU for the structure and fluid solvers, respectively), the computational cost of performing one structural analysis incorporating the 100 pressure loadings (after [140]) is 2.8 min (1 structure solution increment), while cost of each fluid analysis is approximately 30 min (260 fluid solution increment). Thus, the total serial computational time required to generate all training points is approximately 1083 min (30 min if runs are parallelized) with  $I^s=100^8$  and  $I^s=6,760$ .

After the structure and fluid evaluations are performed, the resulting data sets of the fitting parameters are used as training points to construct linear RBF surrogate models of the form:

$$\theta_i = \mathcal{F}^s(q_\infty \mathbf{C}) = \sum_{j=1}^{100} w_{i,j}^s \|q_\infty \mathbf{C} - q_\infty \mathbf{C}^j\|_2 + \gamma_i^s \cdot \{q_\infty C_1, q_\infty C_2, 1\} \quad \forall i = 1, 2, \quad (3.46)$$

and

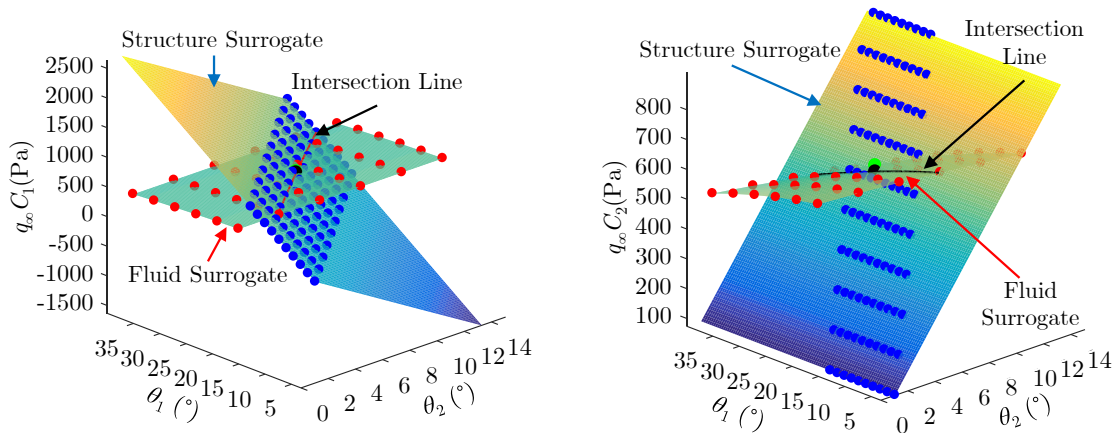
$$C_i = \mathcal{F}_i^f(\theta) = \sum_{k=1}^{36} w_{i,k}^f \|\mathbf{S} - \mathbf{S}^k\|_2 + \gamma_i^f \cdot \{\theta_1, \theta_2, 1\} \quad \forall i = 1, 2. \quad (3.47)$$

The four calibrated surrogate models form a system of equations that is solved using fixed-point iteration, obtaining the USI solution  $(\theta_1, \theta_2, q_\infty C_1, q_\infty C_2) = (25^\circ, 8.1^\circ, 606 \text{ Pa}, 564 \text{ Pa})$ . Due to the low number of fitting parameters for this problem, it is possible to visualize the USI solution. Figure 3.10(a) and Figure 3.10(b) show the fluid and structure surrogate models at a freestream velocity of 30 m/s in the  $q_\infty C_1\text{-}\theta_1\text{-}\theta_2$  space and  $q_\infty C_2\text{-}\theta_1\text{-}\theta_2$  space, respectively. The intersection of the surrogate models in each space forms a line. If the lines are projected into the  $\theta_1\text{-}\theta_2$  space (Fig. 3.10(c)), they intersect at a single point which corresponds exactly to the USI

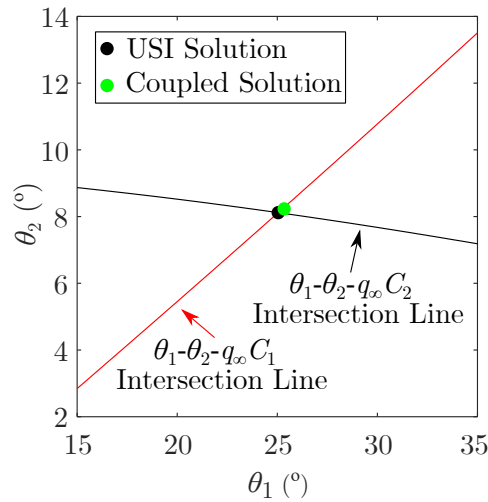
---

<sup>8</sup>Number of copies of the structure in the single batch analysis (100) multiplied by the number of solutions increments for that analysis (1).

solution obtained from the fixed point iteration, demonstrating that the uncoupled method converges to a single solution. Additionally, the values of  $q_\infty C_1$  and  $q_\infty C_2$  at this point along the intersection lines in Fig. 3.10(a) and Fig. 3.10(b) are identical to the USI solution.



(a) Intersection of surrogate models in  $q_\infty C_1$ - $\theta_1$ - $\theta_2$  space. (b) Intersection of surrogate models in  $q_\infty C_2$ - $\theta_1$ - $\theta_2$  space.



(c) Intersection of surrogate models in  $\theta_1$ - $\theta_2$  space.

Figure 3.10: Visualization of the intersection of the structure and fluid surrogate models and USI solution.

Table 3.7: Pressure and shape fitting parameters for the two degree-of-freedom discrete pressure baffle.

Fitting Parameter	FSI (Reference)	USI	USI Error (%)
(Shape Fitting Parameters)			
$\theta_2$ ( $^\circ$ )	25.34	25.04	-1.18
$\theta_1$ ( $^\circ$ )	8.23	8.11	-1.46
(Pressure Coefficient Fitting Parameters)			
$q_\infty C_1$ (Pa)	606	606	0
$q_\infty C_2$ (Pa)	582	564	-3.1

To demonstrate the accuracy of the USI solution, FSI analysis is conducted using the serial coupling scheme with a time step of 0.0025 s in both solvers (and same computational resources).<sup>9</sup> Total computational time for this analysis is 800 min ( $I^s=3,160$ ,  $I^f=3,160$ ). As shown in Fig. 3.10 and Table 3.7, the time-averaged shape and pressure coefficient fitting parameters extracted from the FSI analysis are approximately equal (maximum error of 3.1%) to the USI solution. Similar to the previous demonstration, while the serial computational cost associated with generating the training points for the surrogate models of the uncoupled method and obtaining a USI solution is 35% slower than a single FSI analysis (more fluid evaluations are required for the uncoupled method as well), if the training evaluations are run in parallel, then the uncoupled method becomes approximately 26 times faster. Additionally, if a new design is considered, the uncoupled method can solve the aeroelastic problem approximately 280 times faster than the serial FSI coupling

<sup>9</sup>As with the previous examples, inlet flow is linearly increased to 30 m/s allowing the structure to stabilize under the increasing velocity.

scheme since only the significantly cheaper structure evaluation is reperformed.

#### 3.4.4 Example Demonstration 4: Continuously Flexible Baffle

The problem considered is a two-dimensional flexible cantilevered baffle in a wind tunnel. As with the previous examples, the structure and surrounding flow field are modeled in Abaqus and SC/Tetra, though now a continuous shape must be represented by an approximate fit.

In the structural model (see Fig. 3.11(a)), the baffle is modeled as a deformable shell fixed at one end with a Young's modulus of 1 GPa and a Poisson's ratio of 0.38, which are representative properties of a thermoplastic. The length, thickness, and width of the baffle are 200 mm, 3 mm, and 10 mm, respectively. Symmetry conditions are applied to the edges residing in the  $xy$ -plane. The fluid model (see Fig. 3.11(b)) is identical (size of fluid domain, flow velocity of 30 m/s, etc.) to that of the example in Section 3.4.1 except for the shape of the baffle, which is generated based on the selection of three shape fitting parameters. Each deformed baffle in flow is evaluated using steady flow analysis and the resulting pressure coefficient distribution is recorded.

As with the previous example in Section 3.4.1, pressure coefficient fitting parameters represent the net pressure coefficient between the left and right faces of the baffle at evenly distributed locations ( $s=0.0, 0.05, 0.1, 0.15,$  and  $0.2$  m) along the length of the baffle. In this way, five pressure coefficient fitting parameters ( $C_1-C_5$ ) are used to generate a fit of the pressure distribution as a quartic polynomial  $\hat{p}(s)=q_\infty\hat{C}_p(s)$  (see Eq. (3.36)). Figure 3.12(a) shows the CFD-calculated pressure distribution for the undeformed baffle and fit of the distribution using the quartic polynomial. For the purpose of demonstrating the uncoupled method, the polynomial fit is sufficient.

The fit for the shape of the baffle is generated using the Class/Shape Transfor-

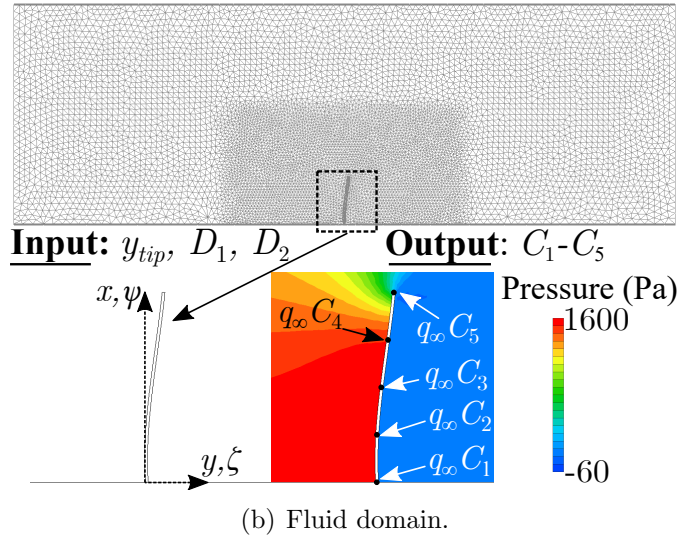
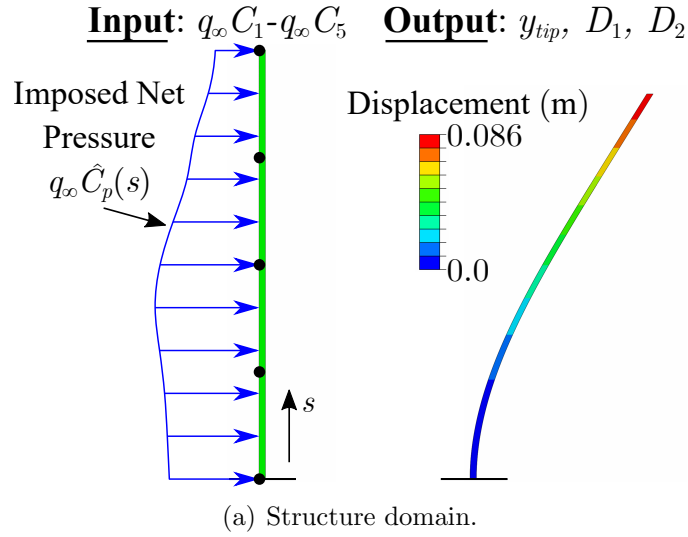


Figure 3.11: Structure and fluid models for the deformable baffle example problem.

mation (CST) method, which combines the concepts of class functions and shape functions [89, 90]. To improve the ease of mathematically representing a geometry for two-dimensional cases, the real  $x$ - $y$  coordinates of a geometry are converted through bijective linear transformation into a nondimensional domain  $\psi$ - $\zeta$ . In this nondimensional domain,  $\psi \in [0,1]$  where  $\psi=0$  occurs at  $x=0$ , while  $\psi=1$  occurs at maximum value of  $x$ . In this work, the CST method is utilized to represent baffle

shapes with two shape coefficients ( $D_1, D_2$ ) and the  $y$ -coordinate of the tip  $y_{tip}$  in the following form:

$$\zeta = \psi(1 - \psi)[D_1(1 - \psi) + D_2\psi] + \psi \frac{y_{tip}}{x_{tip}} \quad (3.48)$$

where  $x_{tip}$  is the  $x$ -coordinate of the baffle tip. The nondimensional coordinates for  $x$  and  $y$  ( $\zeta$  and  $\psi$ ) are defined as

$$\zeta = y/x_{tip}, \quad \psi = x/x_{tip}.$$

After a structural evaluation,  $y_{tip}$  is extracted from the deformed body and the shape coefficients  $D_1$  and  $D_2$  are calculated as

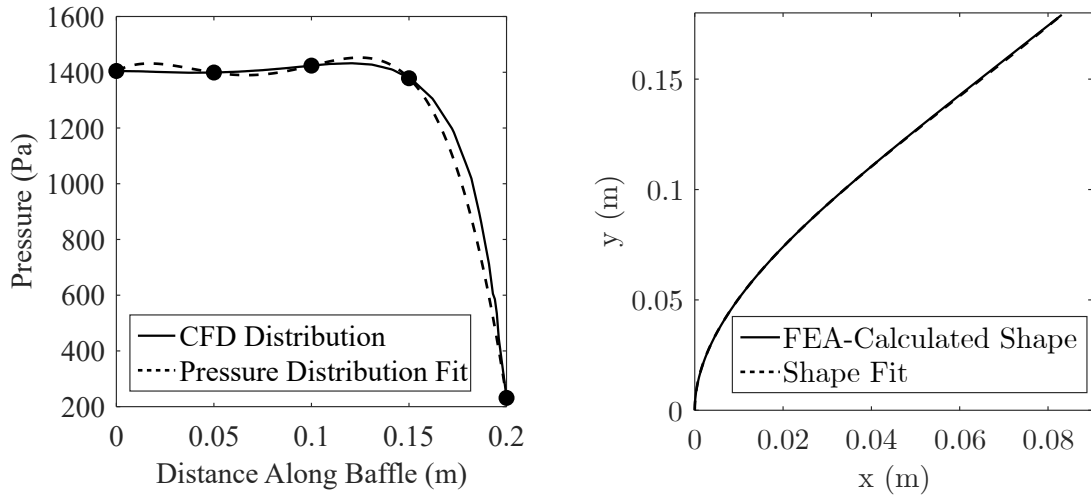
$$D_1 = -y_{tip}/x_{tip} \quad (3.49)$$

and

$$D_2 = \frac{1}{\psi_{MP}} \left[ \frac{\zeta_{MP} - \psi_{MP}\zeta_{tip}}{\psi_{MP}(1 - \psi_{MP})} - D_1(1 - \psi_{MP}) \right], \quad (3.50)$$

where  $\psi_{MP}$  and  $\zeta_{MP}$  are the nondimensional coordinates of the baffle midpoint. Baffle shapes evaluated in the fluid model are generated by calculating values of  $\zeta$  for different values of  $\psi$  using Eq. (4.12), which are then converted back into  $x$ - $y$  coordinates. As shown in Fig. 3.12(b), the approximate shape of a deformed baffle using the class-shape transformation function is nearly identical to the actual shape.

Following the same procedure described in Section 3.2, an initial fluid analysis of the undeformed body is performed followed by a structural analysis using the resulting pressure distribution, thereby obtaining the ICS pressure ( $C_1, C_2, C_3, C_4, C_5$ )=(2.6, 2.6, 2.6, 2.5, 0.43) and shape ( $x_{tip}, D_1, D_2$ )=(0.084, -0.47, -0.15) fitting parameters (see Fig. 3.12). Following the initial evaluations, 3-level, full factorial



(a) Pressure distribution of undeformed baffle. (b) Deformed baffle under pressure loading from undeformed baffle.

Figure 3.12: Comparison of approximations and actual shape/pressure.

design of experiments ( $3^5=243$  structure evaluations and  $3^3=27$  flow evaluations) are conducted to generate training points for the fluid and structure surrogate models. Bounds of the fitting parameters (see Table 3.8) are based on percent changes of the ICS solution to provide a variety of shapes and pressure distributions in the **C-S** region where the USI solution should occur. For the hardware used (standard workstation, 1CPU and 2CPU for the structure and fluid solvers, respectively), the average computational cost of each fluid evaluation is approximately 6 min (670 solution increments) and the cost of performing a single structural analysis consisting of all 243 simulations (after [140]) is 2 min (one solution increment). Thus the total serial computational time required to generate all data is 164 min ( $I^f=18,090$ ,  $I^s=243^{10}$ ).

<sup>10</sup>Number of copies of the structure in the single batch analysis (243) multiplied by the number of solutions increments for that analysis (1).

Table 3.8: Surrogate model input bounds of pressure coefficient and shape fitting parameters for deformable baffle.

Pressure Coefficient		Shape	
Fitting Parameter	Bounds	Fitting Parameter	Bounds
$C_1$	1.5 - 3.5	$x_{tip}$ (m)	0.05 - 0.1
$C_2$	1.6 - 3.7	$D_1$	-0.66 - -0.19
$C_3$	1.6 - 3.7	$D_2$	-0.21 - -0.059
$C_4$	1.5 - 3.6		
$C_5$	0.3 - 0.7		

Using the structure evaluations, cubic RBF surrogate models are developed relating each shape fitting parameter  $S_i$  to the pressure coefficient fitting parameters  $C_1$ - $C_5$ :

$$S_i = \sum_{j=1}^{243} w_{i,j}^s \|q_\infty \mathbf{C} - q_\infty \mathbf{C}_j\|_2^3 + \gamma_i^s \cdot \{q_\infty \mathbf{C}, 1\} \quad \forall i = 1, \dots, 3. \quad (3.51)$$

Similarly, using the fluid evaluations, cubic RBF surrogate models are developed relating each pressure coefficient fitting parameter  $C_i$  to the three shape fitting parameters:

$$C_i = \sum_{k=1}^{27} w_{i,k}^f \|\mathbf{S} - \mathbf{S}_k\|_2^3 + \gamma_i^f \cdot \{\mathbf{S}, 1\} \quad \forall i = 1, \dots, 5. \quad (3.52)$$

The combination of the three structure surrogate models and the five fluid surrogate models creates a system of eight nonlinear algebraic equations, which is solved using fixed point iteration, obtaining the USI solution. Evaluating the Jacobian (not shown for brevity) for the system of eight nonlinear equations at the center of the  $\mathbf{C}$ - $\mathbf{S}$  space for the surrogate input bounds results in a determinant of -2.04, indicating that the solution is unique. The USI solution is then used as an input to perform

a final structure and fluid evaluation, obtaining the USiS solution. As shown in Table 3.9, the shape and pressure fitting parameters from the USI and USiS solutions do not change significantly (largest change is 7%), indicating the surrogate models are accurate in this region of **C-S** space.

Table 3.9: Pressure and shape fitting parameters for deformable baffle example.

<b>Fitting Parameter</b>	<b>FSI (Reference)</b>	<b>USI</b>	<b>USI Error (%)</b>	<b>USiS</b>	<b>USiS Error (%)</b>
(Shape Fitting Parameters)					
$x_{tip}$ (m)	0.0678	0.0666	-1.82	0.0666	-1.82
$D_1$	-0.364	-0.356	-2.20	-0.356	-2.20
$D_2$	-0.0782	-0.0693	-11.3	-0.0706	-9.78
(Pressure Coefficient Fitting Parameters)					
$q_\infty C_1$ (Pa)	1245	1241	-0.299	1229	-1.257
$q_\infty C_2$ (Pa)	1249	1246	-0.217	1234	-1.197
$q_\infty C_3$ (Pa)	1246	1238	-0.603	1227	-1.495
$q_\infty C_4$ (Pa)	1038	1028	-0.952	1016	-2.099
$q_\infty C_5$ (Pa)	226	228	1.094	211	-6.71

Since the **C-S** space for this problem is 8D, it is not possible to fully visualize the intersection of the surrogate models. Forrester in [58] demonstrated how part of a multi-dimensional space could be visualized, specifically for surrogate models built from DOE results by creating a scatterplot matrix of surface plots. For a given model response, Forrester varied two design variables of a surrogate model while holding all other variables constant, generating a surface plot for each combination of design variables. In this work, Forrester’s method is utilized to generate scatterplot

matrices of surface plots for the fitting parameters. For fluid surrogate models, each combination of two shape fitting parameters are varied while all other shape fitting parameters are held constant at the USI solution, generating surface plots of the corresponding pressure coefficient fitting parameter (vice-versa for plots with the structure surrogate models). As shown in Figure 3.13 and 3.14, scatterplot matrices for  $x_{tip}$  and  $q_\infty C_1$ , respectively<sup>11</sup>, the USI solution is in a smooth region of the **C-S** space suggesting that it is easily found using fixed-point iteration.

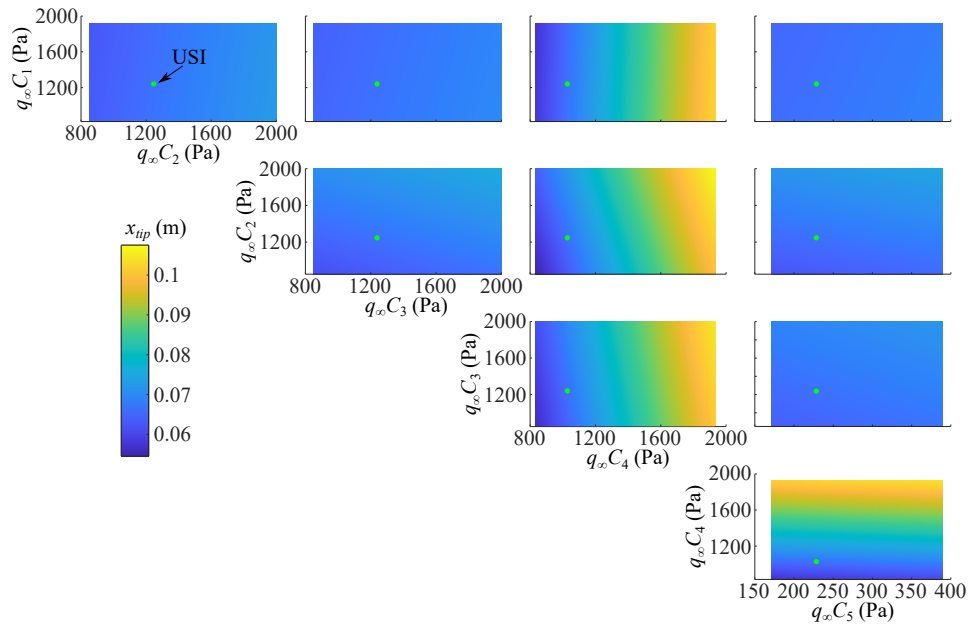


Figure 3.13: Scatterplot matrix of  $x_{tip}$  contours for all combinations of pressure fitting parameters along with the USI solution.

To verify the uncoupled solution, an FSI analysis is conducted until the baffle reaches a steady, equilibrium configuration (same computational resources as uncoupled method). Shape and pressure coefficient fitting parameters are extracted from

<sup>11</sup>Similar figures for the other fitting parameters are found in Appendix C

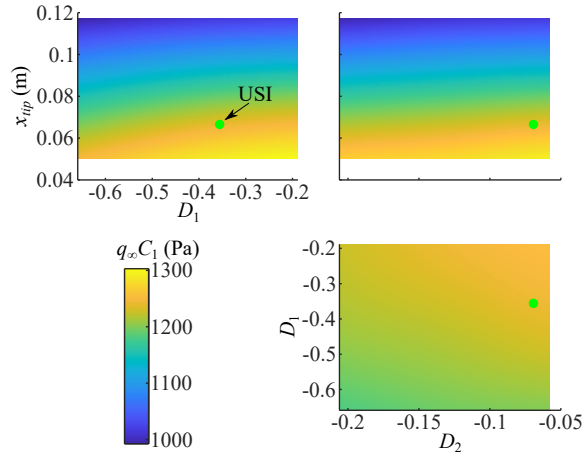


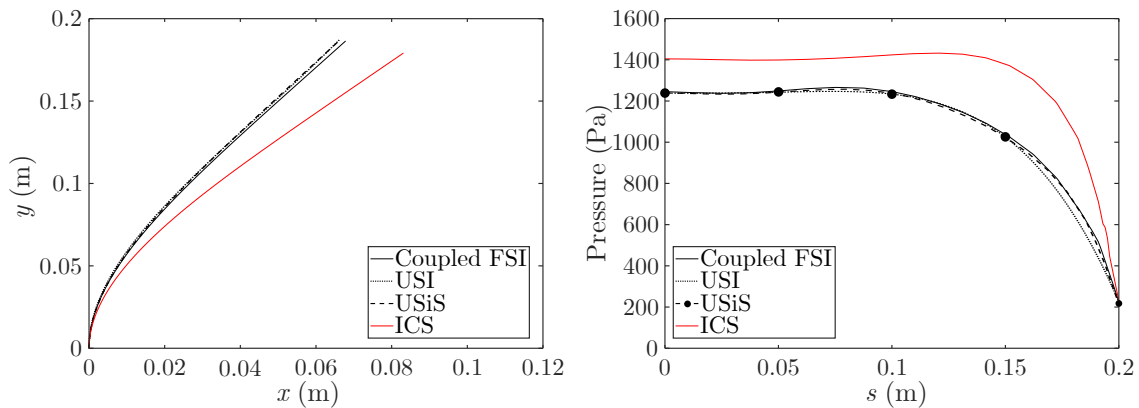
Figure 3.14: Scatterplot matrix of  $q_\infty C_1$  contours for all combinations of shape fitting parameters along with the USI solution.

the final structure/fluid configuration (see Table 3.9). The time span analyzed is 3 s with a base time step of 0.0005 s in the fluid solver and 0.00005 s in the structure solver. The computational cost of the FSI analysis is approximately 3 hr ( $I^f=6,000$ ,  $I^s=42,000$ ), thus the uncoupled method is slightly faster for a single design. Since the uncoupled method requires three times more fluid solution increments than FSI analysis, this computational savings is attributed to the significant amount of structure solution increments performed during the FSI analysis. Note that if fluid evaluations are parallelized, then the uncoupled method becomes significantly faster. As seen in Fig. 3.15(a), the deformed baffle shape and pressure distribution from the steady, equilibrium configuration of the FSI solution is of similar value and shape to both uncoupled SAA solutions (tip deflection error of 2.2%), demonstrating that the uncoupled method accurately solves aeroelastic problems even when both the shape and pressure are approximated. The average percent difference of the pressure and shape fitting parameters between the coupled and uncoupled methods is small (2.05% and 3.32% error for USI and USiS solutions, respectively), and taken to be

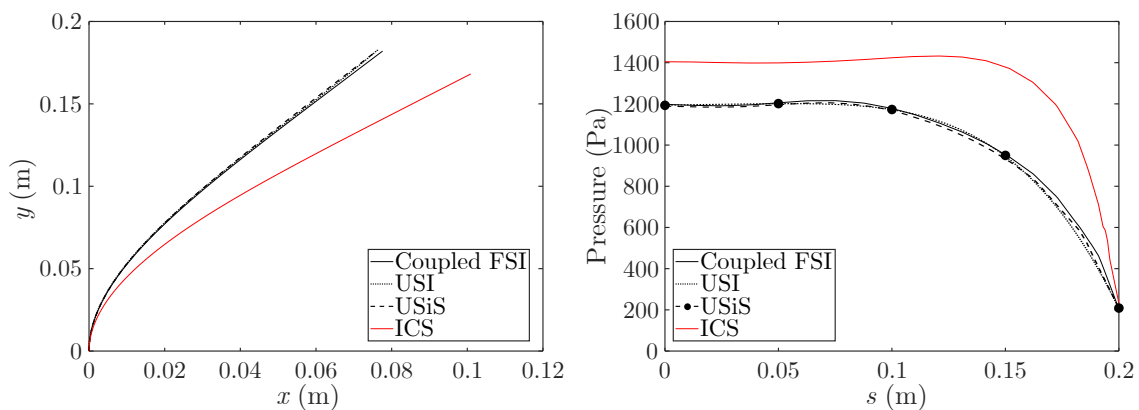
suitable to allow design studies. Additionally, as shown in Fig. 3.15(a), the ICS solution significantly overestimates the FSI solution. This is not surprising given that the structure ICS solution is calculated using the pressure distribution of the undeformed shape (ICS pressure solution) and does not account for the interaction between the structure and fluid domains (i.e., not a physically compatible solution).

To demonstrate the effectiveness of the uncoupled method in the context of iterative design, two new baffles having different material elastic modulus (0.8 GPa and 0.7 GPa) are analyzed. With the uncoupled scheme, only new structure evaluations are conducted (requires only 2 min to generate) for each new material selection while the fluid evaluations from the original baffle are retained. FSI analysis with the serial coupling scheme is also performed, each of which still requires 3 hr. As seen in Fig. 3.15, for the set of fluid evaluations used to generate Fig. 3.15, the uncoupled method accurately finds the SAA solution for the three baffles (2% error in tip deflection). Total serial computational runtime for the three uncoupled solutions (including surrogate model construction) is 168 min (3 structure and 18,090 fluid solution increments) while the computational cost for the three FSI solutions is 360 min (126,480 structure and 18,000 fluid solution increments).

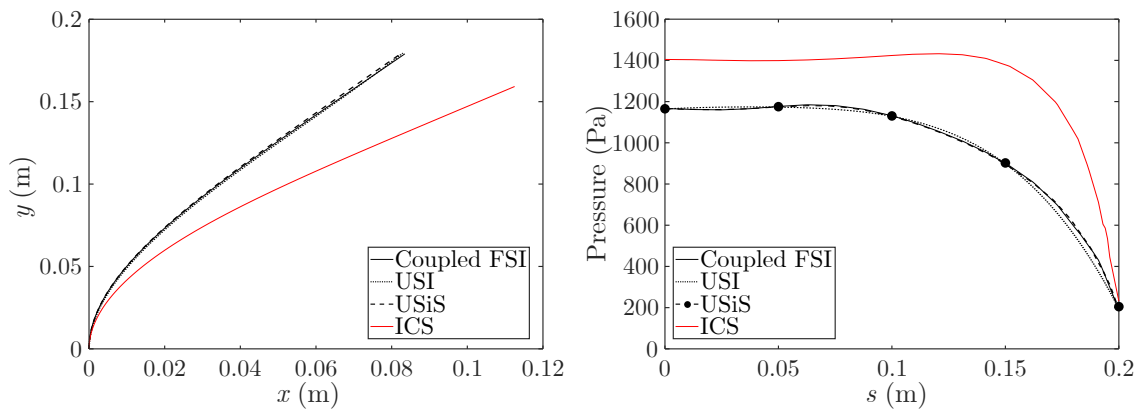
As a final demonstration with this example to show the utility of the uncoupled method, specifically how it is not dependent on the solvers used, SC/Tetra is replaced with Star-CCM+ as the fluid solver [142]. The geometry for the model in Star-CCM+ is generated in the same manner as the previous one. However, the mesh is more refined and turbulent effects are captured with the  $k-\epsilon$  turbulence model. Additionally, for each considered baffle configuration, implicit unsteady flow analysis is conducted instead of steady analysis. Figure 3.16 shows a sample flow result using Star-CCM+. A new 3-level full factorial design of experiment is performed with the fluid model while structure evaluations for the baffle with elastic modulus of 1 GPa



(a) Baffle with 1 GPa elastic modulus.



(b) Baffle with 0.8 GPa elastic modulus.



(c) Baffle with 0.7 GPa elastic modulus.

Figure 3.15: Coupled and uncoupled static aeroelastic results for deformable baffles having different elastic moduli (Single set of 27 fluid runs performed across all results).

are retained. Following the fluid evaluations, fluid surrogate models are constructed and the USI solution is obtained (see Table 3.10). Differences between this USI solution and the one obtained with SC/Tetra are not surprising since the mesh is more refined and different flow analysis is performed.

Table 3.10: USI solution for deformable baffle using Star-CCM+. Differences between solutions believed to be due to differences in mesh refinement and type of flow analysis performed. Note that the displacement values represent the solution of engineering interest.

<b>Fitting Parameter</b>	<b>Value With Star-CCM+</b>	<b>Value With SC/Tetra</b>
$x_{tip}$ (m)	0.067	0.0666
$D_1$	-0.36	-0.356
$D_2$	-0.0765	-0.0693
$q_\infty C_1$ (Pa)	1178	1241
$q_\infty C_2$ (Pa)	1181	1246
$q_\infty C_3$ (Pa)	1194	1238
$q_\infty C_4$ (Pa)	1054	1028
$q_\infty C_5$ (Pa)	228	252

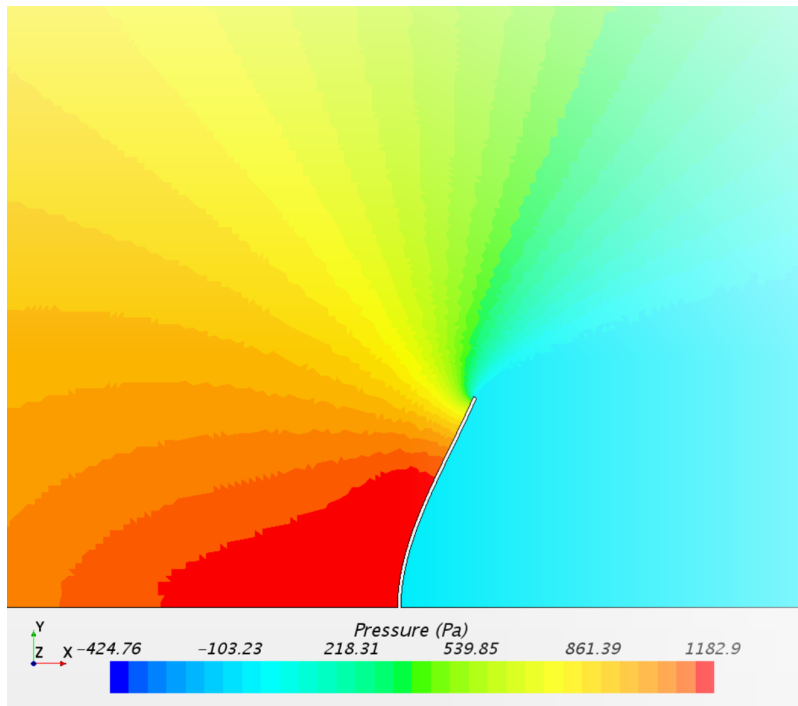


Figure 3.16: Sample pressure distribution of deformable baffle using StarCCM+.

## 4. EXTENSION OF UNCOUPLED METHOD AND OPTIMIZATION APPLICATION

Focus now shifts towards demonstrating two extensions of the uncoupled method: 1) finding SAA solutions at freestream conditions other than those used in fluid simulations for surrogate model construction and 2) prediction of dynamic loaded free response behavior and divergence. Additionally, this chapter implements the uncoupled method within an optimization framework.

### 4.1 Implementation and Demonstration of Uncoupled Method for Multiple Freestream Velocities

The implementation of the uncoupled method for finding SAA solutions at multiple freestream velocities is first addressed. To demonstrate this implementation, simple examples from the previous chapter that only considered a single freestream velocity are revisited.

#### *4.1.1 Solving Aeroelastic Problems for Multiple Freestream Velocities*

For the implementation of the uncoupled method for finding solutions at multiple freestream velocities, surrogate models are built in the same manner as before (Steps 1-5 in Uncoupled Method for SA analysis in Chapter 2). However, now freestream velocity  $v_\infty$  is allowed to be varied, changing  $q_\infty$  in the structure surrogate models. For each considered value of  $v_\infty$ , fixed point iteration is performed to find a new converged set of shape  $\mathbf{S}$  and pressure coefficient  $\mathbf{C}$  fitting parameters. If the converged set of fitting parameters lies within the input bounds of the surrogate models, then they are recorded as the USI solution for the current freestream velocity  $v_\infty$ . Model specific outputs are then calculated in the same manner as before (Eq. (3.26),

Eq. (3.27)). Final structure and fluid evaluations may be performed using the USI solution as inputs to obtain the USiS solution. Note that the fluid USiS solution can be used as a verification of the assumption of constant pressure coefficient distribution across multiple freestream velocities. This usage of the uncoupled method allows for SAA solutions to be obtained instantly for multiple freestream velocities so long as the USI solution remains within the bounds of the calibration points where the surrogate model is accurate. If using the serially coupled FSI scheme, obtaining solutions for multiple freestream conditions requires many coupled analyses (required for steady FSI analysis) or a single expensive coupled analysis in which the freestream conditions are slowly changed. Note that while large bounds on fitting parameter spaces allow for USI solutions to be obtained for a wide range of velocities, localized features of the fitting parameter response to increasing velocity may be missed. Method 4.1 and the accompanying flowchart (Fig. 4.1) summarize this usage of the uncoupled method for SAA at multiple freestream velocities.

Method 4.1: Computational process of uncoupled method for SAA for multiple velocities.

#### **Uncoupled Method for SAA for Multiple Velocities**

- 1) Perform Steps 1-5 of **Uncoupled Method for SAA**.
- 2) Make initial  $\mathbf{C}_1$  and chose starting  $v_\infty$
- 3) Do while  $\mathbf{C}_{g+1} - \mathbf{C}_g \leq tol_c$  and  $\mathbf{S}_g - \mathbf{S}_{g-1} \leq tol_s$ :
  - i) Solve  $\mathbf{S}_g = \mathcal{F}^s(q_\infty \mathbf{C}_g)$
  - ii) Solve  $\mathbf{C}_{g+1} = \mathcal{F}^f(\mathbf{S}_g)$
- 4) If converged set of  $\mathbf{S}_g$  and  $\mathbf{C}_{g+1}$  outside input bounds, stop; Otherwise continue
- 5) Set  $\mathbf{S}_{USI}(v_\infty) = \mathbf{S}_n$  and  $\mathbf{C}_{USI}(v_\infty) = \mathbf{C}_{g+1}$
- 6) Solve  $\mathbf{Y}_{USI}^f(v_\infty) = \mathcal{F}^{fo}(\mathbf{S}_{USI})$  (Eq. (3.26)) and  $\mathbf{Y}_{USI}^s(v_\infty) = \mathcal{F}^{so}(q_\infty \mathbf{C}_{USI})$  (Eq. (3.27))
- 7) Optional: Obtain  $\mathbf{S}_{USiS}(\mathbf{C}_{USI})$ ,  $\mathbf{C}_{USiS}(\mathbf{S}_{USI})$ ,  $\mathbf{Y}_{USiS}^f(\mathbf{S}_{USI})$ , and  $\mathbf{Y}_{USiS}^s(\mathbf{C}_{USI})$  from final structure and fluid evaluations
- 8) Increase  $v_\infty$ , return to Step 3 with  $\mathbf{C}_{USI}$  as initial guess

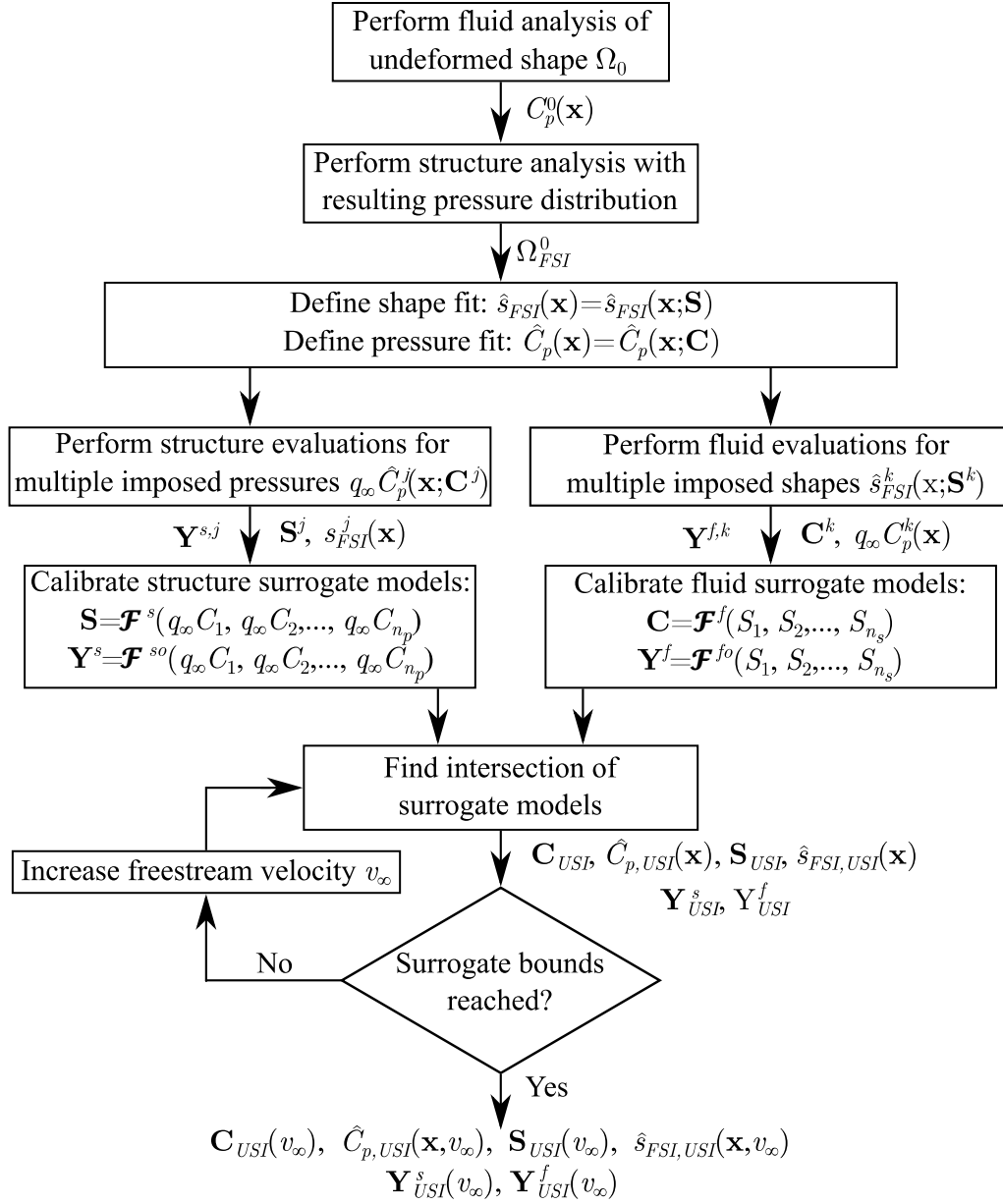


Figure 4.1: Flowchart of uncoupled method for finding SAA solutions at multiple freestream velocities (c.f. Fig. 3.3) [141]\*.

\*Figure 4.1 is reprinted with permission from “An Uncoupled Method for Fluid-Structure Interaction Analysis with Application to Aerostructural Design” by Scholten, W. and Hartl, D., 2020, *AIAA Scitech 2020 Forum*, 1635 [141], Copyright 2020 by The American Institute of Aeronautics and Astronautics, Inc..

This version of the extension is based on the previously discussed assumption that within a reasonable range of Reynold’s number  $\geq 10,000$  (i.e., well within an order of magnitude), the pressure coefficient distribution acting on a body in flow is approximately invariant with respect to Reynold’s number. An alternative for using the uncoupled method to solve aeroelastic problems at for multiple freestream velocities is to add the freestream flow velocity as a parameter that is varied along with shape fitting parameters during the fluid evaluations for surrogate model training. During surrogate model training, instead of calibrating models  $\mathbf{C} = \mathcal{F}^f(\mathbf{S})$ , models of the form  $\mathbf{C} = \mathcal{F}^f(\mathbf{S}, v_\infty)$  are calibrated which interpolate the pressure coefficient fitting parameters across  $\mathbf{S}$  and  $v_\infty$ . Note that Method 4.1 and Fig. 3.3 remain unchanged with the exception of fluid surrogate models  $\mathcal{F}^f$  and  $\mathcal{F}^{fo}$ . This version shall be considered in future work as it removes potential errors introduced by the assumption of a Reynold’s number-invariant pressure coefficient distribution with the cost of increasing surrogate model dimensionality by one.

#### 4.1.2 *Demonstration 1: Two Degree-Of-Freedom Discrete Pressure Baffle*

##### 4.1.2.1 *Original Two Degree-Of-Freedom Discrete Pressure Baffle\**

The first demonstration of the uncoupled method for finding SAA solutions at multiple freestream velocities, is the two degree-of-freedom discrete pressure baffle considered in Section 3.4.2. Note that fluid and structure evaluations are not reperformed. Instead, following the procedure in Section 4.1.1, the surrogate models previously developed in Section 3.4.2 (see (Eq. (3.46) and Eq. (3.47)), are solved using fixed-point iteration for multiple freestream velocities  $v_\infty$  until surrogate bounds are reached. Figure 4.2 shows the pressure and shape fitting parameters of the USI solu-

---

\*Work in this section is reprinted with permission from “An Uncoupled Method for Fluid-Structure Interaction Analysis with Application to Aerostructural Design” by Scholten, W. and Hartl, D., 2020, *AIAA Scitech 2020 Forum*, 1635 [141], Copyright 2020 by The American Institute of Aeronautics and Astronautics, Inc..

tion for each considered freestream velocity. Note that if using a serial FSI scheme, each considered freestream velocity would require a new and expensive FSI analysis while the uncoupled method obtains aeroelastic solutions for multiple flow conditions within seconds.

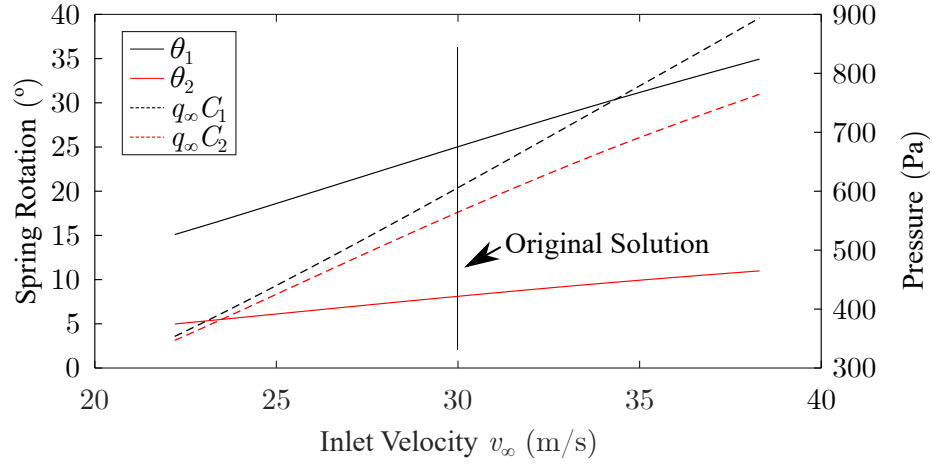


Figure 4.2: Fitting parameters versus freestream velocity for the two plate/bar assembly.

#### 4.1.2.2 Two Degree-Of-Freedom Discrete Pressure Baffle Based on Wind Tunnel Model

To serve as a possible future experimental validation of both the computational solvers and the uncoupled method, a wind tunnel model of the two degree-of-freedom discrete pressure baffle is in development (see Fig. 4.3). The model is comprised of both aluminum and stainless steel components. Both circular plates have a radius of 7.62 cm and thickness of 6.35 mm. The top and bottom support bars have lengths of 20 cm and 25 cm respectively. Each bar/plate is supported by two torsional springs

in series. The effective torsional stiffnesses of the springs in series  $K_1$  and  $K_2$  are assumed to be 3 N-m/rad and 0.6 N-m/rad, respectively. The top series of springs have an undeformed rotation of  $\theta_2=-40^\circ$  but are mechanically stopped at  $\theta_2=-16^\circ$  to avoid contact between the bottom plate and top support bar.

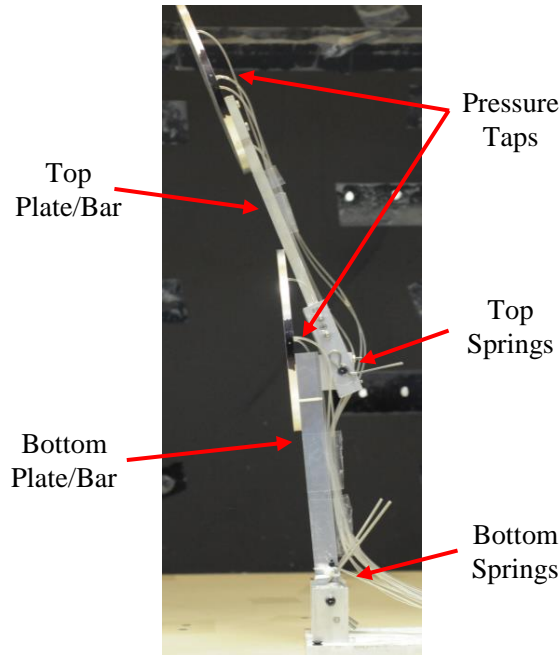


Figure 4.3: In-development wind tunnel model of the two degree-of-freedom discrete pressure baffle.

New structure and fluid models are developed to match the geometry of the wind tunnel model. With the exception of the geometry, the fluid and structure models of this baffle are identical to the ones from the previous design. The mesh parameters are also the same, resulting in a fluid model that is meshed with 2,600,000 elements (2,000,000 tetrahedron and 600,000 prism). The weight of the model, friction, and contact between the bars/plates are currently neglected as the wind tunnel model is

still in development. Additionally, due to the larger plate size, freestream velocity in both structure and fluid models is reduced to 15 m/s. Following the procedure in Section 4.1.1, ten level and six level full factorial DOEs of the fitting parameters are performed on the structure and fluid models, respectively. Bounds of the pressure coefficient fitting parameters in the structure DOE ( $C_1=0.01-1.25$ ,  $C_2=0.01-1.25$ ) are the same ones used for the first two degree-of-freedom discrete pressure baffle design (see Section 3.4.3). Lower bounds of the shape fitting parameters used in the fluid DOE define the undeformed shape while the upper bounds represent maximum rotation of the plates before the structure comes into contact with the floor ( $\theta_1=0^\circ-60^\circ$ ,  $\theta_2=-16^\circ-45^\circ$ ). The computational cost using a standard workstation (1CPU and 2CPU for the structure and fluid solvers, respectively) for each fluid evaluation and a single structure evaluation with all pressure distribution fits are 120 min and 3 min, respectively.

Following the many structure and fluid evaluations, linear RBF surrogate models (see Eq. (3.46) and Eq. 3.47)) are calibrated and USI solutions are obtained using fixed point iteration for many freestream velocities. As an initial verification of the USI solution, USiS solutions are computed. Figure 4.4 shows the shape and pressure fitting parameters with respect to freestream velocity. The serial computational cost to obtain all of these results is approximately 72 hr. Note that, with the expensive fluid evaluations complete, USI solutions for other spring stiffnesses can be obtained for a significantly cheaper cost (3 min). With the exception of  $\theta_2$ , the response of the fitting parameters with respect to freestream velocity is similar to the response of the parameters from the original geometry (see Fig. 4.2). At low freestream velocities, the pressure loading is insufficient to overcome the restoring force of the top torsional spring, resulting in an approximately constant  $\theta_2$  till  $\approx 8$  m/s.

As an initial verification of the USI solution, USiS solutions for the structure

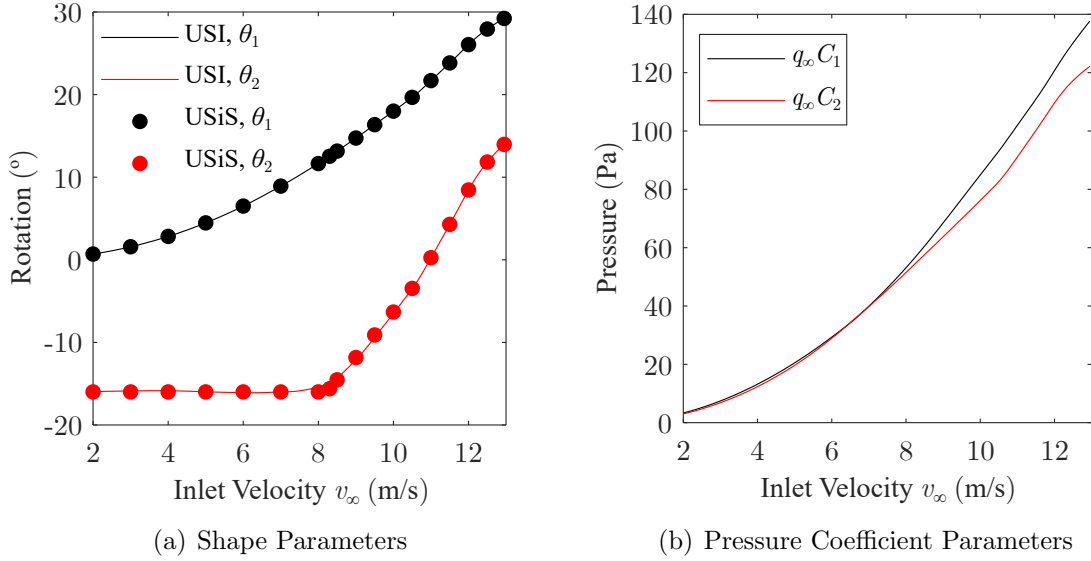


Figure 4.4: Uncoupled solutions versus velocity of wind tunnel model two degree-of-freedom discrete pressure baffle.

are computed. As shown in Fig. 4.4, the USI and USiS solutions of the shape fitting parameters are approximately equal (generally less than 1% difference) for all freestream velocities. The largest discrepancy between the two solutions is between 8 m/s and 8.5 m/s with a maximum difference of 5.6% for  $\theta_2$ . Based on the USiS solution, at a freestream velocity of 8.3 m/s, the pressure loading on the top plate overcomes the restoring force of the spring, resulting in a discontinuous change in the  $\theta_2$  with respect to  $v_\infty$ . Such a feature may be missed if the bounds of the training points for the surrogate model are too large. To demonstrate this, a structure DOE is performed with bounds of  $C_1=0.02-2.2$  and  $C_2=0.02-2.2$ , and new USI and USiS solutions are computed. As shown in Fig. 4.5, the difference between the USI and USiS solutions increases significantly (22% at 8.3 m/s). Additionally, the USI solution predicts that pressure loading on the top plate overcomes the spring restoring force much sooner, clearly demonstrating how large DOE bounds can cause the uncoupled

method to miss localized features.

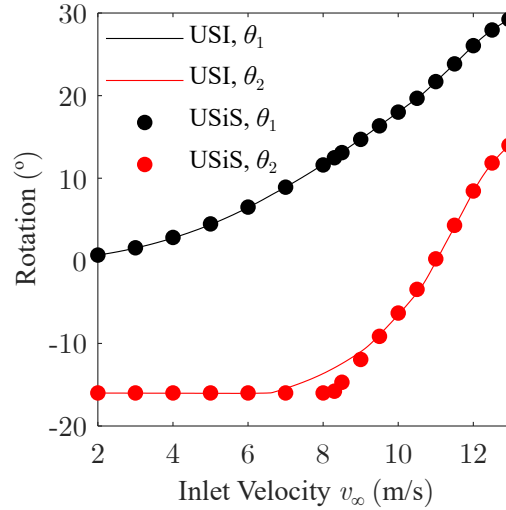
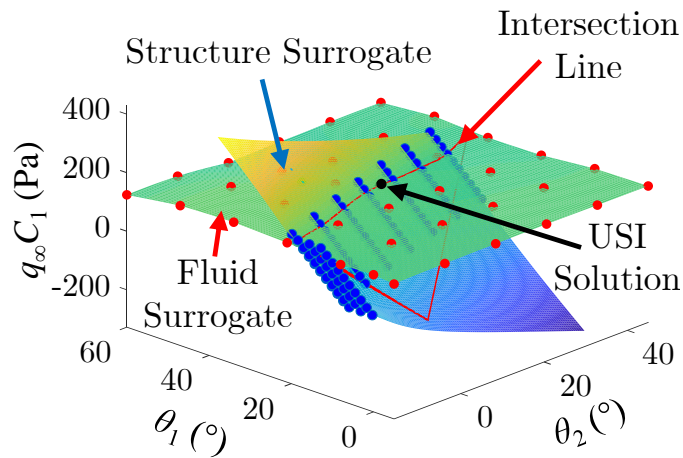


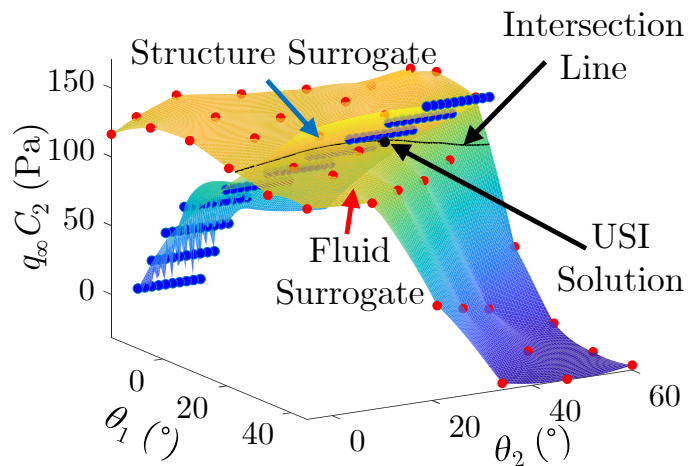
Figure 4.5: Uncoupled solutions versus velocity of wind tunnel model two degree-of-freedom discrete pressure baffle with larger structure DOE bounds.

Another interesting result for this demonstration problem is that bounds of the surrogate models are not reached. Instead, fixed point iteration fails to converge for freestream velocities above 13 m/s. Additionally, as this velocity is approached the number of iterations required for the fixed point iteration method to converge to a USI solution increases exponentially. Examination of the  $q_\infty C_2 - \theta_1 - \theta_2$  space at a freestream velocity of 13 m/s (see Fig. 4.6) shows that the USI solution is near a region of the space with a large gradient. Note, that this gradient is due to top plate becoming completely enveloped in the wake off of the bottom plate. While solutions to the nonlinear system of equations created by the surrogate models may exist for freestream velocities above 13 m/s, the large gradient may be causing the fixed point iteration to fail, presenting a limitation of the current implementation of

the uncoupled method. For higher dimensional problems, examination of scatterplot matrices such as those in Section 3.4.4, may reveal if such gradients exist and if the USI solution is near them.



(a) Intersection of surrogate models in  $q_\infty C_1 - \theta_1 - \theta_2$  space.



(b) Intersection of surrogate models in  $q_\infty C_2 - \theta_1 - \theta_2$  space

Figure 4.6: Visualization of structure and fluid surrogate model intersection at 13 m/s for wind tunnel model of two degree-of-freedom discrete pressure baffle.

### 4.1.3 Demonstration 2: Continuously Flexible Baffle

For a second demonstration of this implementation of the uncoupled method, the flexible baffle problem of Section 3.4.4 is revisited. Using the previously developed five fluid Eq. (3.52) and three structure Eq. (3.52) surrogate models for the baffle with an elastic modulus of 1 GPa, freestream velocity is modified, changing  $q_\infty$  in the structure surrogate models. For each considered freestream velocity, fixed point iteration is performed to find new USI solutions within seconds. Additionally, for multiple freestream velocities up to 39 m/s, the USI solutions are used as inputs to perform final structure and fluid evaluations, obtaining the USiS solution. As shown in Fig. 4.7 and Fig. 4.8, the USI and USiS solutions are almost identical, indicating that the surrogate modeling predictions are physically meaningful for a variety of freestream velocities and that the assumption Reynold's number invariant pressure coefficient distribution is valid.

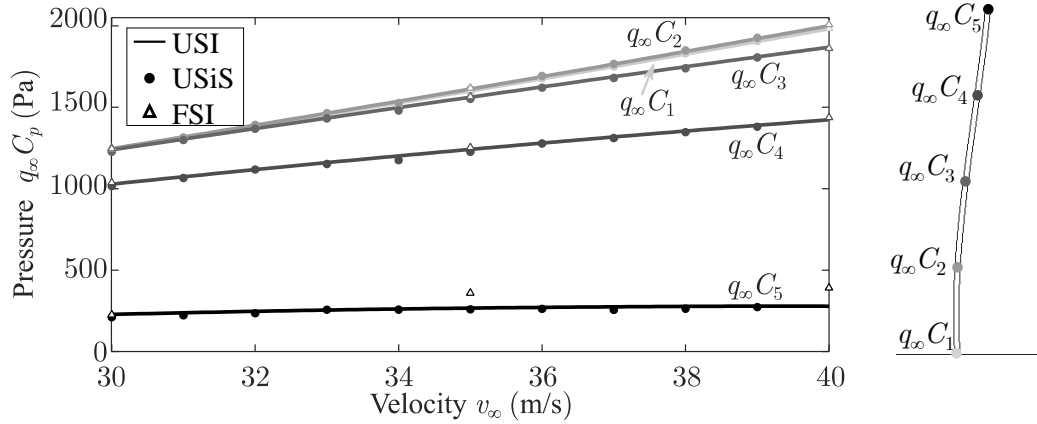


Figure 4.7: Pressure field over the for deformable baffle under multiple flow velocities (Single set of fluid/structure runs for all uncoupled results).

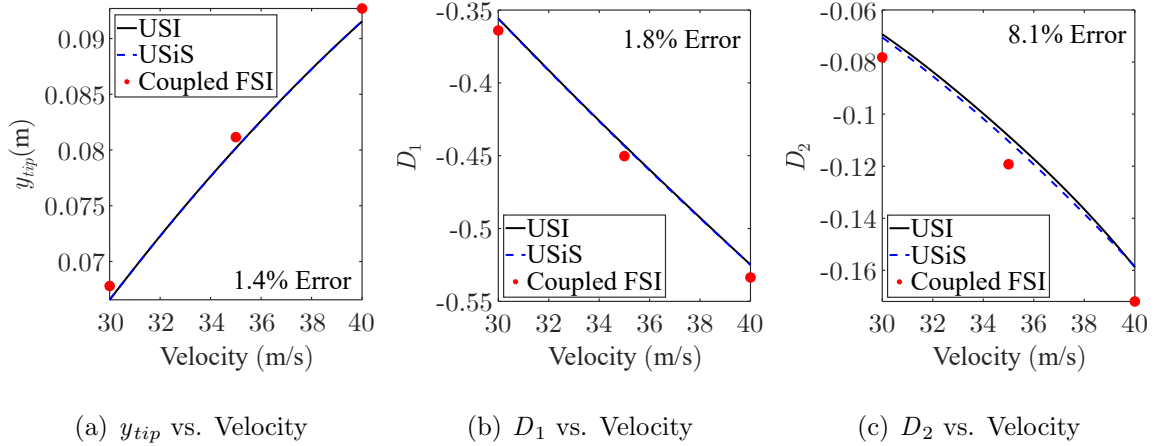


Figure 4.8: Shape fitting parameters (in pressure) for deformable baffle under multiple flow velocities (Single set of fluid/structure runs for all uncoupled results). Average percent error between USiS and FSI solutions also shown.

To provide further verification of the uncoupled solutions, new FSI analyses are conducted for flow velocities of 35 m/s and 40 m/s, each of which requires 3 hr to perform (standard workstation, 2CPU and 1CPU for the fluid and structure solvers, respectively). Shape and pressure coefficient fitting parameters are extracted from the final structure/fluid configuration. As seen in Fig. 4.7 and Fig. 4.8, with the exception of  $C_5$ , the fitting parameters extracted from the FSI solutions are of similar value to the uncoupled solutions, demonstrating that the uncoupled method accurately solves an aeroelastic problem for multiple freestream velocities. Recall that fitting parameter  $C_5$  corresponds to the net pressure at the tip of the baffle. The error between the coupled and uncoupled solutions is attributed to inadequate mesh resolution around the tip of the baffle resulting in discrepancies between the steady and transient fluid domains. As shown in Fig. 4.8, the average percent error between the USiS and FSI solutions are of similar value to those observed in Section 3.4.4, indicating that the extrapolation of freestream velocities to find many uncoupled

solutions is not introducing significant error. Overall, the average percent difference of the shape and pressure fitting parameters between the coupled solution and both uncoupled methods for the three flow velocities is quite small (approximately 4% error). With regards to computational time, the uncoupled method is significantly more efficient. For the 164 min serial (or 25 min parallel) computational cost to generate training data for the surrogate models, the uncoupled method accurately calculates SAA solutions for many freestream velocities. Additionally, if the stiffness of the material is modified (as done in Section 3.4.4), uncoupled solutions for a number of freestream velocities are quickly obtained by performing new static structure evaluations (computational cost of 2 min for the one solution increment). With the legacy serial coupling scheme, a 3 hr long analysis would be required for each stiffness and freestream velocity.

#### 4.1.4 *Demonstration 3: Aeroelastic Pitch-Plunge Wing*

The final demonstration for this implementation of the uncoupled method considers a simple two-dimensional aeroelastic wing based on the work of Hodges, et al. [1], for which an analytical solution exists. Shown in Fig. 4.9, the wing is a rigid body having a NACA0012 airfoil supported by springs for pitch and plunge with stiffnesses  $K_\theta$  and  $K_h$ , respectively. Note that the spring rotation  $\theta$  is measured relative to the initial unloaded angle of attack  $\alpha_0$  such that  $\alpha = \theta + \alpha_0$ . The unstretched length of the plunge spring  $h_0$  is set to zero. Assuming steady-flow theory, the lift is

$$L = C_{l\alpha} \rho b l v_\infty^2 \alpha, \quad (4.1)$$

where  $b$  is the half-chord,  $l$  is the span, and  $C_{l\alpha}$  is the lift-curve slope. The moment at quarter-chord is also assumed to be zero. The resulting static problem is represented

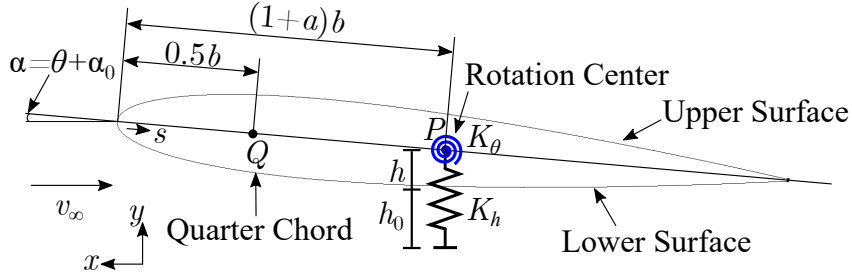


Figure 4.9: Schematic of aeroelastic wing example.

by the following equations:

$$\begin{bmatrix} C_{l\alpha}\rho lb^2v_\infty^2\alpha_0 \\ -C_{l\alpha}(\frac{1}{2} + a)\rho lb^2v_\infty^2\alpha_0 \end{bmatrix} + \begin{bmatrix} b^2K_h & C_{l\alpha}\rho lb^2v_\infty^2 \\ 0 & K_\theta - C_{l\alpha}(\frac{1}{2} + a)\rho lb^2v_\infty^2 \end{bmatrix} \begin{bmatrix} h/b \\ \theta \end{bmatrix} = \begin{bmatrix} 0 \\ 0 \end{bmatrix}. \quad (4.2)$$

where  $a$  is a dimensionless parameter for the location of the rotation center (point  $P$  in Fig. 4.9) of the wing,  $m$  is the mass,  $I_p$  is the moment of inertia about the rotation center, and  $h$  is the stretch of the spring for plunge.

Based on the static analytical solution, this aeroelastic wing undergoes divergence (spring rotation and stretch tends toward infinity) when  $K_\theta - C_{l\alpha}(\frac{1}{2} + a)\rho lb^2v_\infty^2 = 0$ ; thus, the divergence velocity  $v_D$  is

$$v_D = \frac{1}{b} \left( \frac{K_\theta}{C_{l\alpha}(\frac{1}{2} + a)\rho l} \right)^{\frac{1}{2}}. \quad (4.3)$$

For this demonstration, an airfoil with chord of 1 m and span of 0.01 m in flow with density of 1.206 kg/m<sup>3</sup> is used. Prior to performing any fluid or structure analyses, configuration parameters from Hodges ( $a = -0.2$ , assumed  $C_{l\alpha} = 2\pi$ , ratios of stiffness properties) are used to calculate the required values of the mass and stiffness

properties for the airfoils  $K_h=13.6395$  N/m,  $K_\theta=5.1148$  N-m/radian,  $m=0.1894$  kg, and  $I_p=0.0114$  kg/m<sup>2</sup> such that the divergence velocity is 30 m/s. These values are used in the structural and fluid models for this demonstration of the uncoupled method. As with previous examples, Abaqus and SC/Tetra are used as the structure and fluid solvers respectively.<sup>1</sup>

The structural model (Fig. 4.10(a)) consists of a 0.01 m wide rigid body for the outer mold line of the wing and two spring elements, one for pitch, the other for plunge. The outer mold line of the wing is meshed with 1,025 evenly distributed rigid body elements and is one element wide in the  $z$  direction. Static analysis evaluates the stretch and rotation of the springs supporting the wing under pressure loadings  $q_\infty C_p^u(\mathbf{x})$  and  $q_\infty C_p^l(\mathbf{x})$  applied to the upper and lower surfaces of the wing, respectively. Note that the structural model could be simplified to the analytical solution by integrating the applied pressure distribution over both surfaces into a lifting force applied at quarter chord.

The fluid model (see Fig. 4.10(b)) is a 10 m by 10 m by 0.01 m fluid domain centered about the wing. As before, incompressible air with density of 1.206 kg/m<sup>3</sup> and viscosity of  $1.83 \times 10^{-5}$  Pa-s is used. Inlet (freestream) conditions of 20 m/s horizontal velocity are applied to the left face while the right face is given an outlet boundary condition of zero static pressure. Additionally, inlet turbulence is set to default values ( $k=0.0001$  m<sup>2</sup>/s<sup>2</sup> and  $\varepsilon = 0.0001$  m<sup>2</sup>/s<sup>3</sup>). The surface of the wing is given smooth wall conditions. For each deformed configuration, a new fluid model is generated by displacement and rotation of the wing. The model is meshed with 174,000 elements (137,000 prism and 37,000 hexahedron), and is one element wide in the  $z$  direction for pseudo two-dimensional flow. Mesh sizes range from 0.125 m

---

<sup>1</sup>Clearly the structural problem consists merely of a simple sum of moment and forces on a rigid body and could be solved analytically; the use of Abaqus is compatible with the tool and work flow development goals of this effort.

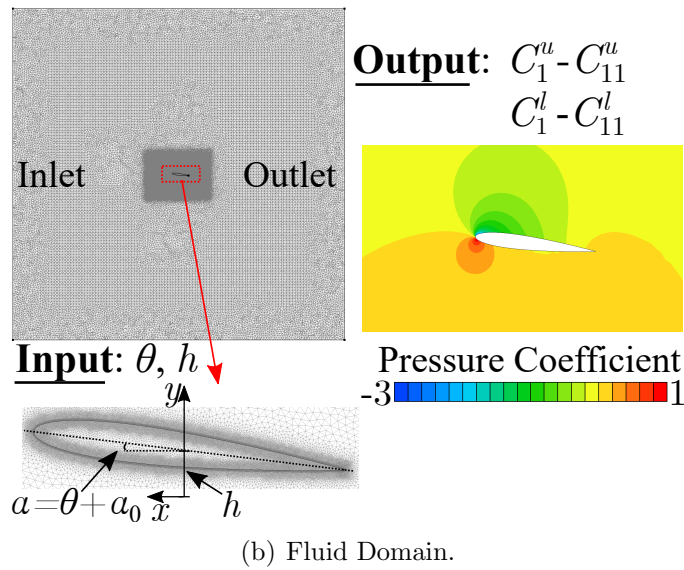
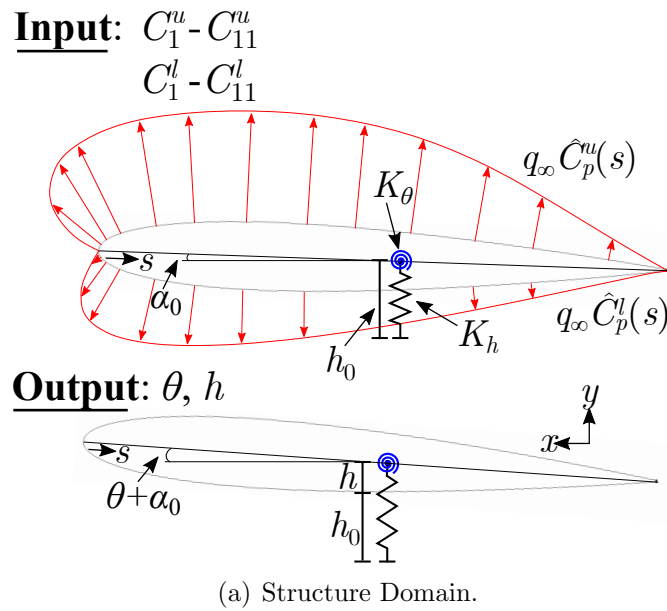


Figure 4.10: Structure and fluid domain models for aeroelastic wing example.

at far field to 0.00195 m near the wing (see Appendix D for the mesh study). Steady flow analysis is conducted for each wing configuration and the resulting pressure distribution is recorded.

Based on exploratory CFD analyses of the wing at different angles of attack, the

pressure coefficient distribution acting on the wing is approximated with fits  $\hat{C}_p^u$  and  $\hat{C}_p^l$ , for the upper and lower surfaces, respectively, each constructed from 11 pressure coefficient fitting parameters such that  $\mathbf{C}^u = C_1^u, \dots, C_{11}^u$  and  $\mathbf{C}^l = C_1^l, \dots, C_{11}^l$ . Note that a fit of the change in pressure distribution between the upper and lower surfaces could be used instead, reducing the number of parameters to 11. However, to further test the uncoupled method with more fitting parameters, fits for the distributions of both surfaces are used. For this example, the fitting parameters are the pressure coefficients at discrete points along the chord of the wing. The fits for both pressure coefficient distributions are linear RBFs of the form

$$\hat{C}_p^u(s) = \sum_{i=1}^{11} w_i^u (s - s_i) \quad (4.4)$$

and

$$\hat{C}_p^l(s) = \sum_{i=1}^{11} w_i^l (s - s_i), \quad (4.5)$$

where  $s$  is distance along the chord,  $s_i$  is the location along the chord of the wing for each training point, and  $w_i^u$  and  $w_i^l$  are weights solved during training of the RBFs by solving the system of linear equations:

$$\begin{bmatrix} C_1^u \\ \vdots \\ C_{11}^u \end{bmatrix} = \begin{bmatrix} \|s_1 - s_1\|_2 & \cdots & \|s_1 - s_{11}\|_2 \\ \|s_2 - s_1\|_2 & \cdots & \|s_2 - s_{11}\|_2 \\ \vdots & \vdots & \vdots \\ \|s_{11} - s_1\|_2 & \cdots & \|s_{11} - s_{11}\|_2 \end{bmatrix} \begin{bmatrix} w_1^u \\ \vdots \\ w_{11}^u \end{bmatrix} \quad (4.6)$$

and

$$\begin{bmatrix} C_1^l \\ \vdots \\ C_{11}^l \end{bmatrix} = \begin{bmatrix} \|s_1 - s_1\|_2 & \cdots & \|s_1 - s_{11}\|_2 \\ \|s_2 - s_1\|_2 & \cdots & \|s_2 - s_{11}\|_2 \\ \vdots & \vdots & \vdots \\ \|s_{11} - s_1\|_2 & \cdots & \|s_{11} - s_{11}\|_2 \end{bmatrix} \begin{bmatrix} w_1^l \\ \vdots \\ w_{11}^l \end{bmatrix} \quad (4.7)$$

As seen Fig. 4.11 the fits match well to computational data and are sufficient for this demonstration.

Regarding the shape fit, since the wing is a rigid body supported by springs, the shape fitting parameters are simply the stretch of the spring for plunge and the rotation of the spring for pitch such that  $\mathbf{S}=(S_1,S_2)=(\theta,h)$ .

With the fits defined, multiple fluid and structure analyses are performed to generate training points for the surrogate models of the shape and pressure coefficient fitting parameters. Bounds of the pressure coefficient fitting parameters for structure evaluations are in Table D.4 found in Appendix D. Since the wing is modeled in a relatively large fluid domain, the stretch of the spring has no effect on the pressure distribution and is thus eliminated from the surrogate models (i.e.,  $C_i=\mathbf{F}^f(\theta) \forall i=1,\dots,22$ ), significantly reducing the number of deformed shapes to consider. Thus, fifteen fluid evaluations are performed varying  $\theta$  from  $-2$  to  $12^\circ$  in  $1^\circ$  increments with an  $\alpha_0=0^\circ$  while stretch of the plunge spring is held constant. This range of angles of attack is chosen to provide a variety of pressure distributions that the RBF pressure fit must accurately approximate. Following each fluid evaluation, the pressure coefficient fitting parameters and the lift coefficient are extracted. For the hardware used in this work (standard workstation, 10CPU), the computational time for each fluid evaluation is approximately 25 min (1,170 solution increments). Based on the lift coefficients obtained from the evaluations of the wing, the lift-curve slope of the NACA0012 in this fluid model is approximately 6.0. Using Eq. (4.3), this lift

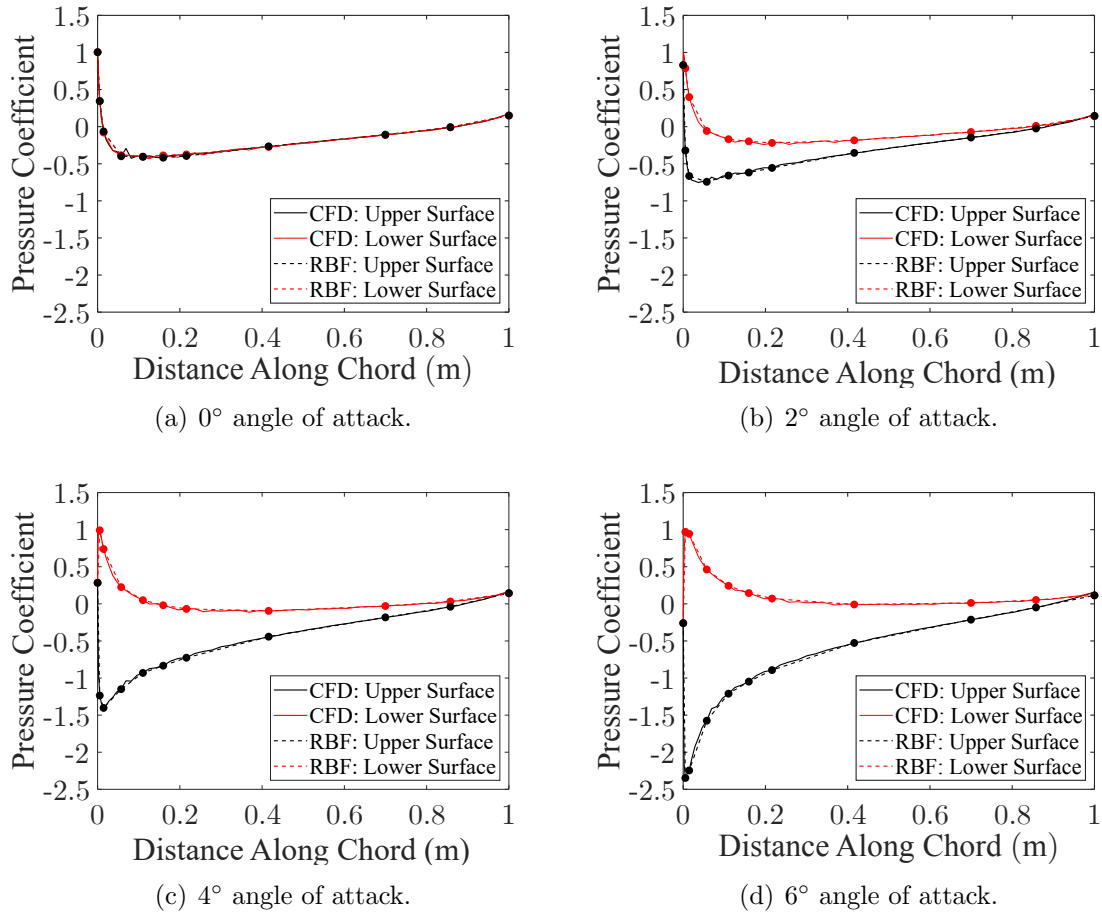


Figure 4.11: Comparison of CFD pressure coefficient distributions and RBF fits for aeroelastic wing example.

coefficient results in a divergence velocity of approximately 30.7 m/s.

In the structure domain, a Latin Hypercube Sampling (LHS) is performed with 220 variations ( $10 \times n_p$ ) of the pressure coefficient fitting parameters. Bounds of the LHS are set as double the percent difference between the pressure fitting parameters of the airfoil at  $2^\circ$  angle of attack and the minimum and maximum values of the pressure fitting parameters from the fluid evaluations.<sup>2</sup> This is deemed sufficient to

<sup>2</sup>If the resulting percent difference is less than 100%, then the bound is adjusted such that it is 100%.

consider a wide range of pressures that the structure may be subjected to for many flow velocities and initial angles of attack. A single structure analysis is performed with 220 copies of the airfoil, each subject to a different pressure loading; runtime is 5 min (standard workstation, 1CPU) with one structure solution increment. The resulting stretch and rotation of the springs for each airfoil is recorded. The total serial computational runtime required to perform the fluid and structural evaluations is 6.3 hr (parallelized time is 25 min) with  $I^f=17,550$  and  $I^s=220^3$ . Using the fluid and structure evaluations as training points, cubic RBF surrogate models for the fitting parameters (see Eq. (3.51) and Eq. (3.52)) are generated. Since rotation of the pitch spring  $\theta$  and angle of attack  $\alpha$  are related by  $\alpha=\theta+\alpha_0$ , the form of the fluid surrogate model is modified as follows:

$$C_i = \mathcal{F}^f(\theta) = \sum_{k=1}^{15} w_{i,k}^f \|\theta - \theta_k - \alpha_0\|^3 + \gamma_i^f \cdot \{\theta, 1\} \quad \forall i = 1, \dots, 22, \quad (4.8)$$

which enables USI solutions to be obtained for different values of  $\alpha_0$  *without* running further fluid and structure evaluations as long as the equivalent angle  $\alpha$  is within the bounds of the training points. Following the procedure described in Section 4.1.1, uncoupled solutions (both USI and USiS) are obtained for multiple freestream velocities at different set angles of attack ( $\alpha_0=0^\circ, 0.2^\circ, 1^\circ, 2^\circ$ ). Thus, for the one set of structure and fluid evaluations, which are performed for *one* freestream velocity and *one* set angle of attack, uncoupled solutions are obtained for multiple freestream velocities *and* set angles of attack (see Fig. 4.12). As shown in Fig. 4.12, the USI and USiS solutions are nearly identical, indicating that the pressure coefficient fit adequately approximates the actual distribution and that the surrogate models capture the relevant physical phenomenon. These results also suggest that the assumption

---

<sup>3</sup>Number of copies of the structure in the single batch analysis (200) multiplied by the number of solutions increments for that analysis (1).

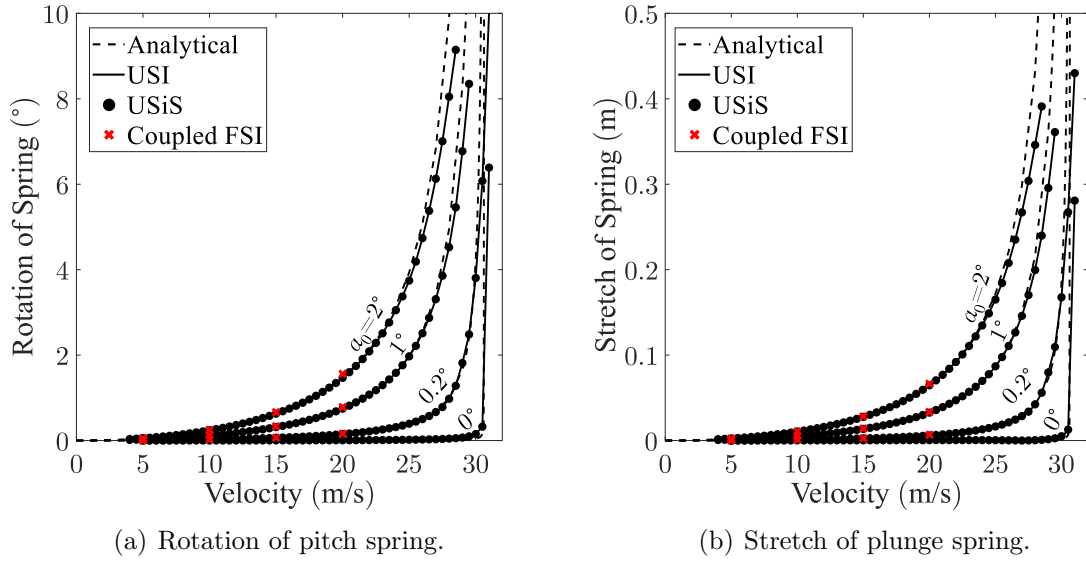


Figure 4.12: Comparison of uncoupled results with analytical and FSI results across multiple velocities and angles of attack.

of constant pressure coefficient distribution is valid for this problem. Additionally, the uncoupled results for all considered values of  $\alpha_0$  agree quite well with the static analytical solutions of Eq. (4.2). While the uncoupled solutions capture the asymptotic behavior observed in the analytical solution as divergence velocity (30.7 m/s) is approached, the uncoupled solutions slightly diverge from the analytical solution at higher flow speeds. This is attributed to the constant lift-curve slope in the analytical solution while the uncoupled solution, which uses a CFD solver for the fluid domain, may exhibit flow separation and thus a lower lift-curve slope at higher inlet velocities.

To further verify the uncoupled solutions, FSI analysis is performed on the wing at three different set angles ( $\alpha_0 = 0.2^\circ, 1^\circ, 2^\circ$ ) and four different flow velocities ( $v_\infty = 5, 10, 15, \text{ and } 20 \text{ m/s}$ ) with the same computational resources. Note that above 20 m/s, for the given stiffness and mass properties of the airfoil, eigenvalue analysis of the

analytical problem from Hodges [1] indicates that the airfoil exhibits flutter. Note that flutter behavior is a different aeroelastic phenomenon than static divergence which both the analytical and uncoupled solutions exhibit. In FSI analysis this flutter results in oscillations in rotation and stretch of the springs that grow in time. Uncoupled solutions in this velocity range represent the time averaged FSI solution. The significant motion of the wing makes FSI analysis difficult without an overset mesh scheme or a damping component to reduce the oscillations, and are thus not performed in this work. This flutter behavior is not observable from the current implementation of the uncoupled method which uses steady fluid and static structure evaluations, and motivates the development of an extension to the uncoupled method that may potentially predict the dynamic behavior (see Section 4.2).

Total computational time for each serially coupled FSI analysis is 15 s with a time step in both solvers of 0.001 s. Average stretch and rotation of the springs from the FSI results (see Fig. 4.12) match quite well with both the uncoupled and analytical solutions, indicating that the uncoupled method is accurate for this problem. Maximum error is 6%, occurring at 20 m/s for the 2° angle of attack case. The computational cost for each FSI analysis for a specific freestream velocity and initial set angle  $\theta_0$  is 12 hr ( $I^f=60,000$ ,  $I^s=15,000$ ) as compared to the serial 6.3 hr (or 25 min if parallelized) required by the uncoupled method for all solutions ( $I^f=17,550$ ,  $I^s=220$ ). Since the uncoupled method requires significantly less solution increments to find an aeroelastic solution, a significant portion of the computational time is associated with the model generation and post-processing of the training evaluations. Additionally, if other spring stiffnesses are considered, a new uncoupled solution only requires 5 min of computational time to solve the single structural evaluation ( $I^f=0$ ,  $I^s=220$ ), while the serial coupled scheme still requires 12 hr (144 times faster).

## 4.2 Free-Response Behavior and Divergence

Since the fluid and structure evaluations are conducted independently and static solutions are assumed for both, the uncoupled SAA method is unable to account for any oscillation of the structure, steady-state or otherwise.<sup>4</sup> This section introduces an extension to the uncoupled method that provides a means of estimating the dynamic free-response behavior of the structure in flow and predicting the velocity at which it may diverge using eigenvalue analysis. Using the resulting pressure distribution from the USI solution for a given problem, the USiS solution is obtained by conducting static analysis of the structural model. The static analysis of the structure solves the system  $[K(\mathbf{u}_s)]\mathbf{u}_s=\mathbf{F}$  where  $[K(\mathbf{u}_s)]$  is the total nonlinear stiffness matrix, which could depend on the steady displacement  $\mathbf{u}_s$ , and  $\mathbf{F}$  is the applied force (mechanical, aerodynamic, etc.). As a result of the aerodynamic loading and any other applied forces, the effective stiffness of the structure  $[K_{eff}]$  becomes

$$[K_{eff}] = [K(\mathbf{u}_s)] - [K_A] \quad (4.9)$$

where  $[K_A]$  is an aerodynamic stiffness matrix generated by the loading. The free response equation of motion for the structure (assuming no damping) about its steady-state, deformed configuration is

$$[M]\ddot{\mathbf{u}} + [K_{eff}]\mathbf{u} = \mathbf{0} \quad (4.10)$$

where  $[M]$  is the mass matrix. Assuming the displacement is harmonic and takes the

---

<sup>4</sup>Note that future implementations of the uncoupled SAA method may be able to create fits for the velocity and acceleration allowing for transient responses to be accounted for.

form  $\mathbf{u} = \phi e^{i\omega t}$ , the eigenvalue problem

$$([K_{eff}(\mathbf{u})] - \omega^2[M])\phi = \mathbf{0} \quad (4.11)$$

is formed and solved to find both the natural frequencies  $\omega$  of the deformed structure and the associated mode shapes  $\phi$ . Structural divergence occurs when the effective stiffness of the structure approaches zero such that natural frequency of the deformed structure also becomes zero.

As an extension to the uncoupled method, once a USiS solution has been found for a given freestream condition, the eigenvalue problem of Eq. 4.11 for the deformed structure is solved, allowing for the estimation of freestream conditions at which a structure undergoes aeroelastic divergence. Note that as surrogate bounds of the structural model are approached at high freestream velocities, static analysis may fail to converge to a USiS solution. If this occurs and the natural frequency appears to be decaying towards zero as velocity is increased, then the results of natural frequency versus velocity may be fit to a function  $\omega = f(v_\infty)$  from which an estimation of the divergence velocity  $v_{div}$  may be extrapolated. Note that this extrapolated value should only be considered as an upper bound for the true  $v_{div}$  which may lay somewhere between the extrapolated velocity and the highest freestream velocity for USiS solutions can be obtained. Additionally, a significant and sudden increase in the natural frequency may indicate aeroelastic divergence. This extension, summarized in Method 4.2, is called the uncoupled aeroelastic divergence prediction method. The method is demonstrated in the next chapter with the SCF application.

Method 4.2: Computational process of uncoupled method for SAA to finding divergence

<b>Uncoupled Aeroelastic Divergence Prediction Method</b>
1) Perform Steps 1-6 and Step 8 of Method 4.1
2) For each $q_\infty \mathbf{C}_{USI}$
ii) Perform structural analysis with $q_\infty \mathbf{C}_{USI}$
ii) Solve Eq. (4.11) using eigenvalue analysis
iii) Extract natural frequency $\omega$
3) Optional: Create function $\omega = f(v_\infty)$
4) Stop

### 4.3 Design Optimization with the Uncoupled Method\*

Focus now shifts towards describing the implementation of the uncoupled method in an optimization scheme and using it in a design problem.

#### *4.3.1 Optimization Framework Incorporating Uncoupled Method*

Figure 4.13 illustrates the proposed optimization framework incorporating the uncoupled method. Prior to conducting the optimization, a few initial structure and fluid analyses are performed for various reference designs  $\Omega_0$ , from which both the deformed shape and pressure distribution are extracted. Based on these results, a shape fit  $\hat{s}_{FSI}(\mathbf{x})$  (Eq. (3.2)) is defined that is fully described by two types of shape fitting parameters: 1)  $\mathbf{S}_s = \{S_{s,1}, \dots, S_{s,n_s,s}\}$ , parameters that are not constant between an undeformed and a deformed configuration (i.e., displacements or positions), and 2)  $\mathbf{S}_c = \{S_{c,1}, \dots, S_{c,n_s,c}\}$ , parameters that are constant between the undeformed and deformed configurations such as length and thickness. Note that the fitting parameters  $\mathbf{S}_c$  can also be included as design variables in an optimization scheme. Steady

---

\*Much of the work in this section is reprinted with permission from “An Uncoupled Method for Fluid-Structure Interaction Analysis with Application to Aerostructural Design” by Scholten, W. and Hartl, D., 2020, *AIAA Scitech 2020 Forum*, 1635 [141], Copyright 2020 by The American Institute of Aeronautics and Astronautics, Inc..

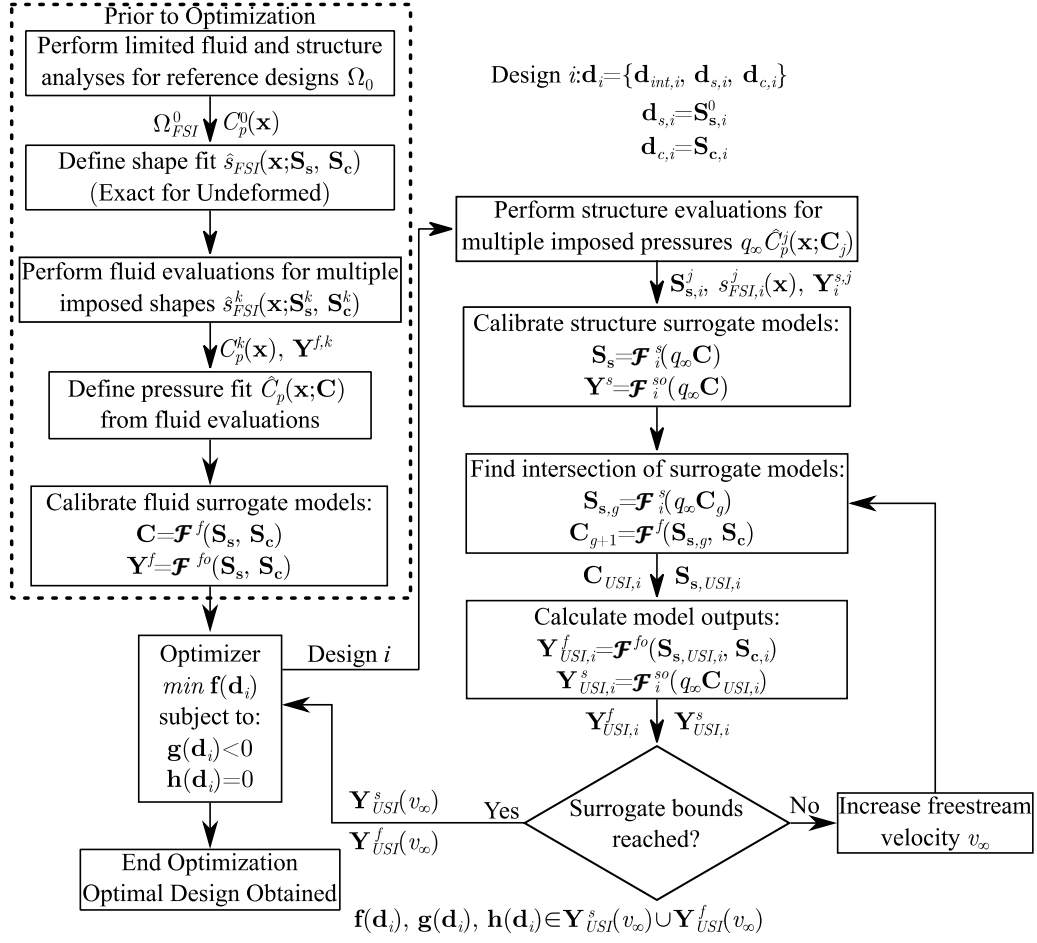


Figure 4.13: Flowchart of optimization incorporating uncoupled method implemented for SAA.

fluid analysis is conducted for  $m_s$  shapes  $\hat{s}_{FSI}^k(\mathbf{x}; \mathbf{S}_s^k, \mathbf{S}_c^k) \forall k = 1, \dots, m_s$  imposed in the fluid domain for a given flow condition from which the pressure coefficient distribution  $C_p^k(\mathbf{x})$  and model-specific responses  $\mathbf{Y}^{f,k}$  are extracted. Using the  $m_s$  shape fits, the pressure coefficient fit  $\hat{C}_p(\mathbf{x}; \mathbf{C})$  and number of fitting parameters  $C$  are defined (Eq. (3.4)). Surrogate models relating the pressure coefficient fitting parameters and model outputs to the shape fitting parameters (Eq. (3.14) and Eq. (3.16), respectively) are then constructed.

With the fluid surrogates developed, structural optimization accounting for the effects of fluid flow is initiated. Each design  $i$  considered during the optimization is defined by three types of design variables: 1)  $\mathbf{d}_{int,i}$ , design variables such as the material properties that do not change the outer mold line of the undeformed reference configuration, 2)  $\mathbf{d}_{s,i}$ , design variables that are values of shape fitting parameters  $\mathbf{S}_s$ , denoted as  $\mathbf{S}_{s,i}^0$ , which describe the undeformed shape, and 3)  $\mathbf{d}_{c,i}$ , all other design variables some of which could be included in  $\mathbf{S}_c$ . Each design is subjected to  $m_p$  pressure loadings  $q_\infty \hat{C}_p^j(\mathbf{x}; \mathbf{C}^j) \forall j = 1, \dots, m_p$  based on variations of the pressure coefficient fitting parameters  $\mathbf{C}$  from which the surface fit of the deformed shape  $\hat{s}_{FSI}^j(\mathbf{x}; \mathbf{S}_{s,i}^j, \mathbf{S}_{c,i})$ , shape fitting parameters  $\mathbf{S}_{s,i}^j$ , and model responses  $\mathbf{Y}^{s,j}$  are extracted. Using results from the structure evaluations, surrogate models  $\mathbf{S}_{s,i} = \mathcal{F}_i^s(q_\infty \mathbf{C})$  (Eq. (3.13)) and  $\mathbf{Y}_i^s = \mathcal{F}_i^{so}(q_\infty \mathbf{C})$  (Eq. (3.15)) are developed. The intersection of the fluid and structure surrogate models for the shape fitting parameters (the USI solution) is found for multiple freestream velocities until surrogate bounds are reached. For each considered velocity, model responses  $\mathbf{Y}_{USI,i}^s$  and  $\mathbf{Y}_{USI,i}^f$  are calculated. All SAA solutions for a given design are returned to the optimizer, which evaluates the design for given objectives  $\mathbf{f}(\mathbf{d}_i)$  subject to constraints  $\mathbf{g}(\mathbf{d}_i)$  and  $\mathbf{h}(\mathbf{d}_i)$ . The entire process for the optimization framework incorporating the uncoupled method for SAA is summarized in Method 4.3.

The optimization framework incorporating the uncoupled method could be considered a hybrid of both the IDF and MDF architectures. It is similar to the IDF architecture since the fluid and structure disciplines are decoupled and evaluated individually using pressure and shape fitting parameters, avoiding the expensive, coupled analysis. However, this optimization framework ensures multidisciplinary feasibility for every iteration of the optimizer while IDF imposes multidisciplinary feasibility as a constraint for the final solution. With regards to an MDF framework,

Method 4.3: Computational process of uncoupled method for SAA in an optimization process

### Uncoupled Method for SAA in an Optimization Scheme

- 1) Perform initial fluid and structure analyses; obtain  $C_p^0(\mathbf{x})$  and  $\Omega_{FSI}^0$
- 2) Define  $\hat{s}_{FSI}$  and  $n_s$   
For accurate solutions,  $\epsilon_s^0$  (Eq. (3.8))  $\leq tol$
- 3) Generate  $\mathbf{S}^k$ ,  $k=1, \dots, m_s$
- 4) Do for  $k=1, \dots, m_s$ :  
i) Perform fluid analysis of body described by  $\hat{s}_{FSI}^k(\mathbf{x}, \mathbf{S}^k)$  (Eq. (3.2))  
ii) Extract  $C_p^k(\mathbf{x})$  and  $\mathbf{Y}^{f,k}(\hat{s}_{FSI}^k(\mathbf{x}; \mathbf{S}^k))$  from results of fluid analysis
- 5) Define  $\hat{C}_p$  and  $n_p$   
For accurate solutions,  $\epsilon_p^0$  (Eq. (3.7))  $\leq tol$
- 6) Calibrate fluid surrogates  $\mathbf{C} = \mathcal{F}^f(\mathbf{S})$  (Eq. (3.14)) and  $\mathbf{Y}^f = \mathcal{F}^{fo}(\mathbf{S})$  (Eq. (3.16))
- 7) Begin structure optimization:
- 8) Consider new design  $i$ :
- 9) Generate  $\mathbf{C}^j$ ,  $j=1, \dots, m_p$
- 10) Do for  $j=1, \dots, m_p$ :  
i) Perform structural analysis with load  $q_\infty \hat{C}_p^j(\mathbf{x}; \mathbf{C}^j)$  (Eq. (3.4))  
ii) Extract  $\mathbf{S}_i^j(q_\infty \hat{C}_p^j(\mathbf{x}; \mathbf{C}^j))$  and  $\mathbf{Y}_i^{s,j}(q_\infty \hat{C}_p^j(\mathbf{x}; \mathbf{C}^j))$  from results of structure analysis
- 11) Calibrate structure surrogates  $\mathbf{S} = \mathcal{F}_i^s(q_\infty \mathbf{C})$  (Eq. (3.13)) and  
 $\mathbf{Y}^s = \mathcal{F}_i^{so}(q_\infty \mathbf{C})$  (Eq. (3.15))
- 12) Make initial guess  $\mathbf{C}_1$
- 13) Do while  $\mathbf{C}_{g+1} - \mathbf{C}_g \leq tol_c$  and  $\mathbf{S}_g - \mathbf{S}_{g-1} \leq tol_s$ :  
i) Solve  $\mathbf{S}_g = \mathcal{F}_i^s(q_\infty \mathbf{C}_g)$   
ii) Solve  $\mathbf{C}_{g+1} = \mathcal{F}_i^f(\mathbf{S}_g)$
- 14) If converged set of  $\mathbf{S}_g$  and  $\mathbf{C}_{g+1}$  outside input bounds, go to Step 19;  
Otherwise continue
- 15) Set  $\mathbf{S}_{USI,i} = \mathbf{S}_g$  and  $\mathbf{C}_{USI,i} = \mathbf{C}_{g+1}$
- 16) Solve  $\mathbf{Y}_{USI,i}^f = \mathcal{F}_i^{fo}(\mathbf{S}_{USI,i})$  (Eq. (3.26)) and  $\mathbf{Y}_{USI,i}^s = \mathcal{F}_i^{so}(q_\infty \mathbf{C}_{USI,i})$  (Eq. (3.27))
- 17) Optional: Obtain  $\mathbf{S}_{USiS,i}(q_\infty \mathbf{C}_{USI,i})$ ,  $\mathbf{C}_{USiS,i}(\mathbf{S}_{USI,i})$ ,  $\mathbf{Y}_{USiS,i}^s(q_\infty \mathbf{C}_{USI,i})$ , and  
 $\mathbf{Y}_{USiS,i}^f(\mathbf{S}_{USI,i})$  from final fluid and structure analyses
- 18) Increase  $v_\infty$ , return to Step 13 with  $\mathbf{C}_{USI}$  as initial guess
- 19) Return results to optimizer for objective/constraint evaluation and return to Step 8 until optimal design reached
- 20) Optimization finished. Optimal design obtained.

the uncoupled optimization framework is similar since the optimizer only handles the design variables. Also, the process of solving for the intersection of the surrogate

models could be considered a multidisciplinary analysis, which the MDF framework performs for every design.

#### *4.3.2 Optimization Application: Shape Memory Alloy Flow Diverter*

In this section, the optimization framework incorporating the uncoupled method is utilized in the design of an SMA flow diverter, which under sufficient flow speed shall redirect flow from one outlet to another. This concept is similar to the industry device known as an excess flow valve. These devices are used to close off flow through a pipe (manually or automatically) when a surge of liquid/gas or a failure upstream occurs. Excess flow valves that close automatically typically use linear springs to regulate the flow through the pipe. The flow diverter design considered here is inspired by Arena's adaptive inlet work [143].

##### *4.3.2.1 Model Description*

The considered problem, shown in Fig. 4.14, is two-dimensional flow (incompressible water) through a tunnel with one inlet and two outlets separated by a splitter. Both outlets are of equal size. A flexible flow diverter is cantilevered at the forward end of the splitter with an undeformed configuration such that when loaded, the flow diverter deflects downward. Under sufficient loading the flow diverter closes off flow to Outlet 1, diverting all flow to Outlet 2. Conceptually, this diverter could be a flow valve for a drainage system that closes off flow to an older portion of the system when the flow rate of water suddenly increases from flooding. As with the previous demonstration, Abaqus and SC/Tetra model the structure and surrounding flow field. The desirable flow diverter design exhibits 1) a large peak flow velocity through Outlet 1 ( $v_{1,max}$ ), and 2) a small change in inlet velocity ( $\Delta v_\infty$ ) between the inlet velocity  $v_{\infty,v_{1,max}}$  at which  $v_{1,max}$  occurs and the inlet velocity  $v_{\infty,v_1=0}$  at which Outlet 1 is closed off ( $v_1=0$  m/s). To satisfy these conflicting design requirements,

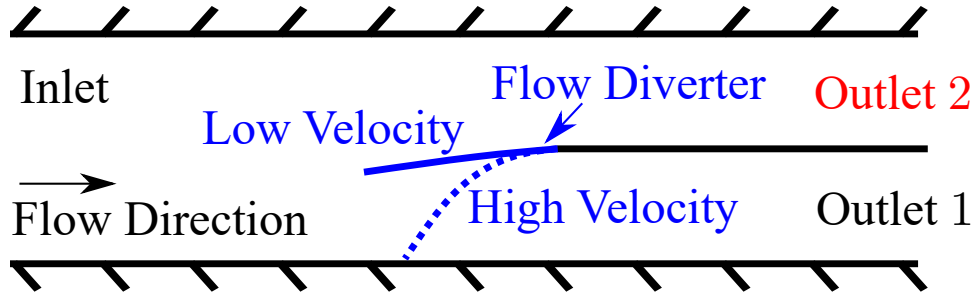


Figure 4.14: Illustration of SMA flow diverter problem.

superelastic SMAs are incorporated into the design of the flow diverter. For this work, the SMA flow diverter is stiff to aerodynamic loading until sufficient loading is applied by increasing the inlet velocity at which point the SMA flow diverter transforms and undergoes significant deformation with little increase in force (decreasing  $\Delta v_\infty$ ). Additionally, once unloaded the diverter returns to its original shape allowing for flow through Outlet 1.

The structural model (see Fig. 4.15(a)) consists of the SMA flow diverter and floor of the tunnel, which are modeled as a deformable shell fixed at one end and an analytical rigid body, respectively. The width of the flow diverter is fixed at 2 mm while the thickness  $t_{SMA}$  and length  $l_{SMA}$  are design variables. Edges aligned in the  $xy$ -plane are assigned symmetry conditions. The diverter is meshed using general shell elements (type S4) with a 0.5 mm size along its curve, and one element in the  $z$  direction. Contact between the flow diverter and floor is modeled with a linear penalty law in the normal direction and with frictionless behaviour in the tangential direction. The thermomechanical response of the SMA flow diverter is captured using the Lagoudas constitutive model with material properties used in previous SMA applications of this work (see Table 2.1). Static analysis is used to evaluate the response of the flow diverter to pressure loadings  $q_\infty \hat{C}_p(\mathbf{x}; \mathbf{C})$ , which represent the

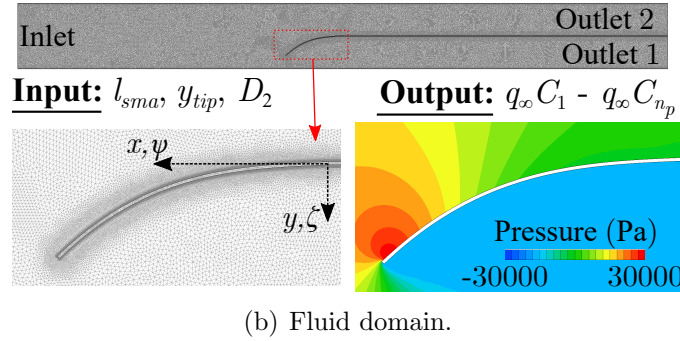
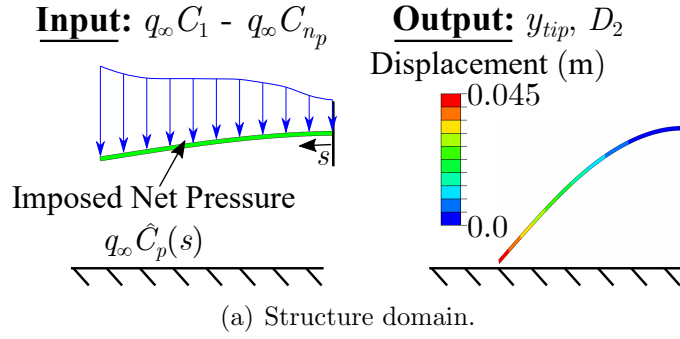


Figure 4.15: Structure and fluid models for SMA flow diverter.

net pressure across the diverter. Following each analysis, the deformed configuration  $\Omega_{FSI}$ , maximum Mises stress  $\sigma_{max}$ , and maximum martensitic volume fraction  $\xi_{max}$  are extracted.

Shown in Fig. 4.15(b), the fluid model is a 1 m by 0.1 m by 0.002 m domain with closed volumes for the splitter and flow diverter. Incompressible water with density of  $998.2 \text{ kg/m}^3$  and viscosity of  $0.001016 \text{ Pa}\cdot\text{s}$  is used. The left face of the fluid domain is assigned an inlet boundary condition of  $5 \text{ m/s}$  horizontal velocity while the two right faces are assigned outlet boundary conditions of zero static pressure. No slip/penetration wall boundary conditions are applied to the surface of the flow diverter, splitter, and tunnel floor/ceiling. The fluid model is meshed using 340,000 elements (150,000 prism and 180,000 hexahedron) with mesh sizes of ranging from  $0.3125 \text{ mm}$  to  $1.25 \text{ mm}$  (see Appendix E for a brief discussion on mesh refine-

ment). Additionally the model is meshed one element wide in the  $z$  direction for two-dimensional flow. For each considered SMA diverter configuration, steady flow analysis is performed and the resulting net pressure distribution  $q_\infty C_p(\mathbf{x})$  and the ratios of outlet velocity to inlet (freestream) velocity  $v_1/v_\infty$  and  $v_2/v_\infty$  are extracted.

#### 4.3.2.2 Shape and Pressure Coefficient Fit Development

Based on a few exploratory structure analyses, the Class/Shape Transformation (CST) method is used to generate the undeformed configuration of the SMA flow diverter and the shape fit of its deformed configuration. Similar to the deformable baffle example, the shape of the flow diverter is represented by a linear CST equation of the form:

$$\zeta = \psi(1 - \psi)[D_1(1 - \psi) + D_2\psi] + \psi \frac{y_{tip}}{x_{tip}} \quad (4.12)$$

where  $x_{tip}/y_{tip}$  is the  $x$ -coordinate/ $y$ -coordinate for the tip of the flow diverter,  $D_1$  and  $D_2$  are CST shape coefficients, and  $\zeta$  and  $\psi$  are nondimensional coordinates defined as

$$\zeta = y/x_{tip}, \quad \psi = x/x_{tip},$$

For a given flow diverter length  $l_{SMA}$  and  $y$ -coordinate of the tip  $y_{tip}$ , the value of  $D_1$  is constrained as

$$D_1 = -y_{tip}/x_{tip}, \quad (4.13)$$

such that the shape of the flow diverter satisfies a cantilever boundary condition.

Therefore the shape is represented by only three fitting parameters ( $n_{s,c}=1$ ,  $n_{s,s}=2$ ):

$l_{SMA}$ ,  $y_{tip}$ , and  $D_2$ .<sup>5</sup> Note that the length is constant between undeformed/deformed

---

<sup>5</sup>Thickness of the flow diverter does change the outer mold line of the body presented to flow. However, based on a few exploratory fluid evaluations (see Appendix E), the thickness has negligible effect on the pressure distribution for the thickness range studied.

configurations while the other shape parameters are not (i.e.,  $\mathbf{S}=\{\mathbf{S}_s, \mathbf{S}_c\}=\{\{y_{tip}, D_2\}, \{l_{SMA}\}\}$ ).

Following each structural evaluation, shape coefficient  $D_2$  is calculated from the deformed shape of the flow diverter as

$$D_2 = \frac{1}{\psi_{MP}} \left[ \frac{\zeta_{MP} - \psi_{MP}\zeta_{tip}}{\psi_{MP}(1 - \psi_{MP})} + y_{tip}/x_{tip}(1 - \psi_{MP}) \right], \quad (4.14)$$

where  $\zeta_{MP}$  and  $\psi_{MP}$  represent the coordinates of the midpoint along the curve of the flow diverter in the nondimensional  $\psi$ - $\zeta$  domain. For fluid evaluations, shapes of the flow diverter are generated in the nondimensional domain using (Eq. (4.12)) for given values of  $y_{tip}$ ,  $l_{sma}$ , and  $D_2$ , which are converted into the real  $x$ - $y$  domain.

For this problem, pressure coefficient fitting parameters represent the net pressure across the flow diverter at various locations along the curve of the diverter forming the net pressure coefficient distribution fit  $\hat{C}_p(s)$ . Following the procedure in Section 4.3.1, 64 fluid evaluations are performed on different flow diverter shapes with variations of the shape fitting parameters defined by a four-level full factorial array. Bounds of the shape fitting parameters are provided in Table 4.1. Bounds for  $y_{tip}$  are the values corresponding to the fully open and closed flow diverters. Lower bound of  $D_2$  corresponds approximately to a flow diverter with minimal curvature while the upper bound is of similar value to the maximum value of  $D_2$  observed during initial structural analyses. Bounds of  $l_{SMA}$  corresponds to the minimum and maximum values of the flow diverter that shall be considered during design optimization. For the hardware used (standard workstation, 10CPU), the average computational cost for each analysis is 100 min (670 fluid solution increments). Note, to prevent contact between the diverter and tunnel floor that would potentially result in mesh generation errors, the upper bound of  $y_{tip}$  is limited to 4.8 cm (96% of half the tunnel

Table 4.1: Surrogate model input bounds of shape fitting parameters for the flow diverter example.

Shape Fitting Parameter	Bounds
$y_{tip}$ (mm)	1 - 49
$l_{sma}$ (m)	0.069 - 0.125
$D_2$	0.0006 - 0.6

height). After each fluid evaluation, the net pressure coefficient distribution across the entire flow diverter (see Fig. 4.16) and the flow velocity through both outlets are extracted. As shown in Fig. 4.16, the pressure distributions for the various diverter shapes are concentrated in four regions each corresponding to a different value of  $y_{tip}$  considered during the full factorial DOE. This suggests that  $y_{tip}$  may have the largest impact on the pressure distribution.

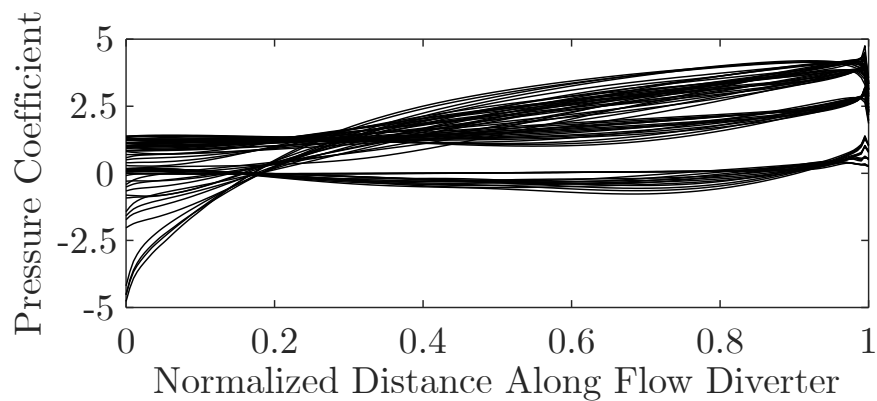


Figure 4.16: Net pressure coefficient distributions on SMA flow diverter from four-level full factorial DOE.

Based on pressure coefficient distributions from the DOE, the form of the fit  $\hat{C}_p(s)$  is chosen as a RBF of the form:

$$\hat{C}_p(s) = \sum_{i=1}^{n_p} w_i \Psi(s - s_i) \quad (4.15)$$

where  $s$  is the nondimensional distance along the curve,  $s_i \forall i=1, \dots, n_p$  are the  $n_p$  locations along the diverter for the fitting parameters, and the weights  $w_i$  are solved during calibration by solving the following system of equations:

$$\begin{bmatrix} C_1 \\ \vdots \\ C_{n_p} \end{bmatrix} = \begin{bmatrix} \Psi(s_1 - s_1) & \cdots & \Psi(s_1 - s_{n_p}) \\ \Psi(s_2 - s_1) & \cdots & \Psi(s_2 - s_{n_p}) \\ \vdots & \vdots & \vdots \\ \Psi(s_{n_p} - s_1) & \cdots & \Psi(s_{n_p} - s_{n_p}) \end{bmatrix} \begin{bmatrix} w_1 \\ \vdots \\ w_{n_p} \end{bmatrix} \quad (4.16)$$

For a given number of fitting parameters and type of RBF (cubic or linear), optimization is performed to determine the locations along the diverter for the fitting parameters that generate a fit with the minimal average normalized root mean square error (NRSME) relative to the computational data from the full factorial array DOE. Each optimization is conducted using the Scipy Differential Evolution method with 100 generations and 100 population members. The results of the optimizations are shown in Fig. 4.17. As expected, as the number of fitting parameters increases, the error decreases. Based on the results, a cubic RBF using eight pressure coefficient fitting parameters with  $(s_1, \dots, s_8) = (0.012, 0.083, 0.257, 0.537, 0.772, 0.896, 0.942, 0.987)$  is chosen as the fit to approximate the computational CFD data.

Using pressure fitting parameters extracted from the fluid evaluations at the optimally determined locations as training points, cubic RBF surrogate models with polynomial tails relating the pressure coefficient fitting parameters to the three shape

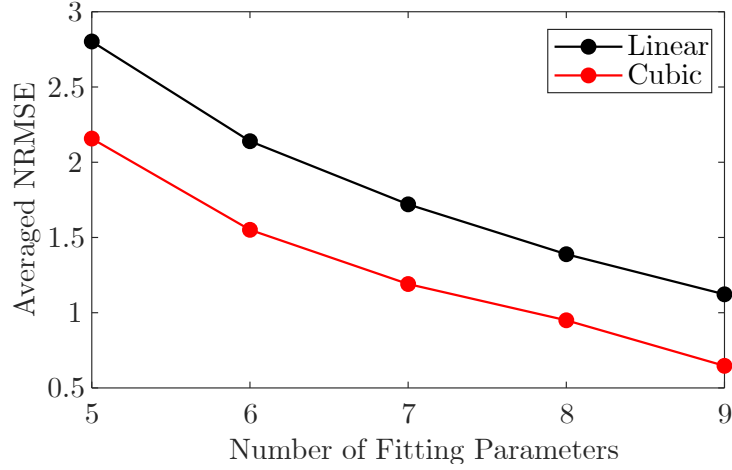


Figure 4.17: Error between fit and CFD calculated pressure distribution for different number of fitting parameters and RBF type.

fitting parameters are constructed in the following form:

$$C_i = \mathcal{F}_i^f(\mathbf{S}) = \sum_{k=1}^{64} w_{i,k} \|\mathbf{S} - \mathbf{S}^k\|_2^3 + \gamma_i^f \cdot \{\mathbf{S}, 1\} \quad \forall i = 1, 8. \quad (4.17)$$

This pressure coefficient fit is then converted from the nondimensional  $s$  domain into the dimensional  $x$ - $y$  domain using the geometry of the undeformed flow diverter. Thus for a given distribution in the  $s$  domain, many different distributions in the  $x$ - $y$  domain can be obtained depending on the shape of the undeformed flow diverter. However, this has no effect on the USI solution for a given design as the same undeformed geometry is used for all structure evaluations of surrogate training data. Additionally, using the results from the fluid evaluations, surrogates relating model responses  $v_1/v_\infty$  and  $v_2/v_\infty$  to the shape fitting parameters (see Eq. (3.16))

are constructed in the following form:

$$\frac{v_1}{v_\infty}, \frac{v_2}{v_\infty} = \mathcal{F}^{fo}(\mathbf{S}) = \sum_{k=1}^{64} w_k^{fo} \|\mathbf{S} - \mathbf{S}^k\|_2^3 + \gamma^{fo} \cdot \{\mathbf{S}, 1\}. \quad (4.18)$$

#### 4.3.2.3 Sample Flow Diverter Demonstration

As a demonstration of the uncoupled method for this problem, a flow diverter with length and thickness of 9.7 cm and 0.19 cm, respectively, is considered. Note that this design is used as the median of the design space considered in the coming optimizations. The undeformed configuration of the diverter is defined by shape fitting parameters  $y_{tip}^0=0.005$  m and  $D_2^0=0.025$ . Additionally, the ambient temperature is 300 K. Similar to the earlier demonstrations, a Latin Hypercube sampling with 135 variations<sup>6</sup> of the pressure coefficient parameters (bounds of parameters shown in Table 4.2) is performed in eight structure analyses each of which uses 15 of the variations (after [140]) and the resulting shape fitting parameters  $y_{tip}$  and  $D_2$  are recorded. Bounds of the pressure coefficient fitting parameters are based on the minimum and maximum values from the 4-level full factorial DOE of fluid evaluations.<sup>7</sup> The computational cost (standard workstation, 10CPU) to perform the structure analyses is approximately 20 min (total of 518 structure solution increments). Using the results from the LHS and the unloaded, undeformed configuration as training points, cubic RBF surrogate models with polynomial tails for the shape fitting parameters are constructed as follows:

$$S_i = \mathcal{F}_i^s(q_\infty \mathbf{C}) = \sum_{j=1}^{136} w_{i,j}^s q_\infty \|\mathbf{C} - \mathbf{C}^j\|_2^3 + \gamma_i^s \cdot \{q_\infty \mathbf{C}, 1\} \quad \forall i = 1, 2. \quad (4.19)$$

---

<sup>6</sup>Number of samples based on suggested sample size from Jin, et al. for a large-scale problem [56].

<sup>7</sup>Lower bounds of  $C_5$ - $C_8$  are further adjusted to ensure a variety of deformed flow diverters are obtained.

Table 4.2: Surrogate model input bounds of pressure coefficient fitting parameters for SMA flow diverter.

<b>Fitting Parameters</b>	<b>Bounds</b>	<b>Fitting Parameters</b>	<b>Bounds</b>
$C_1$	-3.8 - 1.4	$C_5$	-0.8 - 4
$C_2$	-2 - 1.4	$C_6$	-0.85 - 4.2
$C_3$	-0.3 - 1.5	$C_7$	-0.4 - 4.2
$C_4$	-0.65 - 3.2	$C_8$	-0.45 - 4.3

Additionally, using these structure results, surrogate models relating maximum Mises stress and martensitic volume fraction to the pressure coefficient fitting parameters (see Eq. (3.15)) are constructed in the following form:

$$\sigma_{max}, \xi_{max} = \mathcal{F}^{so}(q_\infty \mathbf{C}) = \sum_{j=1}^{136} w_j^{so} q_\infty \|\mathbf{C} - \mathbf{C}^j\|_2^3 + \gamma^{so} \cdot \{q_\infty \mathbf{C}, 1\}. \quad (4.20)$$

Following the procedure in Section 4.1.1, USI solutions are determined for multiple velocities as shown in Fig. 4.18 and Fig. 4.19 by changing the freestream velocity and re-performing the fixed point iteration. As expected, the diverter exhibits little deformation (Fig. 4.18(a),(b)) at low velocities resulting in an approximately linear relation between the inlet and outlet velocities (Fig. 4.19(i)). Additionally, since the diverter is undergoing small deformations at low freestream velocities, the pressure coefficient fitting parameters (Fig. 4.19(a)-(h)) and maximum stress (Fig. 4.18(c)) do not change. However, as  $v_{1,max}$  is approached, the diverter begins to significantly deform, diverting flow away from Outlet 1 and towards Outlet 2, and significantly changing the pressure distribution acting on the diverter.

Total serial computational cost to obtain these results using the uncoupled method

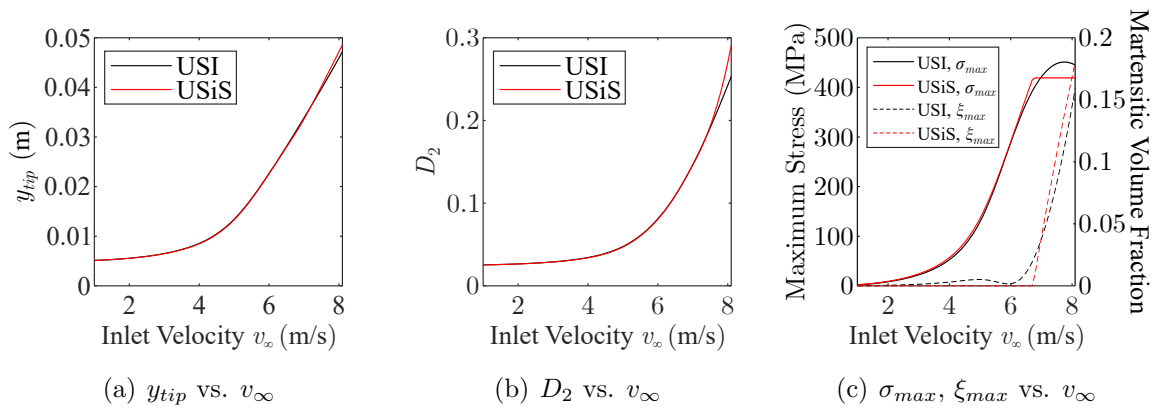


Figure 4.18: Shape fitting parameters, maximum stress, and maximum martensitic volume fraction of USI and USiS solutions for multiple inlet velocities from the sample (median) design of the SMA flow diverter.

is 107 hr (or 100 min if all runs are parallelized) with  $I^f=192,000$  and  $I^s=7,770^8$ . Note that with the fluid evaluations complete, each new flow diverter design requires only re-performing of the cheaper structure evaluations ( $I^f=0$ ,  $I^s=7,770$ ). Obtaining results in Fig. 4.18 and Fig. 4.19 with the serial FSI scheme requires multiple coupled analyses with different inlet velocities or one long coupled analysis with a sufficiently slow change in inlet velocity, both of which are computationally expensive. To serve as an initial test for the accuracy of the USI solution, one final static structure and steady flow fluid analysis are performed using the USI solutions as inputs. As shown in Fig. 4.18 and Fig. 4.19, the USI and USiS solutions for the shape fitting parameters, a majority of pressure fitting parameters, and most importantly the outlet velocities are approximately equal for a wide range of inlet velocities. For pressure coefficient fitting parameters  $C_1$ - $C_3$ , the USI and USiS solutions show similar trends, but the USI solution is generally higher. Note, that these parameters are near the root of the diverter and are lower in value than other pressure fitting parameters

<sup>8</sup>Number of copies of the structure per batch analysis (15) multiplied by the average number of solutions increments for all analyses (518).

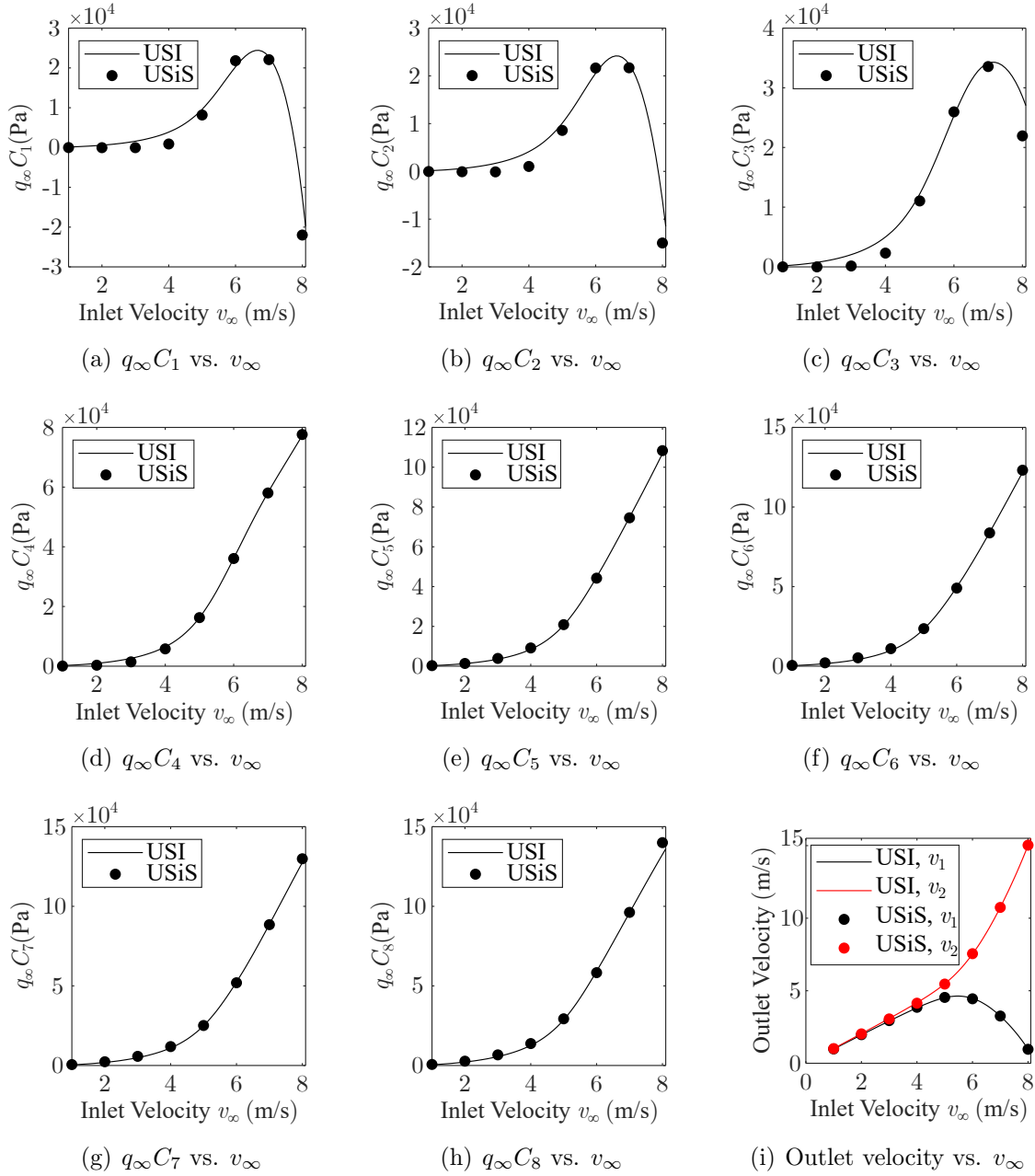


Figure 4.19: Pressure fitting parameters and outlet velocities from USI and USiS solutions for multiple inlet velocities from the sample (median) design of the SMA flow diverter.

and thus exact matching between the USI and USiS solutions is not as critical. As shown in Fig. 4.16, the pressure distribution from  $s=0-0.2$  varies significantly be-

tween each considered diverter shape, which may result in a less accurate surrogate approximation. Either a larger full factorial array or an LHS may improve the fit of these parameters. Overall, the good matching of pressure coefficient fitting parameters between the USI and USiS solutions indicates that assumption of constant pressure coefficient for different freestream velocities provides adequate loadings for the structure and can be used in design studies of the flow diverter. The USI and USiS solutions of maximum stress match quite well until the SMA material starts to transform, at which point the USI solution overpredicts the stress. This is due to the discontinuous change in stress of the SMA material once transformation is initiated that a cubic RBF cannot fit well. More training points for the structure surrogate model may improve the ability of the model to capture the initiation of transformation. Overall, these results indicate that the shape and pressure coefficient fits are adequate for preliminary design optimization.

#### 4.3.2.4 Optimization Problem and Results

The objectives for this design optimization (see Fig. 4.20) are to maximize  $v_{1,max}$ , the peak velocity through Outlet 1, and minimize  $\Delta v_\infty$ , the change in inlet velocity between the inlet velocity at which  $v_{1,max}$  occurs and the inlet velocity at which Outlet 1 is closed off. Tip location of the diverter is used as a metric for closure of Outlet 1. For  $y_{tip}$  greater than 4.8 cm, Outlet 1 is considered to be closed.

Constraints used in this optimization are: 1) Outlet 1 must be closed off before an inlet velocity of 8 m/s is reached, and 2) maximum Mises stress anywhere in the SMA flow diverter  $\sigma_{max}^{SMA}$  must be less than 700 MPa (yield stress of the material). The fitness values for any designs that violate these constraints are penalized.

Design variables in this optimization are the thickness  $t_{SMA}$  and length  $l_{SMA}$  of the flow diverter. With regards to the optimization flowchart in Fig. 4.13, the thick-

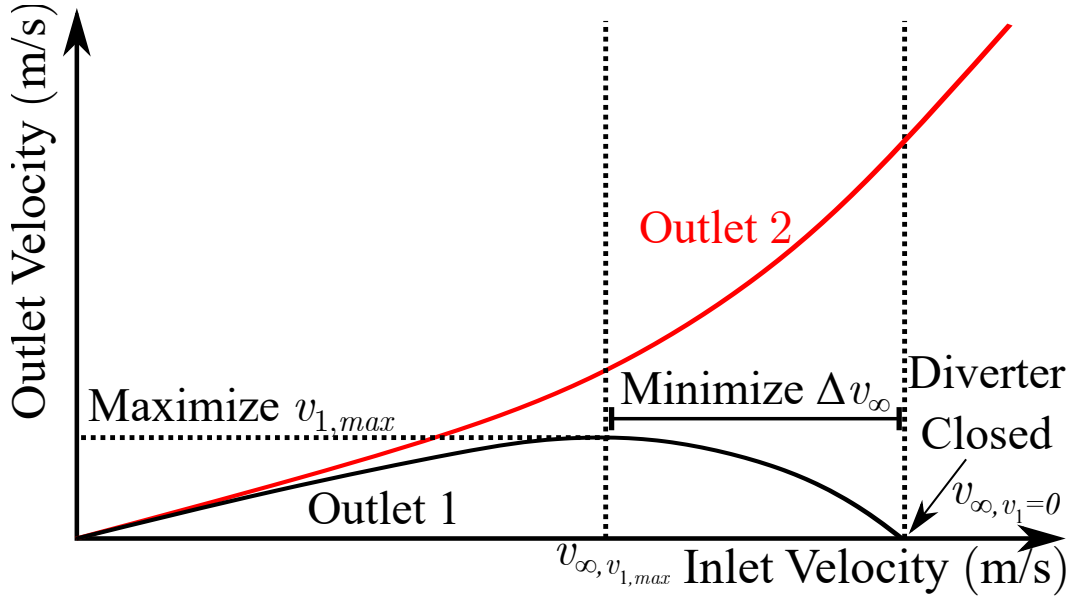


Figure 4.20: Illustration of SMA flow diverter optimization objectives.

ness and length are contained within  $\mathbf{d}_{int}$  and  $\mathbf{d}_c$ , respectively. For this work, the values of shape fitting parameters  $\mathbf{S}_s^0$  that exactly describe the undeformed configuration of the SMA flow diverter are  $y_{tip}^0=0.005$  m and  $D_2^0=0.025$ . Additionally, the ambient temperature is set to 290 K. This is lower than the ambient temperature of the sample design from the previous section as flow diverters at 300 K did not exhibit a large amount of transformation, thus limiting the potential benefit of the SMA material.

The design optimization problem is summarized in Fig. 4.21. Preliminary de-

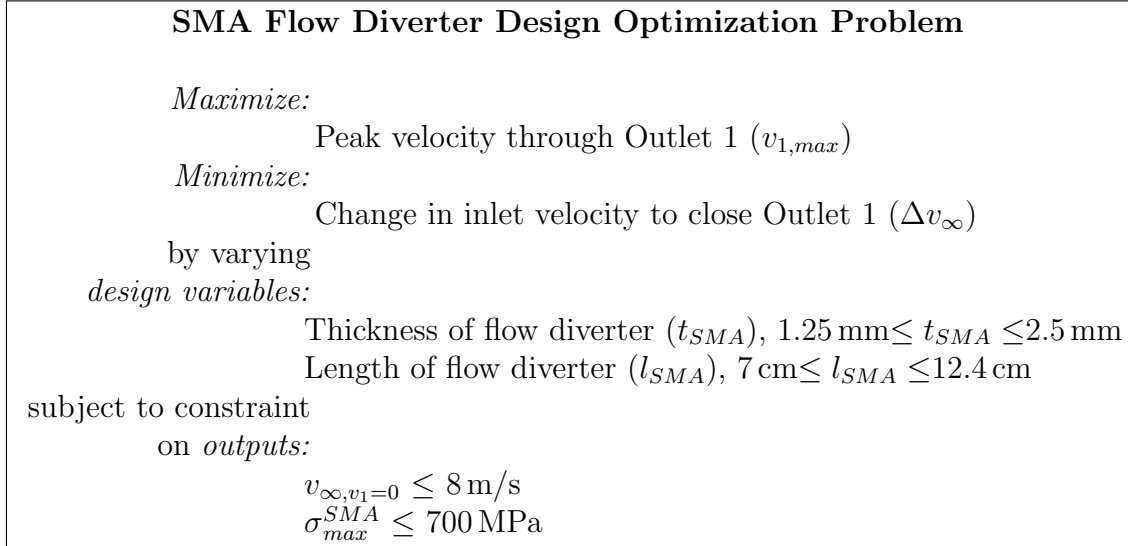


Figure 4.21: Summary of the SMA flow diverter optimization problem.

sign optimization of the SMA flow diverter is performed using the Non-Dominate Sorting Genetic Algorithm II (NSGA-II) tool in the Distributed Evolutionary Algorithms in Python (DEAP) package with a population of 12 members evaluated over 12 generations (and one seeding generation). Following the method in Section 4.3.1, each considered design is evaluated using structural analysis with a Latin Hypercube Sampling of 135 variations of the pressure fitting parameters using bounds from Table 4.2. Note, that each design is evaluated using the same Latin Hypercube Sampling to avoid any variation in model response (see Appendix E for further discussion on variation in model response). Surrogate models are then developed and USI solutions are obtained for multiple flow conditions. Since the fluid surrogate is being reused for every design, the average computational cost to evaluate each design (both LHS and

fixed point iteration of the surrogate models for multiple velocities), is approximately 30 min. Thus the computational cost to perform all generations in the optimization is approximately 78 hr ( $\approx 80,000$  structure solution increments) or 185 hr if including the training of the fluid surrogate (192,000 fluid solution increments)

Figure 4.22 shows the  $v_{1,max}$ - $\Delta v_\infty$  objective space for all designs considered during the optimization that satisfy constraints along with the associated martensitic volume fraction for each of those designs. Note that each point in the figure represents an SAA solution obtained in approximately 30 min with the uncoupled method. As seen in the figure, the two objectives are inversely related (i.e., improvement for one objective results in decreased performance for another objective). Along the non-dominated frontier, between the best performing design for  $\Delta v_\infty$  ( $t_{SMA}=1.3$  mm and  $l_{SMA}=11.8$  cm) and the best performing design for  $v_{1,max}$  ( $t_{SMA}=1.9$  mm and  $l_{SMA}=10$  cm),  $\Delta v_\infty$  and  $v_{1,max}$  vary by 39% and 114%, respectively, indicating that the peak flow velocity is highly sensitive to the design variables. Additionally, designs with large martensitic volume fractions greater than 0.4 typically exhibit a large  $v_{1,max}$  and moderate values of  $\Delta v_\infty$ . Examination of the non-dominated frontier clearly demonstrates the effect of incorporating superelastic SMA material into the design of the flow diverter. At a  $\Delta v_\infty$  of 2.16 m/s, the design on the non-dominated frontier exhibits a martensitic volume fraction of 0.05. The next design on the non-dominated frontier however exhibits a martensitic volume fraction of 0.7 and a 56% increase in  $v_{1,max}$  for a small (0.01 m/s) increase in  $\Delta v_\infty$ . Out of the designs on the non-dominated frontier, the closest one to the utopia point is  $v_{1,max}=2.16$  m/s and  $\Delta v_\infty=4.42$  m/s. The outlet velocities versus inlet velocity for this design is shown in Fig. 4.22. The corresponding length and thickness for this design are  $l_{SMA}=10$  cm,  $t_{SMA}=1.9$  mm, respectively. Additionally, this design also exhibits the highest martensitic volume fraction of all designs on the non-dominated frontier. It

is suspected that further generations may result in a non-dominated frontier with designs that exhibit a higher martensitic volume fraction even closer to the utopia point. Also shown in Fig. 4.22 is the median design, design at the center of the design space ( $l_{SMA}=9.7$  cm,  $t_{SMA}=1.8$  mm)<sup>9</sup>, which lies on the non-dominated frontier.

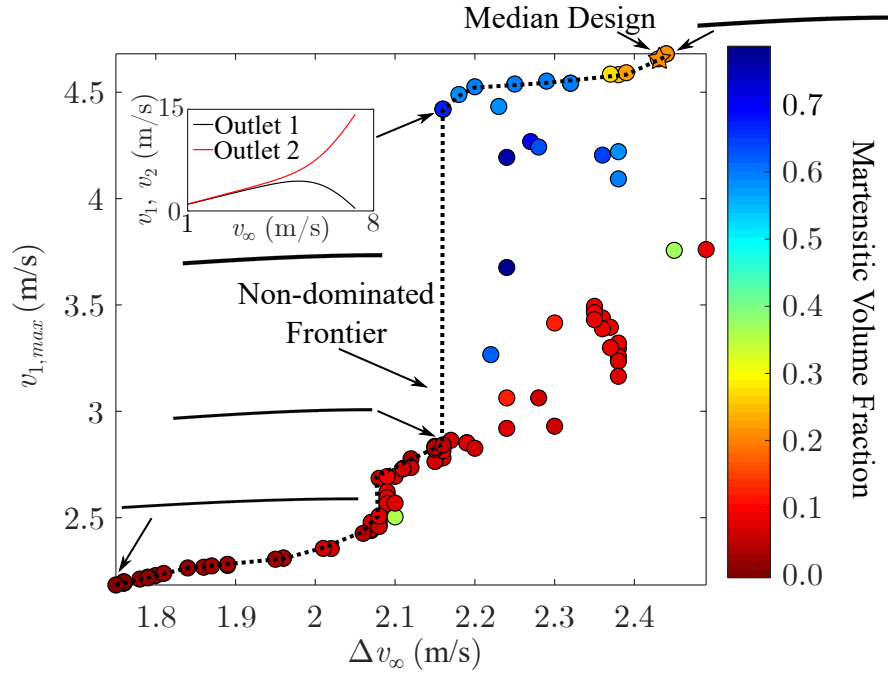


Figure 4.22:  $v_{1,max}$ - $\Delta v_\infty$  objective space with martensitic volume fraction.

To further demonstrate the utility of the uncoupled method in an optimization scheme, the design problem is now changed by considering additional design variables: the undeformed  $y$ -coordinate of the tip  $y_{tip}^0$  and the undeformed CST coefficient  $D_2^0$ . Note, that both design variables are contained within  $\mathbf{d}_c$  in Fig. 4.13 and thus represent the undeformed shape fitting parameters  $\mathbf{S}^0$  for the problem. If

<sup>9</sup>Sample design from the previous section.

performing the optimization with either the MDF or IDF architectures, this change in the design problem requires re-performance of the computationally expensive coupled analyses or fluid analyses, respectively. However, with the uncoupled method, these additional design variables are accounted for in the shape fitting parameters  $y_{tip}$  and  $D_2$ , allowing the fluid surrogate models to be retained. A new optimization is performed with the four design variables using the same algorithm and number of generations/population members. Figure 4.23 shows the  $v_{1,max}$ - $\Delta v_\infty$  objective space for all designs considered during this new optimization. With the additional design variables, the non-dominated frontier has moved further towards the utopia point. As expected, the non-dominated frontier optimal designs exhibit a higher Martensitic volume fraction, indicating that the diverter is undergoing more transformation. The effect of the transformation can be further seen in the included outlet velocities versus the inlet velocity plot. As compared to the plot in Fig. 4.22, while  $v_{\infty,v_1=0}$  is of similar value, the curves for the outlet velocities are significantly stiffer, indicating that the diverter rapidly closes. Additionally, all diverters on the non-dominated frontier are of similar design ( $t_{sma}=1.49$  mm,  $l_{sma}=8.14$  cm,  $y_{tip}^0=2.92$  mm,  $D_2^0=0.180$ ), exhibiting an inflection point in their curve.

As a final demonstration, the design problem is further changed by considering a linear elastic material. As this change has no impact on the outer mold line of the diverter, fluid surrogate models are once again retained, and the optimization is re-performed. Figure 4.24(a) shows the  $v_{1,max}$ - $\Delta v_\infty$  objective space for the three optimizations, all of which are performed with the same set of fluid results. For the linear-elastic flow diverter, the relation between  $v_{1,max}$  and  $\Delta v_\infty$  is approximately linear, resulting in significantly less optimal designs as compared to an SMA flow diverter. Another interesting result that further demonstrates the effectiveness of the SMA flow diverter is the comparison of  $v_{\infty,v_1,max}$  and  $v_{\infty,v_1=0}$ . As shown in

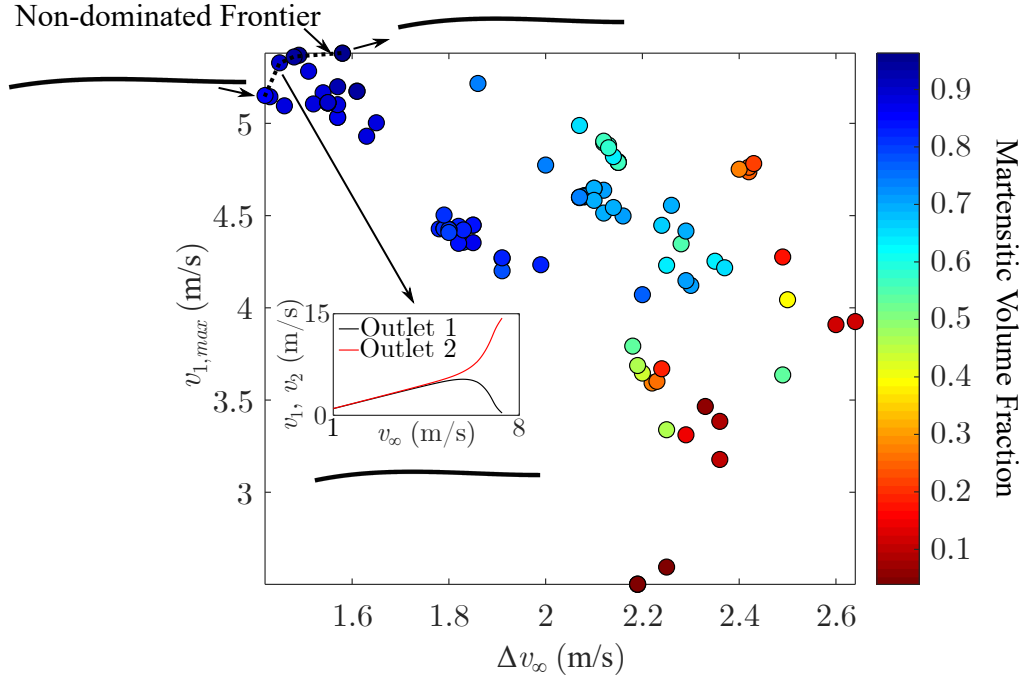


Figure 4.23:  $v_{1,max}-\Delta v_{\infty}$  objective space for optimization with added design variables.

Fig. 4.24(b), for the linear elastic flow diverter,  $v_{\infty,v_{1,max}}$  and  $v_{\infty,v_1=0}$  are linearly related. SMA flow diverters however, exhibit a linear relation at low  $v_{\infty,v_1=0}$  but at high  $v_{\infty,v_1=0}$  a strong positive nonlinear relation with  $v_{\infty,v_{1,max}}$ . At low  $v_{\infty,v_1=0}$ , SMA flow diverters do not exhibit significant transformation resulting in behaviour similar to the linear designs. At high  $v_{\infty,v_1=0}$ , the nonlinear relation is due to the significant amount of transformation in the SMA material that allows the diverter to quickly close.

#### 4.3.2.5 Coupled FSI Analysis

To serve as a verification of the computational results with the uncoupled method, an FSI model using the serial coupling scheme is developed. Due to the computational cost associated with running the coupled analysis, only one flow diverter

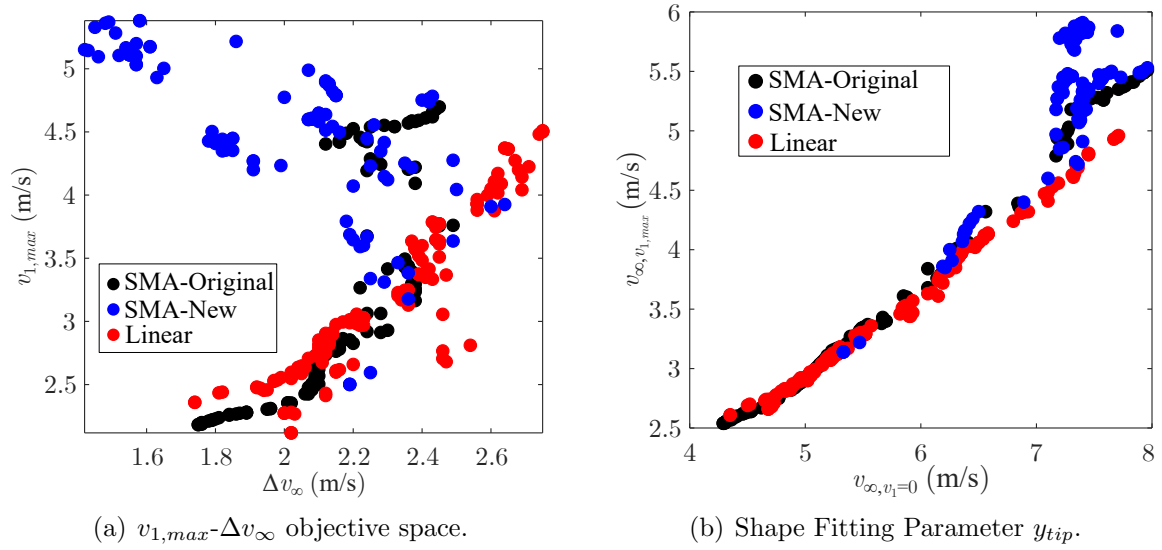


Figure 4.24: Comparison of all three optimizations.

design is considered. The chosen design is the sample investigated in Section 4.3.2.3 ( $t_{sma}=0.19$  cm,  $l_{sma}=9.7$  cm,  $y_{tip}^0=0.005$  m and  $D_2^0=0.025$ ). Note that this is also the median design from the optimizations. A design on the non-dominated frontier is not considered as the FSI model is developed concurrently with the optimization.

Due to the large deformation and contact between the flow diverter and tunnel floor, a single mesh is not sufficient in the fluid model. Instead, an overset mesh scheme is implemented (see Fig. 4.25) with two meshes: 1) the slave mesh consisting of the flow diverter, splitter wall, and a surrounding fluid volume, and 2) the master mesh consisting of the tunnel. For the master mesh, the mesh size in the vicinity of the flow diverter and splitter wall is decreased to allow for adequate interpolation between the outer boundary of the slave mesh and the master mesh. The resulting fluid model consists of 730,000 elements (560,000 prism and 170,000 hexahedron). In the structural domain, the deformable shell is replaced by a deformable solid that is meshed with 776 brick elements of type C3D20R (four elements through the

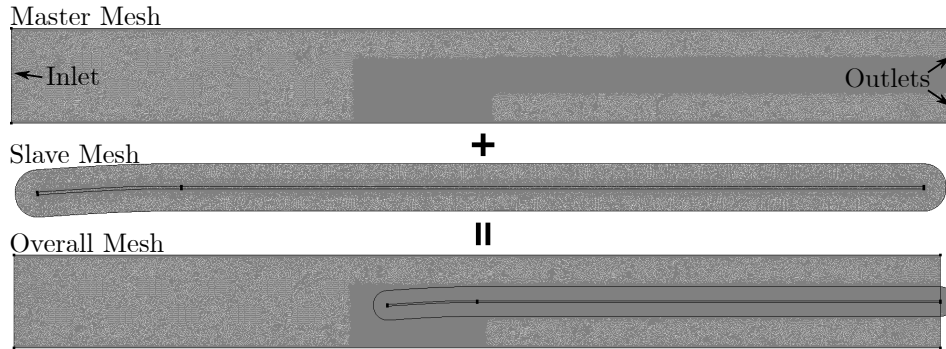


Figure 4.25: Overset mesh implementation of fluid model for FSI analysis of the SMA flow diverter.

thickness)<sup>10</sup>. The interface between the structure and fluid domains is the outer mold line of the flow diverter. All boundary conditions (walls, outlets, symmetry, etc.) from the CFD and static FEA models are still applied. Since this model is developed concurrently with the optimization, the ambient temperature is set to value considered during the optimization (290 K).<sup>11</sup>

Prior to conducting the FSI analysis, steady CFD analysis is performed to develop the flow field for an initial freestream inlet velocity of 1 m/s. Using this as initial conditions, FSI analysis is then performed with a time step of 0.0005 s in both the structure and fluid solvers. During the analysis the inlet velocity is at 1 m/s for 0.1 s to stabilize the structure. Then the velocity is linearly increased to 6.5 m/s over 5 s.

Figure 4.26 shows the response of the shape fitting parameters and outlet velocity relative to the inlet velocity for both the uncoupled SAA and FSI solutions. Both solutions match well for low inlet velocities indicating that the uncoupled solution is

<sup>10</sup>Continuum shell elements are more preferable to use in this problem compared to brick elements. However, the constitutive model used to capture SMA response is not compatible with continuum shell elements.

<sup>11</sup>Note that this is different than the ambient temperature of the sample design in Section 4.3.2.3 which is performed prior to the optimization and FSI analysis.

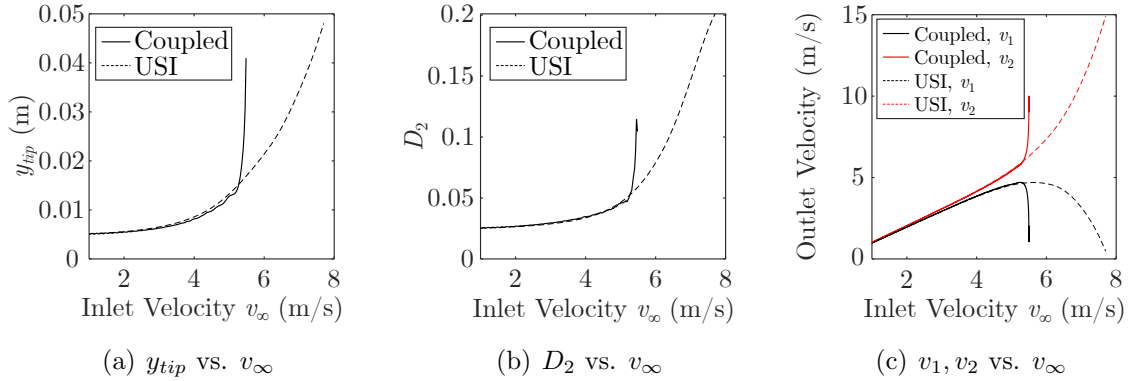


Figure 4.26: Shape fitting parameters and outlet velocity from USI and coupled solutions for multiple inlet velocities.

accurate for low deformation. However, at approximately 5.2 m/s, the flow diverter in the coupled solution rapidly deforms towards the closed position while in the uncoupled solution the diverter is only 34.2% closed. Note, that this rapid closing leads to destabilization of the coupled analysis. Computational cost to perform the analysis until it destabilizes is 41 hr with  $I^f=48,880$  and  $I^s=8,400$  (standard workstation, 10CPU and 1CPU for the fluid and structure solvers, respectively)<sup>12</sup>. Assuming this computational cost for each design, generating Fig. 4.22 with FSI analysis requires  $\approx 6400$  hr with  $\approx 7,625,000$  and  $\approx 1,310,000$  fluid and structure increments. Both the time and number of solution increments are orders of magnitude higher than the uncoupled method.

Due to the rapid deformation of the flow diverter at 5.2 m/s, it is possible that at higher velocities, two shape fitting parameters are not sufficient to accurately describe the deformed shape of the flow diverter during FSI analysis. The diverter may be exhibiting a shape that promotes a large pressure loading. An improved shape fit with an additional fitting parameter may yield a USI solution that better

<sup>12</sup>Using 10CPU for the structure solver only reduced computational time to 39.5 hr.

matches the coupled solution. Fluid and structure evaluations to develop surrogate training data are reperformed utilizing a quadratic CST equation for the shape fit in the following form

$$\zeta = \psi(1 - \psi)\left[\frac{1}{2}D_1(1 - \psi)^2 + D_2\psi(1 - \psi) + 2D_3\psi^2\right] + \psi\frac{y_{tip}}{x_{tip}}. \quad (4.21)$$

In the structure domain, the same LHS using the 135 variations of the pressure fitting parameters is performed, and shape fitting parameters corresponding to the new shape fit are extracted. In the fluid domain, instead of performing a four-level full factorial (which would require 256 fluid evaluations), an LHS with 64 variations of the shape fitting parameters is performed. Surrogate models are then developed and new USI solutions are obtained. As shown in Fig. 4.27, the additional shape fitting parameter has not improved the USI solution, suggesting that the rapid divergence is due to another factor.

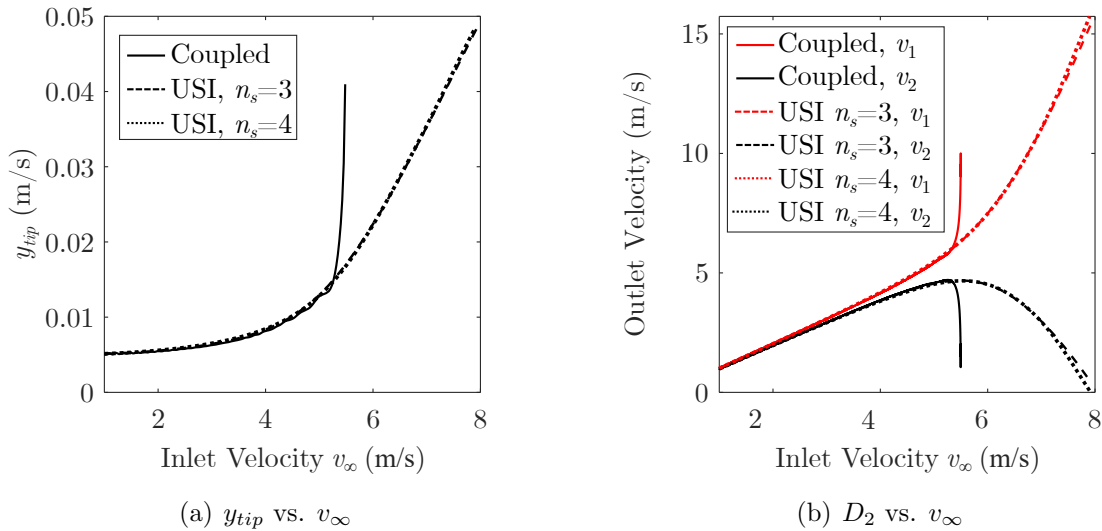


Figure 4.27: Tip displacement and outlet velocity from coupled FSI and USI solutions with  $n_s=3$  and  $n_s=4$  for multiple inlet velocities.

Prior to the significant deformation, oscillations in both  $y_{tip}$  and  $D_2$  are present suggesting that the diverter may be behaving dynamically. This behavior of the diverter in flow is further investigated by performing another FSI analysis, but the freestream velocity is increased to 5 m/s instead. As shown in Fig. 4.28, once the constant inlet velocity of 5 m/s is reached, the diverter begins to oscillate with increasing amplitude that destabilizes the analysis. This suggests that in dynamic fluid flow at high inlet velocities, the flow diverter does not exhibit the desired time-averaged steady equilibrium behavior that the uncoupled method predicts. Instead, the growing oscillations indicate that the diverter may be fluttering. Introducing numerical damping may limit the dynamic behavior. As the current implementation of the uncoupled method only predicts SAA solutions of the final or time-averaged configurations, the dynamic behavior exhibited by the diverter cannot be accounted for. Note that if the analysis had not destabilized, it is possible that the uncoupled solution would have represented a time-averaged configuration of the coupled solution similar to the aeroelastic wing example from Section 4.1.4.

To provide an initial assessment of the dynamic behavior of the flow diverter using the uncoupled method, the free-response/divergence prediction from Section 4.2 is used. Using the USI solutions of the pressure fitting parameters from both shape fits as inputs, static structure analysis is performed for each considered freestream velocity, followed by an eigenvalue analysis about the deformed state. Figure 4.29, shows the eigenvalues of the first four modes of the flow diverter relative to freestream velocity along with the mode shapes. The first mode exhibits strengthening with increasing freestream velocity while the other mode shapes exhibit weakening. Thus, as inlet velocity is increased, the flow diverter may exhibit larger oscillations based on the higher modes. All four modes exhibit a discontinuous change in eigenvalue at an inlet velocity of 6.35 m/s which corresponds with the onset of phase transformation.

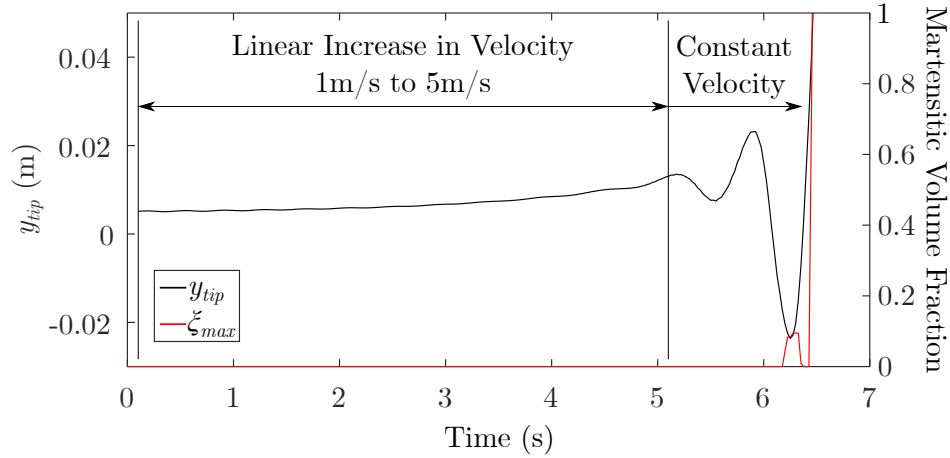


Figure 4.28: Tip displacement and maximum martensitic volume fraction of the diverter in fluid flow with inlet velocity increasing from 1 m/s to 5 m/s.

This suggests that the superelastic behavior of the SMA material may be leading to loss of stability of the flow diverter at high velocities. This can be further seen in Fig. 4.28 with the maximum martensitic volume fraction. As the flow diverter oscillates at higher velocities during the FSI analysis with increasing amplitude, the deformation initiates phase transformation possibly leading to further deformation as the diverter becomes unstable. Since the uncoupled method only predicts the mean response of the flow diverter it is unable to account for the amplitude of the oscillation which may be generating undesirable dynamic behavior.

Future work with the uncoupled method will need to incorporate better predictions of dynamic behavior or, at a minimum, indicate the flow condition at which an uncoupled solution represents the time-averaged configuration instead of the final equilibrium configuration. While matching the FSI solution for all freestream velocities is desirable, it is not critical for this problem as it is purely theoretical and used only to develop/test an optimization scheme with the uncoupled method.

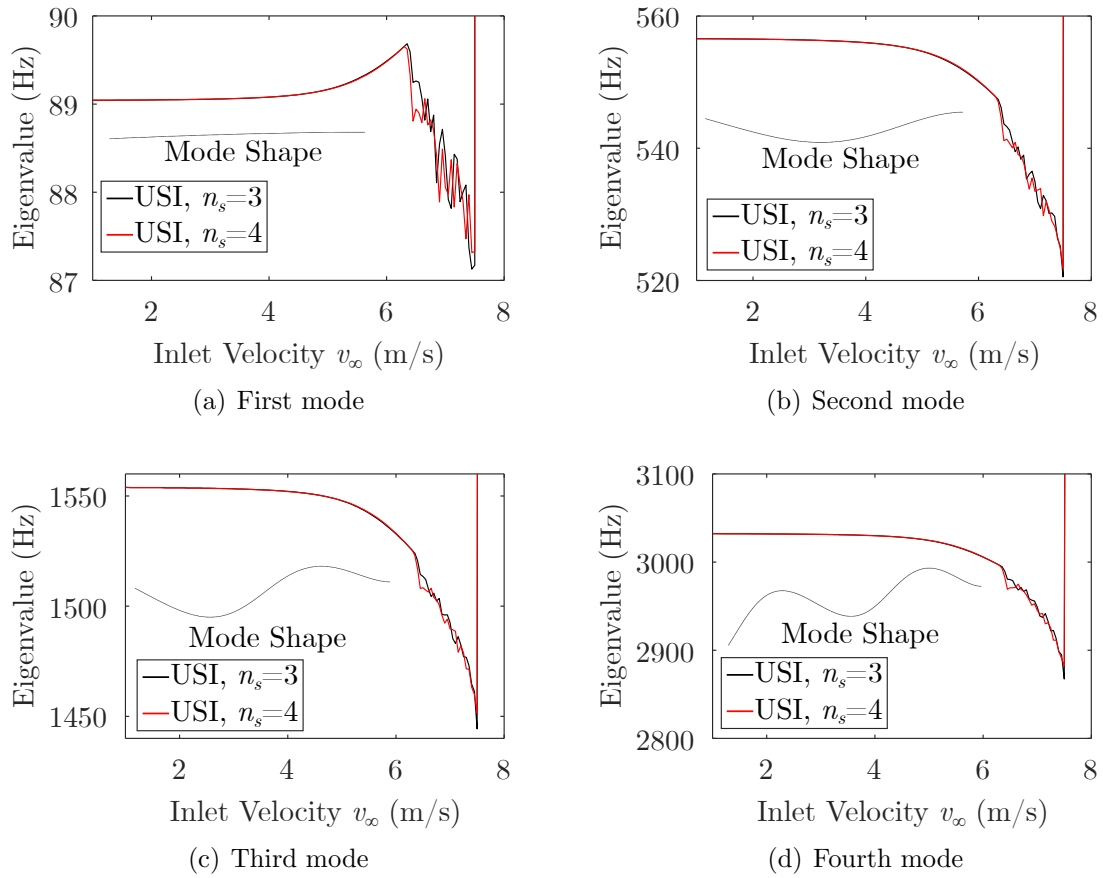


Figure 4.29: Eigenvalues for first four mode shapes with  $n_s=3$  and  $n_s=4$  for multiple inlet velocities.

## 5. APPLICATION OF UNCOUPLED METHOD TO MODEL SCALE SLAT-COVE FILLER

Focus now returns to the motivating problem of this work, the SMA SCF. The uncoupled method presented in this work is now applied to the SMA SCF. A brief description of the models is provided, followed by development of the shape and pressure coefficient fits, and presentation of preliminary results.

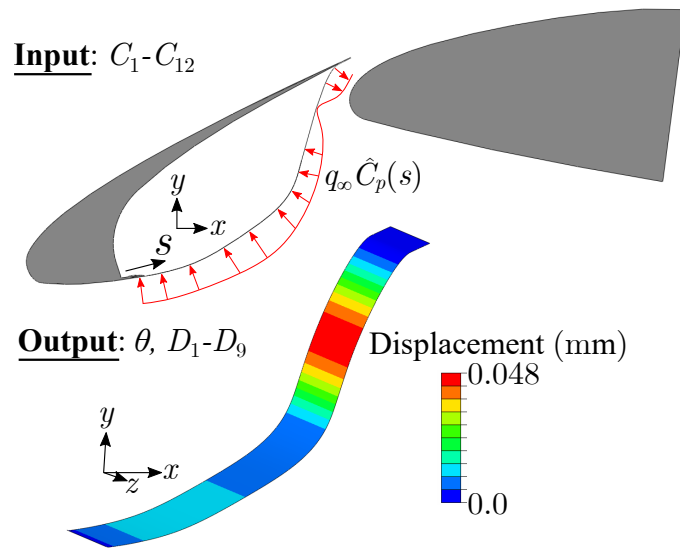
### 5.1 General Descriptions of Fluid and Structure Models

The structure and fluid models used in this chapter are identical to the ones used in Section 2.2. For brevity only a brief description of the models is provided here. The reader is encouraged to read the more detailed descriptions of the model in Section 2.2.

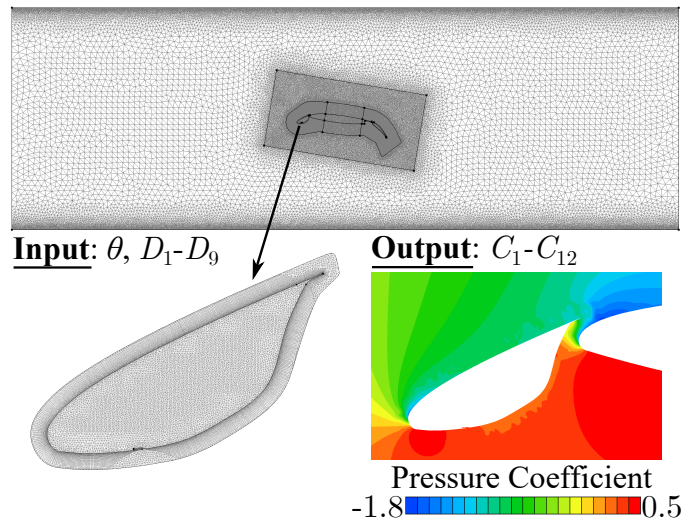
The structure model (see Fig. 5.1(a)) consists of the slat/SCF OML<sup>1</sup>, modeled as a deformable shell, and rigid bodies for the hinge, main wing leading-edge, and slat. Material response of the SMA SCF is captured by the Lagoudas constitutive model, which is implemented in Abaqus as a UMAT. The SCF portion of the shell is tied to the rigid body slat near the trailing edge and to the hinge. The slat portion of the shell is tied to the rigid body slat such that it is also rigid. All components are one element wide in the spanwise direction, and symmetry conditions are applied to edges of the OML shell aligned with the X-Y plane. For the implementation of the uncoupled method to the SCF, pressure distributions (approximate fits or CFD extracted data) are applied to the SCF as point clouds of  $x$ ,  $y$ ,  $z$ , and  $P$  data. Static analysis evaluates SCF response to each considered loading, and the resulting

---

<sup>1</sup>Recall that the entire OML of the slat/SCF is used so that solvers are coupled with a single closed volume.



(a) Structure domain



(b) Fluid domain

Figure 5.1: Structure and fluid domains of SMA SCF with uncoupled method applied.

deformed shape and fitting parameters are extracted.

The fluid model (see Fig. 5.1(b)) is a 2D slice of the wing and test section of the Texas A&M University 3 ft-by-4 ft (0.91 m-by-1.22 m) wind tunnel. An overset mesh is used to accommodate the large deformations associated with high lift device

articulation. Specifically, the slat/SCF and flap are moveable with deformable slave meshes while the main wing and surrounding fluid volume of the test section are the master mesh. Boundary conditions applied to the model include 1) smooth, no-slip/penetration walls on the surface of the wing, ceiling, and floor, 2) freestream flow at the inlet, and 3) zero static pressure at the outlet. Turbulent effects due to separation and recirculation are captured with the  $k$ - $\omega$  turbulence model [110]. For this work approximately laminar flow at the inlet is assumed ( $k$  and  $\varepsilon$  set to  $0.0001 \text{ m}^2/\text{s}^2$  and  $0.0001 \text{ m}^2/\text{s}^3$ , respectively). For each considered SCF shape, steady CFD analysis is performed and the resulting pressure distribution and fitting parameters are extracted. Freestream velocity is set to  $25 \text{ m/s}$  for all CFD analyses used in surrogate model construction.

Currently for this work, the uncoupled method is only applied to the case of the slat in a fixed and fully deployed position with the wing at  $8^\circ$  angle of attack relative to the stowed chord. Future work may consider the slat/SCF in different levels of deployment and angles of attack.

## 5.2 Development of Shape and Pressure Coefficient Fits

Figure 5.2 shows the undeformed shape of the SCF and the resulting pressure coefficient distribution obtained from CFD analysis. Both the SCF shape and the pressure coefficient distribution exhibit considerable nonlinear behavior requiring extensive studying to develop accurate fits.

### 5.2.1 Shape Fit

Due to the complex shape of the SCF, the CST method is chosen as the form of the shape fit for the deformed SCF configurations. All CST coefficients  $D_1, \dots, D_{n_{CST}}$ , where  $n_{CST}$  is the number of coefficients, and the rotation of the hinge  $\theta$  are used as shape fitting parameters ( $\mathbf{S}=\{D_1, \dots, D_{n_{CST}}, \theta\}$ ). Unlike the flow diverter and de-

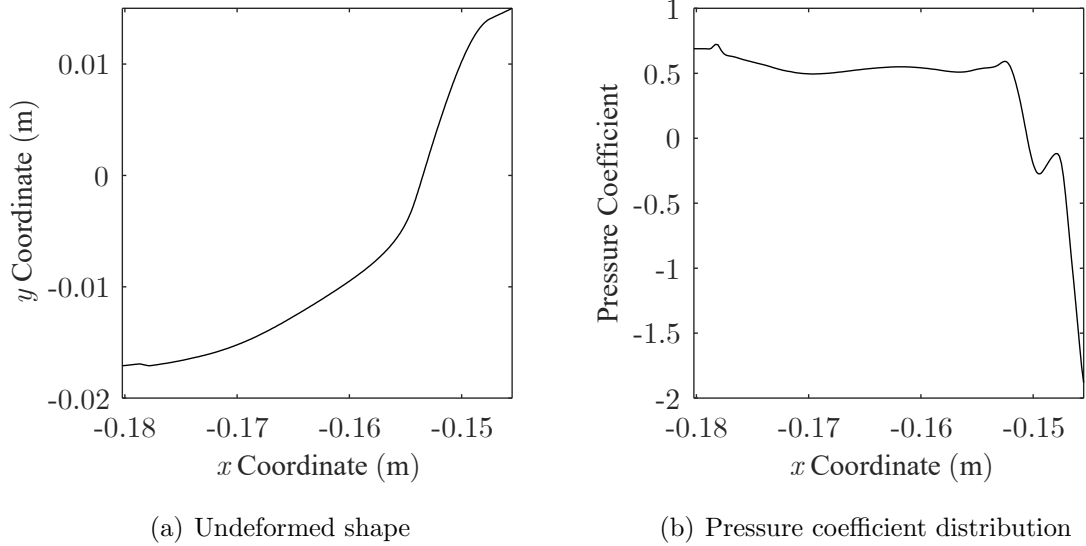


Figure 5.2: Undeformed SCF shape and pressure distribution from CFD analysis using undeformed shape.

formable baffle examples, the shape of the SCF is represented by a  $n_{CST} - 1$  order CST equation of the form:

$$\zeta(\psi) = (1 - \psi) \sum_{i=0}^{n_{CST}} D_{i+1} K_{i,n_{CST}} \psi^i (1 - \psi)^{n_{CST}-i} + \psi \Delta \zeta_{TE}. \quad (5.1)$$

where  $n_{CST}$  is the number of CST shape coefficients. Figure 5.3 illustrates this process of obtaining a shape fit for the SCF from the fitting parameters. The CST method specifically generates the shape of the deformable portion of the SCF (i.e., not the SCF-Hinge Arm or portion of the SCF tied to the slat) in a scaled, rotated, and translated  $\psi$ - $\zeta$  coordinate system. The rotation  $\beta$  and translation  $\Delta x$ ,  $\Delta y$  of this coordinate system compared to the global  $x$ - $y$  system is defined such that ends of the deformable portion of the SCF are aligned with the  $\psi$  axis with one end at the origin. The  $\psi$  component of the rotated/translated SCF geometry is then scaled

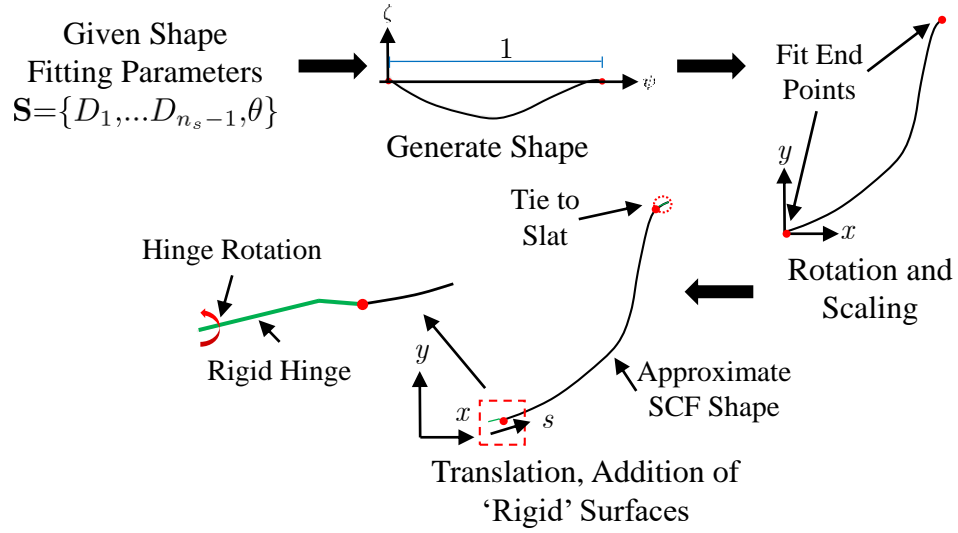


Figure 5.3: Illustration of shape fitting parameters are used to generate SCF shape.

by  $\Delta L$  such that the other end of the deformable SCF is at  $\psi = 1$ .<sup>2</sup> Note that  $\beta$ ,  $\Delta x$ ,  $\Delta y$ , and  $\Delta L$  are dependent on the hinge rotation  $\theta$ . Mathematically, the  $\psi$ - $\zeta$  coordinate system is related to the global  $x$ - $y$  coordinate system by the following coordinate transformation equation:

$$\begin{bmatrix} \psi \\ \zeta \end{bmatrix} = \begin{bmatrix} \frac{1}{\Delta L(\theta)} & 0 \\ 0 & 1 \end{bmatrix} \begin{bmatrix} \cos(\beta(\theta)) & -\sin(\beta(\theta)) \\ \sin(\beta(\theta)) & \cos(\beta(\theta)) \end{bmatrix} \begin{bmatrix} x + \Delta x(\theta) \\ y + \Delta y(\theta) \end{bmatrix}. \quad (5.2)$$

For fluid evaluations with a given set of shape fitting parameters, once the SCF shape is generated in the  $\psi$ - $\zeta$  system, it is transformed into the  $x$ - $y$  system with Eq. (5.2) and the SCF-Hinge Arm and portion of the SCF tied to the slat are added to the geometry. Following a structure evaluation, the process described above and shown in Fig. 5.3 is reversed. The SCF-Hinge arm and portion of the SCF tied to

<sup>2</sup>This scaling leaves  $\zeta$  in units of length.

the slat are removed and then the entire geometry is translated, rotated and scaled into the  $\psi$ - $\zeta$  system using Eq. (5.2). For a given  $n_{CST}$ , the CST coefficients that best describe this modified geometry are then found using a gradient optimization with an objective of minimizing the mean square error between the fit and geometry. Figure 5.4 shows the mean square error between the shape fit and actual geometry for both undeformed and deformed configurations of the SCF. The deformed SCF configuration is from static FEA analysis of a monolithic 0.0508 mm thick SMA SCF subjected to the steady-state pressure loading (see Fig. 5.2(b)) extracted from CFD of the wing at  $8^\circ$  angle of attack in 25 m/s flow. As shown, the error appears to converge for both configurations with nine CST coefficients. The shape fitting parameters for the undeformed SCF configuration and deformed configuration of the monolithic 0.0508 mm thick SCF (values for the ICS) are  $(\theta, D_1, \dots, D_9) = (0^\circ, 0.00003, 0.0042, 0.0082, 0.017, -0.015, 0.083, -0.041, 0.05, -0.016)$  and  $(\theta, D_1, \dots, D_9) = (0.51^\circ, 0.000029, 0.0042, 0.0077, 0.018, -0.02, 0.094, -0.053, 0.051, -0.017)$ , respectively.

The effect of the shape fit on the pressure distribution is also considered. For many of the shape fits shown in Fig. 5.4, steady CFD analysis is performed and the resulting pressure distribution is extracted. Figure 5.5 shows the root mean square error between pressure coefficient distributions of the undeformed SCF for the actual geometry and the shape fit. Additionally, Fig. 5.5 shows a few plots of pressure coefficient versus the normalized distance along the entire SCF  $s$ .<sup>3</sup> Excluding  $s \geq 0.9$ , with nine shape coefficients, the pressure coefficient distribution of the shape fit matches well with the one from the actual geometry. Above  $s = 0.9$ , the distribution from the shape fit is lower. However, this region is near portion of the SCF tied to the slat and thus its influence on the structure should be smaller.

---

<sup>3</sup>For  $s \geq 0.955$ , the SCF is tied to the slat, and thus is not included in the pressure distribution plots in Fig. 5.5

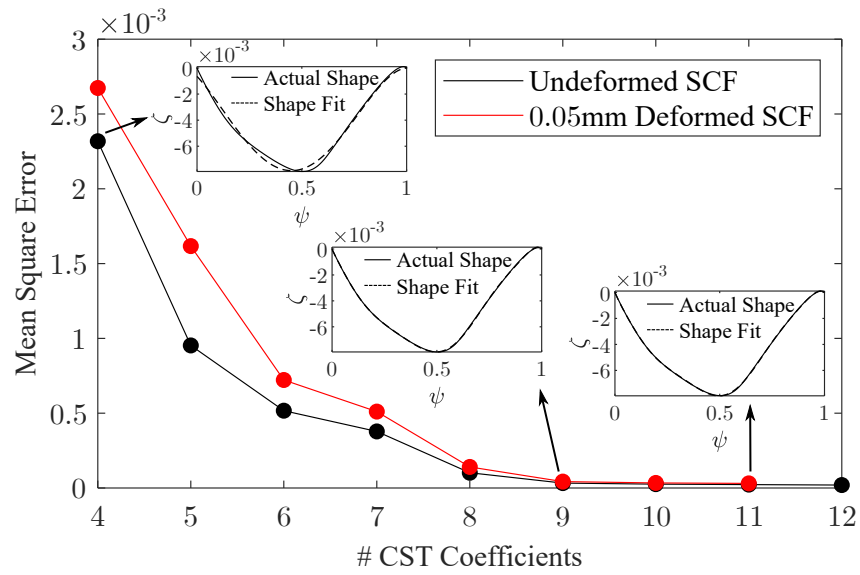


Figure 5.4: Mean square error of shape for different number of CST coefficients.

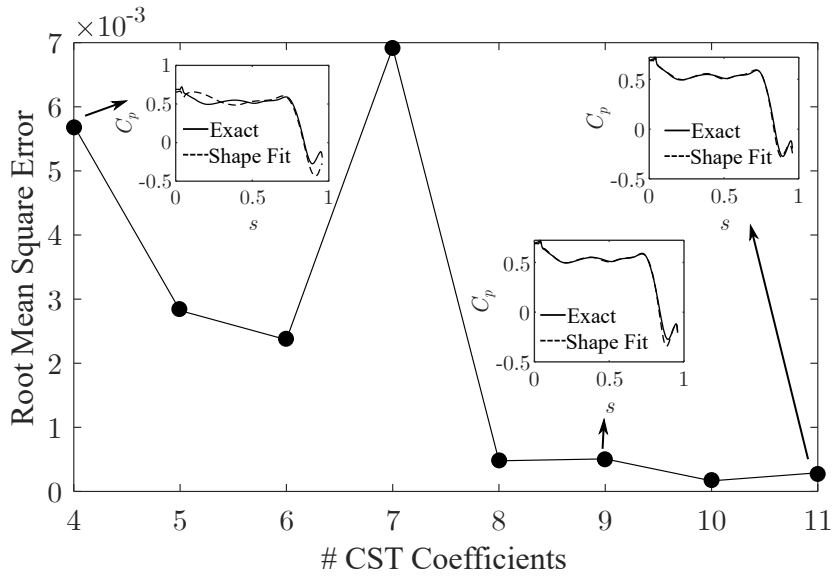


Figure 5.5: Mean square error of pressure for different number of CST coefficients.

### 5.2.2 Pressure Coefficient Fit

The pressure coefficient distribution in Fig. 5.2(b) is highly nonlinear and cannot be fit with a simple polynomial distribution. Instead, similar to the other demonstrations in this work with complex pressure distributions, an RBF of the following form is used as the fit:

$$\hat{C}_p(s) = \sum_{i=1}^{n_p} w_i \Psi(s - s_i) \quad (5.3)$$

where  $s_i \forall i=1, \dots, n_p$  are the  $n_p$  evenly distributed locations along the curve of the SCF from  $s=0$  to  $s=0.955$  for the fitting parameters, and the weights  $w_i$  are solved during calibration by solving a system of equations (see Eq. (4.16)).

Three different RBFs are considered as the functional form of the fit: 1) cubic, linear, and thin-plate spline (TPS). For a given RBF type and number of fitting parameters, the resulting pressure coefficient fit is constructed and the normalized root mean square error (NRMSE) relative to the CFD-computed distributed is computed (see Fig. 5.6). Overall, both TPS and cubic RBFs generate better fits than a linear RBF as the linear RBF requires more fitting parameters to achieve a similar value of NRMSE. At  $n_p$  greater than 12, the TPS and cubic RBFs exhibit approximately the same NRMSE and appear to be converging towards a constant NRMSE. Note that NRMSE is not converging towards zero due to a small peak in the distribution at  $s=0.04$  generated by the discontinuous change in the SCF-hinge arm. Resolving this feature with additional fitting parameters would result in further reduction of error. For this work, a cubic RBF with 12 fitting parameters is deemed sufficient to approximate the distribution. The pressure coefficient fitting parameters that define the distribution from CFD analysis of the undeformed shape (ICS pressure coefficient fitting parameters) are ( $C_1, \dots, C_{12} = 0.69, 0.6, 0.51, 0.51, 0.54, 0.54, 0.51, 0.54, 0.58, 0.44, -0.18, -0.12$ ).

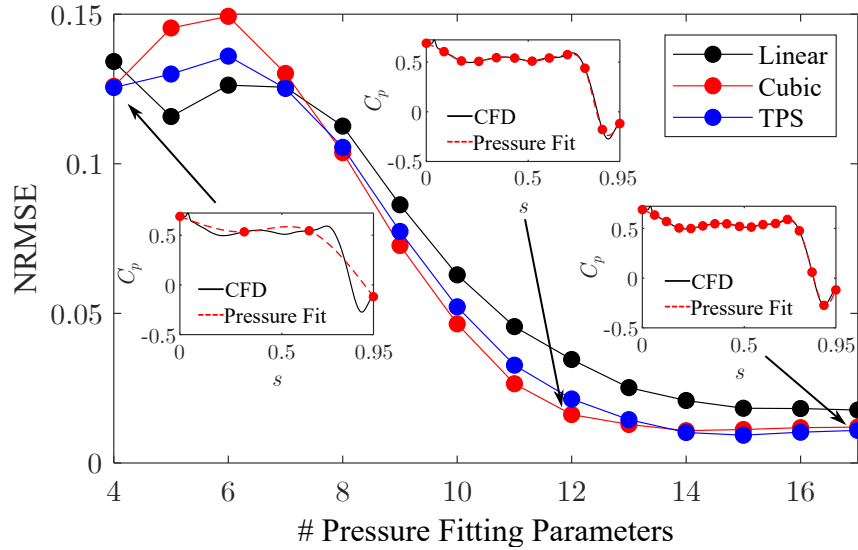


Figure 5.6: Root mean square error of pressure coefficient distribution fit for different RBF types and number of fitting parameters.

### 5.2.3 Determining Significant Fitting Parameters

The developed pressure coefficient and shape fits require a total of 22 fitting parameters ( $n_s=10$ ,  $n_p=12$ ). Unlike the aeroelastic wing example, the parameters are almost evenly split between the structure and fluid domains, thus requiring many structure and fluid evaluations to generate accurate surrogate models.<sup>4</sup> The number of evaluations may be reduced by setting some of the fitting parameters equal to the values from an ICS. Such parameters need to either have low impact on the results or not change significantly between undeformed and deformed configurations.

To sufficiently explore the **C-S** space for evaluation of fitting parameter influence, DOEs based on Taguchi orthogonal arrays are performed. Specifically for the structure model, a Taguchi L64 with bounds of  $\pm 30\%$  from the pressure fitting pa-

<sup>4</sup>Based on Jin's work [56], the number of evaluations for an LHS of the structure and fluid models are 273 and 198, respectively.

rameters of the ICS are used, while the fluid model is evaluated with a Taguchi L27 with bounds of  $\pm 10\%$  for the CST coefficients from the ICS of the 0.0508 mm SCF and  $0^\circ$  to  $10^\circ$  for  $\theta$ . These bounds are deemed sufficient to evaluate the significance of each fitting parameter. For the hardware used (standard workstation 1CPU and 10CPU for the structure and fluid solvers, respectively), the average computational time required for each structure and fluid evaluation is approximately 1.14 min (10 solution increments) and 2 hr (2,420 solution increments), respectively. Thus the serial computational cost to perform the Taguchi DOEs is approximately 55.2 hr (2 hr if performed in parallel) requiring 640 structure and 65,340 fluid solution increments. The influence of each shape fitting parameter on each of the pressure coefficient fitting parameters (and vice versa) are evaluated using a statistical technique known as analysis of variance (ANOVA) to obtain the  $p$ -value [144], a measure of statistical significance between an input and an output. Note that a  $p$ -value less than 0.05 indicates statistical significance. Table F.1 and Table F.2 in Appendix F show the  $p$ -values associated with the structure and fluid DOEs, respectively.

Based on the DOEs and  $p$ -values, shape fitting parameters  $D_1$ ,  $D_2$ , and  $D_9$  are set as constants as they have no statistically significant effect on the pressure fitting parameters during the fluid DOE and exhibit small changes between the undeformed and deformed configurations. Additionally, during the structure DOE,  $D_2$  and  $D_9$  only change by 13% and 6% respectively. While  $D_8$  has a significant influence on  $C_{10}$ - $C_{12}$ , it only changes by 4% during the structure DOEs, and thus, is also set as a constant. Examining the influence of the pressure coefficient fitting parameters,  $C_1$ ,  $C_{11}$ , and  $C_{12}$  are set as constants since they have no statistically significant effect on any shape fitting parameter. In total, four shape and three pressure coefficient fitting parameters are set to constants from the ICS, significantly reducing the number of evaluations needed to adequately explore the **C-S** space with an LHS for the structure

(165 evaluations, 39% reduction) and fluid model (84 evaluations, 58% reduction).

### 5.3 Uncoupled Solutions for the SCF

With the **S-C** reduced by setting some of the fitting parameters equal to ICS values, focus shifts to finding uncoupled solutions for a few model scale SCF designs. Uncoupled solutions at a single freestream velocity are first discussed, followed by presentation of results at multiple freestream velocities and estimations of dynamic behavior and divergence (Method 4.2).

#### 5.3.1 Uncoupled Solutions for Single Freestream Velocity

In the fluid domain, an LHS of steady CFD analyses is performed with 84 SCF configurations based on variations of shape fitting parameters  $D_3$ - $D_7$  and  $\theta$  (see Fig. 5.7) while the other parameters are set to constant values of the ICS for a 0.0508 mm-thick SCF ( $D_1=0.000029$ ,  $D_2=0.0042$ ,  $D_8=0.051$ ,  $D_9=-0.017$ ). Bounds of the LHS are shown in Table 5.1. Bounds are set as percent changes of the ICS solution and based on the change of the shape fitting parameters between the undeformed and deformed SCF configurations while also ensuring that the resulting SCF shape does not intersect the outer mold line of the slat. The cost of each fluid analysis is approximately 2 hr (2420 solution increments). Using the results from the LHS as training points, linear and cubic RBF fluid surrogate models of the following form are developed:

$$C_i = \mathcal{F}_i^f(\mathbf{S}) = \sum_{k=1}^{84} w_{i,k}^f \Psi(\|\mathbf{S} - \mathbf{S}^k\|_2) + \gamma_i^f \cdot \{\mathbf{S}, 1\} \quad \forall i = 1, 9. \quad (5.4)$$

In the structure domain the following SCF designs are considered: 1) 0.0508 mm monolithic SCF, 2) 0.04572 mm monolithic SCF, and 3) a multi-thickness SCF with

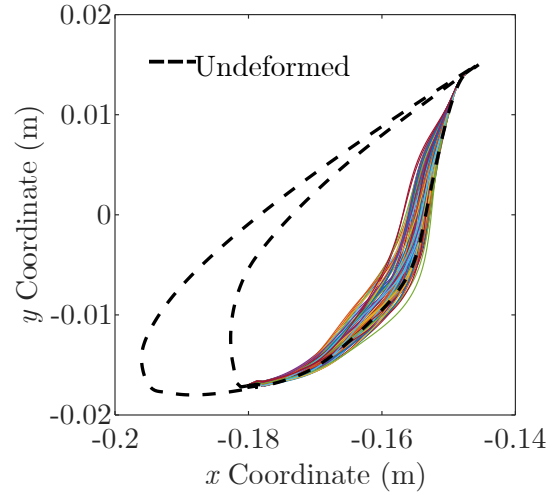


Figure 5.7: Shapes considered during fluid LHS of SCF. Dashed black line indicates the slat and undeformed SCF.

Table 5.1: Surrogate model input bounds of fitting parameters for SCF.

Shape Fitting Parameter	Bounds	Pressure Fitting Parameter	Bounds
$D_3$	0.005 - 0.01	$C_2$	0.4 - 0.8
$D_4$	0.015 - 0.022	$C_3$	0.35 - 0.68
$D_5$	-0.032 - -0.015	$C_4$	0.35 - 0.68
$D_6$	0.085 - 0.10	$C_5$	0.38 - 0.71
$D_7$	-0.08 - -0.042	$C_6$	0.37 - 0.71
$\theta$ ( $^\circ$ )	-0.5 - 10.7	$C_7$	0.35 - 0.68
-	-	$C_8$	0.37 - 0.71
-	-	$C_9$	0.4 - 0.75
-	-	$C_{10}$	0.3 - 0.57

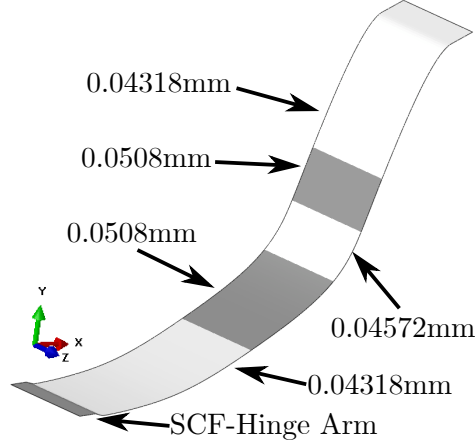


Figure 5.8: Distribution of thickness for multi-thickness SCF.

thicknesses distributed as shown in Fig. 5.8<sup>5</sup>. For each SCF design, a structure LHS is performed, analyzing the SCF response using static FEA to 165 variations of the pressure loading based on the pressure fitting parameters. Bounds for the LHS are shown in Table 5.1 and are based on approximately  $\pm 30\%$  of the ICS solution such that training data for the structure surrogate should be in the region of the **C-S** space near the USI solution. Note that structure runs for this example are not performed in batches (i.e., multiple copies subjected to different loadings). Under sufficient loading, the hinge may begin to rotate, bringing the SCF into its stowed configuration. However, the dynamic nature of the SCF stowage cannot be captured in static analysis and may destabilize it. Similar to the fluid model, cubic and linear RBF surrogates are calibrated for the structure model as:

$$S_i = \mathcal{F}_i^s(\mathbf{C}) = \sum_{k=1}^{165} w_{i,j}^s \Psi(\|\mathbf{C} - \mathbf{C}^j\|_2) + \gamma_i^s \cdot \{\mathbf{C}, 1\} \quad \forall i = 1, 6. \quad (5.5)$$

<sup>5</sup>Thickness distribution is randomly assigned to mimic a design that could be potentially considered during design studies/optimization.

Once surrogate models are constructed (serial computational cost of approximately 171 hr with  $I^f=203,280$  and  $I^s=1,650$ ), USI and USiS solutions for each design are obtained. As shown in Tables F.3, F.4, and F.5 in Appendix F, overall the shape and pressure fitting parameters for the USI and USiS solutions are of similar value for all considered designs. Average percent difference for the shape and pressure coefficient fitting parameters, including those in the USI solution fixed to constant values, for all considered designs are 5.2% and 5.6%, respectively. Shape fitting parameters  $D_1$  and  $\theta$  exhibit the largest change between the USI and USiS solutions. This is understandable as the value of  $\theta$  is quite small and  $D_1$  is the shape coefficient most directly effected by it. Ignoring these two shape coefficients reduces the average percent change to 1.1%. With regards to the pressure coefficient fitting parameters, the value of the average percent difference is mainly due to  $C_{11}$  and  $C_{12}$ , which exhibit the largest difference between the two uncoupled solutions. Note that both values are deemed insignificant based on results of the Taguchi DOEs, thus large differences between the uncoupled solutions for these parameters should not effect the overall solution. Overall, the low difference between the shape and pressure fitting parameters indicate that the fits adequately approximate the shape and pressure distribution of the SCF, and that the surrogate models are capturing relevant physical phenomenon. Additionally, as an initial measure of error, the results suggest that the uncoupled method is accurate for this problem.

To verify the uncoupled solutions, fully coupled serial FSI analysis is conducted for each of the SCF designs. Shape and pressure coefficient fitting parameters are extracted from the time-average equilibrium configuration. Each analysis is conducted with a time span of 0.5 s and time step of 0.00005 s. The computational cost of each FSI analysis is approximately 20.5 hr ( $I_f=20,000$ ,  $I_s=10,000$ ) with a standard workstation (10CPU and 1CPU for the fluid and structure solvers, respectively). This is

faster when compared to the serial cost of obtaining one solution using the uncoupled method (226.4 hr including the Taguchi DOEs with  $I_f=268,600$  and  $I_s=2,290$ ). However, if both the Taguchi DOEs and LHS evaluations for surrogate training are separately run in parallel, computational cost of the uncoupled method reduces to 4 hr (2 hr for each set of fluid evaluations). Additionally, evaluating new designs using the uncoupled method only requires a serial computational cost of approximately 2.8 hr (7.2 times faster than the serial scheme), or if all structure evaluations are performed in parallel, a cost of 1.14 min (1,080 times faster). As shown in Tables F.3, F.4, and F.5 in Appendix F, the fitting parameters extracted from FSI analysis are of similar value to both the USI and USiS solutions. Excluding parameters  $D_1$ ,  $\theta$ ,  $C_{11}$ , and  $C_{12}$ , the average percent error of the USI and USiS solutions relative to the FSI solutions are 1.7% and 1.9%, respectively.<sup>6</sup>

Accuracy of the uncoupled method is further demonstrated by examining the SCF shape generated by the shape parameters in the  $\psi$ - $\zeta$  space. Figure 5.9 shows the error  $\Delta\zeta$  measured as the difference in  $\zeta$  between the coupled solution and either the uncoupled solutions (USI and USiS), the ICS solution, or the undeformed shape (for reference). For reference, the curvilinear length of the SCF is 53.3 mm. The NRMSE associated with each curve in Figure 5.9 relative to the coupled solution is shown in Table 5.2. For all three designs, the USI and USiS solutions exhibited a lower NRMSE as compared to the ICS solution, demonstrating how the ICS solution is not sufficient for estimating SCF response in dynamic fluid flow. As seen in Fig. 5.9, the USI curves oscillate about the USiS solution. This result is not surprising as the USiS solution is computed from the fits of the deformed shape and pressure distribution allowing for “smoothing” of any numerical features (such as oscillations) introduced by the

---

<sup>6</sup>Note that the justifications for the differences in these parameters between the USI and USiS solutions are still true for the difference between the uncoupled and coupled solutions.

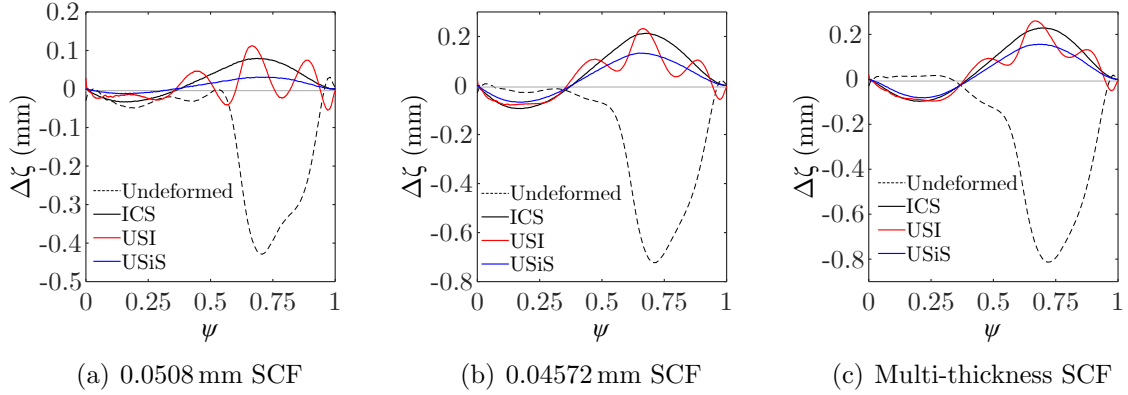


Figure 5.9: Error (measured as  $\Delta\zeta$ ) relative to the coupled solution for each design. For reference, the curvilinear length of the SCF is 53.3 mm

fits and for improvement of the uncoupled solution as clearly shown in Table 5.2, which shows a significant drop in NRMSE between the USI and USiS solutions.

Overall, these results show that the uncoupled solution for a single freestream velocity is accurate for this problem. The ability to find accurate FSI solutions for multiple different SCF designs, especially the multi-thickness SCF, without performing the expensive coupled analysis is critical in future design efforts of the SCF such as the tailoring work of the full scale SCF from Chapter 2 where the interaction between the fluid and structure is strong.

### 5.3.2 Uncoupled Solutions for Multiple Freestream Velocities and Divergence

While the bounds of the pressure fitting parameters for the LHS of the structure model from the previous section are sufficient to find USI solutions for a freestream velocity of 25 m/s, they are not large enough to enable calculation of USI solutions for high freestream velocities. A new structure LHS (bounds shown in Table 5.3) with 165 pressure distributions is performed for the 0.0508 mm monolithic SCF. The bounds are chosen to consider a wide range of pressure distributions that the SCF

Table 5.2: NRMSE (%) relative to the coupled solution in  $\psi$ - $\zeta$  frame for each SCF design.

Case	0.0508 mm SCF	0.04572 mm SCF	Multi-thickness SCF
Undeformed	2.37	4.06	4.74
ICS	0.55	1.47	1.59
USI	0.52	1.2	1.42
USiS	0.22	0.93	1.11

may be subjected to for a variety of freestream conditions. Of the 165 considered distributions, static FEA only converged for 162 of them. Failed evaluations exhibited sufficient loading to begin stowage of the SCF. The successful runs are used as training points to generate a new structure surrogate model. A new structure LHS with similar bounds is also performed for the 0.04572 mm monolithic SCF. However, for brevity discussion of results is focused on the 0.0508 mm monolithic SCF.

Additionally, the fluid surrogate model is recalibrated using an additional 84 evaluations from an LHS with slightly modified bounds on the shape fitting parameters. With these new surrogate models, USI and structure USiS solutions are obtained for a number of freestream velocities. As shown in Fig. 5.10, the shape fitting parameters of both uncoupled solutions show the same general trends. Note that static FEA fails to converge to a solution above a freestream velocity of 34 m/s. Since the USI solution is from a mathematical function, it is continuous while the USiS solution appears to be discontinuous. Additionally, at low freestream velocities, both solutions are of similar value indicating that the uncoupled method is accurate in that region. However, at approximately 31 m/s the two solutions begin to diverge for most of the shape fitting parameters, with the USiS solution rapidly changing

Table 5.3: Surrogate model input bounds of pressure coefficient for 0.0508 mm monolithic SCF to find solutions at multiple freestream velocities.

<b>Pressure Fitting Parameters</b>	<b>Bounds</b>
$C_2$	0.12 - 1.45
$C_3$	0.1 - 1.25
$C_4$	0.1 - 1.25
$C_5$	0.1 - 1.3
$C_6$	0.1 - 1.3
$C_7$	0.1 - 1.2
$C_8$	0.1 - 1.3
$C_9$	0.1 - 1.4
$C_{10}$	0.09- 1.35

with velocity. This may be due to all of the pressure fitting parameters approaching upper limits of the structure surrogates (see Fig. 5.11) and possible lack of sufficient training points in that region of the  $\mathbf{C} - \mathbf{S}$  space as the bounds of the LHS are quite large. Examining the deformed shapes from which the USiS fitting parameters are extracted (see Fig. 5.12(a)) further shows the large change in shape with increasing velocity. In general, as the freestream velocity is increased, the SCF deforms inward towards the cove wall. Additionally, with each incremental increase in freestream velocity, especially at high velocities, the deformation of the SCF grows significantly. Based on the behavior of the shape fitting parameters at high velocities and the change of SCF configuration between 33 m/s and 34 m/s the SCF may be nearing an instability, especially since static FEA cannot converge for solutions above 34 m/s.

Similar to the previous demonstrations with the SMA diverter and the two plate/bar assembly, large bounds for the surrogate models can lead to inaccura-

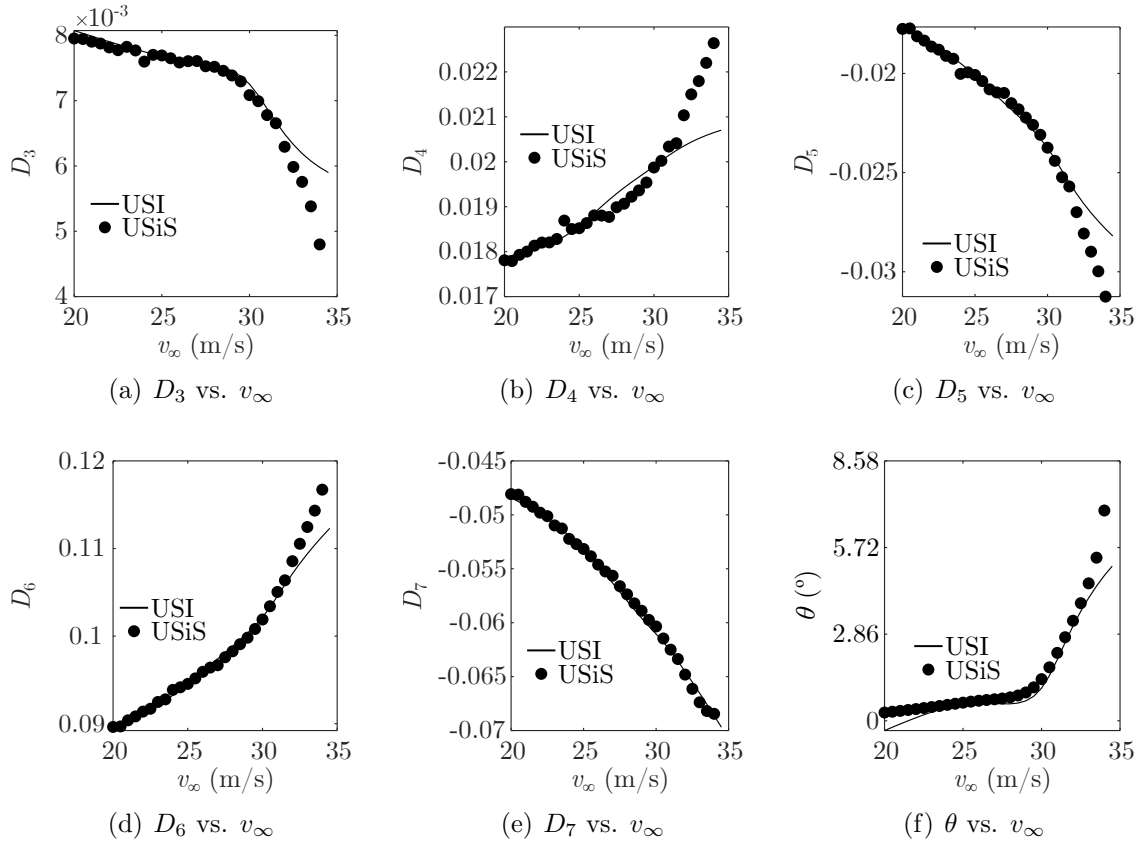


Figure 5.10: Shape fitting parameters from USI and USiS solutions for multiple freestream velocities from 0.0508 mm monolithic SCF.

cies locally. As shown in Fig. 5.12(b) at a freestream velocity of 25 m/s, the new surrogate models result in a USiS that is of similar shape to the ICS instead of the FSI solution. NRMSE of the USI and USiS solutions are 0.67 and 0.54, respectively. This increase in error of the uncoupled solution relative to the FSI solution indicates that more training points must be considered if accurate USI solutions are to be obtained for a large range of freestream velocities.

While there is some error in the current surrogate models, the uncoupled solutions are deemed sufficient to be used in estimates of free response behavior and divergence. Following Method 4.2 in Section 4.2, for each structure USiS solution,

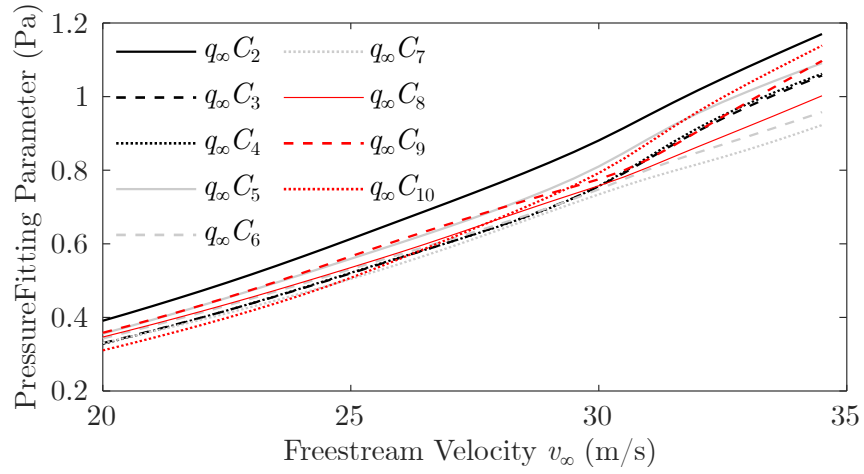


Figure 5.11: USI pressure fitting parameters for multiple freestream velocities from 0.0508 mm monolithic SCF.

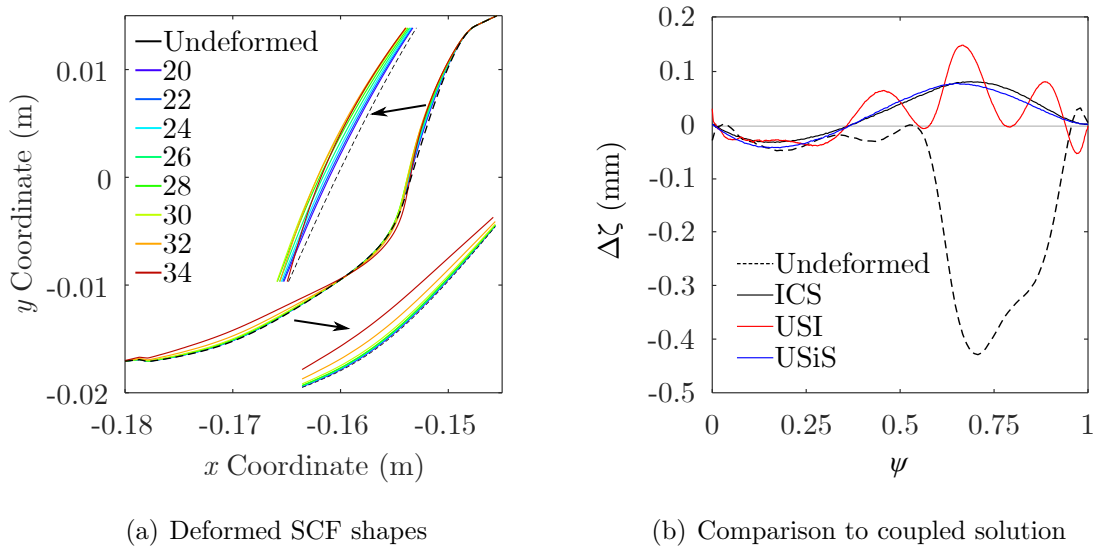


Figure 5.12: Deformed SCF shapes for multiple freestream velocities and comparison to FSI solution at 25 m/s freestream velocity.

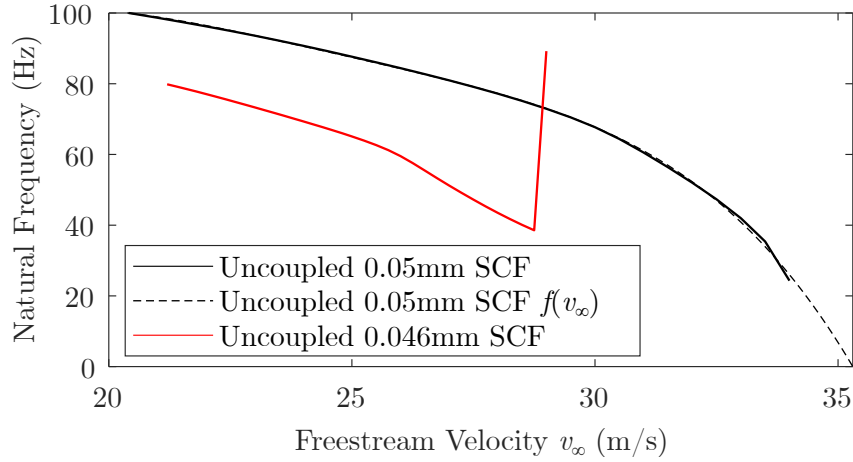


Figure 5.13: Natural frequency vs. freestream velocity for two monolithic SCF designs.

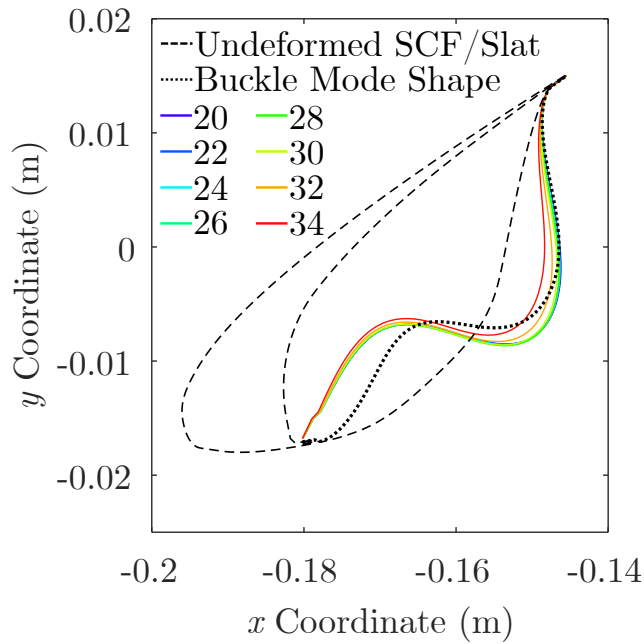
eigenvalue analysis is performed on the deformed structure and both the first mode shape and natural frequency  $\omega$  are extracted. For reference, the natural frequency of the undeformed 0.0508 mm and 0.04572 mm monolithic SCFs are 165 Hz and 148 Hz, respectively. Figure 5.13 shows the natural frequency of the two SCF designs for different freestream velocities. Recall that for the divergence prediction with the uncoupled method (Section 4.2), aeroelastic divergence occurs when the natural frequency of the deformed structure goes to zero or possibly when it suddenly increases. As shown in Fig. 5.13, the natural frequency response for both SCF designs decreases in an approximately exponential manner. The natural frequency does not reach zero for the 0.0508 mm monolithic SCF as static FEA fails to converge to solutions above 34 m/s. Instead, a fourth order polynomial  $\omega=f(v_\infty)$  is constructed and used to extrapolate the natural frequency towards zero which suggests that aeroelastic divergence will occur by a freestream velocity of 35 m/s. As shown in Fig. 5.14(a), the mode shapes of the SCF are of similar form. However, similar to the results in

Fig. 5.12(a), as freestream velocity increases the mode shape shifts further towards the cove wall at an increasing rate. For the 0.04572 mm monolithic SCF, the natural frequency response exhibits a large discontinuous change at a freestream velocity of 29 m/s, and is believed to be indicative of aeroelastic divergence. This discontinuous change is further seen in the mode shapes of the structure (Fig. 5.14(b)). Excluding the mode shape from the USiS solution at 27 m/s, the mode shapes for the structure below a freestream velocity of 29 m/s are of similar form to the equivalent reflected mode shapes (i.e., multiply the mode shape by a scale factor of -1) of the 0.0508 mm monolithic SCF (see Fig. 5.14(a)).<sup>7</sup> At a freestream velocity of 29 m/s, the first mode shape of the structure changes, which aligns with the change in natural frequency observed in Fig. 5.13. Interestingly, this mode shape closely resembles the mode shape obtained from buckling analysis, further reinforcing the assessment that aeroelastic divergence of the 0.04572 mm monolithic SCF is occurring at 29 m/s.

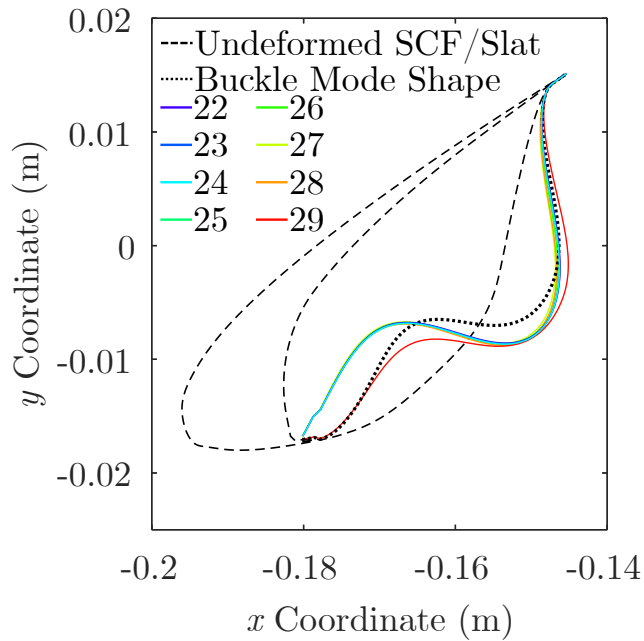
To serve as verification of the divergence behavior, FSI analyses of the 0.0508 mm monolithic SCF are performed. Freestream velocity is initially constant at 25 m/s for 0.125 s to develop flow and then increased to 34 m/s over two time periods: 1) 0.25 s and 2) 0.5 s (see Fig. 5.15). Two linear increases of velocity are considered to assess if transient effects associated with the change in velocity are present and have a significant impact on the displacement. To accommodate the increasing velocity, analysis time step is set to  $1.25 \times 10^{-5}$  s. For the hardware used (standard workstation, 10CPU and 1CPU for the fluid and structure solvers, respectively), the computational cost of the analyses with the 0.25 s and 0.5 s velocity ramps are 84 hr and 130 hr, respectively. Figure 5.15 shows the displacement of the node (marked in red) near the trailing end of the SCF which undergoes to highest deformation during

---

<sup>7</sup>Note that the mode shape from the USiS solution at 27 m/s is of similar form to the nonreflected mode shapes of the 0.0508 mm monolithic SCF.



(a) 0.0508 mm monolithic SCF



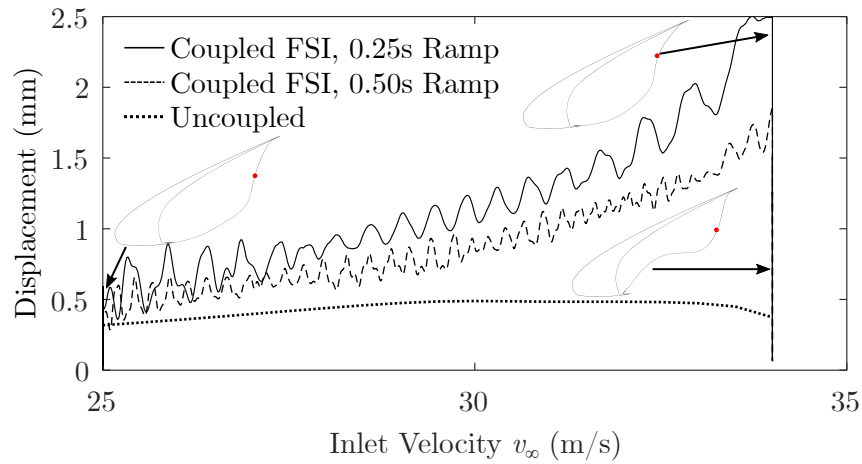
(b) 0.04572 mm monolithic SCF

Figure 5.14: Mode shapes of the deformed SCF for different freestream velocities extracted from eigenvalue analysis along with buckling mode shape.

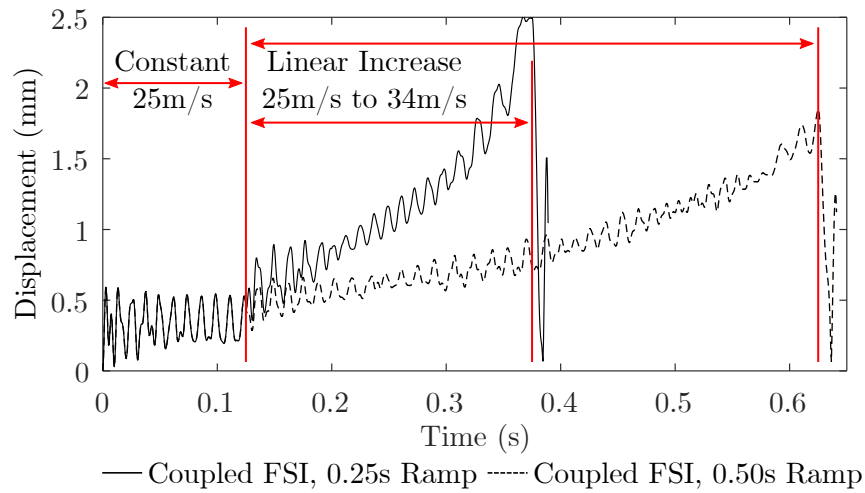
FSI analysis. As shown in Fig. 5.15, the SCF deformation grows with freestream velocity reaching 34 m/s without going unstable. Additionally, the hinge remains in a deployed position. Note that as the velocity is increased towards 34 m/s, the oscillation grows (especially for the 0.25 s case), possibly indicating that the structure is approaching an instability. Shortly after the reaching 34 m/s, the SCF becomes unstable as it is unable to maintain its deployed shape. As the SCF goes unstable, it begins to oscillate significantly and the hinge rotates the SCF into a stowed configuration (see Fig. 5.15(a) at 34 m/s). While both coupled solutions do exhibit a potential divergence at 34 m/s, the magnitude of the displacement is considerably different indicating that transient effects introduced by the linear increase in velocity are impacting the deformation of the SCF. Ideally, the coupled FSI should be performed again with a slower increase in velocity. However, such an analysis would result in even more computational expense. Overall, these results match well with the divergent freestream velocity predicted by the uncoupled method.

Additionally shown in Fig. 5.15 is the SCF displacement corresponding to the USiS solution which does not match either of the coupled FSI solutions. For the uncoupled solution, the displacement of the node increases at a much lower rate compared to the coupled solutions till  $\approx 30$  m/s. Above 30 m/s, the displacement of this node is approximately constant. Note that based on Fig. 5.12 and Fig. 5.10, the overall SCF shape is still changing with velocity. The error between the solutions is attributed to the transient effects associated with the increasing freestream velocity in the coupled FSI solutions which the uncoupled method cannot account for. Additionally, an error of  $\approx 0.1$  mm is already present between the solutions at 25 m/s (see Fig. 5.12) and should be present for all considered freestream velocities. This error could be reduced with surrogate models that are trained while satisfying infill criteria [58]. Finally, the assumption of constant pressure coefficient distribution may

not be valid. Future work should consider developing fluid surrogate models that relate the pressure coefficient distribution to both the shape and freestream velocity for this problem.



(a) SCF Displacement vs. freestream velocity



(b) SCF Displacement vs. time

Figure 5.15: Displacement of SCF during FSI analysis with linearly increasing freestream velocity (c.f. Fig. 5.13) along with uncoupled solution. Displacement corresponds to the node marked in red.

## 6. CONCLUSIONS AND FUTURE WORK

### 6.1 Summary and Conclusions

The goal of this work was to introduce a new uncoupled method for SAA that focuses on problems exhibiting a steady-state equilibrium configuration. Specifically this work focused on: 1) provide motivation for such the method with the SMA SCF, a morphing aerostructure problem, evaluated using the legacy serial approach, 2) mathematically develop the uncoupled method and demonstrate its use for many examples while verifying results with the serial coupling scheme, 3) demonstrate how the uncoupled method could be extended to find accurate SAA solutions for multiple flow conditions and possibly predict free-response behavior and aeroelastic divergence, 4) implement the uncoupled method in an optimization scheme and apply it to a design problem, and 5) demonstrate the uncoupled method with the SMA SCF problem.

FSI analysis with the serial coupling scheme was performed on both model scale and full scale versions of the SMA SCF, a morphing aerostructure that reduces the noise produced by the wing of a typical transport-class aircraft. The fixed-fully deployed load cases demonstrated the large computational cost (52 hr for model scale SCF, 85 hr for full scale SCF) of obtaining a steady equilibrium solution for a single design and flow condition. These runtimes limited assessment of the SCF to a few designs. Additionally, strong coupling between the structure and fluid (especially at full scale) was observed indicating that, to properly understand the behavior of the SCF in flow, FSI analysis had to be performed. FSI analysis of the SCF was also conducted during a full retraction/deployment cycle. To accommodate the complicated mesh deformation and rigid body motion, both overset meshes and a

remeshing scheme were implemented, further complicating the analysis.

This work showed the mathematical development and implementation of the uncoupled method. This method removes the coupling between the fluid and structure solvers and generates functional fits that are fully defined by fitting parameters for both the shape of the body and pressure distribution. Instead of performing a single coupled analysis, many individual and parallelizable structure and fluid analyses are conducted, each with a unique set of fitting parameters. Surrogate models of the fitting parameters are developed from the results of these evaluations. The surrogate models form a system of equations, the solution of which is the uncoupled SAA solution.

The uncoupled method was first demonstrated on multiple examples where the solution at a single flow condition was of interest. Examples included a single degree-of-freedom rigid baffle, a two degree-of-freedom discrete pressure baffle, and a cantilevered deformable baffle. For each case, the uncoupled method was shown to be significantly less computationally expensive (see Table 6.1) and require less solution increments (see Table 6.2) for finding aeroelastic solutions as compared to the serial coupling scheme while still maintaining accuracy relative to the coupled solution. The low degrees of freedom associated with these simple problems also allowed for the intersection of the surrogate models of fitting parameters to be visually shown to be a single point. It was further shown via the deformable baffle example that, in the context of structural design studies, fluid results could be re-used while only structure properties were modified, resulting in new uncoupled solution with little computational expense.

Using an assumption that the pressure coefficient distribution is constant for a given shape within a reasonable range of freestream conditions, the uncoupled method was then demonstrated to find SAA solutions for multiple flow conditions

Table 6.1: Computational times associated with finding aeroelastic solutions in a design study using the serial FSI coupling scheme and the uncoupled method. In parenthesis are the times associated with finding uncoupled solutions if all evaluations (fluid and/or structure) are performed in parallel.

Test Case	Time For Coupled Sol. (min)	Time For First USI Solution (min)	Time For New Structure Solution (min)
1DOF Baffle	36	55 (6)	0.92*
2DOF Baffle	37	82 (5)	2*
2DOF Pressure Baffle	800	1083 (30)	2.8*
Deformable Baffle	180	164 (6)	2*
Aeroleastic Wing	720	378 (25)	5*
Flow Diverter	2,430	6,420 (100)	25*
SMA SCF	1,230	13,580 (240)	188 (1.14)

\*Structure evaluations already performed in parallelized batch manner after [140]. Decrease in computational time possible if all evaluations are further parallelized.

with the problems of a simple rigid circular plate/bar assembly and a cantilevered deformable baffle. With the simple rigid circular plate/bar assembly specifically, features in the **S-C** space were investigated that could cause the uncoupled method to either not converge towards a solution or miss local features in the model response. For the 2DOF-aeroelastic wing example, the uncoupled method was shown to be accurate as compared to both an analytical solution and FSI analysis for multiple freestream velocities and initial angles of attack. Computational efficiency of the uncoupled method was also clearly demonstrated as the computational cost to generate the required surrogate training data for *multiple* flow conditions and initial angles of attack was 2 times less than a single FSI analysis for *one* flow conditions and initial

Table 6.2: Solution increments associated with finding aeroelastic solutions in a design study using the serial FSI coupling scheme and the uncoupled method.

<b>Test Case</b>	$I^f$ ( $I^s$ ) For Coupled Sol.	$I^f$ ( $I^s$ ) For USI Solution	$I^f$ ( $I^s$ ) For New Structure Solution
1DOF Baffle	12,000 (14,000)	17,550 (243**)	0 (243**)
2DOF Baffle	14,360 (2,000)	9,760 (243**)	0 (243**)
2DOF Pressure Baffle	3160 (3160)	6,760 (100**)	0 (100**)
Deformable Baffle	6,000 (42,000)	18,090 (243**)	0 (243**)
Aeroelastic Wing	60,000 (15,000)	17,550 (220**)	0 (220**)
Flow Diverter	48,880 (8,400)	192,000 (7,770**)	0 (7,770**)
SMA SCF	20,000 (10,000)	268,600 (2,290)	0 (1650)

\*\*Structure evaluations performed in parallelized batch manner after [140]. Solution increments listed here are the number of copies of the structure in the single batch analysis multiplied by the number of increments for that analysis.

angles of attack. Furthermore, with the ability to re-use data sets, new designs could be evaluated 144 times faster than the FSI approach.

An optimization framework incorporating the uncoupled method was also proposed that demonstrated its capability to re-use fluid results when the structure domain was modified. With this optimization framework, analysis driven optimization was performed on the design of an SMA flow diverter with objectives of maximizing peak flow velocity through one outlet while minimizing the change in inlet velocity required to divert flow from the same outlet. For each design considered, new structure surrogate models were created from which new uncoupled solutions were obtained for a variety of flow conditions with a *single* set of fluid results. The optimization problem was then modified through the addition of new design variables and consideration of linear materials, further demonstrating the efficiency and utility

of the uncoupled method.

Finally, the uncoupled method was implemented on the SMA SCF. Approximations of the shape and pressure distribution, requiring a large number of fitting parameters, were developed. Using Taguchi DOEs, significant fitting parameters were identified and used to develop fluid and structure surrogate models from LHS evaluations. The SCF was first evaluated with the uncoupled method for a single freestream velocity. Uncoupled solutions were obtained for multiple SCF designs and shown to be accurate as compared coupled solutions within error of less than 2%. While the serial computational cost associated with obtaining the surrogate training data was 11 times more expensive than a FSI analysis for one design, the serial cost to find new solutions with the uncoupled method is 7.2 faster (possibly 1100 times faster if parallelized). Uncoupled solutions of the SCF were also obtained for multiple flow conditions. Both the USI and USiS solutions showed similar values for the fitting parameters for many of the considered freestream conditions. However, the solutions diverged at high velocities possibly due to a lack of sufficient training data. Additionally, the accuracy of the uncoupled solution relative to the one from FSI analysis decreased due to the large bounds considered during surrogate training. However, when examining the free-response behavior of the SCF, the uncoupled method accurately predicted the approximate freestream velocity at which the SCF would undergo aerostatic divergence.

## 6.2 Future Work

Future work shall continue to develop the uncoupled method. The method shall be applied to more complicated aeroelastic problems and to problems from different coupled disciplines including thermomechanics. Complicated aeroelastic problems including 3D problems will enable assessment of the uncoupled method's scalability.

The uncoupled method shall also be extended with estimation of dynamic behavior either by furthering the free-response/divergence predictions from the eigenvalue analysis presented in this work or by the creation of fits for the velocity and acceleration of both the structure and fluid domains. This will be critical for problems such as the SMA flow diverter where the structure and fluid exhibit highly coupled dynamic behavior that is not accounted for in the uncoupled method. Formal optimization studies that compare the uncoupled method to the other optimization schemes such as the MDF/IDF frameworks and adjoint method shall also be considered. As shown in the two plate/bar assembly and the SMA SCF problems, large bounds for the surrogate models can increase the error of the uncoupled method. Incorporation of infill criteria satisfaction during the surrogate model training will reduce this effort. Future work may also consider the implementation of machine learning models to either replace surrogate models or to develop machine learning-informed surrogate models, ensuring that the approximations of the structure and fluid domain are optimized for accuracy.

## REFERENCES

- [1] Dewey H Hodges and G Alvin Pierce. *Introduction to structural dynamics and aeroelasticity*, volume 15. Cambridge University Press, 2011.
- [2] Yuri Bazilevs, Victor M Calo, Yongjie Zhang, and Thomas JR Hughes. Isogeometric fluid–structure interaction analysis with applications to arterial blood flow. *Computational Mechanics*, 38(4-5):310–322, 2006.
- [3] David MacPhee and Asfaw Beyene. Fluid-structure interaction of a morphing symmetrical wind turbine blade subjected to variable load. *International Journal of Energy Research*, 37(1):69–79, 2013.
- [4] RL Campbell and EG Paterson. Fluid–structure interaction analysis of flexible turbomachinery. *Journal of Fluids and Structures*, 27(8):1376–1391, 2011.
- [5] T Tezduyar and Y Osawa. Fluid–structure interactions of a parachute crossing the far wake of an aircraft. *Computer Methods in Applied Mechanics and Engineering*, 191(6-7):717–726, 2001.
- [6] Thuan Lieu, Charbel Farhat, and Michel Lesoinne. Reduced-order fluid/structure modeling of a complete aircraft configuration. *Computer Methods in Applied Mechanics and Engineering*, 195(41-43):5730–5742, 2006.
- [7] Armin Beckert and Holger Wendland. Multivariate interpolation for fluid-structure-interaction problems using radial basis functions. *Aerospace Science and Technology*, 5(2):125–134, 2001.
- [8] Benjamin KS Woods, Iman Dayyani, and Michael I Friswell. Fluid/structure-interaction analysis of the fish-bone-active-camber morphing concept. *Journal of Aircraft*, 52(1):307–319, 2014.

- [9] Adam J Culler and Jack J McNamara. Studies on fluid-thermal-structural coupling for aerothermoelasticity in hypersonic flow. *AIAA Journal*, 48(8):1721–1738, 2010.
- [10] S. Oehler, D. Hartl, T. Turner, and D. Lagoudas. Modeling fluid structure interaction with shape memory alloy actuated morphing aerostructures. *Proceedings of SPIE*, 8343, 2012.
- [11] W. Scholten, R. Patterson, M. Eustice, S. Cook, t. Strganac, T. Turner, and D. Hartl. Aerodynamic and structural evaluation of an sma slat-cove filler using computational and experimental tools at model scale. *ASME 2018 Conference on Smart Materials, Adaptive Structures and Intelligent Systems*, 8129, 2018.
- [12] Pedro BC Leal, Marcelo A Savi, and Darren J Hartl. Aero-structural optimization of shape memory alloy-based wing morphing via a class/shape transformation approach. *Proceedings of the Institution of Mechanical Engineers, Part G: Journal of Aerospace Engineering*, page 0954410017716193.
- [13] D. Willis, E. Israeli, P. Presson, M. Drela, and J. Peraire. A computational framework for fluid structure interaction in biologically inspired flapping flight. *AIAA Paper*, 3473, 2007.
- [14] Toshiyuki Nakata and Hao Liu. A fluid–structure interaction model of insect flight with flexible wings. *Journal of Computational Physics*, 231(4):1822–1847, 2012.
- [15] TCS Rendall and CB Allen. Unified fluid–structure interpolation and mesh motion using radial basis functions. *International Journal for Numerical Methods in Engineering*, 74(10):1519–1559, 2008.

- [16] Gene Hou, Jin Wang, and Anita Layton. Numerical methods for fluid-structure interaction—a review. *Communications in Computational Physics*, 12(2):337–377, 2012.
- [17] Friedrich-Karl Benra, Hans Josef Dohmen, Ji Pei, Sebastian Schuster, and Bo Wan. A comparison of one-way and two-way coupling methods for numerical analysis of fluid-structure interactions. *Journal of applied mathematics*, 2011, 2011.
- [18] Frank M White and Isla Corfield. *Viscous fluid flow*, volume 3. McGraw-Hill New York, 2006.
- [19] K Maute and M Allen. Conceptual design of aeroelastic structures by topology optimization. *Structural and Multidisciplinary Optimization*, 27(1-2):27–42, 2004.
- [20] Marco Evangelos Biancolini, Ubaldo Cella, Corrado Groth, and Massimiliano Genta. Static aeroelastic analysis of an aircraft wind-tunnel model by means of modal rbf mesh updating. *Journal of Aerospace Engineering*, 29(6):04016061, 2016.
- [21] H. Heo, J. Ju, and D. Kim. Compliant cellular structures: Application to a passive morphing airfoil. *Composite Structures*, 106:560–569, 2013.
- [22] Markus Glück, Michael Breuer, Franz Durst, Ansgar Halfmann, and Ernst Rank. Computation of fluid–structure interaction on lightweight structures. *Journal of Wind Engineering and Industrial Aerodynamics*, 89(14-15):1351–1368, 2001.
- [23] P Girodroux-Lavigne, JP Grisval, S Guillemot, M Henshaw, A Karlsson, V Selmin, J Smith, E Teupootahiti, and B Winzell. Comparison of static and

- dynamic fluid-structure interaction solutions in the case of a highly flexible modern transport aircraft wing. *Aerospace Science and Technology*, 7(2):121–133, 2003.
- [24] Pinar Acar and Melike Nikbay. Steady and unsteady aeroelastic computations of hienasd wing for low and high reynolds numbers. In *54th AIAA/ASME/ASCE/AHS/ASC Structures, Structural Dynamics, and Materials Conference*, page 1800, 2013.
- [25] Pedro B Leal, Ted Giblette, Douglas F Hunsaker, and Darren J Hartl. Extended 3d class/shape transformation equations for multicomponent aircraft assemblies. In *AIAA Scitech 2019 Forum*, page 0604, 2019.
- [26] Patrick Le Tallec and Jean Mouro. Fluid structure interaction with large structural displacements. *Computer Methods in Applied Mechanics and Engineering*, 190(24-25):3039–3067, 2001.
- [27] PH Saksono, WG Dettmer, and D Perić. An adaptive remeshing strategy for flows with moving boundaries and fluid–structure interaction. *International Journal for Numerical Methods in Engineering*, 71(9):1009–1050, 2007.
- [28] Bret Stanford, Peter Ifju, Roberto Albertani, and Wei Shyy. Fixed membrane wings for micro air vehicles: Experimental characterization, numerical modeling, and tailoring. *Progress in Aerospace Sciences*, 44(4):258–294, 2008.
- [29] Samuel C Miller, Markus P Rumpfkeil, and James J Joo. Fluid-structure interaction of a variable camber compliant wing. In *53rd AIAA Aerospace Sciences Meeting*, page 1235, 2015.
- [30] Scott T Miller, RL Campbell, CW Elsworth, JS Pitt, and DA Boger. An over-set grid method for fluid-structure interaction. *World Journal of Mechanics*,

- 4(07):217, 2014.
- [31] David W MacPhee and Asfaw Beyene. Experimental and fluid structure interaction analysis of a morphing wind turbine rotor. *Energy*, 90:1055–1065, 2015.
- [32] James H Mabe, Darren J Hartl, Nathan Tichenor, Murphy Zackery, Eric Blades, and Michael Nucci. Fluid-structure interaction modeling of a shape-memory alloy actuated supersonic wind tunnel model. In *AIAA Scitech 2019 Forum*, page 0602, 2019.
- [33] Gaetano Arena, Rainer MJ Groh, Alex Brinkmeyer, Raf Theunissen, Paul M Weaver, and Alberto Pirrera. Adaptive compliant structures for flow regulation. *Proc. R. Soc. A*, 473(2204):20170334, 2017.
- [34] Bret K Stanford and Philip S Beran. Analytical sensitivity analysis of an unsteady vortex-lattice method for flapping-wing optimization. *Journal of Aircraft*, 47(2):647–662, 2010.
- [35] Hogeon Kim, Seunghoon Lee, Eunkuk Son, Seungmin Lee, and Soogab Lee. Aerodynamic noise analysis of large horizontal axis wind turbines considering fluid–structure interaction. *Renewable Energy*, 42:46–53, 2012.
- [36] M Smith, P Wilkin, and M Williams. The advantages of an unsteady panel method in modelling the aerodynamic forces on rigid flapping wings. *Journal of Experimental Biology*, 199(5):1073–1083, 1996.
- [37] Petros Koumoutsakos, Anthony Leonard, and F Pepin. Boundary conditions for viscous vortex methods. *Journal of Computational Physics*, 113(1):52–61, 1994.

- [38] J. Strelec, D. Lagoudas, M. Khan, and J. Yen. Design and implementation of a shape memory alloy actuated reconfigurable airfoil. *Journal of Intelligent Material Systems and Structures*, 14(4-5):257–273, 2003.
- [39] D. MacPhee and A. Beyene. Fluid-structure interaction of a morphing symmetrical wind turbine blade subjected to variable load. *International Journal of Energy Research*, 37(1):69–79, 2011.
- [40] Jae-Sung Bae, T Michael Seigler, and Daniel J Inman. Aerodynamic and static aeroelastic characteristics of a variable-span morphing wing. *Journal of Aircraft*, 42(2):528–534, 2005.
- [41] S. Daynes and P. Weaver. Design and testing of a deformable wind turbine control surface. *Smart Materials and Structures*, 21(10):105019, 2012.
- [42] Joaquim RRA Martins and Andrew B Lambe. Multidisciplinary design optimization: a survey of architectures. *AIAA Journal*, 51(9):2049–2075, 2013.
- [43] K. Maute and G. Reich. Integrated multidisciplinary topology optimization approach to adaptive wing design. *Journal of Aircraft*, 43(1):253–263, 2006.
- [44] Srinivas Kodiyalam and Jaroslaw Sobieszczanski-Sobieski. Multidisciplinary design optimisation-some formal methods, framework requirements, and application to vehicle design. *International Journal of Vehicle Design*, 25(1-2):3–22, 2001.
- [45] Evin J Cramer, John E Dennis, Jr, Paul D Frank, Robert Michael Lewis, and Gregory R Shubin. Problem formulation for multidisciplinary optimization. *SIAM Journal on Optimization*, 4(4):754–776, 1994.
- [46] Thomas P Combes, Arif S Malik, Götz Bramesfeld, and Mark W McQuilling. Efficient fluid-structure interaction method for conceptual design of flexible,

- fixed-wing micro-air-vehicle wings. *AIAA Journal*, 53(6):1442–1454, 2015.
- [47] Joaquim R RA Martins, Juan J Alonso, and James J Reuther. High-fidelity aerostructural design optimization of a supersonic business jet. *Journal of Aircraft*, 41(3):523–530, 2004.
- [48] Jan EK Hoogervorst and Ali Elham. Wing aerostructural optimization using the individual discipline feasible architecture. *Aerospace Science and Technology*, 65:90–99, 2017.
- [49] Alp Dener and Jason E Hicken. Revisiting individual discipline feasible using matrix-free inexact-newton-krylov. In *10th AIAA Multidisciplinary Design Optimization Conference*, page 0110, 2014.
- [50] Yuping He and John Mcphee. Multidisciplinary optimization of multibody systems with application to the design of rail vehicles. *Multibody System Dynamics*, 14(2):111–135, 2005.
- [51] Ruben Perez, Hugh Liu, and Kamran Behdinan. Evaluation of multidisciplinary optimization approaches for aircraft conceptual design. In *10th AIAA/ISSMO multidisciplinary analysis and optimization conference*, page 4537, 2004.
- [52] Timothy W Simpson, Timothy M Mauery, John J Korte, and Farrokh Mistree. Kriging models for global approximation in simulation-based multidisciplinary design optimization. *AIAA Journal*, 39(12):2233–2241, 2001.
- [53] SILVIA Volpi, MATTEO Diez, and FREDERICK Stern. Towards the high-fidelity multidisciplinary design optimization of a 3d composite material hydrofoil. In *Proc. of 7th International Conference on Computational Methods in Marine Engineering (MARINE 2017), Nantes, France, 15-17 May, 2017*.

- [54] Bryan Glaz, Tushar Goel, Li Liu, Peretz P Friedmann, and Raphael T Haftka. Multiple-surrogate approach to helicopter rotor blade vibration reduction. *AIAA Journal*, 47(1):271–282, 2009.
- [55] CC Long, AL Marsden, and Y Bazilevs. Shape optimization of pulsatile ventricular assist devices using fsi to minimize thrombotic risk. *Computational Mechanics*, 54(4):921–932, 2014.
- [56] Ruichen Jin, Wei Chen, and Timothy W Simpson. Comparative studies of metamodelling techniques under multiple modelling criteria. *Structural and Multidisciplinary Optimization*, 23(1):1–13, 2001.
- [57] Rolland L Hardy. Multiquadric equations of topography and other irregular surfaces. *Journal of Geophysical Research*, 76(8):1905–1915, 1971.
- [58] Alexander Forrester, Andy Keane, et al. *Engineering design via surrogate modelling: a practical guide*. John Wiley & Sons, 2008.
- [59] Timothy Simpson, Vasilli Toropov, Vladimir Balabanov, and Felipe Viana. Design and analysis of computer experiments in multidisciplinary design optimization: a review of how far we have come-or not. In *12th AIAA/ISSMO multidisciplinary analysis and optimization conference*, page 5802, 2008.
- [60] Songqing Shan and G Gary Wang. Survey of modeling and optimization strategies to solve high-dimensional design problems with computationally-expensive black-box functions. *Structural and Multidisciplinary Optimization*, 41(2):219–241, 2010.
- [61] Timothy W Simpson, Andrew J Booker, Dipankar Ghosh, Anthony A Giunta, Patrick N Koch, and R-J Yang. Approximation methods in multidisciplinary

- analysis and optimization: a panel discussion. *Structural and Multidisciplinary Optimization*, 27(5):302–313, 2004.
- [62] Shinkyu Jeong, Mitsuhiro Murayama, and Kazuomi Yamamoto. Efficient optimization design method using kriging model. *Journal of Aircraft*, 42(2):413–420, 2005.
- [63] Nestor V Queipo, Raphael T Haftka, Wei Shyy, Tushar Goel, Rajkumar Vaidyanathan, and P Kevin Tucker. Surrogate-based analysis and optimization. *Progress in Aerospace Sciences*, 41(1):1–28, 2005.
- [64] J-C Jouhaud, Pierre Sagaut, Marc Montagnac, and Julien Laurenceau. A surrogate-model based multidisciplinary shape optimization method with application to a 2d subsonic airfoil. *Computers & Fluids*, 36(3):520–529, 2007.
- [65] Shengyin Wang and Michael Yu Wang. Radial basis functions and level set method for structural topology optimization. *International Journal for Numerical Methods in Engineering*, 65(12):2060–2090, 2006.
- [66] Richard E Bellman. *Adaptive control processes: a guided tour*, volume 2045. Princeton university press, 2015.
- [67] Jerome Sacks, William J Welch, Toby J Mitchell, and Henry P Wynn. Design and analysis of computer experiments. *Statistical Science*, pages 409–423, 1989.
- [68] David S Broomhead and David Lowe. Radial basis functions, multi-variable functional interpolation and adaptive networks. Technical report, Royal Signals and Radar Establishment Malvern (United Kingdom), 1988.
- [69] Michael CH Wu, David Kamensky, Chenglong Wang, Austin J Herrema, Fei Xu, Marco S Pigazzini, Aekaansh Verma, Alison L Marsden, Yuri Bazilevs, and Ming-Chen Hsu. Optimizing fluid–structure interaction systems with immerso-

- geometric analysis and surrogate modeling: Application to a hydraulic arresting gear. *Computer Methods in Applied Mechanics and Engineering*, 316:668–693, 2017.
- [70] Ricardo M Paiva, André R D. Carvalho, Curran Crawford, and Afzal Suleman. Comparison of surrogate models in a multidisciplinary optimization framework for wing design. *AIAA Journal*, 48(5):995–1006, 2010.
- [71] XB Lam, YS Kim, AD Hoang, and CW Park. Coupled aerostructural design optimization using the kriging model and integrated multiobjective optimization algorithm. *Journal of Optimization Theory and Applications*, 142(3):533–556, 2009.
- [72] Mengchuang Zhang, Wenxuan Gou, Lei Li, Fan Yang, and Zhufeng Yue. Multidisciplinary design and multi-objective optimization on guide fins of twin-web disk using kriging surrogate model. *Structural and Multidisciplinary Optimization*, 55(1):361–373, 2017.
- [73] Silvia Volpi. High-fidelity multidisciplinary design optimization of a 3d composite material hydrofoil. 2018.
- [74] Anoop A Mullur and Achille Messac. Extended radial basis functions: more flexible and effective metamodeling. *AIAA Journal*, 43(6):1306–1315, 2005.
- [75] Anoop A Mullur and Achille Messac. Metamodeling using extended radial basis functions: a comparative approach. *Engineering with Computers*, 21(3):203, 2006.
- [76] Michael Eldred and Daniel Dunlavy. Formulations for surrogate-based optimization with data fit multifidelity and reduced-order models. In *11th*

- AIAA/ISSMO Multidisciplinary Analysis and Optimization Conference*, page 7117, 2006.
- [77] Earl H Dowell and Kenneth C Hall. Modeling of fluid-structure interaction. *Annual Review of Fluid Mechanics*, 33(1):445–490, 2001.
- [78] David J Lucia, Philip S Beran, and Walter A Silva. Reduced-order modeling: new approaches for computational physics. *Progress in Aerospace Sciences*, 40(1-2):51–117, 2004.
- [79] David Amsallem and Charbel Farhat. Interpolation method for adapting reduced-order models and application to aeroelasticity. *AIAA Journal*, 46(7):1803–1813, 2008.
- [80] Rajan Filomeno Coelho, Piotr Breitkopf, and Catherine Knopf-Lenoir. Model reduction for multidisciplinary optimization-application to a 2d wing. *Structural and Multidisciplinary Optimization*, 37(1):29–48, 2008.
- [81] Jaime G Carbonell, Ryszard S Michalski, and Tom M Mitchell. An overview of machine learning. In *Machine Learning*, pages 3–23. Elsevier, 1983.
- [82] David Amsallem, Julien Cortial, and Charbel Farhat. Towards real-time computational-fluid-dynamics-based aeroelastic computations using a database of reduced-order information. *AIAA Journal*, 48(9):2029–2037, 2010.
- [83] Gang Chen, Yingtao Zuo, Jian Sun, and Yueming Li. Support-vector-machine-based reduced-order model for limit cycle oscillation prediction of nonlinear aeroelastic system. *Mathematical Problems in Engineering*, 2012, 2012.
- [84] Samy Missoum, Christoph Dribusch, and Philip Beran. Reliability-based design optimization of nonlinear aeroelasticity problems. *Journal of Aircraft*, 47(3):992–998, 2010.

- [85] Christoph Dribusch, Samy Missoum, and Philip Beran. A multifidelity approach for the construction of explicit decision boundaries: application to aeroelasticity. *Structural and Multidisciplinary Optimization*, 42(5):693–705, 2010.
- [86] Helmut Sobieczky. Parametric airfoils and wings. In *Recent development of aerodynamic design methodologies*, pages 71–87. Springer, 1999.
- [87] Shigeru Obayashi, Daisuke Sasaki, Yukishiro Takeguchi, and Naoki Hirose. Multiobjective evolutionary computation for supersonic wing-shape optimization. *IEEE Transactions on Evolutionary Computation*, 4(2):182–187, 2000.
- [88] Jerome Lepine, Jean-Yves Trepanier, and Francois Pepin. Wing aerodynamic design using an optimized nurbs geometrical representation. In *38th Aerospace Sciences Meeting and Exhibit*, page 669, 2000.
- [89] Pedro BC Leal and Darren J Hartl. Structurally consistent class/shape transformation equations for morphing airfoils. *Journal of Aircraft*, pages 1–12, 2018.
- [90] Brenda M Kulfan. Recent extensions and applications of the ‘cst’ universal parametric geometry representation method. *The Aeronautical Journal*, 114(1153):157–176, 2010.
- [91] Tong Zhao, Yufei Zhang, Haixin Chen, Yingchun Chen, and Miao Zhang. Supercritical wing design based on airfoil optimization and 2.75 d transformation. *Aerospace Science and Technology*, 56:168–182, 2016.
- [92] Brenda Kulfan. New supersonic wing far-field composite-element wave-drag optimization method. *Journal of Aircraft*, 46(5):1740–1758, 2009.

- [93] Robert Christie, Alexander Heidebrecht, and David MacManus. An automated approach to nacelle parameterization using intuitive class shape transformation curves. *Journal of Engineering for Gas Turbines and Power*, 139(6):062601, 2017.
- [94] Brenda M Kulfan. Universal parametric geometry representation method. *Journal of Aircraft*, 45(1):142–158, 2008.
- [95] W. Gleine, K. Mau, and U. Carl. Aerodynamic noise reducing structure for aircraft wing slats. US Patent 6,394,396, 2002.
- [96] C. Streett, J. Casper, D. Lockard, M. Khorrami, R. Stoker, R. Elkoby, W. Wennenman, and J. Underbrink. Aerodynamic noise reduction for high-lift devices on a swept wing model. *AIAA Paper*, 212, 2006.
- [97] W. Horne, K. James, T. Arledge, P. Soderman, N. Burnside, and S. Jaeger. Measurements of 26 percent-scale 777 airframe noise in the nasa ames 40 by 80 foot wind tunnel. *AIAA Paper*, 2810, 2005.
- [98] T. Imamura, H. Ura, Y. Yokokawa, S. Enomoto, K. Yamamoto, and T. Hirai. Designing of slat cove filler as a noise reduction device for leading-edge slat. *AIAA Paper*, 3473, 2007.
- [99] W. Scholten, D. Hartl, T. Turner, and R. Kidd. Development and analysis-driven optimization of a superelastic slat-cove filler for airframe noise reduction. *AIAA Journal*, 54(3):1078–1094, 2015.
- [100] D. Lagoudas (Editor). *Shape Memory Alloys: Modeling and Engineering Applications*. Springer Science+Business Media LCC, New York, NY, 2008.
- [101] D. Hartl and D. Lagoudas. Aerospace applications of shape memory alloys. *Proceedings of the Institution of Mechanical Engineers, Part G: Journal of*

- Aerospace Engineering*, 221(4):535–552, 2007.
- [102] L. Campanile. Lightweight shape-adaptable airfoils: A new challenge for an old dream. In D. Wagg, I. Bond, P. Weaver, and M. Friswell, editors, *Adaptive Structures: Engineering Applications*, pages 89–135. John Wiley and Sons, Chichester, UK, 2007.
- [103] D. Lagoudas, Z. Bo, and M. Qidwai. A unified thermodynamic constitutive model for sma and finite element analysis of active metal matrix composites. *Mechanics of Composite Materials and Structures*, 3(2):153–179, 1996.
- [104] F Auricchio and E Sacco. A one-dimensional model for superleastic shape-memory alloys with different elastic properties between austenite and martensite. *International Journal of Non-Linear Mechanics*, 32(6):1101–1114, 1997.
- [105] D. Lagoudas, D. Hartl, Y. Chemisky, L. Machado, and P. Popov. Constitutive model for the numerical analysis of phase transformation in polycrystalline shape memory alloys. *International Journal of Plasticity*, 32:155–183, 2012.
- [106] ASTM International. E345:standard test methods of tension testing of metallic foil. 2016.
- [107] W. Scholten, R. Patterson, Q. Chapelon, D. Hartl, T. Strganac, and T. Turner. Computational and experimental fluid-structure interaction assessment of a high-lift wing with a slat-cove filler for noise reduction. In *AIAA Scitech 2017 Forum*, page 0732, 2020.
- [108] A. Bertram. *Elasticity and Plasticity of Large Deformations: An Introduction*. Springer Science+Business Media LCC, New York, NY, 2005.
- [109] Software Cradle Co., Ltd., Woodlands Hills, CA. *SC/Tetra User’s Guide*, 2015.

- [110] F. Menter. Zonal two equation  $k-\omega$  turbulence models for aerodynamic flows. *AIAA Paper*, 2906, 1993.
- [111] David C. Wilcox. *Turbulence Modeling for CFD*. DCW Industries, Inc., 1998.
- [112] J. Vassberg, M. DeHann, S. Rivers, and R. Wahls. Development of a common research model for applied cfd validation studies. *AIAA Paper*, 6919, 2008.
- [113] D. Lacy and A. Sclafani. Development of the high lift common research model (hl-crm): A representative high lift configuration for transonic transports. *54th AIAA Aerospace Sciences Meeting*, (AIAA 2016-0308), 2016.
- [114] Dassault Systemes of America Corp., Woodlands Hills, CA. *Analysis User's Manual*, 2011.
- [115] T. Turner and D. Long. Development of a sma-based, slat-gap filler for airframe noise reduction. *AIAA*, (AIAA 2015-0730), 2015.
- [116] G. Arena, W. Scholten, R. Groh, D. Pirrera, T. Turner, and D. Hartl. A tailored nonlinear slat-cove filler for airframe noise reduction. *ASME 2018 Conference on Smart Materials, Adaptive Structures and Intelligent Systems*, 8079, 2018.
- [117] G. Arena, W. Scholten, R. Groh, A. Pirrera, T. Turner, and D. Hartl. Tailoring the superelastic response of a deployable slat-cove filler for airframe noise reduction, in development. 2020.
- [118] Rainer M J Groh, Daniele Avitabile, and Alberto Pirrera. Generalised path-following for well-behaved nonlinear structures. *Computer Methods in Applied Mechanics and Engineering*, 331:394–426, 2018.

- [119] GA Bibo, PJ Hogg, and M Kemp. Mechanical characterisation of glass-and carbon-fibre-reinforced composites made with non-crimp fabrics. *Composites Science and Technology*, 57(9-10):1221–1241, 1997.
- [120] PD Soden, MJ Hinton, and AS Kaddour. Lamina properties, lay-up configurations and loading conditions for a range of fibre reinforced composite laminates. In *Failure Criteria in Fibre-Reinforced-Polymer Composites*, pages 30–51. Elsevier, 2004.
- [121] Gaetano Arena, Rainer M J Groh, Alberto Pirrera, William Scholten, Darren Hartl, and Travis Turner. A tailored nonlinear slat-cove filler for airframe noise reduction. In *ASME 2018 Conference on Smart Materials, Adaptive Structures and Intelligent Systems*, pages V001T03A017–V001T03A017. American Society of Mechanical Engineers, 2018.
- [122] E Llorente, A Gorostidi, M Jacobs, WA Timmer, X Munduate, and O Pires. Wind tunnel tests of wind turbine airfoils at high reynolds numbers. In *Journal of Physics: Conference Series*, volume 524, page 012012. IOP Publishing, 2014.
- [123] Vincent Chin, David Peters, Frank Spaid, and Robert McGhee. Flowfield measurements about a multi-element airfoil at high reynolds numbers. In *23rd Fluid Dynamics, Plasmadynamics, and Lasers Conference*, page 3137, 1993.
- [124] Kaiser Freudenreich, K Kaiser, AP Schaffarczyk, H Winkler, and B Stahl. Reynolds number and roughness effects on thick airfoils for wind turbines. *Wind Engineering*, 28(5):529–546, 2004.
- [125] Robert McLean Pinkerton. *The variation with Reynolds number of pressure distribution over an airfoil section*. US Government Printing Office, 1938.

- [126] Junhui Huang, Thomas C Corke, and Flint O Thomas. Plasma actuators for separation control of low-pressure turbine blades. *AIAA journal*, 44(1):51–57, 2006.
- [127] E Baydar and Y Ozmen. An experimental and numerical investigation on a confined impinging air jet at high reynolds numbers. *Applied Thermal Engineering*, 25(2-3):409–421, 2005.
- [128] Y Qiu, Y Sun, Y Wu, and Y Tamura. Effects of splitter plates and reynolds number on the aerodynamic loads acting on a circular cylinder. *Journal of Wind Engineering and Industrial Aerodynamics*, 127:40–50, 2014.
- [129] FE Ames, NJ Fiala, and JD Johnson. Gill slot trailing edge heat transfer: Effects of blowing rate, reynolds number, and external turbulence on heat transfer and film cooling effectiveness. In *ASME Turbo Expo 2007: Power for Land, Sea, and Air*, pages 351–362. American Society of Mechanical Engineers Digital Collection, 2007.
- [130] Ira H Abbott and Albert E Von Doenhoff. *Theory of wing sections: including a summary of airfoil data*. Courier Corporation, 2012.
- [131] Rajan Filomeno Coelho, Piotr Breitkopf, Catherine Knopf-Lenoir, and Pierre Villon. Bi-level model reduction for coupled problems. *Structural and Multidisciplinary Optimization*, 39(4):401–418, 2009.
- [132] Jack J McNamara, Andrew R Crowell, Peretz P Friedmann, Bryan Glaz, and Abhijit Gogulapati. Approximate modeling of unsteady aerodynamics for hypersonic aeroelasticity. *Journal of Aircraft*, 47(6):1932–1945, 2010.
- [133] Kirk R Brouwer and Jack J McNamara. Generalized treatment of surface deformation for high-speed computational fluid dynamic surrogates. *AIAA*

- Journal*, pages 1–12, 2019.
- [134] Abhijit Gogulapati, Kirk R Brouwer, XQ Wang, Raghavendra Murthy, Jack J McNamara, and Marc P Mignolet. Full and reduced order aerothermoelastic modeling of built-up aerospace panels in high-speed flows. In *58th AIAA/ASCE/AHS/ASC Structures, Structural Dynamics, and Materials Conference*, page 0180, 2017.
- [135] Gert-Martin Greuel and Gerhard Pfister. *A Singular introduction to commutative algebra*. Springer Science & Business Media, 2012.
- [136] David Eisenbud and E Graham Evans. Every algebraic set in space is the intersection of hypersurfaces. *Inventiones Mathematicae*, 19(2):107–112, 1973.
- [137] James Lambers and Amber Sumner. *Explorations in Numerical Analysis*. World Scientific Publishing Company, 2018.
- [138] Robin Hartshorne. *Algebraic geometry*, volume 52. Springer Science & Business Media, 2013.
- [139] William Fulton. *Intersection theory*, volume 2. Springer Science & Business Media, 2013.
- [140] Brent R Bielefeldt, Darren J Hartl, and Ergun Akleman. L-system-generated topology optimization of compliant mechanisms using graph-based interpretation. In *ASME 2018 International Design Engineering Technical Conferences and Computers and Information in Engineering Conference*. American Society of Mechanical Engineers Digital Collection, 2018.
- [141] William Scholten and Darren J Hartl. An uncoupled method for fluid-structure interaction analysis with application to aerostructural design. In *AIAA Scitech 2020 Forum*, page 1635, 2020.

- [142] Siemens Digital Industries Software. *StarCCM+ User's Manual*, 2019.
- [143] Gaetano Arena, Rainer MJ Groh, Alex Brinkmeyer, Raf Theunissen, Paul M. Weaver, and Alberto Pirrera. Adaptive compliant structures for flow regulation. *Proceedings of the Royal Society A: Mathematical, Physical and Engineering Sciences*, 473(2204):20170334, 2017.
- [144] Michael H Kutner, Christopher J Nachtsheim, John Neter, William Li, et al. *Applied linear statistical models*, volume 5. McGraw-Hill Irwin New York, 2005.
- [145] William David Scholten. Analysis and wind tunnel testing of a superelastic slat-cove filler for airframe noise reduction. Master's thesis, 2016.
- [146] Kalyanmoy Deb. *Multi-objective optimization using evolutionary algorithms*, volume 16. John Wiley & Sons, 2001.
- [147] Frank M White. *Fluid Mechanics, 5th edition*. McGraw-Hill Education, 2015.

## APPENDIX A

### MODEL SCALE SCF: FLUID MESH STUDIES, HINGE PLACEMENT OPTIMIZATION, AND FLAP KINEMATICS

#### A.1 Mesh and Prism Layer Studies

##### *A.1.1 Mesh Study*

Mesh refinement studies are conducted on the CFD model in the fully deployed with SCF configuration at  $12^\circ$  angle of attack in order to balance the objectives of computational accuracy and expense. Note, that for this model, the main wing, high-lift devices, and surrounding fluid are incorporated into a single mesh. It is assumed that obtaining a refined mesh for this configuration would be sufficient for obtaining accurate results for other configurations and angles of attack. The mesh study focuses on setting the mesh sizes of the outer, middle and inner regions. During the study, the mesh size for one region is changed while the mesh sizes for the other two regions are held constant at a baseline size (25.6 mm, 6.4 mm and 0.8 mm for the outer, middle and inner regions, respectively). These baseline sizes are established by chosen mesh sizes from a previous mesh study of the CRM wing [145]. This study is conducted prior to the study of the prism layer so the following default parameters are used: first layer thickness of 0.04 mm, variation of thickness of 1.1, 10 prism layers (resulting total thickness is 0.637 mm). In addition, inlet turbulence is set to default values ( $k=0.0001 \text{ m}^2/\text{s}^2$  and  $\varepsilon = 0.0001 \text{ m}^2/\text{s}^3$ ). During this study, changes in both the lift and drag coefficient are examined. Tables A.1, A.2 and A.3 show the results of the mesh studies. In general, a more refined mesh is more computationally expensive. For all meshes considered during the outer and middle region studies, both

the lift and drag coefficient did not significantly change indicating that a coarse mesh in those regions is sufficient to capture the flow effects. However, each refinement of the inner mesh region results in a large change of both lift and drag coefficients. This is expected since the prism layer elements (and thus the boundary layer) are directly affected by the mesh size of the inner region. A prism layer study would better capture the boundary layer and thus the flow near the wall than significant mesh refinement of the inner region. Based on the low variation of lift coefficient, the mesh sizes for the outer and middle regions are set to 25.6 mm and 3.2 mm, respectively. The mesh size for the inner region is set to 0.8 mm since prism layer studies would better refine the mesh near the surface of the wing. This refined mesh results in a lift coefficient of 2.39 and a drag coefficient of 0.31. Note that in the overset mesh version of the model, the inner region in the vicinity of the slat and flap are refined to 0.4 mm to improve interpolation between the master and slave meshes.

Table A.1: Mesh study of outer region.

<b>Element Size (mm)</b>	$C_L$	$C_D$	<b>% change in <math>C_L</math></b>	<b>% change in <math>C_D</math></b>	<b>Time (hr)</b>
25.6	2.42	0.31	-	-	6.92
12.8	2.39	0.32	1.12	-0.74	7.33
6.4	2.4	0.31	-0.51	0.30	6.45

### *A.1.2 Prism Layer Study*

Prism layer elements are inserted along the surface of the wing and tunnel wall in order to improve the calculation of the boundary layer. Accuracy of the prism

Table A.2: Mesh study of middle region.

<b>Element Size (mm)</b>	$C_L$	$C_D$	<b>% change in <math>C_L</math></b>	<b>% change in <math>C_D</math></b>	<b>Time (hr)</b>
6.4	2.42	0.31	-	-	6.92
3.2	2.38	0.31	1.59	-0.06	7.22
1.6	2.34	0.31	1.68	0.05	9.38
0.8	2.34	0.30	-0.20	3.31	17.60

Table A.3: Mesh study of inner region.

<b>Element Size (mm)</b>	$C_L$	$C_D$	<b>% change in <math>C_L</math></b>	<b>% change in <math>C_D</math></b>	<b>Time (hr)</b>
0.8	2.42	0.31	-	-	6.92
0.4	2.69	0.30	-11.36	5.51	19.0
0.2	2.80	0.29	-3.81	3.16	61.25

layer is dependent on the selection of the prism layer parameters: the thickness of the first layer, change of thickness between layers and total number of layers, and in turn overall thickness of the prism layer. A study of the prism layer is conducted to find a prism layer that sufficiently captures the boundary layer across the surface of the wing. As with the mesh study, it is assumed that a refined prism layer for one configuration would be sufficient for all other configurations.

The first part of the prism layer study examines the effect of the total prism layer thickness on lift and drag coefficients. During this portion of the study, the thickness of the first layer is set to 0.04 mm while the number of layers and variation of thickness

are adjusted to achieve different total thicknesses and keep the thickness of the last layer similar to the element size of the inner region. As shown in Table A.4, the lift and drag coefficients converge as the total thickness of the prism layer is increased, thus a total thickness of 3.05 mm is chosen.

Table A.4: Total thickness of prism layer study.

<b>Total Thickness (mm)</b>	$C_L$	$C_D$	<b>% change in <math>C_L</math></b>	<b>% change in <math>C_D</math></b>	<b>Time (hr)</b>
0.637	2.39	0.31	-	-	7.83
1.04	2.64	0.30	10.69	-5.40	8.0
1.54	2.73	0.30	3.47	0.15	8.0
2.02	2.76	0.30	0.74	-0.10	7.5
2.56	2.77	0.30	0.54	0.51	8.38
3.05	2.78	0.30	0.29	0.35	8.12

The second part of the prism layer study examines the effect of the first layer thickness on flow results. In this portion of the study, the thickness of the first layer is modified while a total prism layer thickness of 3.05 mm is maintained by adjusting the number of prism layers and variation of thickness. As shown in Table A.5, the drag coefficient is approximately constant for all considered thicknesses while the lift coefficient converges to approximately 2.78 with a thickness of 0.04 mm.

The final part of the prism layer study examines effect of the number of prism layers on flow characteristics. For this portion of the study, first layer thickness and total thickness are fixed at 0.04 mm and 3.05 mm, respectively. To maintain the total prism layer thickness as the number of layers are increased, the variation of thickness

Table A.5: First layer thickness of prism layer study.

<b>First Layer Thickness (mm)</b>	$C_L$	$C_D$	<b>% change in <math>C_L</math></b>	<b>% change in <math>C_D</math></b>	<b>Time (hr)</b>
0.640	2.88	0.30	-	-	5.25
0.320	2.85	0.29	-1.10	-2.83	6.33
0.160	2.82	0.30	-1.05	1.62	9.0
0.080	2.80	0.30	-0.70	-0.21	9.25
0.040	2.78	0.30	-0.68	0.47	8.12
0.030	2.78	0.30	-0.05	0.61	9.18
0.020	2.78	0.30	-0.04	0.32	10.35
0.010	2.77	0.30	-0.16	-0.57	10.81
0.005	2.76	0.30	-0.49	0.65	12.16

is decreased accordingly. As shown in Table A.6, neither the lift or drag coefficient are significantly effected by changes in the number of layers. Based on these results, a low number of prism layers could be used. However, to enable consideration of small mesh sizes of the inner fluid region, the variation of thickness and number of layers are set to 1.0825 and 25, respectively.

## A.2 Hinge Optimization

This section describes the optimization of the hinge in the model scale SMA SCF used in Chapter 2 and Chapter 5. This optimization is included herein to demonstrate familiarity with surrogate modeling and optimization.

The first model scale implementation of the SMA SCF utilized a long hinge (8 mm) with an axis flush with the slat-cove wall [107] for ease of manufacturing. However, when experimentally tested during slat retraction, this hinge configuration caused high contact loading between the SMA SCF and the main wing resulting in

Table A.6: Number of layers and thickness variation of prism layer study.

Variation of Thickness	Number of Layers	$C_L$	$C_D$	% change in $C_L$	% change in $C_D$	Time (hr)
1.42	10	2.77	0.30	-	-	7.13
1.185	16	2.78	0.30	0.19	0.90	8.12
1.125	20	2.78	0.30	0.04	-0.28	10.25
1.0825	25	2.77	0.30	-0.28	0.61	12.33
1.057	30	2.77	0.30	0.05	-0.39	14.25

significant deformation of the slat. This prompted an optimization study to redesign the hinge such that the  $x$  and  $y$  components of the contact loading ( $F_x$  and  $F_y$ ) during slat retraction between the main wing and SCF is minimized.

Instead of building multiple hinge prototypes, optimization is performed on a surrogate for the structural model of the scaled SMA SCF (see Chapter 2 for description of the model).<sup>1</sup> The two design variables considered during this optimization are the location of hinge axis  $\delta_h$  and length of the hinge arm  $l_h$  (see Fig. A.1). To develop the surrogate of the structure model, a 10-level ( $10^2=100$  runs) full factorial DOE is performed. For each considered design in the DOE, slat retraction/deployment is performed. Following each analysis, the maximum contact forces ( $F_{x,max}$  and  $F_{y,max}$ ) normalized by the spanwise length of the SMA SCF and the maximum stress in the SMA flexures ( $\sigma_{max}^{SMA}$ ) are extracted. Using these results, cubic RBFs of the following form are constructed:

<sup>1</sup>Due to the cost associated with slat retraction/deployment analysis (approximately 30 min), optimization on the full structural model is not performed.

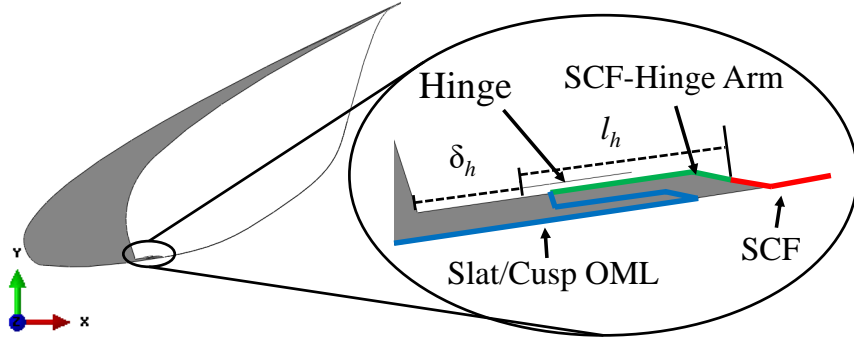


Figure A.1: Illustration of optimization problem for hinge placement.

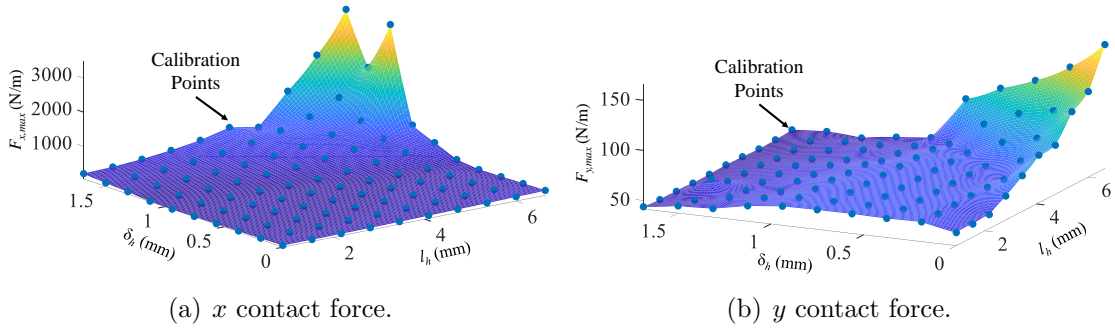


Figure A.2: Surrogate models and calibration points for contact loading.

$$F_{x,max}, F_{y,max}, \sigma_{max}^{SMA} = \sum_{i=1}^{100} w_i ((l_h - l_{h,i})^2 + (\delta_h - \delta_{h,i})^2)^{3/2} + \gamma \cdot \{l_h, \delta_h, 1\}. \quad (\text{A.1})$$

Figure A.2 shows the surrogate models of the maximum contact forces along with the calibration points from the DOE. While the original design ( $l_h=8$  mm,  $\delta_h=0$  mm) is in a region of low  $F_{x,max}$ , it exhibits a high  $F_{y,max}$ , which is believed to be the cause of the large slat deformation. Based on Fig. A.2, it is clear that a small hinge length is desirable.

Multi-objective design optimization is performed over the surrogate models to

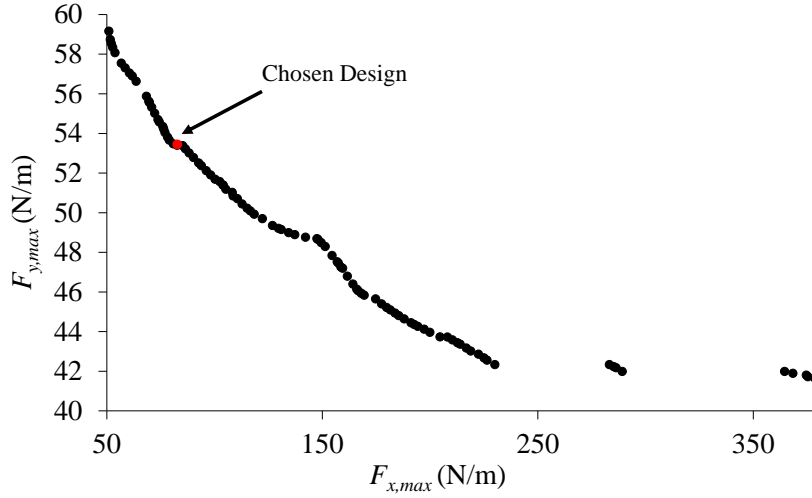


Figure A.3:  $F_{x,max}$ - $F_{y,max}$  objective space from the final generation.

minimize both components of the contact loading using the Non-Sorting Genetic Algorithm II (NSGA-2) [146]. The optimization is conducted for 100 generations with a population of 100 members (100,000 evaluations total). The only constraint considered in this optimization is that the stress in the SMA flexures not exceed the yield stress of the SMA material (700 MPa). Figure A.3 shows the  $F_{x,max}$ - $F_{y,max}$  objective space from the final generation. As seen in the figure, the two objectives are inversely related, i.e., an improvement in one objective results in decreased performance of the other. The chosen design, marked in red, has a  $l_h$  and  $\delta_h$  of 2.4 mm and 1.1 mm, respectively.

### A.3 Flap Kinematics

The motion of the flap during retraction/deployment in the wind tunnel model is constrained by two circular tracks with radii of  $r_a$  and  $r_b$ . Considering the flap to be a rigid body, the motion of the flap can be described as a three-bar linkage problem with lengths  $r_a$ ,  $r_b$ , and  $l_{ab}$  (see Fig. A.4). Specifically, as point  $A$  is translated in the horizontal  $x$  and vertical  $y$  directions along the aft flap track, it is also rotated by

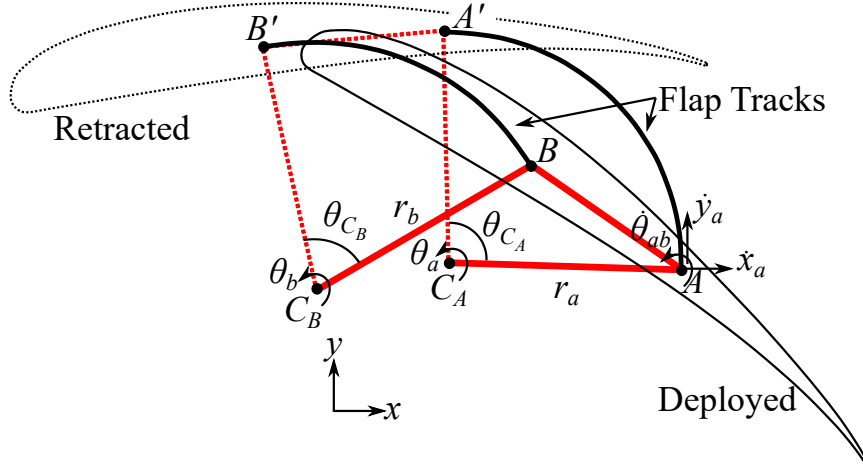


Figure A.4: Illustration of flap motion.

$\theta_{ab}$  to ensure that point  $B$  remains in the forward track. The translational equations of motion for points  $A$  and  $B$  are

$$\dot{x}_a = -\dot{\theta}_a r_a \sin(\dot{\theta}_a t + \theta_{a,0}), \quad (\text{A.2})$$

$$\dot{y}_a = \dot{\theta}_a r_a \cos(\dot{\theta}_a t + \theta_{a,0}), \quad (\text{A.3})$$

$$\dot{x}_b = -\dot{\theta}_b r_b \sin(\dot{\theta}_b t + \theta_{b,0}), \quad (\text{A.4})$$

and

$$\dot{y}_b = \dot{\theta}_b r_b \cos(\dot{\theta}_b t + \theta_{b,0}), \quad (\text{A.5})$$

where  $\theta_{a,0}$  and  $\theta_{b,0}$  are the initial angles between points  $C_A$  and  $A$  and points  $C_B$  and  $B$ , respectively, for either the fully deployed or retracted positions of the flap, and where  $\dot{\theta}_a$  and  $\dot{\theta}_b$  are constant rotation rates applied to points  $C_A$  and  $C_B$ , respectively. These rotation rates are equal to the total rotations of  $C_A$  and  $C_B$  ( $\theta_{C_A}$  and  $\theta_{C_B}$ , respectively) divided by the specified total time  $t_{total}$  required for the flap to fully retract or deploy (i.e.,  $\dot{\theta}_a = \theta_{C_A}/t_{total}$  and  $\dot{\theta}_b = \theta_{C_B}/t_{total}$ ). The rotation  $\theta_{AB}$  applied to

point  $A$  is given by the following equation of motion:

$$\dot{\theta}_{ab} = \frac{(\dot{y}_b - \dot{y}_a)(x_b - x_a) - (y_b - y_a)(\dot{x}_b - \dot{x}_a)}{(x_b - x_a)^2}, \quad (\text{A.6})$$

where  $x_a$  and  $y_a$  are the coordinates of point  $A$ , and where  $x_b$  and  $y_b$  are the coordinates of point  $B$  given by:

$$x_a = r_a \cos(\dot{\theta}_a t + \theta_{a,0}) + x_{C_A}, \quad (\text{A.7})$$

$$y_a = r_a \sin(\dot{\theta}_a t + \theta_{a,0}) + y_{C_A}, \quad (\text{A.8})$$

$$x_b = r_b \cos(\dot{\theta}_b t + \theta_{b,0}) + x_{C_B}, \quad (\text{A.9})$$

and

$$y_b = r_b \sin(\dot{\theta}_b t + \theta_{b,0}) + y_{C_B}, \quad (\text{A.10})$$

where  $x_{C_A}$  and  $y_{C_A}$  are the coordinates of point  $C_A$ , and where  $x_{C_B}$  and  $y_{C_B}$  are the coordinates of point  $C_B$ . These equations of motion for point  $A$  are implemented in user defined functions in SC/Tetra that linearly relate the rotation of point  $C_A$  (and thus the flap) to the time of the analysis. Inputs to the user function is the current time of the analysis and the total time required for full retraction or deployment.

## APPENDIX B

### CLASS/SHAPE TRANSFORMATION METHOD FOR THE DESCRIPTION OF SOLID-FLUID BOUNDARIES

The class/shape transformation (CST) method combines the concepts of class functions and shape functions. To improve the ease of mathematically representing a geometry for two-dimensional cases, the real  $x$ - $y$  coordinates of a geometry are converted through bijective linear transformation into a nondimensional domain  $\psi$ - $\zeta$ . In this nondimensional domain,  $\psi \in [0,1]$  where  $\psi=0$  occurs at  $x=0$ , while  $\psi=1$  occurs at maximum value of  $x$ . The general form of a CST equation is

$$\zeta(\psi) = C(\psi)B(\psi) + \psi\Delta\zeta_{TE} \quad (\text{B.1})$$

where  $C$  is a class function,  $B$  is a shape function, and  $\Delta\zeta$  is the value of  $\zeta$  at  $\psi=1$ . Class functions have been traditionally tuned to define geometric features present in aerostructures. For an aircraft these features could be fuselages, wings, and nacelles. Here, they are more generally used to help define end conditions of a surface in the domain  $\psi$ - $\zeta$ . The class function is

$$C_{N_1}^{N_2}(\psi) = \psi^{N_1}(1 - \psi)^{N_2} \quad (\text{B.2})$$

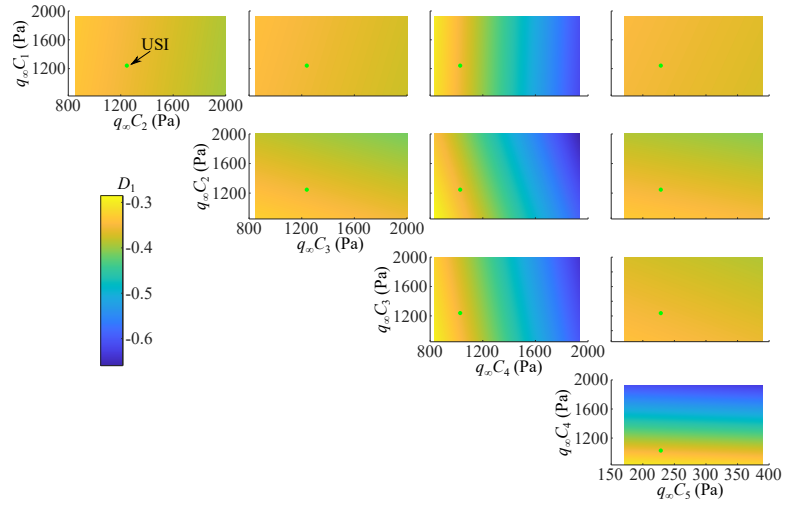
where  $N_1$  and  $N_2$  are parameters used to adjust the function for different features. A surface is further defined by the shape function, which is a summation of Bernstein polynomials  $B_i$  of order  $n$  multiplied by a shape coefficient  $D_i$ . The form of the shape function is

$$B(\psi) = \sum_{i=0}^n D_i B_i(\psi) = \sum_{i=0}^n D_i K_{i,n} \psi^i (1 - \psi)^{n-i} \quad (\text{B.3})$$

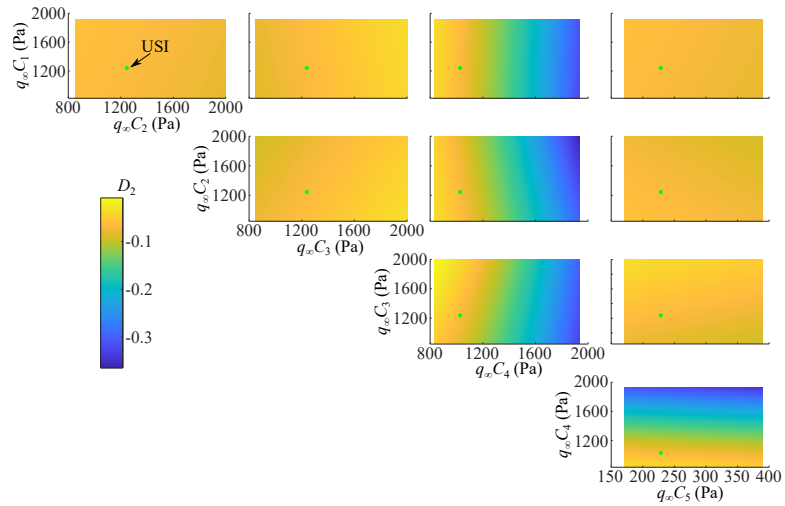
where  $K_{i,n} = i! / (n-i)!$ .

## APPENDIX C

### DEFORMABLE BAFFLE EXAMPLE: SCATTERMATRIX PLOTS

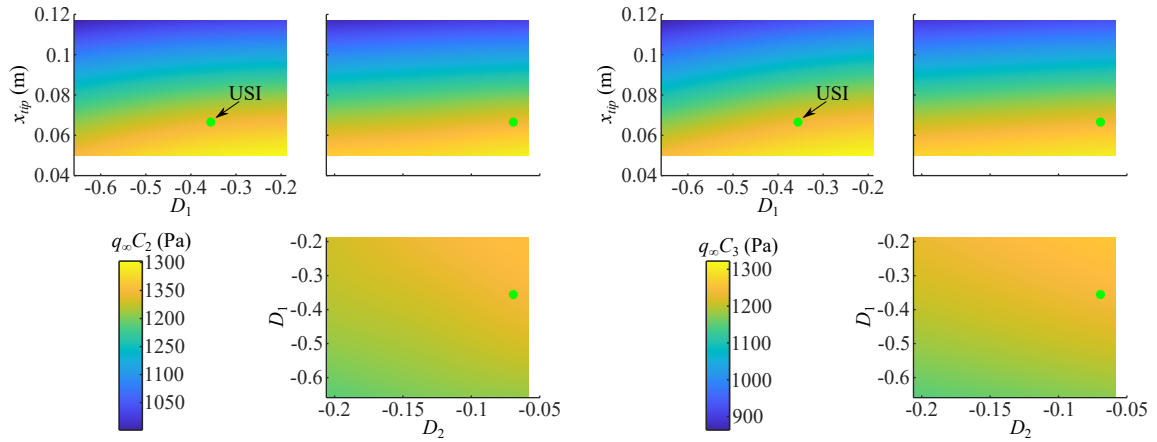


(a) Scatterplot  $D_1$  scatterplot matrix.

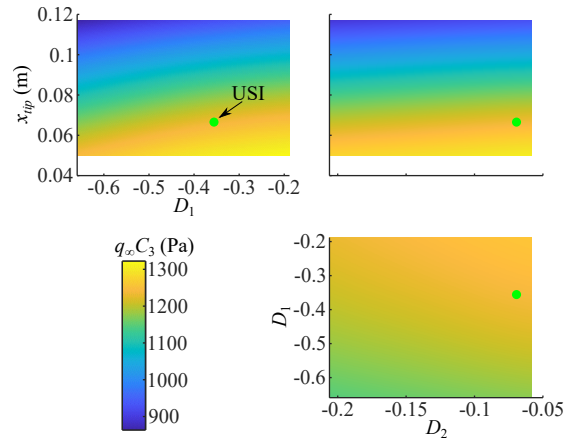


(b) Scatterplot  $D_2$  scatterplot matrix.

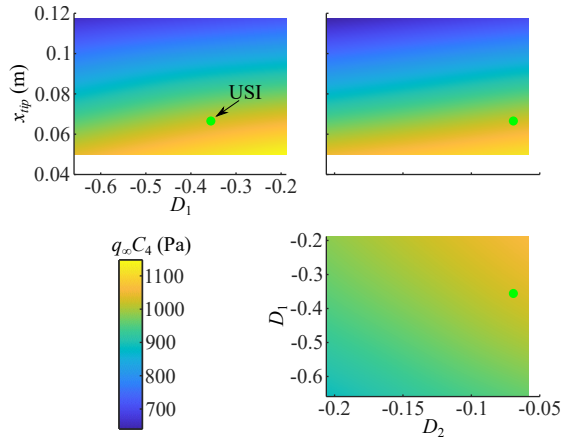
Figure C.1: Scatterplot matrix of  $D_1$  and  $D_2$  contours for all combinations of pressure fitting parameters along with USI solution.



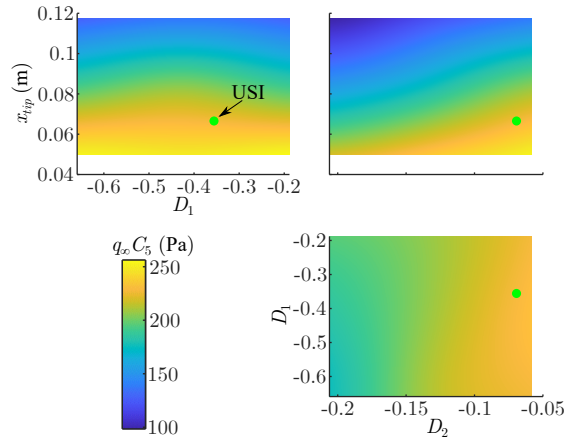
(a) Scatterplot  $C_2$  scatterplot matrix.



(b) Scatterplot  $C_3$  scatterplot matrix.



(c) Scatterplot  $C_4$  scatterplot matrix.



(d) Scatterplot  $C_5$  scatterplot matrix.

Figure C.2: Scatterplot matrix of  $C_2$ - $C_5$  contours for all combinations of shape fitting parameters along with USI solution.

## APPENDIX D

### AEROELASTIC WING EXAMPLE: MESH REFINEMENT STUDY AND FITTING PARAMETER BOUNDS

#### D.1 Mesh Refinement Study

To ensure that the flow field around the aeroelastic wing is accurately modeled, especially since an analytical solution for the aeroelastic problem is available for comparison, mesh refinement studies are performed with the wing at  $6^\circ$  angle of attack in 30 m/s flow. Similar to the mesh refinement study on the CRM wing, it is assumed that a refined mesh for this configuration is suitable for obtaining results for all other configurations.

The first part of the refinement study focuses on the mesh surrounding the airfoil in two regions of the fluid domain: 1) a 2 m by 3 m rectangular region, referred to herein as Region 1, centered around the airfoil and 2) an inner region comprised of a 0.1 m offset from the airfoil surface, referred to herein as Region 2. Note that in the farfield, beyond Region 1, a mesh size of 0.125 m is used as fluid results in this region are fairly uniform and unimportant. Similar to the previous mesh study, the mesh size of one fluid region is fixed (1.95 mm and 15.625 mm for Region 2 and Region 1, respectively) while the other is varied. Prism layer parameters used in this portion of the study are: first layer thickness of 0.65 mm, variation of thickness of 1.1, 3 prism layers (default values). For each mesh considered, lift coefficient is extracted. As shown in Table D.1, a mesh size of 15.625 mm is sufficient for Region 1. However, for Region 2, the lift coefficient changes significantly, indicating that the prism layer mesh now must be refined.

Table D.1: Mesh study of Region 1 for aeroelastic wing example. Region 2 element size set to 1.95 mm.

<b>Element Size (mm)</b>	$C_L$	<b>% change in <math>C_L</math></b>
31.25	0.573	-
15.625	0.513	-10.5
7.8125	0.509	-0.910

Table D.2: Mesh study of Region 2 for aeroelastic wing example. Region 1 element size set to 15.625 mm.

Tables A.1, A.2 and A.3 show the results of the mesh studies.

<b>Element Size (mm)</b>	$C_L$	<b>% change in <math>C_L</math></b>
3.91	0.484	-
1.95	0.513	6.09
0.977	0.596	16.2

The second portion of the mesh study focuses on the prism layer to ensure accurate calculation of the boundary layer on the airfoil. As mentioned in the previous mesh refinement study (see Appendix A), the prism layer is defined by the thickness of the first layer, change of thickness between layers and total number of layers. Based on flat-plate boundary layer theory [147], the thickness of the first layer  $t_1$  is calculated using the following equations:

$$t_1 = \frac{y^+ \mu}{\rho v_\infty} \sqrt{\frac{2}{C_f}} \quad (\text{D.1})$$

$$C_f = \frac{0.026}{Re^{1/7}} \quad (\text{D.2})$$

where  $y^+$  is a nondimensional parameter related to  $t_1$ ,  $\mu$  is the fluid viscosity,  $C_f$  is the coefficient of friction, and  $Re$  is the Reynolds number. For the given geometry, fluid properties, flow speed, and a desired  $y^+$  of 1, the required thickness of the first layer is 0.0125 mm. With the thickness of the first layer determined, the effect of total number of prism layers and change of thickness on the fluid results is now investigated. Both parameters are varied to increase the total prism layer height in 0.5 mm and 1 mm increments until the lift coefficient converges. As shown in Table D.3, the lift coefficient is converging towards 0.64. From these results, the chosen number of layers and thickness variation are 37 and 1.12, respectively.

Table D.3: Prism layer study for aeroelastic wing example.

Tables A.1, A.2 and A.3 show the results of the mesh studies.

<b>Number Layers</b>	<b>Thickness Variation</b>	<b>Total Thickness (mm)</b>	$C_L$	<b>% change in <math>C_L</math></b>
13	1.33	1.5	0.629	-
17	1.24	2	0.630	0.252
22	1.18	2.5	0.633	0.462
26	1.15	3	0.636	0.531
31	1.12	3.5	0.637	0.112
36	1.10	4	0.638	0.191
40	1.09	4.5	0.639	0.105
26	1.18	5.1	0.640	0.111
31	1.15	6.0	0.640	0.043
37	1.12	7.1	0.640	0.062

## D.2 Fitting Parameter Bounds

Table D.4: Surrogate model input bounds of pressure coefficient fitting parameters for pitch-plunge airfoil.

Fitting Parameter	Bounds	Fitting Parameter	Bounds
$C_1^l$	-3.9 - 1.7	$C_1^u$	-4 - 1.65
$C_2^l$	-0.16 - 1.6	$C_2^u$	-6.5 - 1.1
$C_3^l$	-0.6 - 1.6	$C_3^u$	-5.5 - 0.6
$C_4^l$	-0.75 - 1.3	$C_4^u$	-3 - 0.1
$C_5^l$	-0.7 - 0.95	$C_5^u$	-2.5 - 0
$C_6^l$	-0.6 - 0.75	$C_6^u$	-1.85 - 0
$C_7^l$	-0.55 - 0.6	$C_7^u$	-1.5 - 0
$C_8^l$	-0.4 - 0.3	$C_8^u$	-0.85 - 0
$C_9^l$	-0.5 - 1.1	$C_9^u$	-1 - 0.3
$C_{10}^l$	-0.2 - 0.55	$C_{10}^u$	-0.35 - 0.2
$C_{11}^l$	-0.4 - 0.4	$C_{11}^u$	-0.3 - 0.3

## APPENDIX E

### SMA FLOW DIVERTER: MESH STUDY AND SHAPE PARAMETER STUDY

#### E.1 Mesh Refinement Study

As this fluid results are to be used during the optimization of the flow diverter, an accurate and computationally efficient mesh is required. As with previous studies, the same geometry ( $y_{tip}=0.01$  m,  $D_2=0.2$ ,  $l_{sma}=0.1$  m,  $t_{sma}=0.001$  m) and flow condition ( $v_\infty=6$  m/s) is used for each considered mesh. Note that given the aspect ratio of the fluid domain, the overall mesh and prism layer are refined together instead of separate studies. To accurately capture the relevant flow effects while maintaining computational efficiency, mesh sizes are specified for two regions: 1) Region 1, the fluid domain near the flow diverter, splitter, and tunnel walls, and 2) Region 2, the fluid domain surrounding Region 1. For each mesh considered, the sum of forces in  $x$  and  $y$  are extracted.

Similar to the other mesh studies in this work, the surrounding fluid domain is first refined (see Table E.1). Prism layer parameters, first layer thickness, variation of thickness, and number of layers, are set to 0.02 mm, 1.1, and 25, respectively, such that the thickness of the final layer is of similar value to the baseline mesh size of Region 1. Additionally, note that for the given dimensions of the diverter, fluid properties and flow speed, a  $y^+$  of 1 is obtained with first layer thickness of approximately 0.03 mm (see Eq. (D.1)). Thus a first layer thickness of 0.02 mm is sufficient for a baseline prism layer parameter. As shown in Table E.1, the force components are sensitive to the mesh size of Region 2. However, further refinement of the entire fluid domain becomes computationally infeasible. Thus, a size of 1.25 mm

Table E.1: Mesh study of Region 2 for flow diverter. Region 1 mesh size set to 0.3125 mm.

<b>Element Size (mm)</b>	$F_x$ (N)	$F_y$ (N)	% change in $F_x$	% change in $F_y$
5	0.267	1.82	-	-
2.5	0.258	1.74	-3.26	-4.43
1.25	0.256	1.7	-0.846	-2.20

Table E.2: Mesh study total prism layer thickness.

<b>Thickness Variation</b>	<b>Number Layers</b>	<b>Total Thickness (mm)</b>	$F_x$ (N)	$F_y$ (N)	% change in $F_x$	% change in $F_y$
1.21	13	1	0.261	1.763	-	-
1.1355	19	1.5	0.254	1.690	-2.48	-4.10
1.1	25	2	0.256	1.705	0.803	0.870
1.0766	32	2.5	0.255	1.687	-0.484	-1.065

is chosen for Region 2 and focus is shifted towards the mesh near the walls. Total thickness of the prism layer elements is evaluated next. For this portion of the study, mesh sizes of Region 1 and Region 2 are set to 1.25 mm and 0.3125 mm, respectively. To consider different total thicknesses, the number of layers and variation of thickness are modified while the first layer thickness is set to 0.02 mm. As shown in Table E.2, an approximately 1% difference in force components is achieved with a total thickness of 2 mm.

Mesh refinement of Region 1 is then performed. In this portion of the study, variation of thickness and number of layers is changed to 1.4109 and 11, respectively, resulting in a total thickness of 2 mm for the prism layer. As shown in Table E.3,

Table E.3: Mesh study of Region 1 for flow diverter example.

Element Size (mm)	$F_x$	$F_y$	% change in $F_x$	% change in $F_y$
1.25	0.247	1.736	-	-
0.625	0.249	1.757	1.08	1.16
0.3125	0.252	1.780	1.05	1.34

each considered mesh size slightly effects the force components. Further refinement of this region leads to excessively long computational runtimes, so the mesh size is set to 0.3125 mm.

Finally, the prism layer is refined. Note, that for computational efficiency, only the prism layers on the flow diverter and splitter are modified. As the first layer thickness is modified, the number of layers and variation in thickness are modified to maintain a total thickness of 2 mm. As expected (see Table E.4), the forces vary as the prism layer is modified, generally increasing as the thickness decreases. Unfortunately, the force components do not appear fully converged and further refinement leads to excessively long computational runtimes. As this fluid model is only being used in a preliminary optimization a first layer thickness of 0.0025 mm is deemed sufficient.

## E.2 Shape Parameter Study

Both thickness and length of the SMA flow diverter are design variables and affect the outer mold line presented to flow. Due to the curse of dimensionality, it is desirable to only consider shape parameters that influence the pressure distribution on the diverter, reducing the total number of evaluations required to explore the  $\mathbf{S}$  space. To determine if either the thickness or length has a negligible effect on the pressure distribution two studies are performed. Note that in both studies, the shape

Table E.4: Mesh study prism layer.

<b>Thickness Variation</b>	<b>Number Layers</b>	<b>First Layer Thickness (mm)</b>	$F_x$ (N)	$F_y$ (N)	<b>% change in <math>F_x</math></b>	<b>% change in <math>F_y</math></b>
1.104	25	0.02	0.254	1.806	-	-
1.1094	30	0.01	0.252	1.784	-0.90	-1.21
1.1116	36	0.005	0.256	1.834	1.65	2.84
1.1132	42	0.0025	0.260	1.877	1.51	2.33

parameters  $y_{tip}$  and  $D_2$  are set to 0.01 m and 0.2, respectively. For the first study, thickness is held constant while five different diverter lengths are considered. As shown in Fig. E.1, the length has a significant impact on the pressure distribution and thus must be included as a shape fitting parameter. In a similar fashion, for the second study, length is constant while thickness is varied. As shown in Fig. E.2, the thickness only affects the distribution at the tip of the diverter. Due to its overall small effect on the pressure distribution, the thickness is not included as a shape parameter and is held constant for all fluid evaluations.

### E.3 LHS Variation Study

As mentioned in previous sections, an insufficient number of training points and large bounds for the surrogate model may result in the uncoupled method missing local features of the fitting parameter response to different freestream velocities. Additionally, if using LHS as the sampling technique for either the fluid or structure surrogate models, two different LHSs may result in considerably different model response. For optimization of the flow diverter, a low variation in the surrogate models calibrated by an LHS is desired, increasing confidence in the accuracy of the results. This section examines the effect of the LHS on model response.

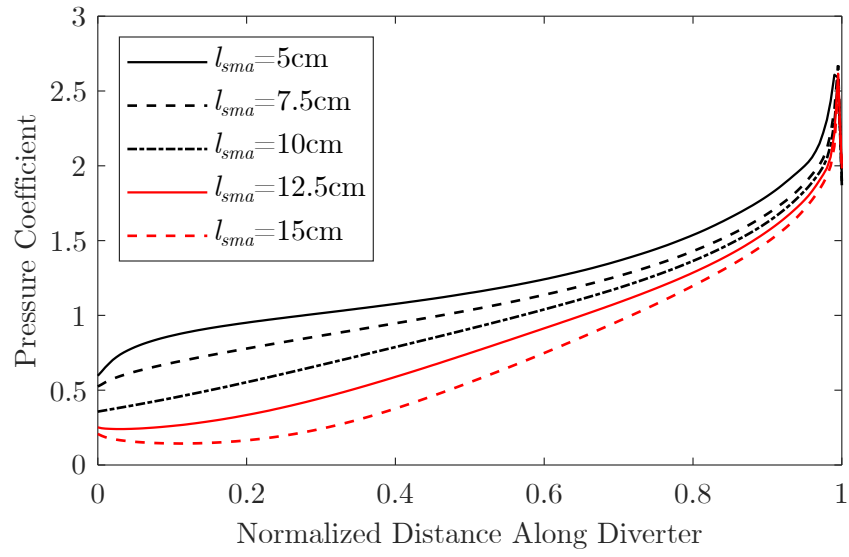


Figure E.1: Pressure coefficient distributions from length study.

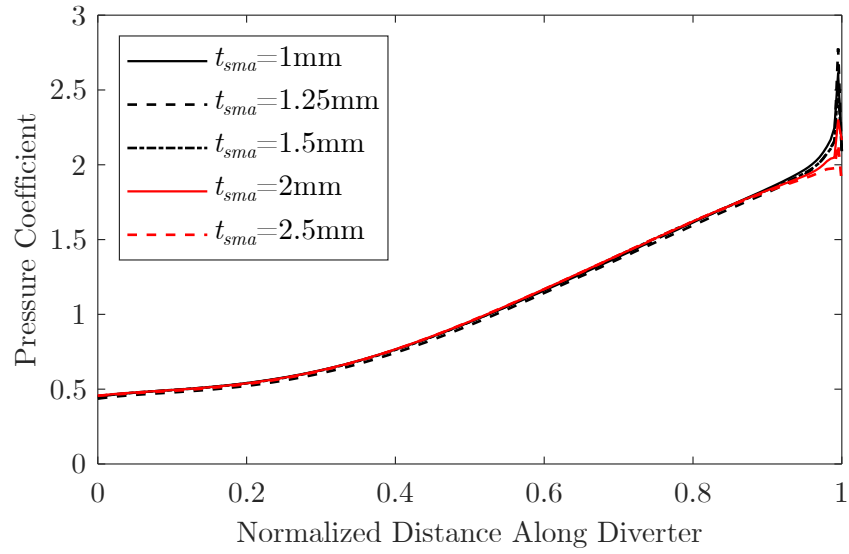


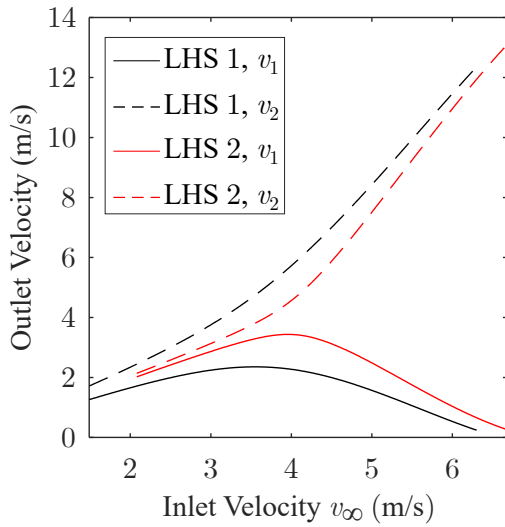
Figure E.2: Pressure coefficient distributions from thickness study.

For this study, a flow diverter with undeformed configuration of  $y_{tip}=5$  mm,  $D_1=0.05$  (cantilever constraint on  $D_1$  not enforced), and  $D_2=0.025$ , and length and thickness of 0.124 m and 2 mm, respectively is considered. Two LHSs on the structure model of the flow diverter are performed with 80 variations (small set for a multi-dimensional problem [56]) of the pressure fitting parameters. During all structure evaluations, the ambient temperature is 300 K and freestream velocity (for dynamic pressure) is 10 m/s. For both LHSs, a structure surrogate model is calibrated. Bounds of the fitting parameters are the same for both samplings. The fluid surrogate model is calibrated from a LHS with 45 variations of  $y_{tip}$ ,  $l_{sma}$ ,  $D_2$ , and  $D_1$ . Table E.5 shows the bounds for both the pressure and shape fitting parameters. Using fixed point iteration, USI solutions are found using each structure surrogate model. As shown in Fig. E.3(a), the USI solutions of the same design for the outlet velocity are considerably different. This is attributed to the low number of sampling points and the large bounds on pressure. From both samples, approximately 70% of the pressure loadings result in the diverter contacting the floor and thus the same values for  $y_{tip}$  and  $D_1$ . This variation in the outlet velocities, from which the optimization objectives are derived, is not acceptable.

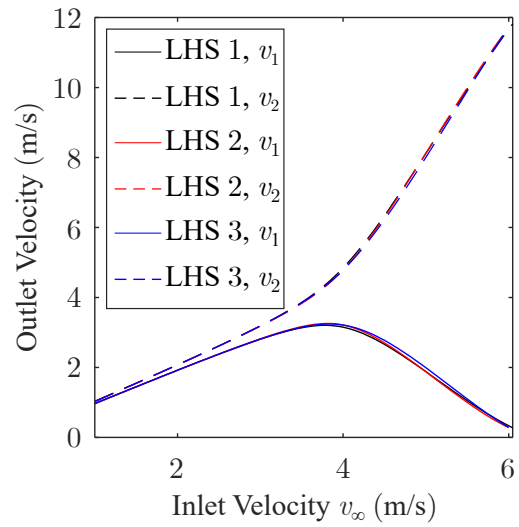
In an effort to reduce the variation in USI results, the freestream velocity applied to the structure is reduced to 8 m/s, decreasing the pressure loading on the diverter, and the number of training points is increased to 136 (LHS with 135 sampling and the undeformed configuration). Three new LHSs are performed using the same bounds for the pressure coefficients (Table E.5). Note for the three samples, approximately 40% of pressure loadings cause the diverter to contact the floor. As shown in Fig. E.3(b), the resulting USI solutions match quite well and are sufficient for the design optimization. The reduced pressure bounds and increased number of points as improved the consistency of the uncoupled solution.

Table E.5: Fitting parameter bounds for LHS variation study.

Fitting Parameters	Bounds	Fitting Parameters	Bounds
$C_1$	-1.55 - 1.9	$C_5$	-1.3 - 3.2
$C_2$	-1.85 - 1.7	$C_6$	0 - 4.3
$C_3$	-1.5 - 1.85	$C_7$	0 - 4.4
$C_4$	-0.75 - 2.5	$C_8$	0 - 4.4
$y_{tip}$ (mm)	2 - 49	$l_{sma}$ (m)	0.069 - 1.25
$D_1$	0 - 1	$D_2$	0 - 1



(a) 80 LHS, large pressure bounds



(b) 135 LHS, low pressure bounds

Figure E.3: Outlet velocity vs. inlet velocity for different structure LHSs.

APPENDIX F

UNCOUPLED SOLUTIONS OF MODEL SCALE SCF

Table F.1: p-value table from structure DOE of the SMA SCF.  $p$ -values in green indicate statistical significance.<sup>1</sup>

$C/D$	$D_1$	$D_2$	$D_3$	$D_4$	$D_5$	$D_6$	$D_7$	$D_8$	$D_9$	$\theta$
$C_1$	0.959	0.477	0.962	0.955	0.969	0.927	0.988	0.82	0.98	0.526
$C_2$	0.927	0	0.219	0.054	0.234	0.124	0.994	0.359	0.953	0
$C_3$	0.032	0.014	0	0	0.008	0.009	0.985	0.332	0.722	0.005
$C_4$	0.017	0.209	0.006	0.718	0.382	0.111	0.871	0.901	0.384	0.11
$C_5$	1	0.175	0.408	0.999	0.061	0.006	1	0.507	0.932	0.26
$C_6$	0.093	0.742	0.826	0.057	0	0.021	0.663	0.386	0.883	0.98
$C_7$	0.963	0.346	0.451	0.882	0.864	0.683	0.949	0.384	0.75	0.448
$C_8$	0	0.33	0.001	0	0	0.096	0.07	0.893	0.003	0.065
$C_9$	0.348	0.349	0.187	0.998	0.986	0.199	0	0	0	0.338
$C_{10}$	0.881	0.945	0.969	0.372	0.357	0.166	0.013	0.71	0.545	0.978
$C_{11}$	0.896	0.941	1	0.991	0.997	0.996	0.999	0.273	0.985	0.974
$C_{12}$	0.959	0.992	0.999	1	1	0.999	0.995	0.97	0.985	0.998

<sup>1</sup> In Table F.1,  $p$ -values are a measure of significance for the influence of each pressure fitting parameter on each shape fitting parameter.

Table F.2:  $p$ -value table from fluid DOE of the SMA SCF.  $p$ -values in green indicate statistical significance<sup>2</sup>

<b>C/D</b>	$D_1$	$D_2$	$D_3$	$D_4$	$D_5$	$D_6$	$D_7$	$D_8$	$D_9$	$\theta$
$C_1$	0.999	0.243	0.687	0.615	0.838	0.677	0.983	0.974	0.864	0
$C_2$	0.988	0.903	0.23	0.181	0.648	0.333	0.965	0.991	0.7	0
$C_3$	0.989	0.148	0.434	0.445	0.332	0	0.79	0.968	0.747	0.397
$C_4$	0.999	0.792	0.12	0.202	0.863	0	0.629	0.972	0.904	0.968
$C_5$	0.97	0.91	0.234	0.004	0.835	0.003	0.407	0.969	0.745	0.991
$C_6$	0.993	0.862	0.997	0.076	0.08	0	0.914	0.92	0.914	0.986
$C_7$	0.996	0.99	0.872	0.963	0.803	0	0.304	0.942	0.985	0.908
$C_8$	1	0.97	0.927	0.951	0.595	0	0.52	0.996	0.977	0.957
$C_9$	0.985	0.834	0.973	0.842	0.538	0	0.649	0.985	0.974	0.72
$C_{10}$	0.991	0.987	0.989	0.851	0.883	0.916	0.003	0	0.865	0.952
$C_{11}$	0.993	0.997	0.972	0.997	0.996	0.779	0.67	0	0.237	0.99
$C_{12}$	0.808	0.974	0.853	0.946	0.852	0.981	0.14	0	0.102	0.814

<sup>2</sup> In Table F.2,  $p$ -values are a measure of significance for the influence of each pressure fitting parameter on each shape fitting parameter.

Table F.3: Pressure and shape fitting parameters for 0.0508 mm monolithic SCF.

<b>Fitting Parameter</b>	<b>FSI (Reference)</b>	<b>USI</b>	<b>USI Error (%)</b>	<b>USiS</b>	<b>USiS Error (%)</b>
(Shape Fitting Parameters)					
$D_1$	0.00003	0.000029	3.33	0.000026	13.33
$D_2$	0.00420	0.00416	1.14	0.00421	0.21
$D_3$	0.00780	0.00776	0.49	0.00770	1.27
$D_4$	0.0186	0.0185	0.29	0.0186	0.42
$D_5$	-0.0201	-0.0199	0.85	-0.0202	0.20
$D_6$	0.0944	0.0942	0.14	0.0945	0.13
$D_7$	-0.0536	-0.0533	0.39	-0.0536	0.15
$D_8$	0.0509	0.0513	0.79	0.0514	1.03
$D_9$	-0.0171	-0.0171	0.35	-0.0172	0.99
$\theta$	0.00332	0.00568	71	0.00524	58
(Pressure Coefficient Fitting Parameters)					
$C_1$	0.684	0.689	0.80	0.698	2.11
$C_2$	0.601	0.600	0.05	0.619	2.99
$C_3$	0.505	0.505	0.04	0.521	3.08
$C_4$	0.518	0.509	1.73	0.523	0.95
$C_5$	0.559	0.543	2.88	0.558	0.16
$C_6$	0.550	0.526	4.27	0.531	3.41
$C_7$	0.523	0.512	2.05	0.519	0.87
$C_8$	0.552	0.542	1.94	0.543	1.61
$C_9$	0.579	0.574	0.75	0.567	1.99
$C_{10}$	0.536	0.507	5.52	0.513	4.31
$C_{11}$	-0.068	-0.179	161.19	-0.212	209
$C_{12}$	-0.114	-0.118	3.50	-0.223	95

Table F.4: Pressure and shape fitting parameters for 0.04572 mm monolithic SCF.

<b>Fitting Parameter</b>	<b>FSI (Reference)</b>	<b>USI</b>	<b>USI Error (%)</b>	<b>USiS</b>	<b>USiS Error (%)</b>
(Shape Fitting Parameters)					
$D_1$	0.000028	0.000028	0	0.000035	25
$D_2$	0.00425	0.00412	2.97	0.00409	3.60
$D_3$	0.00778	0.00746	4.15	0.00780	0.27
$D_4$	0.0190	0.0194	2.01	0.0187	1.72
$D_5$	-0.0221	-0.0228	3.19	-0.0220	0.48
$D_6$	0.0991	0.100	1.26	0.0998	0.68
$D_7$	-0.0605	-0.0600	0.84	-0.0604	0.18
$D_8$	0.0519	0.0525	1.23	0.0531	2.25
$D_9$	-0.0181	-0.0178	1.37	-0.0184	1.79
$\theta$	0.000171	0.0147	8470	0.00986	5667
(Pressure Coefficient Fitting Parameters)					
$C_1$	0.684	0.689	0.80	0.682	0.31
$C_2$	0.587	0.606	3.18	0.616	4.88
$C_3$	0.493	0.512	3.81	0.526	6.69
$C_4$	0.495	0.518	4.80	0.527	6.64
$C_5$	0.534	0.551	3.14	0.562	5.21
$C_6$	0.527	0.524	0.63	0.525	0.40
$C_7$	0.508	0.510	0.39	0.510	0.41
$C_8$	0.534	0.538	0.69	0.534	0.15
$C_9$	0.551	0.566	2.75	0.552	0.20
$C_{10}$	0.573	0.543	5.25	0.548	4.45
$C_{11}$	-0.00626	-0.179	2800	-0.180	2820
$C_{12}$	-0.0789	-0.118	50	-0.236	199

Table F.5: Pressure and shape fitting parameters for multi-thickness SCF.

<b>Fitting Parameter</b>	<b>FSI (Reference)</b>	<b>USI</b>	<b>USI Error (%)</b>	<b>USiS</b>	<b>USiS Error (%)</b>
(Shape Fitting Parameters)					
$D_1$	0.000021	0.000021	0	0.000022	4.76
$D_2$	0.00434	0.00428	1.57	0.00432	0.62
$D_3$	0.0206	0.00710	4.51	0.00714	4.01
$D_4$	-0.0247	0.0206	0.16	0.0206	0.11
$D_5$	-0.0609	-0.0247	0.004	-0.0248	0.53
$D_6$	0.101	0.101	0.17	0.101	0.34
$D_7$	-0.0609	-0.0596	2.21	-0.0600	1.61
$D_8$	0.0499	0.0508	1.88	0.0507	1.61
$D_9$	-0.0176	-0.0175	0.72	-0.0176	0.28
$\theta$	-0.00008	0.00518	6570	0.00267	3430
(Pressure Coefficient Fitting Parameters)					
$C_1$	0.666	0.689	3.50	0.675	1.37
$C_2$	0.587	0.604	2.81	0.604	2.81
$C_3$	0.493	0.518	5.00	0.516	4.78
$C_4$	0.494	0.520	5.15	0.515	4.22
$C_5$	0.534	0.554	3.63	0.552	3.29
$C_6$	0.527	0.530	0.51	0.526	0.25
$C_7$	0.508	0.511	0.62	0.511	0.54
$C_8$	0.534	0.536	0.37	0.536	0.26
$C_9$	0.553	0.564	1.85	0.555	0.29
$C_{10}$	0.567	0.541	4.53	0.553	2.49
$C_{11}$	-0.0118	-0.179	1410	-0.152	1180
$C_{12}$	-0.138	-0.118	14	-0.239	74